

Ministry of Science and Higher Education of the Russian Federation
ITMO University

ISSN 2220-8054

NANOSYSTEMS:
PHYSICS, CHEMISTRY, MATHEMATICS

2024, volume 15 (1)

Наносистемы: физика, химия, математика

2024, том 15, № 1



NANOSYSTEMS:

PHYSICS, CHEMISTRY, MATHEMATICS

ADVISORY BOARD MEMBERS

Chairman: V.N. Vasiliev (*St. Petersburg, Russia*),
V.M. Buznik (*Moscow, Russia*); V.M. Ievlev (*Voronezh, Russia*), P.S. Kop'ev (*St. Petersburg, Russia*), N.F. Morozov (*St. Petersburg, Russia*), V.N. Parmon (*Novosibirsk, Russia*),
A.I. Rusanov (*St. Petersburg, Russia*)

EDITORIAL BOARD

Editor-in-Chief: I.Yu. Popov (*St. Petersburg, Russia*)

Section Co-Editors:

Physics – V.M. Uzdin (*St. Petersburg, Russia*),

Material science – V.V. Gusarov (*St. Petersburg, Russia*); O.V. Al'myasheva (*St. Petersburg, Russia*);

Chemistry – V.K. Ivanov (*Moscow, Russia*),

Mathematics – I.Yu. Popov (*St. Petersburg, Russia*).

Editorial Board Members:

V.M. Adamyan (*Odessa, Ukraine*); A.P. Alodjants (*St. Petersburg, Russia*); S. Bechta (*Stockholm, Sweden*); J. Behrndt (*Graz, Austria*); A. Chatterjee (*Hyderabad, India*); A.V. Chizhov (*Dubna, Russia*); A.N. Enyashin (*Ekaterinburg, Russia*), P.P. Fedorov (*Moscow, Russia*); E.A. Gudilin (*Moscow, Russia*); H. Jónsson (*Reykjavik, Iceland*); A.A. Kiselev (*Durham, USA*); Yu.S. Kivshar (*Canberra, Australia*); S.A. Kozlov (*St. Petersburg, Russia*); P.A. Kurasov (*Stockholm, Sweden*); A.V. Lukashin (*Moscow, Russia*); I.V. Melikhov (*Moscow, Russia*); G.P. Miroshnichenko (*St. Petersburg, Russia*); I.Ya. Mittova (*Voronezh, Russia*); H. Najjar (*Monastir, Tunisia*), Nguyen Anh Tien (*Ho Chi Minh, Vietnam*); V.V. Pankov (*Minsk, Belarus*); K. Pankrashkin (*Orsay, France*); A.V. Ragulya (*Kiev, Ukraine*); V. Rajendran (*Tamil Nadu, India*); A.A. Rempel (*Ekaterinburg, Russia*); V.Ya. Rudyak (*Novosibirsk, Russia*); H.M. Sedighi (*Ahvaz, Iran*); D Shoikhet (*Karmiel, Israel*); M.N. Smirnova (*Moscow, Russia*); P. Stovicek (*Prague, Czech Republic*); V.M. Talanov (*Novocherkassk, Russia*); A.Ya. Vul' (*St. Petersburg, Russia*); A.V. Yakimansky (*St. Petersburg, Russia*), V.A. Zagrebnov (*Marseille, France*).

Editors:

I.V. Blinova; A.I. Popov; A.I. Trifanov; E.S. Trifanova (*St. Petersburg, Russia*),
R. Simoneaux (*Philadelphia, Pennsylvania, USA*).

Address: ITMO University, Kronverkskiy pr., 49, St. Petersburg 197101, Russia.

Phone: +7(812)607-02-54, **Journal site:** <http://nanojournal.ifmo.ru/>,

E-mail: nanojournal.ifmo@gmail.com

AIM AND SCOPE

The scope of the journal includes all areas of nano-sciences. Papers devoted to basic problems of physics, chemistry, material science and mathematics inspired by nanosystems investigations are welcomed. Both theoretical and experimental works concerning the properties and behavior of nanosystems, problems of its creation and application, mathematical methods of nanosystem studies are considered.

The journal publishes scientific reviews (up to 30 journal pages), research papers (up to 15 pages) and letters (up to 5 pages). All manuscripts are peer-reviewed. Authors are informed about the referee opinion and the Editorial decision.

CONTENT

MATHEMATICS

- Y. Bekakra, A. Bouziani
Existence and uniqueness theorem for a weak solution of fractional parabolic problem by the Rothe method 5
- B.I. Andrew, A. Anuradha
A Graph spectral analysis of nonane isomers 16
- I.M. Mavlonov, A.M. Sattarov, S.A. Karimova, F.H. Haydarov
On solutions to nonlinear integral equation of the Hammerstein type and its applications to gibbs measures for continuous spin systems 23
- R.R. Kucharov, T.M. Tuxtamurodova
Non-compact perturbation of the spectrum of multipliers given by a special form 31

PHYSICS

- V.Ya. Rudyak, S.L. Krasnolutskii, E.V. Lezhnev
Molecular dynamics study of nanofluids viscosity with carbon tubes 37
- Nguyen Van Vinh, Nguyen Pham Quynh Anh
Features of surface Bessel plasmon-polaritons in optical anisotropic hyperbolic metamaterials 46
- K.A. Chichay, I.S. Lobanov, V.M. Uzdin
The structure of magnetic domain walls in cylindrical nano- and microwires with inhomogeneous anisotropy 55
- S.V. Belibikhin, N.N. Konobeeva
Extremely short optical pulses in a thin polymer film with carbon nanotubes 60

CHEMISTRY AND MATERIAL SCIENCE

- V.A. Vorotnikov, S.A. Belyakov, A.V. Ivanov, Yu.V. Novikova, A.Yu. Stroeve, V.V. Grebenev, D.N. Khmelenin, O.V. Emelyanova, M.S. Plekhanov, A.V. Kuzmin
Equilibrium of intrinsic and impurity point defects in Ca-doped $\text{Sm}_2\text{Zr}_2\text{O}_7$ 65

P.E. Kazin, A.E. Sleptsova, A.V. Vasiliev, A.A. Eliseev, R.E. Dinnebier, S. Bette Single-domain particles of manganese-for-iron substituted M-type barium hexaferrite: synthesis, crystal structure, and magnetic properties	80
V.P. Tolstoy, E.E. Shilovskikh, L.B. Gulina The effect of Ag(0) colloidal crystals and nanoribbons formation as a result of the redox reaction between Ce(III) and Ag(I) cations occurring on the surface of an aqueous solution of their salts mixture	98
Zh. Liu, S.V. Golodukhina, S.V. Kameneva, A.D. Yapryntsev Fluorination of Eu-doped layered yttrium hydroxides: the role of anionic composition	104
R.Sh. Abiev, A.V. Zdravkov, Yu.S. Kudryashova, A.A. Alexandrov, S.V. Kuznetsov, P.P. Fedorov Synthesis of strontium fluoride nanoparticles in a microreactor with intensely swirling flows	115
A.V. Ankudinov, M.S. Dunaevskiy, A.A. Krasilin, M.M. Khalisov, E.K. Khrapova Determining Young's and shear moduli of a rod-shaped object in an AFM bending test	122
A.V. Kaplin, E.A. Eremina, M.V. Korobov Sorption of polar and non-polar liquids by GO powders according to DSC experiments	130
R.K. Shukla, Anchal Srivastava, Shikha Rani, Nidhi Singh, Vishnu Kumar Dwivedi, Sharda Pandey, Navina Wadhvani Simulation and evaluation of perovskite solar cells utilizing various electron transport layers	135
Information for authors	147

Existence and uniqueness theorem for a weak solution of fractional parabolic problem by the Rothe method

Y. Bekakra^{1,a}, A. Bouziani^{1,2,b}

¹ICOSI Laboratory, Abbes Laghrour University, Khenchela, 04000, Algeria

²L'arbi Ben M'hidi University, Oum El Bouagui, 04000, Algeria

^ayoucef.bekakra@univ-khenchela.dz, ^baefbouziani1963@gmail.com

Corresponding author: Y. Bekakra, youcef.bekakra@univ-khenchela.dz

PACS 02.60–x, 47.11.Bc, 02.30.Jr

ABSTRACT This paper aims to study the existence and uniqueness of a weak solution for the boundary value problem of a time fractional equation involving the Caputo fractional derivative with an integral operator. By utilizing the discretization method, we first derive some a priori estimates for the approximate solutions at the points (x, t_j) . We then evaluate the accuracy of the proposed method to demonstrate that the implemented sequence of α -Rothe functions converges in a certain sense, and its limit is the solution (in a weak sense) of our problem. It must be pointed out that the constructed L1 scheme is designed to approximate the Caputo fractional derivative mentioned in the problem.

KEYWORDS weak solution, a priori estimates, Fractional diffusion equation, Rothe's method

ACKNOWLEDGEMENTS The authors would like to thank the reviewer for his valuable comments and suggestions.

FOR CITATION Bekakra Y., Bouziani A. Existence and uniqueness theorem for a weak solution of fractional parabolic problem by the Rothe method. *Nanosystems: Phys. Chem. Math.*, 2024, **15** (1), 5–15.

1. Introduction

In the beginning, fractional calculus was developed as a pure mathematical concept. In recent decades, its use has expanded into a variety of different fields of science, such as physics, mechanics, economics, and engineering (see, for instance, [1–4]).

The time-fractional-order diffusion equations (TFDEs) have attracted many scholars' attention, it is worth mentioning that the crucial importance of this kind of fractional equations is due to its wide use in many real-world applications in the fields of biology [5], chemistry [6], engineering [7]. It is pointed out that this kind of equation also appears, especially in nanofluid [8–10], nanotechnology [11, 12] and nanophysics [13–15].

In [16], authors studied the following time-fractional diffusion equation:

$${}_0^C D_t^\alpha u(\mathbf{x}, t) = \Delta u(\mathbf{x}, t) + f(\mathbf{x}, t), \quad (\mathbf{x}, t) \in Q$$

where ${}_0^C D_t^\alpha$ is the Caputo fractional derivative of order α ($0 < \alpha < 1$). They prove the existence and uniqueness of the solution by using the Lax-Milgram Lemma in some suitable Sobolev spaces. Paper [17] dealt with a time fractional equation on the metric star graph. The authors applied the method of energy integrals to construct Green's matrix-function and discussed applications to nanostructures.

Accordingly, various types of numerical methods have been applied to study this concept. One such method that has drawn the attention of many scholars is the Rothe method. Researchers have exploited and enhanced this technique for study of various differential fractional equations [18–20]. Yang [21] presented a difference scheme for a kind of linear space-time fractional convection-diffusion equation using a finite difference method. Du et al. [22] apply the Rothe method to establish existence, uniqueness, and a priori estimate for a strong solution to an approximate fractional problem.

Assume that $y = y(x, t)$ is a Lipschitz function with respect to t and let G be a bounded domain in multiply connected Ω with a Lipschitz boundary Γ , we consider two-dimensional time fractional equation with an integral operator of the following form:

$$\begin{aligned} \partial_{0t}^\alpha y(x, t) - \Delta y &= \int_0^t \kappa(x, s, y(x, s)) ds + f(x) \quad \text{in } Q = G \times (0, T), \quad 0 < \alpha < 1, \\ y(x, 0) &= 0, \\ B_1 y &= 0 \quad \text{on } \Gamma \times (0, T), \end{aligned} \quad (1)$$

where $\partial_{0t}^\alpha u(x, t)$ denotes the Caputo fractional derivative of order α ($0 < \alpha < 1$), $f \in L^2(G)$, and B_1 is a given linear operator. Additionally, it is assumed that the kernel $\kappa(x, t, u)$ satisfying the following conditions:

$$\|\kappa(x, t_2, y_2) - \kappa(x, t_1, y_1)\| \leq C \left(|t_2 - t_1| + \frac{1}{h^{\alpha-1}} \|y_2 - y_1\| \right), \quad (2)$$

$$y_1, y_2 \in L_2(G), \quad t_1, t_2 \in I = [0, T].$$

$$u \in \vartheta \Rightarrow \kappa \in L_2(G). \quad (3)$$

Here ϑ is the space defined as follows

$$\vartheta = \left\{ \nu; \nu \in W_2^{(k)}(G), B_1 \nu = 0, \text{ in the sense of traces} \right\}. \quad (4)$$

In the context of nanomaterials, equation (1) could model the movement of a particle or the diffusion of heat or matter through a medium with non- standard diffusion properties. Details for nanomaterials could be as follows:

Memory and non-locality: Nanomaterials can exhibit memory effects due to their interaction with a non-homogeneous environment, where the past influences the present movement.

Heterogeneous Diffusion: In heterogeneous media, such as nanopores, diffusion is not uniform and is affected by the structure of the material. The function $\kappa(x, s, y(x, s))$ could represent how the heterogeneous medium affects diffusion. It is worth mentioning that the boundary conditions considered in our problem may reflect the interactions of the particle energy with the boundaries of the nanomaterial, which could be reactive surfaces or interfaces with other materials.

First, we introduce the Caputo finite difference formula to discretize the time-fractional derivative of order α [23]:

$$\frac{\partial^\alpha y(x, t_j)}{\partial t^\alpha} = \frac{h^{-\alpha}}{\Gamma(2-\alpha)} \sum_{k=0}^{j-1} (z_{j-k}(x) - z_{j-k-1}(x)) \sigma_k \quad 0 < \alpha < 1, \quad (5)$$

where

$$\sigma_k = [(k+1)^{1-\alpha} - k^{1-\alpha}] \quad k = 0, 1, \dots,$$

while $z_j(x)$ denotes the numerical approximation to the exact solution $y(x, t_j)$, $t_j = jh$, $0 \leq j \leq p$, where $h = \frac{T}{p}$ is the time step. It is straightforward to check that

$$\sigma_j > 0, \quad j = 0, 1, \dots, p,$$

$$1 = \sigma_0 > \sigma_1 > \dots > \sigma_p.$$

The organization of the paper is as follows: In Section 2, some preliminary facts regarding fractional calculus and some notations are presented. In Section 3, we obtain a priori estimates. Sections 4 and 5 are devoted to discussing the existence and uniqueness of the weak solution, respectively.

2. Preliminaries

In the first part of this section, we recall some basic background of fractional calculus that we will need in the sequel.

Definition 1. [24] The Riemann-Liouville fractional integration $I_{0,t}^\alpha$ of order $\alpha > 0$ of function $\varphi(t)$ is defined as:

$$I_{0,t}^\alpha \varphi(t) = \frac{1}{\Gamma(\alpha)} \int_0^t (t-s)^{\alpha-1} \varphi(s) ds \quad (\alpha > 0, t > 0),$$

where Γ is the well-known Euler Gamma-function.

Definition 2. [24] The Caputo derivative of fractional order $\alpha \in]0; 1[$ of function $u(t)$ is defined as:

$$\partial_{0,t}^\alpha u(t) = \frac{1}{\Gamma(1-\alpha)} \int_0^t (t-s)^{-\alpha} u'(s) ds.$$

Theorem 2.1. [25] If $x(t) \in C^0[0, T]$ for $T > 0$ and $\alpha > 0$, then

$$I_{0,t}^\alpha x(0) = 0.$$

Theorem 2.2. [25] If $x(t) \in C^1[0, T]$ and $0 < \alpha < 1$, then

$$\partial_{0,t}^\alpha I_{0,t}^\alpha x(t) = x(t).$$

Lemma 2.1 (Gronwall's lemma [26]). Let η_1, \dots, η_j be nonnegative numbers satisfying $\eta_1 \leq A$, $\eta_i \leq A + Bh \sum_{k=1}^{i-1} \eta_k$, $\forall i = 2, \dots, j$, where A, B , and h are positive constants. Then

$$\eta_i \leq A \exp[B(i-1)h], \quad i = 1, 2, \dots, j.$$

Theorem 2.3. *If a sequence $\{x_n\}$ in a Hilbert space H is a weakly convergent to $x \in H$, then the following statements hold:*

$$\partial_{0,t}^\alpha x_n \rightharpoonup \partial_{0,t}^\alpha x \quad \text{in } H, \quad (6)$$

$$I_{0,t}^\alpha x_n \rightharpoonup I_{0,t}^\alpha x \quad \text{in } H. \quad (7)$$

For the proof of our theorem, we need the following lemma.

Lemma 2.2. *[26] A sequence $\{x_n\}$ in Hilbert space H converges weakly to $x \in H$ implying that for any bounded linear functional g defined on H we have*

$$g(x_n) \rightarrow g(x).$$

Proof of Theorem 2.3 (6) The caputo derivative is a bounded linear functional. Consequently, from

$$x_{n_k} \rightharpoonup x,$$

it follows according to the preceding lemma that

$$\partial_{0,t}^\alpha x_{n_k} \rightharpoonup \partial_{0,t}^\alpha x.$$

Finally, the strong convergence implies weak convergence and this proof is completed.

(7) The proof is the same as for the previous case.

Lemma 2.3. *[27] Any absolutely continuous function $v(t)$ on $[0, T]$ satisfies the inequality*

$$(v, \partial_{0,t}^\alpha v) \geq \frac{1}{2} \partial_{0,t}^\alpha \|v\|^2, \quad 0 < \alpha < 1.$$

Lemma 2.4. *[27] Let a nonnegative absolutely continuous function $y(t)$ satisfy the inequality*

$$\partial_{0,t}^\alpha y(t) \leq c_1 y(t) + c_2(t), \quad 0 < \alpha \leq 1,$$

for a. a. t in $[0, T]$, where $c_1 > 0$ and $c_2(t)$ is an integrable nonnegative function on $[0, T]$. Then

$$y(t) \leq y(0)E_\alpha(c_1 t^\alpha) + \Gamma(\alpha)E_{\alpha,\alpha}(c_1 t^\alpha) D_{0t}^{-\alpha} c_2(t)$$

where $E_\alpha(z) = \sum_{n=0}^{\infty} \frac{z^n}{\Gamma(\alpha n + 1)}$ and $E_{\alpha,\mu}(z) = \sum_{n=0}^{\infty} \frac{z^n}{\Gamma(\alpha n + \mu)}$ are the Mittag-Leffler functions.

The following assertions are presented at the end of this section. Let $\|\cdot\|$ and (\cdot, \cdot) denote $L_2(G)$ -norm and $L_2(G)$ -inner product, respectively. By $W_2^{(k)}(G)$ we denote the usual Sobolev space. We denote the bilinear form corresponding to the operator $-\Delta u$ by $b_\zeta(\cdot, \cdot)$:

$$b_\zeta(u, v) = \sum_{i=1}^N \int_G \frac{\partial v}{\partial x_i} \frac{\partial u}{\partial x_i} dx.$$

Definition 3. *[26] The form $b_\zeta(v, u)$ is called ϑ -elliptic if a constant η can be found such that*

$$b_\zeta(v, v) \geq \eta \|v\|_{W_2^{(k)}(G)}^2 \quad \forall v \in \vartheta. \quad (8)$$

In $L_2(I, \vartheta)$, the scalar product is provided by:

$$(y_1, y_2)_{L_2(I, \vartheta)} = \int_I (y_1(t), y_2(t))_H dt,$$

and, consequently, the norm is given by:

$$\|y\|_{L_2(I, \vartheta)}^2 = \int_I \|y(t)\|_\vartheta^2 dt. \quad (9)$$

3. Weak Formulation and a priori estimates

Substituting (5) into (1), we get

$$\frac{h^{-\alpha}}{\Gamma(2-\alpha)} \sum_{k=0}^{j-1} (z_{j-k}(x) - z_{j-k-1}(x)) \sigma_k - \Delta z_j(x) = h(\kappa_0 + \kappa_1 + \dots + \kappa_{j-1}) + f, \quad 0 < \alpha < 1. \quad (10)$$

With simplification by omitting the dependence of $z_j(x)$ on x , (10) can be rewritten as follows:

$$-\Gamma(2-\alpha)\Delta z_j + \frac{z_j - z_{j-1}}{h^\alpha} = - \left(\sum_{k=1}^{j-1} \frac{z_{j-k} - z_{j-k-1}}{h^\alpha} \sigma_k \right) + \Gamma(2-\alpha)h(\kappa_0 + \kappa_1 + \dots + \kappa_{j-1}) + \Gamma(2-\alpha)f, \quad 0 < \alpha < 1,$$

where

$$\kappa_j(x) = \kappa(x, jh, z_j(x)), \quad j = 1, \dots, p.$$

Hence, the integral identities i.e. the corresponding weak formulation has the following form:

$$\begin{aligned} & \Gamma(2 - \alpha)b_\zeta(z_j, v) + \frac{1}{h^\alpha} (z_j - z_{j-1}, v) \\ &= \left(-\frac{1}{h^\alpha} \sum_{k=1}^{j-1} (z_{j-k} - z_{j-k-1}) w_k + \Gamma(2 - \alpha)h (\kappa_0 + \kappa_1 + \dots + \kappa_{j-1}) + \Gamma(2 - \alpha)f, v \right) \end{aligned} \quad (11)$$

$\forall v \in \vartheta, \quad 0 < \alpha < 1.$

Thus, we can construct the α -Rothe function $y_1(t) = y_1(x, t)$ defined in the intervals $I_j = [t_{j-1}, t_j], j = 1, \dots, p$, by:

$$y_1(t) = z_{j-1} + \frac{z_j - z_{j-1}}{h^\alpha} (t - t_{j-1})^\alpha \quad 0 < \alpha < 1.$$

In the same way, we get, for the divisions $d_n, n = 2, 3, \dots$, with

$$h_n = \frac{T}{2^{n-1}p}$$

the α -Rothe sequence

$$\{y_n(t)\} \quad (12)$$

of functions:

$$y_n(t) = z_{j-1}^n + \frac{z_j^n(x) - z_{j-1}^n(x)}{h_n^\alpha} (t - t_{j-1}^n)^\alpha \quad 0 < \alpha < 1. \quad (13)$$

Now, we are in a position to establish some a priori estimates.

Lemma 3.1. *There exist two constants c_1, c_2 independent of α and j such that*

$$\|z_j\| \leq c_1, \quad j = 1, \dots, p, \quad (14)$$

$$\|Z_j\| \leq c_2, \quad j = 1, \dots, p, \quad (15)$$

with

$$Z_j(x) = \frac{z_j(x) - z_{j-1}(x)}{h^\alpha}.$$

Proof. First, since y belongs to the Lipschitz class with respect to t and because of $z_0 = 0$, it produces

$$\|z_j\| \leq \|z_1\| + \|z_2 - z_1\| + \dots + \|z_j - z_{j-1}\| \leq ljh \leq lT = c_1,$$

where l is the Lipschitz constant.

Next, putting $v = Z_1$ in the first integral identity (11), we get

$$\Gamma(2 - \alpha)b_\zeta(z_1, Z_1) + \frac{1}{h^\alpha} (z_1, Z_1) = \Gamma(2 - \alpha) (h\kappa_0 + f, Z_1), \quad 0 < \alpha < 1.$$

Hence, due to the Schwartz inequality and the fact that $b_\zeta(z_1, Z_1) = \frac{1}{h^\alpha} b_\zeta(z_1, z_1) \geq 0$ we obtain that

$$\|Z_1\| \leq \Gamma(2 - \alpha) (h \|\kappa_0\| + \|f\|). \quad (16)$$

Subtracting the integral identities (11) written for $j = 1$ from that written for $j = 2$, we obtain

$$\Gamma(2 - \alpha)b_\zeta(z_2 - z_1, v) + (Z_2 - Z_1, v) = (-\sigma_1 Z_1 + \Gamma(2 - \alpha)h\kappa_1 + f, v) \quad \forall v \in \vartheta.$$

Putting $v = Z_2$, we get

$$\|Z_2\| \leq (\sigma_0 - \sigma_1) \|Z_1\| + \Gamma(2 - \alpha)h \|\kappa_1\|. \quad (17)$$

Similarly, one obtains

$$\|Z_3\| \leq (\sigma_0 - \sigma_1) \|Z_2\| + (\sigma_1 - \sigma_2) \|Z_1\| + \Gamma(2 - \alpha)h \|\kappa_2\|.$$

Following this procedure, one comes to the estimation

$$\|Z_j\| \leq \sum_{k=1}^{j-1} (\sigma_{k-1} - \sigma_k) \|Z_{j-k}\| + \Gamma(2 - \alpha)h \|\kappa_{j-1}\|. \quad (18)$$

Adding up (16)–(18) yields

$$\|Z_j\| \leq \Gamma(2 - \alpha)\psi_0 \|f\| + \Gamma(2 - \alpha)h (\psi_0 \|\kappa_0\| + \psi_1 \|\kappa_1\| + \dots + \psi_{j-1} \|\kappa_{j-1}\|) \quad (19)$$

with

$$\psi_m = (\sigma_0 - \sigma_1)^{j-(m+1)} + \sum_{k=1}^{j-(m+2)} (\sigma_0 - \sigma_1)^{j-k-(m+2)} (\sigma_k - \sigma_{k-1}) (j - k - (m + 1)),$$

for all $m = 0, 1, \dots, j - 1.$

Now, we can easily proof that $\psi_0 < \psi_1 < \dots < \psi_{j-1} = 1$, so (19) yields

$$\|Z_j\| \leq \Gamma(2 - \alpha) [\|f\| + h (\|\kappa_0\| + \|\kappa_1\| + \dots + \|\kappa_{j-1}\|)]. \quad (20)$$

In the other hand, by using the fact that $z_0 = 0$, we obtain from (2) that

$$\begin{aligned} \|\kappa_1\| &\leq \|\kappa_0\| + \|\kappa_1 - \kappa_0\| \\ &\leq \|\kappa_0\| + C \left(h + \frac{\|z_1\|}{h^{\alpha-1}} \right) \\ &= \|\kappa_0\| + Ch (1 + \|Z_1\|). \end{aligned}$$

Then,

$$\begin{aligned} \|\kappa_2\| &\leq \|\kappa_0\| + \|\kappa_2 - \kappa_0\| \\ &\leq \|\kappa_0\| + C \left(2h + \frac{\|z_2\|}{h^{\alpha-1}} \right) \\ &\leq \|\kappa_0\| + Ch \left(2 + \frac{\|z_2 - z_1\|}{h^\alpha} + \frac{\|z_1\|}{h^\alpha} \right) \\ &= \|\kappa_0\| + Ch (2 + \|Z_1\| + \|Z_2\|) \\ &= \|\kappa_0\| + Ch (2 + \|Z_1\| + \|Z_2\|). \end{aligned}$$

Hence, using the analogous arguments, we can conclude that

$$\begin{aligned} \|\kappa_{j-1}\| &\leq \|\kappa_0\| + \|\kappa_{j-1} - \kappa_0\| \\ &\leq \|\kappa_0\| + Ch (j - 1 + \|Z_1\| + \|Z_2\| + \dots + \|Z_{j-1}\|). \end{aligned} \quad (21)$$

Inserting these results into (20), we obtain

$$\begin{aligned} \|Z_j\| &\leq \Gamma(2 - \alpha) [\|f\| + jh \|\kappa_0\| + Ch^2 (1 + 2 + \dots + j - 1)] \\ &\quad + Ch^2 [(j - 1) \|Z_1\| + (j - 2) \|Z_2\| + \dots + \|Z_{j-1}\|]. \end{aligned}$$

Now, $(j - 1)h < ph = T$. Thus, we have

$$\begin{aligned} \|Z_j\| &\leq \Gamma(2 - \alpha) [\|f\| + T \|\kappa_0\| + CT^2 (1 + 2 + \dots + j - 1)] \\ &\quad + CT h (\|Z_1\| + \|Z_2\| + \dots + \|Z_{j-1}\|) \quad j = 1, 2, \dots, p. \end{aligned}$$

Using Lemma 2.1, we get, finally

$$\begin{aligned} \|Z_j\| &\leq \Gamma(2 - \alpha) (\|f\| + T \|\kappa_0\| + CT^2) e^{CT(j-1)h} \\ &\leq \Gamma(2 - \alpha) (\|f\| + T \|\kappa_0\| + CT^2) e^{CT^2}, \quad j = 1, 2, \dots, p. \end{aligned}$$

Then (15) holds with $c_2 = \Gamma(2 - \alpha) (\|f\| + T \|\kappa_0\| + CT^2) e^{CT^2}$, and so the proof is complete. \square

Remark 1. The estimates (14), (15) are independent of h , consequently, they remain valid for any division d_n , $n = 1, 2, \dots$. Thus, we have

$$\|z_j^n\| \leq c_1, \quad (22)$$

$$\|Z_j^n\| \leq c_2, \quad (23)$$

for all $n = 1, 2, \dots$, and $1 \leq j \leq 2^{n-1}p$, where

$$Z_j^n(x) = \frac{z_j^n(x) - z_{j-1}^n(x)}{h_n^\alpha}. \quad (24)$$

Recall that the space \mathcal{V} is determined by (4). Taking into account (22) and using (8), we arrive at the following corollary:

Corollary 3.1. There exists a constant c_3 such that

$$\|z_j^n\|_{\mathcal{V}} \leq c_3, \quad (25)$$

for all $n = 1, 2, \dots$, and $1 \leq j \leq 2^{n-1}p$.

Lemma 3.2. $\|\kappa_j^n\|$ is uniformly bounded with respect to j and n as well, where $\kappa_j^n(x) = \kappa(x, jh_n, z_j^n(x))$.

Proof. For the division d_n , due to (21), one obtains

$$\|\kappa_j^n\| \leq \|\kappa_0^n\| + Ch_n (j + \|Z_1^n\| + \|Z_2^n\| + \dots + \|Z_j^n\|).$$

Taking into account (23), we come to the inequality

$$\|\kappa_j^n\| \leq \|\kappa_0^n\| + CT + CTc_2 = c_4. \quad (26)$$

\square

4. Existence of weak solution

This section is devoted to proving the existence of a weak solution to our problem. For this purpose, let's start with the following lemma:

Lemma 4.1. *The α -Rothe sequence (12) admits a subsequence $\{y_{n_k}(t)\}$ weakly convergent in $L_2(I, \vartheta)$ to function $y \in L_2(I, \vartheta)$, we write*

$$y_{n_k} \rightharpoonup y \quad \text{in } L_2(I, \vartheta). \quad (27)$$

Proof. Since $L_2(I, \vartheta)$ is a Hilbert space it is sufficient to show that the α -Rothe sequence (12) is bounded in this space. Keeping in mind that

$$0 \leq \left(\frac{t - t_{j-1}^n}{h_n} \right)^\alpha \leq 1 \quad \text{in } I_j^n,$$

and by (13), (25), we obtain, for arbitrary $t \in I$,

$$\begin{aligned} \|y_n(t)\|_{\vartheta} &= \left\| z_{j-1}^n \left(1 - \frac{(t - t_{j-1}^n)^\alpha}{h_n^\alpha} \right) + z_j^n \frac{(t - t_{j-1}^n)^\alpha}{h_n^\alpha} \right\|_{\vartheta} \\ &\leq \left\| \left(1 - \frac{(t - t_{j-1}^n)^\alpha}{h_n^\alpha} \right) z_{j-1}^n \right\|_{\vartheta} + \left\| \frac{(t - t_{j-1}^n)^\alpha}{h_n^\alpha} z_j^n \right\|_{\vartheta} \\ &\leq \left(1 - \frac{(t - t_{j-1}^n)^\alpha}{h_n^\alpha} \right) c_3 + \frac{(t - t_{j-1}^n)^\alpha}{h_n^\alpha} c_3 = c_3. \end{aligned}$$

From (9), we get, for $n = 1, 2, \dots$

$$\|y_n(t)\|_{L_2(I, \vartheta)}^2 = \int_0^T \|y_n(t)\|_{\vartheta}^2 dt \leq c_3^2 T.$$

Thus, the α -Rothe sequence (12) is bounded in $L_2(I, \vartheta)$, and the proof is finished. \square

Remark 2. [26] *Note that besides (27) it holds that*

$$y_{n_k} \rightarrow y \quad \text{in } C(I, L_2(G)). \quad (28)$$

Now, taking into account (23) and using the same reasoning as in the proof of the preceding corollary, we arrive at the following corollary:

Corollary 4.1. *There exists a subsequence $\{\mathbb{Y}_{n_k}^\alpha(t)\}$ and a function \mathbb{Y}^α such that*

$$\mathbb{Y}_{n_k}^\alpha \rightharpoonup \mathbb{Y}^\alpha \quad \text{in } L_2(I, L_2(G)), \quad (29)$$

where

$$\mathbb{Y}_n^\alpha(t) : I \rightarrow L_2(G), \quad n = 1, 2, \dots$$

defined by

$$\mathbb{Y}_n^\alpha(t) = \begin{cases} \Gamma(\alpha + 1) Z_1^{n, \alpha} & \text{for } t = 0, \\ \Gamma(\alpha + 1) Z_j^{n, \alpha} & \text{for } t \in \tilde{I}_j^n = (t_{j-1}^n, t_j^n], \quad j = 1, \dots, 2^{n-1}p. \end{cases} \quad (30)$$

Lemma 4.2.

$$\partial_{0,t}^\alpha y(t) = \mathbb{Y}^\alpha(t) \quad \text{in } L_2(I, L_2(G)) \quad \text{for a. a. } t \in I. \quad (31)$$

Proof. It follows from (13) and (30) that

$$\frac{1}{\Gamma(\alpha)} \int_0^t (t-s)^{\alpha-1} \mathbb{Y}_{n_k}^\alpha(t)(s) ds = y_{n_k}(t). \quad (32)$$

Recalling the definition of the Riemann-Liouville integral, the left-hand side of (32) is nothing but $I_{0,t}^\alpha \mathbb{U}_{n_k}^\alpha(t)$, hence (32) becomes

$$I_{0,t}^\alpha \mathbb{Y}_{n_k}^\alpha(t) = y_{n_k}(t). \quad (33)$$

Applying the Caputo derivative $\partial_{0,t}^\alpha$ to the both sides of (33), we get by Theorem 2.2

$$\partial_{0,t}^\alpha y_{n_k}(t) = \mathbb{Y}_{n_k}^\alpha(t). \quad (34)$$

Applying now (6) for (27), we obtain in view of (29), (34), and by the uniqueness of the weak limit that

$$\partial_{0,t}^\alpha y(t) = \mathbb{Y}^\alpha(t) \quad \text{in } L_2(G) \quad \text{for a.a. } t \in I.$$

The proof is finished. \square

Corollary 4.2. *The function $y(t)$ verifies*

$$y(0) = 0 \quad \text{in } C(I, L_2(G)), \quad (35)$$

$$y \in AC(I, L_2(G)). \quad (36)$$

Proof. From (7), (27), and (33), following the same reasoning as in the proof of (31), we get

$$I_{0,t}^\alpha \mathbb{Y}^\alpha(t) = y(t).$$

Hence, by Theorem 2.1, we complete the proof. \square

Lemma 4.3. [26] *If*

$$y_{n_k} \rightharpoonup y \quad \text{in } L_2(I, \vartheta),$$

then also

$$\tilde{y}_{n_k} \rightharpoonup y \quad \text{in } L_2(I, \vartheta), \quad (37)$$

where $\{\tilde{y}_n(t)\}$ is the sequence defined by:

$$\tilde{y}_n(t) = \begin{cases} z_1^n & \text{for } t = 0 \\ z_j^n & \text{in } I_j^n = (t_{j-1}^n, t_j^n], j = 1, \dots, p. \end{cases} \quad (38)$$

Let

$$w(t) = w(x, t) = \kappa(x, t, y(x, t)). \quad (39)$$

Since $y \in \vartheta$ for a. a. $t \in I$, we have, by (3) $w \in L_2(G)$ for a.a. $t \in I$. Consequently, we obtain the following corollary.

Corollary 4.3.

$$\lim_{n_k \rightarrow \infty} \tilde{w}_{n_k}(t) = w(t) \quad \text{in } L_2(G) \quad \text{for a.a. } t \in I, \quad (40)$$

where

$$\tilde{w}_n(t) : I \rightarrow L_2(G), \quad n = 1, 2, \dots$$

is defined by

$$\tilde{w}_n(t) = \begin{cases} \kappa_0^n & \text{for } t = 0, \\ \kappa_{j-1}^n & \text{in } \tilde{I}_j^n = (t_{j-1}^n, t_j^n], j = 1, \dots, 2^{n-1}p. \end{cases}$$

Proof. Let $\varepsilon > 0$ be given. We have to show that

$$\|w(t) - \tilde{w}_{n_k}(t)\| \leq \varepsilon \quad \text{for a.a. } t \in I \quad \text{if } n_k > n_0(\varepsilon). \quad (41)$$

By (2) we obtain for fixed division d_{n_k} and for arbitrary $t \in \tilde{I}_{j+1}^{n_k}$

$$\begin{aligned} \|w(t) - \tilde{w}_{n_k}(t)\| &= \|\kappa(x, t, y(t)) - \kappa(x, jh_{n_k}, z_j^{n_k})\| \\ &\leq C \left(|t - jh_{n_k}| + \frac{1}{h_{n_k}^{\alpha-1}} \|y(t) - z_j^{n_k}\| \right) \leq C [h_{n_k} + \|y(t) - y(jh_{n_k})\|] + \\ &\quad + \|y(jh_{n_k}) - z_j^{n_k}\|. \end{aligned}$$

Choosing $\eta = \frac{\varepsilon}{3C}$, we get the desired result due to (28) and (36). \square

Remark 3. (40), (41) imply that the function $w(t)$ is Bochner integrable as an abstract function from I into $L_2(G)$. Consequently, we can define the following functions

$$\mathbb{W}(t) = \int_0^t w(s) ds, \quad (42)$$

$$\mathbb{W}_n(t) = \int_0^t \tilde{w}_n(s) ds. \quad (43)$$

The proof of the following corollary is essentially the same as that in [26]. For the sake of convenience we give the proof.

Corollary 4.4. *Define*

$$\tilde{\mathbb{W}}_n(t) = \begin{cases} h_n \kappa_0^n & \text{for } t = 0, \\ h_n (\kappa_0^n + \dots + \kappa_{j-1}^n) & \text{in } \tilde{I}_j^n, \end{cases} \quad (44)$$

then

$$\lim_{n_k \rightarrow \infty} \tilde{\mathbb{W}}_{n_k} = \mathbb{W} \quad \text{in } L_2(I, L_2(G)). \quad (45)$$

Proof. First, from (41) we immediately obtain

$$\lim_{n_k \rightarrow \infty} \mathbb{W}_{n_k} = \mathbb{W} \quad \text{in } L_2(I, L_2(G)). \quad (46)$$

From (43), (44), we get for $t \in \tilde{I}_j^n$:

$$\begin{aligned} \mathbb{W}_n(t) - \widetilde{\mathbb{W}}_n(t) &= \int_0^{h_n} \tilde{w}_n(s) ds + \dots + \int_{(j-2)h_n}^{(j-1)h_n} \tilde{w}_n(s) ds + \\ &+ \int_{(j-1)h_n}^t \tilde{w}_n(s) ds - \widetilde{\mathbb{W}}_n(t) = h_n (\kappa_0^n + \dots + \kappa_{j-2}^n) + \\ &+ [t - (j-1)h_n] \kappa_{j-1}^n - h_n (\kappa_0^n + \dots + \kappa_{j-1}^n) = (t - jh_n) \kappa_{j-1}^n. \end{aligned}$$

Hence, for $t \in \tilde{I}_j^n$ it holds that

$$\left\| \mathbb{W}_n(t) - \widetilde{\mathbb{W}}_n(t) \right\| \leq h_n \left\| \kappa_{j-1}^n \right\|.$$

Combining (46), (26), we complete the proof of Corollary 3.4. \square

We're now prepared to demonstrate in which senses the function $y(t)$ satisfies the given equation (1). In view of (24), we can rewrite the integral identities (11) for the division d_n in the following way:

$$\begin{aligned} \Gamma(2-\alpha) b_\zeta(z_j^n, v) + \left(\sum_{k=0}^{j-1} Z_{j-k}^n \sigma_k, v \right) \\ = \Gamma(2-\alpha) (h_n (\kappa_0^n + \kappa_1^n + \dots + \kappa_{j-1}^n) + \Gamma(2-\alpha) f, v) \quad \forall v \in \vartheta, \quad 0 < \alpha < 1. \end{aligned} \quad (47)$$

Let $v(t)$ be a fixed abstract function from $L_2(I, \vartheta)$. Using (30), (38) and (44) and defining the abstract function $f(t)$ from I into $L_2(G)$ by $f(t) = f \quad \forall t \in I$, we transform (47) to the form

$$\Gamma(2-\alpha) b_\zeta(\tilde{y}_n, v) + \frac{1}{\Gamma(\alpha+1)} \left(\sum_{l=0}^{j-1} \sigma_l \mathbb{Y}_n^\alpha, v \right) = \Gamma(2-\alpha) (\widetilde{\mathbb{W}}_n, v) + \Gamma(2-\alpha) (f, v) \quad \text{for a.a. } t \in I. \quad (48)$$

Taking into consideration the indices n_k from (27) only and integrating (48) with n replaced by n_k between the limits $t = 0$ and $t = T$, we get

$$\begin{aligned} \Gamma(2-\alpha) \int_0^T b_\zeta(\tilde{y}_{n_k}, v) dt + \frac{1}{\Gamma(\alpha+1)} \sum_{l=0}^{j-1} \sigma_l \int_0^T (\mathbb{Y}_{n_k}^\alpha, v) dt \\ = \Gamma(2-\alpha) \int_0^T (\widetilde{\mathbb{W}}_{n_k}, v) dt + \Gamma(2-\alpha) \int_0^T (f, v) dt. \end{aligned} \quad (49)$$

Hence,

$$v \in L_2(I, \vartheta) \Rightarrow v \in L_2(I, L_2(G)).$$

Thus, (29), (31) imply

$$\lim_{n_k \rightarrow \infty} \frac{1}{\Gamma(\alpha+1)} \int_0^T \left(\sum_{l=0}^{j-1} \sigma_l \mathbb{Y}_{n_k}^\alpha, v \right) dt = \frac{1}{\Gamma(\alpha+1)} \sum_{l=0}^{j-1} \sigma_l \int_0^T (\partial_{0t}^\alpha y, v) dt.$$

Similarly, by (45), one obtains

$$\lim_{n_k \rightarrow \infty} \Gamma(2-\alpha) \int_0^T (\widetilde{\mathbb{W}}_{n_k}, v) dt = \Gamma(2-\alpha) \int_0^T (\mathbb{W}, v) dt,$$

where $\mathbb{W}(t) = \int_0^t \kappa(x, s, y(x, s)) ds$, by (39), (42). Finally, for $v \in L_2(I, \vartheta)$ fixed,

$$\int_0^T b_\zeta(y, v) dt$$

is a bounded linear functional in $L_2(I, \vartheta)$. Thus,

$$\lim_{n_k \rightarrow \infty} \Gamma(2-\alpha) \int_0^T b_\zeta(\tilde{y}_{n_k}, v) dt = \Gamma(2-\alpha) \int_0^T b_\zeta(y, v) dt$$

holds by (37). Consequently, for $n_k \rightarrow \infty$, (49) gives one

$$\int_0^T b_\zeta(y, v) dt + \frac{1}{\Gamma(\alpha+1)} \sum_{l=0}^{j-1} \sigma_l \int_0^T (\partial_{0t}^\alpha y, v) dt = \Gamma(2-\alpha) \int_0^T (\mathbb{W}, v) dt + \Gamma(2-\alpha) \int_0^T (f, v) dt. \quad (50)$$

Due to the fact that function $v \in L_2(I, \vartheta)$ is chosen arbitrarily, (50) holds for every $v \in L_2(I, \vartheta)$. In this weak sense, equation (1) is fulfilled. Thus, the function $y(t)$ satisfies

$$y \in L_2(I, \vartheta) \cap AC(I, L_2(G)), \quad (51)$$

$$\partial_{0,t}^\alpha y(t) \in L_2(I, L_2(G)), \quad (52)$$

$$y(0) = 0 \text{ in } C(I, L_2(G)), \quad (53)$$

$$\begin{aligned} & \int_0^T b_\zeta(y, v) dt + \frac{1}{\Gamma(\alpha + 1)} \sum_{l=0}^{j-1} \sigma_l \int_0^T (\partial_{0,t}^\alpha y, v) dt \\ & = \Gamma(2 - \alpha) \int_0^T (\mathbb{W}, v) dt + \Gamma(2 - \alpha) \int_0^T (f, v) dt \quad \forall v \in L_2(I, \vartheta). \end{aligned} \quad (54)$$

Definition 4. Function $y(t)$ satisfying (51) – (54) is called weak solution to our problem.

5. Uniqueness

To establish uniqueness, we assume the existence of two distinct weak solutions y_1 and y_2 and come to a contradiction. Denote their difference by

$$y^* = y_1 - y_2.$$

Therefore, to prove the uniqueness, it suffices to show that $y^* = 0$.

By (51) – (54), $y^*(t)$ satisfies

$$\begin{aligned} y^* & \in L_2(I, \vartheta), \\ y^* & \in AC(I, L_2(G)), \\ \partial_{0,t}^\alpha y^* & \in L_2(I, L_2(G)), \\ y^*(0) & = 0 \text{ in } C(I, L_2(G)), \end{aligned}$$

$$\begin{aligned} & \Gamma(2 - \alpha) \int_0^T b_\zeta(y^*, v) dt + \int_0^T \left(\sum_{l=1}^{j-1} \sigma_l \partial_{0,t}^\alpha y^*, v \right) dt \\ & = \Gamma(2 - \alpha) \int_0^T \left(\int_0^t [\kappa(x, s, y_2(s)) - \kappa(x, s, y_1(s))] ds, v \right) dt \quad \forall v \in L_2(I, \vartheta). \end{aligned} \quad (55)$$

According to (2), we have

$$\begin{aligned} & \left\| \int_0^t [\kappa(x, s, y_2(s)) - \kappa(x, s, y_1(s))] ds \right\| \\ & \leq \int_0^t \|\kappa(x, s, y_2(s)) - \kappa(x, s, y_1(s))\| ds \\ & \leq \int_0^t \frac{C}{h^{\alpha-1}} \|y_2(s) - y_1(s)\| ds = \frac{C}{h^{\alpha-1}} \int_0^t \|y^*(s)\| ds \leq C \int_0^t \|y^*(s)\| ds. \end{aligned} \quad (56)$$

Let us divide the interval I into a finite number of subintervals of lengths l . The function $y(t)$ belongs to $C(I, L_2(G))$ hence the function $\|y(t)\|$ is continuous in the interval $[0, l]$. Consequently, $\|y(t)\|$ attains its maximum on this interval at a certain point $t_1 \in [0, l]$. Let

$$\max_{t \in [0, l]} \|y^*(t)\| = \|y^*(t_1)\|. \quad (57)$$

For $v(t)$ in (55), let us choose the function

$$v(t) = \begin{cases} y^*(t) & \text{for } t \in [0, t_1], \\ 0 & \text{for } t \in (t_1, T]. \end{cases}$$

Thus, we obtain

$$\begin{aligned} & \Gamma(2 - \alpha) \int_0^{t_1} b_\zeta(y^*, y^*) dt + \sum_{l=1}^{j-1} \sigma_l \int_0^T (y^*, \partial_{0,t}^\alpha y^*) dt \\ & = \Gamma(2 - \alpha) \int_0^{t_1} \left(y^*, \int_0^t [\kappa(x, s, y_2(s)) - \kappa(x, s, y_1(s))] ds \right) dt. \end{aligned} \quad (58)$$

ϑ -ellipticity of the form $b_\zeta(v, y)$ gives us that

$$\Gamma(2 - \alpha) \int_0^{t_1} b_\zeta(y^*, y^*) dt \geq 0. \quad (59)$$

Additionally, according to Lemma 2.3, one has

$$\int_0^{t_1} \left(y^*, \sum_{l=1}^{j-1} \sigma_l \partial_{0t}^\alpha y \right) dt \geq \frac{\sum_{l=1}^{j-1} \sigma_l}{2} \int_0^{t_1} \partial_{0t}^\alpha \|y\|^2 = c_5 \partial_{0t}^\alpha \|y(t_1)\|^2, \quad (60)$$

where c_5 is a constant. (56) yields

$$\begin{aligned} & \left\| \Gamma(2-\alpha) \int_0^{t_1} \left(y^*, \int_0^t [\kappa(x, s, y_2(s)) - \kappa(x, s, y_1(s))] ds \right) dt \right\| \\ & \leq \Gamma(2-\alpha) \int_0^{t_1} \|y^*(t_1)\| \left\| \int_0^t [\kappa(x, s, y_2(s)) - \kappa(x, s, y_1(s))] ds \right\| \\ & \leq \Gamma(2-\alpha) \int_0^l \|y^*(t_1)\| \left(C \int_0^l \|y^*(s)\| ds \right) \leq Cl^2 \|y^*(t_1)\|^2. \end{aligned} \quad (61)$$

Combining (58) – (61), we can get

$$\partial_{0t}^\alpha \|y^*(t_1)\|^2 \leq c_6 \|y^*(t_1)\|^2,$$

where c_6 is a constant. Using Lemma 2.4, we obtain with regard to (35),

$$\|y^*(t_1)\| = 0.$$

Formula (57) then implies

$$y^*(t) = 0 \text{ in } L_2(G) \quad \forall t \in [0, l]. \quad (62)$$

Performing the same consideration in the interval $[l, 2l]$ with the function

$$v(t) = \begin{cases} y^*(t) & \text{for } t \in [0, t_2], \\ 0 & \text{for } t \in (t_2, T], \end{cases}$$

where t_2 is a point at which $\|y(t)\|$ attains its maximum in the interval $[l, 2l]$, and using the just obtained result (62), we obtain that

$$y^*(t) = 0 \text{ in } L_2(G) \quad \forall t \in [l, 2l].$$

After a finite number of steps we thus come to the conclusion that

$$y^*(t) = 0 \text{ in } L_2(G) \quad \forall t \in I.$$

Hence, the uniqueness is proved.

6. Conclusion and future scope

Two objectives have been successfully reached in this study. Firstly, a new function has been constructed using the method of discretization for a time fractional equation. Secondly, the proposed method has been validated by demonstrating the convergence of the α -Rothe sequence to the unique weak solution of our problem. As we've seen, TFDE is closely linked to various nanoscience phenomena, consequently, the authors are optimistic that the results obtained can be extended to a wide range of nanoscience applications, thus offering a promising avenue for further exploration (Non-Fourier conduction, confinement effects, Phonon-Phonon and Phonon-Defect Interactions...).

References

- [1] Carpinteri A., Mainardi F. *Fractals and Fractional Calculus in Continuum Mechanics*. Springer, Berlin, 1997.
- [2] Tien D. Fractional stochastic differential equations with applications to finance. *Journal of Mathematical Analysis and Applications*, 2013, **397**(1), P. 334–348.
- [3] Kenneth S.M., Betram R. *An Introduction to the Fractional Calculus and Fractional Differential Equations*. Wiley, NewYork, 1993.
- [4] West B.J., Grigolini P. *Applications of Fractional Calculus in Physics*. World Scientific, Singapore, 1998.
- [5] Vineet K.S., Sunil K., Mukesh K.A., Brajesh K.S. Two-dimensional time fractional-order biological population model and its analytical solution. *Egyptian Journal of Basic and Applied Sciences*, 2014, **1**(1), P. 71–76.
- [6] Ahmad H., Hossein J., Pranay G., Vernon Ariyan. Solving Time-Fractional Chemical Engineering Equations. *Thermal Science*, 2020, **24**(1), P. 157–164.
- [7] Khan N.A., Asmat A., Amir M. Approximate solution of time-fractional chemical engineering equations: a comparative study. *International Journal of Chemical Reactor Engineering*, 2010, **8**(1). Article A19.
- [8] Aman S., Khan I., Ismail Z., Salleh M.Z. Thili I. A new Caputo time fractional model for heat transfer enhancement of water based graphene nanofluid. *An application to solar energy. Results in Physics*, 2018, **9**, P. 1352–1362.
- [9] Aman S., Khan I., Ismail Z., Salleh M.Z. Applications of fractional derivatives to nanofluids: exact and numerical solutions. *Mathematical Modelling of Natural Phenomena*, 2018, **13**(1), P. 1–12.
- [10] Hasin F., Ahmad Z., Ali F., Khan N., Khan I. A time fractional model of Brinkman-type nanofluid with ramped wall temperature and concentration. *Advances in Mechanical Engineering*, 2022, **14**(5), 168781322210960.
- [11] Baleanu D., Guvenc Z.B., Machado J.A.T. *New Trends in Nanotechnology and Fractional Calculus Applications*. Springer, Netherlands, 2009.
- [12] Zada L., Rashid N., Samia S.B. An efficient approach for solution of fractional order differential-difference equations arising in nanotechnology. *Applied Mathematics E-Notes*, 2020, P. 297–307.

- [13] Aldea A., Barsan V. *Trends in nanophysics*. Springer, Berlin Heidelberg, 2010.
- [14] Lobo R.F., Pinheiro M.J. *Advanced Topics in Contemporary Physics for Engineering: Nanophysics, Plasma Physics, and Electrodynamics*. CRC Press, 2022.
- [15] Uchaikin V.V. *Fractional derivatives for physicists and engineers* Berlin: Springer, 2013.
- [16] Nazdar A.A., Davood R. Identifying an unknown time-dependent boundary source in time-fractional diffusion equation with a non-local boundary condition. *Journal of Computational and Applied Mathematics*, 2019, **355**, P. 36–50.
- [17] Sobirov Z.A., Rakhimov K.U., Ergashov R.E. Green's function method for time-fractional diffusion equation on the star graph with equal bonds. *Nanosystems: Physics, Chemistry, Mathematics*, 2021, **12**(3), P. 271–278.
- [18] Bahuguna D., Jaiswal A. Application of Rothe's method to fractional differential equations. *Malaya Journal of Matematik*, 2019, **7**(3), P. 399–407.
- [19] Zeng B. Existence for a class of time-fractional evolutionary equations with applications involving weakly continuous operator. *Fractional Calculus and Applied Analysis*, 2023, **26**, P. 172–192.
- [20] Raheem A., Bahuguna D. Rothe's method for solving some fractional integral diffusion equation. *Applied Mathematics and Computation*, 2014, **236**, P. 161–168.
- [21] Yang Z. A finite difference method for fractional partial differential equation. *Applied Mathematics and Computation*, 2009, **215**(2), P. 524–529.
- [22] Du G., Lu C., Juang Y. Rothe's method for solving multi-term Caputo-Katugampola fractional delay integral diffusion equations. *Mathematical Methods in the Applied Sciences*, 2023, **45**(12), P. 7426–7442.
- [23] Lin Y., Xu C. Finite difference/spectral approximations for the time-fractional diffusion equation. *Journal of Computational Physics*, 2007, **225**, P. 1533–1552.
- [24] Kilbas A.A., Srivastava H.M., Trujillo J.J. *Theory and Applications of Fractional Differential Equations*. Elsevier, Amsterdam, 2006.
- [25] Li C., Weihua D. Remarks on fractional derivatives. *Applied Mathematics and Computation*, 2007, **187**(2), P. 777–784.
- [26] Rektorys K. *The Method of Discretization in Time and Partial Differential Equations* D. Reidel Publishing Company, Dordrecht, 1982.
- [27] Alikhanov A.A. A priori estimates for solutions of boundary value problems for fractional-order equations. *Differential Equations*, 2010, **46**(5), P. 660–666.

Submitted 29 August 2023; revised 12 January 2024; accepted 14 January 2024

Information about the authors:

Y. Bekakra – Department of Mathematics and Informatics, ICOSI Laboratory, Abbes Laghrour University, Khenchela, 04000, Algeria; ORCID 0000-0001-5672-4348; youcef.bekakra@univ-khenchela.dz

A. Bouziani – Department of Mathematics and Informatics, ICOSI Laboratory, Abbes Laghrour University, Khenchela, 04000, Algeria; Department of Mathematics, L'arbi Ben M'hidi University, Oum El Bouagui, 04000, Algeria; ORCID 0000-0002-1216-8033; aefbouziani1963@gmail.com

Conflict of interest: the authors declare no conflict of interest.

Graph spectral analysis of nonane isomers

Barnabas I. Andrew^{1,a}, Ambarishan Anuradha^{1,b}¹SRM Institute of Science and Technology, Kattankulathur, Tamil Nadu 603203, India^aab8559@srmist.edu.in, ^banuradha@srmist.edu.in

Corresponding author: A. Anuradha, anuradha@srmist.edu.in

PACS 05C05, 05C38, 05C50, 05C90

ABSTRACT A group of substances known as alkanes is made up of carbon and hydrogen atoms bound together only by single covalent bond with the chemical formula C_nH_{2n+2} . Isomers are those molecules with identical chemical formula but different structural arrangement. Due to this, their corresponding molecular graphs differ in structure thereby leading to distinct spectral parameters. In this work, the spectral parameters of all isomers of nonane C_9H_{20} have been computed and its relationship with its eigenvalue-based entropy is established. The spectral results are then correlated with the density value of the nonane isomers and it is found that the “spectral gap” is closely associated to that of density.

KEYWORDS Alkane isomers, graph energy, spectrum, spectral gap, eigenvalue-based entropy

FOR CITATION Andrew B.I., Anuradha A. Graph spectral analysis of nonane isomers. *Nanosystems: Phys. Chem. Math.*, 2024, **15** (1), 16–22.

1. Introduction

Organic chemistry deals with structures, compositions, properties, reactions, and preparation of carbon-containing compounds. The simplest organic compounds are hydrocarbons [1], which just have carbon and hydrogen atoms and can be either straight or branched chains with the same empirical formula but different characteristics. Alkanes are such kind of hydrocarbon. Alkanes are with identical empirical formula C_nH_{2n+2} and distinct arrangements of atoms joined only by single bonds. Alkanes with four or more carbon atoms can have more than one arrangement of atoms, thereby forming isomers. A linear alkane with the formula C_9H_{20} is nonane. It is a colourless, flammable liquid that is mostly extracted from crude oil and it is used in automobile fuels. The isomers of nonane have carbon chain branches at different locations in the chain leading to the compound having different IUPAC names. Altogether, nonane has 35 isomers, including the straight-chain compound n -nonane.

In chemical graph theory [2], the structural arrangement of molecules are depicted as chemical graphs. The organic chemical compounds are represented by their graph structure where the carbon atoms are represented by vertices and the relation between carbon atoms are represented by edges. This representation is widely used in cheminformatics. Predictions of structure-property relationships and (quantitative) structure activity are based on computed graph parameters. The physical characteristics of molecules can then be reflected in these graphs as graph-theoretical descriptors or indices. Spectrum of the graph is one such kind of descriptors. In quantum chemistry, the highest energy level of molecule is represented by the spectral radius of graph. Hence, it is advantageous to estimate the energy of molecules if the spectral radius has adequate upper bounds. The second-largest eigenvalue of the graph is closely related to the molecule stability and associated chemical characteristics. The spectral gap is the result obtained by subtracting the second-largest eigenvalue from that of the largest eigenvalue and is often used as a measure of the convergence rate in numerical methods in computational chemistry. A large spectral gap is associated with fast convergence, while a smaller spectral gap indicates slower convergence. Entropy is a measureable physical characteristics and a scientific notion that is frequently connected to a condition of disorder, unpredictability or uncertainty. The fundamental thermophysical quantities known as graph entropies [3] are used to quantify the heterogeneity and relative stabilities of molecules. They are defined for various graph invariants. Eigenvalue-based entropy is a kind of graph entropy that has been extensively studied which depends on the adjacency matrix of the graph. An indicator of a connection or statistical association between two variables is a correlation coefficient [4]. Note that the graphs considered in this paper are combinatorial graphs in which edges are relations between vertices only. In literature, there are also metric graphs in which certain differential operator is defined on the edges [5]. In this metric-model, the spectrum is not bounded above and the spectral gap is also defined differently as the difference between the last (smallest) and second smallest eigenvalues [6]. In the present work, the spectral parameters of all isomers of nonane have been computed and its relationship with the corresponding eigenvalue-based entropy is established. Then the spectral parameters are correlated with the density of nonane isomers in order to find which parameter has the best correlation with the density of nonane isomers.

2. Preliminaries

A graph denoted as $G = (V, E, \psi_G)$ consists of a collection of two sets: a set (necessarily nonempty) of vertices V , a set of edges E , and a relation $\psi_G : E \rightarrow V \times V$ termed as incidence relation. Adjacency matrix is a binary matrix which reflects whether two vertices v_i, v_j in the graph are adjacent or not. If they are adjacent then its entry in the matrix will be 1 and all the non-adjacent pairs are made 0. A characteristic polynomial can be derived from the matrix by using $P(A; \lambda) = \det(A - \lambda I_n)$ where I_n is the identity matrix. Note that $n = |V|$. By solving the characteristic equation, eigenvalues of the matrix are obtained. The highest among all the eigenvalues is known as spectral radius. The sum of absolute eigenvalues is termed as graph energy [7]. The arrangement of distinct eigenvalues along with their algebraic multiplicities is called as spectrum. When arranged in a non-increasing order, the difference between the first two eigenvalues is known as the spectral gap.

Two nonisomorphic graphs having same spectrum are called cospectral graphs and two non-cospectral graphs having same energy are called equienergetic graphs. If $\lambda_1, \lambda_2, \dots, \lambda_n$ denote the eigenvalues of $A(G)$ and $E(G)$ denote the energy

of G , then the eigenvalue-based entropy [8] I of G is defined as $I(A) = - \sum_{j=1}^n \frac{|\lambda_j|}{E(G)} \log \frac{|\lambda_j|}{E(G)}$. Spearman's rank

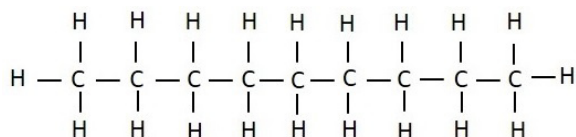
correlation coefficient, also known as the Spearman coefficient correlation [9], is a statistical measure used to assess the strength and direction of the monotonic relationship between two variables. This coefficient is especially valuable when the relationship between the variables does not strictly adhere to a linear pattern, but rather exhibits a monotonic trend. The coefficient itself ranges between -1 and 1 . A value of -1 indicates a perfect negative monotonic relationship. Conversely, a value of 1 represents a perfect positive monotonic relationship whereas, 0 suggests no monotonic relationship between the variables. The p-value indicates the likelihood of obtaining a result extreme (on both ends) than the observed result, assuming there is no relationship between variables. Covariance quantifies the extent to which variables vary together. The test statistic is a numerical summary used in hypothesis testing to compare the observed data to a distribution or critical values. It helps one to determine the statistical significance of the result and whether to reject the null hypothesis. Sample size is the number of observations in a sample which affects the reliability of estimates.

3. Literature Survey

A. E. Brouwer and W. H. Haemers [10] cover a variety of topics in spectral graph theory and highlight the critical role that linear algebra plays in graph theory in their book Spectra of Graphs. R. Balakrishnan and K. Ranganathan [7] explain clearly the requisite for this study of chemical-graph and spectral basis. D. A. Spielman [11] gave an overview of certain spectrum applications and shed some light on the combinatorial relevance of the eigenvectors and eigenvalues. Ivan Gutman et al. [12] have put forth an innovative method for calculating the total pi-electron energy of a conjugated hydrocarbon using spectral moments along with coining certain outstanding problems. F. Harary and A. J. Schwenk [13] have developed a methodical approach for identifying graphs with integral spectra. O. Ahmadi et al. [14] have shown that only a small percentage of graphs contain an integral spectrum. G. Indulal et al. [15] have constructed numerous classes of integral graphs and by defining a new composition on three graphs. M. Dehmer and A. Mowshowitz [16] have done a survey on describing methods to measure graph entropy and to demonstrate its wide applicability. M. Dehmer [17] has introduced a general framework for defining the graph entropy based on a local-information graph and information-related functions derived from a graph's topology. Y. Sun and H. Zhao [8] have defined the eigenvalue-based entropy for the directed bipartite network.

4. Nonane and its Isomers

The nonane isomers having empirical formula C_9H_{20} are the subject of this study (refer Fig. 1). Nonane comes in 35 different isomers. Nonane naturally occurs in crude oil. One of the by-products of the fractional distillation of crude oil is kerosene fraction. Despite being insoluble in water, it is a good solvent for a variety of chemicals. Nonane is primarily used as an aviation and automotive fuel.



(a) n -Nonane (N_1)



(b) molecular graph of n -Nonane (N_1)

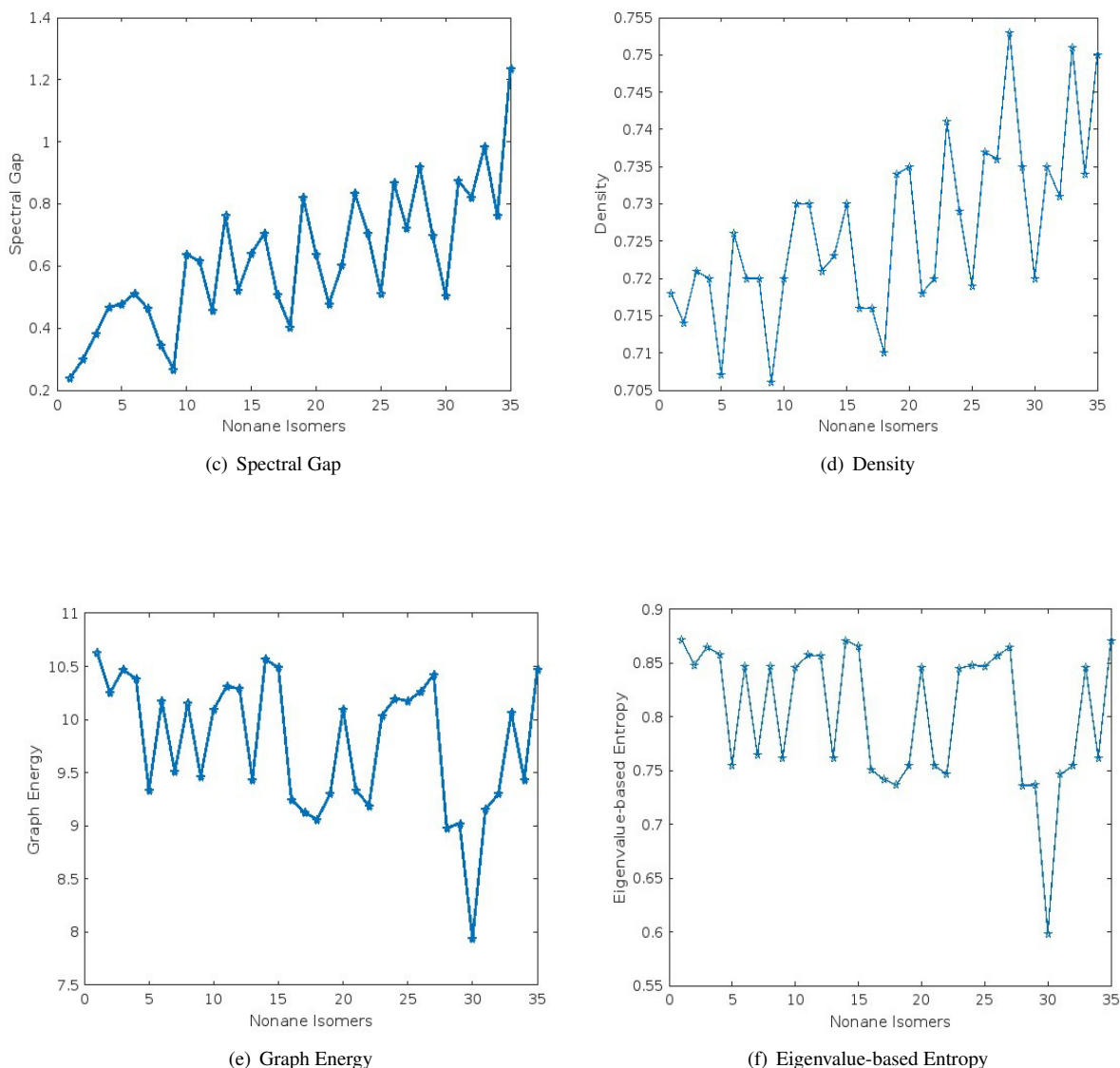


FIG. 2. 2D graph of spectral parameters

6. Observations

1. Isomers that have their third positioned carbon atoms in their spine to be branched are found to have an increase in their density values compared to their predecessors.
2. Except for N_5 , it can be observed from Fig 2 that the second-largest eigenvalue is inversely proportional to the spectral radius.
3. Except for N_6 , it can be noticed that the spectral gap is directly proportional to the spectral radius.
4. Fig. 2 (e and f) proves that the graph energy is directly proportional to the eigenvalue-based entropy.
5. The pairs of non-isomorphic graphs (N_5, N_{21}) , (N_6, N_{25}) , (N_{10}, N_{20}) , (N_{13}, N_{34}) and (N_{19}, N_{32}) are having the same spectrum and thus, they are cospectral graphs.
6. The pairs of graphs (N_3, N_9) , (N_5, N_{21}) , (N_6, N_{25}) , (N_{10}, N_{20}) , (N_{13}, N_{34}) , (N_{18}, N_{27}) and $(N_{19}, N_{30}, N_{32}, N_{35})$ have the same spectral radius.
7. The spectral radius increases based on the number of branches and their positions along the spine. Closer proximity between the branches leads to a higher spectral radius, indicating greater connectivity within the structure. This is due to the fact that branching affects the number of bonds and distance between atoms, which can result in different graph representations with distinct adjacency matrices.
8. The sets of graphs (N_5, N_{21}) , (N_6, N_{25}) , (N_{10}, N_{20}) , (N_1, N_3, N_{12}) , (N_9, N_{18}, N_{30}) , $(N_{13}, N_{15}, N_{19}, N_{23}, N_{24}, N_{27}, N_{28}, N_{31}, N_{32}, N_{34})$ have the same second highest eigenvalues.
9. The pairs of non-isomorphic graphs (N_5, N_{21}) , (N_6, N_{25}) , (N_{10}, N_{20}) , (N_{13}, N_{34}) and (N_{19}, N_{32}) are having the same spectral gap.

10. The pair of graphs $(N_3, N_{35}), (N_5, N_{21}), (N_6, N_{25}), (N_{13}, N_{34}), (N_{18}, N_{29})$ and (N_{19}, N_{32}) have the same energy, thus, they are equienergetic graphs.
11. The pair of graphs $(N_5, N_{21}), (N_6, N_{25}), (N_{10}, N_{20}), (N_{13}, N_{34}), (N_{18}, N_{29})$ and (N_{19}, N_{32}) have the same eigenvalue-based entropy.
12. The pair of graphs (N_{18}, N_{29}) have the same entropy though they are not equienergetic whereas the graphs (N_3, N_{35}) have different entropies though they have the same graph energy.
13. The isomer pairs $(N_1, N_{21}), (N_3, N_{13}), (N_7, N_8, N_{10}, N_{22}, N_{30}), (N_{11}, N_{12}, N_{15}), (N_{16}, N_{17}), (N_{19}, N_{34}), (N_{20}, N_{29}, N_{31})$ have the same density.

TABLE 1. Extremal graphs of nonane

Parameters	Density	Spectral Radius	Second Largest Eigenvalue	Spectral gap	Graph energy	Eigenvalue-based entropy
Highest valued isomer	N_{28}	N_{28}	(N_9, N_{18}, N_{30})	N_{35}	N_1	N_1
Least valued isomer	N_9	N_1	N_{35}	N_1	N_{30}	N_{30}

7. Correlation Coefficient of nonane density

The correlation coefficient between the density and the spectral parameters of 35 nonane isomers has been calculated and presented in the following table 2. In this analysis, the density values of all 35 nonane isomers are fixed as variables of Y, and they are correlated with spectral parameters as variables of X. The correlation coefficients provide insights into the strength and direction of the linear relationships between the density and the spectral parameters. Additionally, a graphical representation of the correlations is provided. This analysis utilizes the entire sample size of 35 nonane isomers to explore the relationships between the density and the spectral parameters.

TABLE 2. Correlation coefficient between the density and the spectral parameters of nonane

Correlation	Spectral Radius	Second Largest Eigenvalue	Spectral gap	Graph energy	Eigenvalue-based entropy
Correlation Coefficient	0.59499	-0.81322	0.80398	0.11307	0.12701
P value	6.96e-5	5.613e-9	4.3332e-10	0.3794	0.2161
Covariance	7.296e-4	-1.4e-3	2.13e-3	1.123e-3	1.598e-4
Sample Size	35	35	35	35	35
Test statistic	4.5471	-7.7908	8.7296	0.891	1.2612

From the above parameters, the following graphs (Fig 3) have been plotted to have a comparative view among the results obtained.

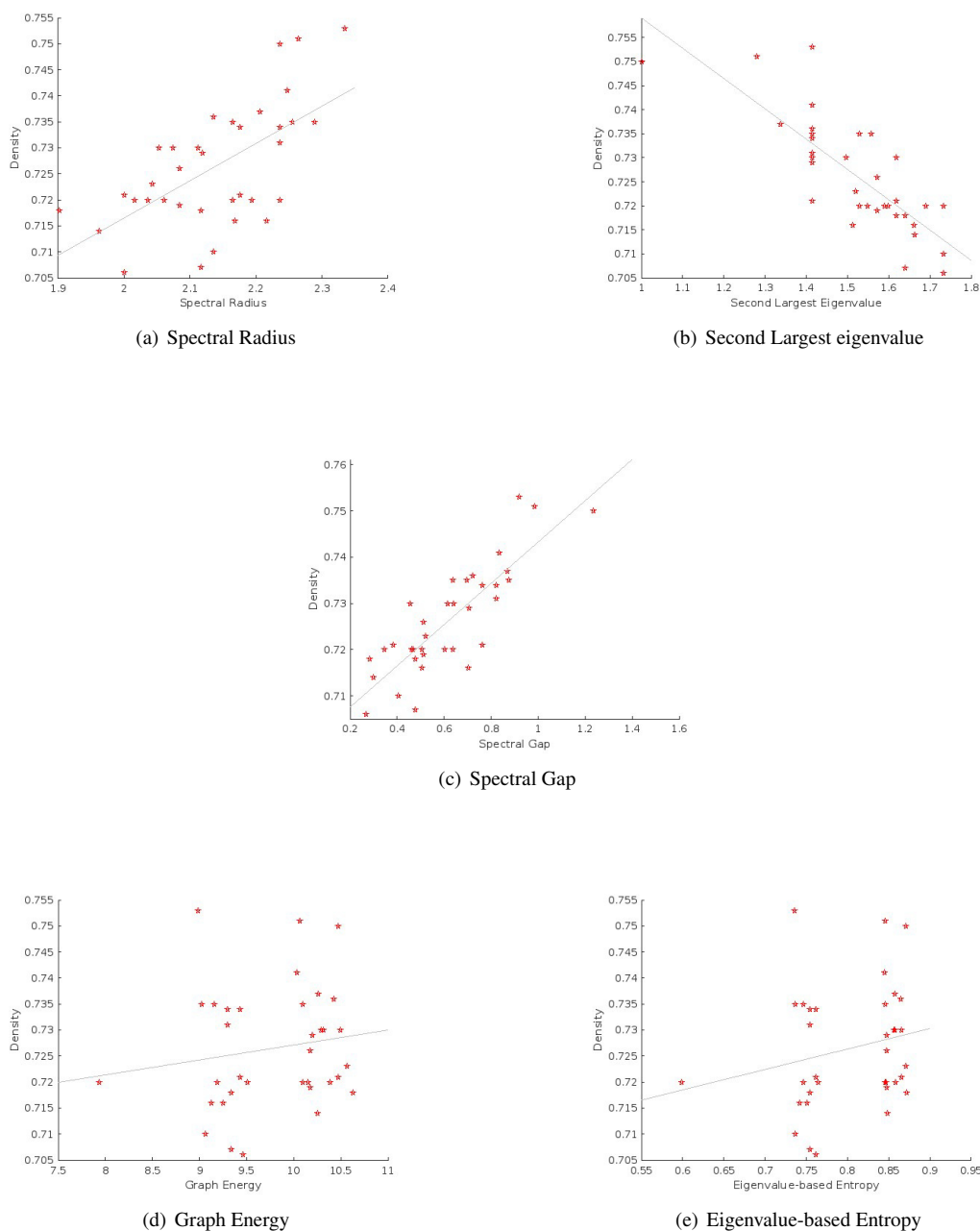


FIG. 3. Graphical representation of Correlation Coefficient between density and spectral parameters of nonane isomers

8. Observation

1. From the above table 2 we can notice that the spectral gap has maximum correlation with the density of nonane.
2. A correlation coefficient of 0.80398 suggests a strong positive correlation between the variables in the sample of 35 observations(isomers). It indicates that there is a strong tendency for the variables to increase or decrease together.
3. The extremely small p-value $4.3332e-10$ indicates that the observed data is highly unlikely to occur by chance if the null hypothesis is true based on sample of 35 observations. This suggests strong evidence against the null hypothesis and supports the presence of a significant effect or relationship in your data.
4. The covariance measures the extent to which two variables vary together. With a covariance of $2.13e-3$ in the sample of 35 observations, it suggests a positive covariance between the variables, indicating that they tend to vary in a similar direction.
5. The correlation coefficient of -0.81322 indicates a strong negative monotonic relationship between the two variables. This means that as one variable increases, the other variable tends to decrease. The negative sign indicates the direction of the relationship.

6. The p-value of $5.613e-9$ is extremely small, suggesting strong evidence against the null hypothesis. In this case, it indicates that the observed correlation coefficient is significantly different from zero. Thus, we can conclude that there is a statistically significant correlation between the two variables.
7. The covariance of $-1.4e-3$ indicates a negative relationship between the variables.
8. The sample size of 35 indicates the number of data points used to calculate the correlation coefficient. A larger sample size generally provides more reliable estimates of the correlation between variables.
9. The test statistic of -7.7908 is likely associated with a significance test for the correlation coefficient. The exact interpretation of this value depends on the specific test employed.
10. Except the second largest eigenvalue, all other spectral parameters has positive correlation with the density of nonane.

9. Conclusion

To extend this further, we could try to investigate the relationship between graph energy and graph entropy in detail for different classes of molecular graphs beyond the isomers of nonane. By analyzing a larger and more diverse set of molecular graphs, we would be able to draw more general conclusions about the relationship between graph energy and graph entropy, and identify any patterns or trends across different classes of molecules. We could also explore some of the underlying chemical and physical factors that contribute to these properties, such as bond strength, electronic interactions, and molecular shape. This type of research could have potential applications in fields such as drug discovery, materials science, and catalysis.

References

- [1] Arora A. *Hydrocarbons (Alkanes, Alkenes and Alkynes)* Discovery Publishing House, 2006.
- [2] Balaban A.T. Applications of graph theory in chemistry. *Journal of chemical information and computer sciences*, 1985, **25**(3), P. 334–343.
- [3] Dehmer M., Emmert-Streib F., Chen Z., Li X., Shi Y. eds. *Mathematical Foundations and Applications of Graph Entropy*. John Wiley & Sons, 2017.
- [4] Asuero A.G., Sayago A. and González A.G. The correlation coefficient: An overview. *Critical Reviews in Analytical Chemistry*, 2006, **36**(1), P. 41–59.
- [5] Berkolaiko G., Kuchment P., *Introduction to Quantum Graphs*. American Mathematical Soc. Providence, 2013.
- [6] Blinova I.V., Popov A.I. and Bosova A.A. Spectral gaps for star-like quantum graph and for two coupled rings. *Nanosystems: Phys. Chem. Math.*, 2022, **13**(3), P. 245–249.
- [7] Balakrishnan R., Ranganathan K. *A Textbook of Graph Theory*. Springer Science & Business Media, 2012.
- [8] Sun Y. and Zhao H. Eigenvalue-based entropy and spectrum of bipartite digraph. *Complex & Intelligent Systems*, 2022, **8**(4), P. 3451–3462.
- [9] Jerrold H.Z. Spearman rank correlation. *Encyclopedia of biostatistics*, 2005, **7**.
- [10] Brouwer A.E., Haemers W.H. *Spectra of Graphs*. Springer Science & Business Media, 2011.
- [11] Spielman D.A. Spectral graph theory and its applications. In 48th Annual IEEE Symposium on Foundations of Computer Science (FOCS'07), *IEEE*, 2007, P. 29–38.
- [12] Gutman I., Trinajstić N. Graph theory and molecular orbitals. total φ -electron energy of alternant hydrocarbons. *Chemical Physics Letters*, 1972, **17**(4), P. 535–538.
- [13] Harary F., Schwenk A.J. Which graphs have integral spectra? In *Graphs and Combinatorics: Proceedings of the Capital Conference on Graph Theory and Combinatorics at the George Washington University June*, 1973, P. 18–22.
- [14] Ahmadi O., Alon N., Blake I.F. and Shparlinski I.E. Graphs with integral spectrum *Linear Algebra and its Applications*, 2009, **430**(1), P. 547–552.
- [15] Indulal G., Balakrishnan R., Anuradha A. Some new families of integral graphs. *Indian Journal of Pure and Applied Mathematics*, 2014, **45**(6), P. 805–817.
- [16] Dehmer M. and Mowshowitz A. A history of graph entropy measures. *Information Sciences*, 2011, **181**(1), P. 57–78.
- [17] Dehmer M. Information processing in complex networks: Graph entropy and information functionals. *Applied Mathematics and Computation*, 2008, **201**(1-2), P. 82–94.
- [18] Rodríguez-Velázquez J.A. and Balaban A.T. Two new topological indices based on graph adjacency matrix eigenvalues and eigenvectors. *Journal of Mathematical Chemistry*, 2019, **57**, P. 1053–1074.
- [19] Puth M.T., Neuhäuser M., Ruxton G.D. Effective use of pearson's product-moment correlation coefficient. *Animal Behaviour*, 2014, **430**(1), P. 183–189.
- [20] C. Book. N-decane basic information, 2023.
URL/arXiv: https://www.chemicalbook.com/ProductChemicalPropertiesCB6392378_EN.htm

Submitted 16 October 2023; revised 6 January 2024

Information about the authors:

Barnabas I. Andrew – Department of Mathematics, Faculty of Engineering and Technology, SRM Institute of Science and Technology, Kattankulathur, Tamil Nadu 603203, India; ORCID 0009-0002-3858-7399; ab8559@srmist.edu.in

Ambarishan Anuradha – Department of Mathematics, Faculty of Engineering and Technology, SRM Institute of Science and Technology, Kattankulathur, Tamil Nadu 603203, India; ORCID 0000-0002-2200-688X; anuradha@srmist.edu.in

Conflict of interest: the authors declare no conflict of interest.

On solutions to nonlinear integral equation of the Hammerstein type and its applications to Gibbs measures for continuous spin systems

Ismoil M. Mavlonov^{3,a}, Aloverdi M. Sattarov^{4,b}, Sevinchbonu A. Karimova³, Farhod H. Haydarov^{1,2,3,c}

¹Institute of Mathematics, Tashkent, Uzbekistan

²New Uzbekistan University, Tashkent, Uzbekistan

³National University of Uzbekistan, Tashkent, Uzbekistan

⁴University of Business and Science, Namangan, Uzbekistan

^amavlonovismoil16@gmail.com, ^bsaloberdi90@mail.ru, ^chaydarov_imc@mail.ru,

Corresponding author: I. M. Mavlonov, mavlonovismoil16@gmail.com

ABSTRACT The paper deals with the problem of constructing kernels of Hammerstein-type equations whose positive solutions are not unique. This problem arises from the theory of Gibbs measures, and each positive solution of the equation corresponds to one translation-invariant Gibbs measure. Also, the problem of finding kernels for which the number of positive solutions to the equation is greater than one is equivalent to the problem of finding models which has phase transition. In these articles, the number of solutions corresponding to the constructed kernels does not exceed 3, and in turn, it only gives us a chance to check the existence of phase transitions. The constructed kernels in this paper are more general than the kernels in the above-mentioned papers and except for checking phase transitions, it allows us to classify the set of Gibbs measures.

KEYWORDS Generalized SOS model, spin values, Cayley tree, gradient Gibbs measure, periodic boundary law

ACKNOWLEDGEMENTS We thank the referee for careful reading of the manuscript; in particular, for some comments, useful discussions, and suggestions which have improved the paper.

FOR CITATION Mavlonov I.M., Sattarov A.M., Karimova S.A., Haydarov F.H. On solutions to nonlinear integral equation of the Hammerstein type and its applications to Gibbs measures for continuous spin systems. *Nanosystems: Phys. Chem. Math.*, 2024, **15** (1), 23–30.

1. Introduction

The Hammerstein equation covers a large variety of areas and is of much interest to a wide audience due to the fact that it has applications in numerous areas. Several problems arise in differential equations (ordinary and partial), for instance, elliptic boundary value problems whose linear parts possess Green's function can be transformed into the Hammerstein integral equations. Equations of the Hammerstein type play a crucial role in the theory of optimal control systems and in automation and network theory (see e.g., [1]).

The Hammerstein equation is a mathematical model that describes the response of a system to an input signal. It is commonly used in control systems engineering and signal processing.

Let $G(u(t))$ represent the static nonlinearity component of the system, which is a function of the input signal, and $H(u(t))$ represent the dynamic linear component of the system, which is a linear function of the input signal. Then the equation is typically represented as: $y(t) = G(u(t)) + H(u(t))$, where $y(t)$ and $u(t)$ represent the output and input signal to the system at time t .

The Hammerstein equation allows one modeling of systems that exhibit both linear and nonlinear behavior, making it useful in various applications.

In statistical mechanics, the Gibbs measure is a probability distribution that describes the equilibrium state of a system. It is commonly used to describe systems with countable spin values, where the spins can take on a finite or countably infinite number of discrete values. However, there are also models with uncountable spin values, where the spins can take uncountably many values, such as in continuous spin systems. In these cases, the Gibbs measure needs to be adapted to handle the uncountable nature of the spin values.

The definition of the Gibbs measure for models with uncountable spin values often involves considering the Hamiltonian or energy function that governs the system. The Gibbs measure assigns a probability to each spin configuration based on its energy, such that spin configurations with lower energy have higher probabilities.

Specifically, for a given spin configuration, the probability assigned by the Gibbs measure is proportional to the exponential of the negative energy of that configuration. The proportionality constant is chosen such that the total probability

assigned by the Gibbs measure sums to 1 over all possible spin configurations. Note that all the above-mentioned and additional information can be found in References [2–4].

In recent years, increasing attention was given to models with a *uncountable* many spin values on particle systems (especially, the Cayley tree). By this time, models with four interactions with the set of spin values $[0, 1]$ were considered, and the following results were achieved: In [5] splitting Gibbs measures on the Cayley tree of order k are described by solutions to a special nonlinear integral equation of Hammerstein's type. The existence of positive solutions to the nonlinear integral equation of Hammerstein's type and a sufficient condition of the uniqueness of the equation given in [6]. Also, in [7–10], results on non-uniqueness of positive solutions to the equation with non-degenerate kernels are given and for the case of degenerate kernel can be seen in [11, 12]. Finally, in [13, 14] translation-invariant Gibbs measures for models with four competing interactions are described by solutions to the Lyapunov integral equation. In this paper, we construct more general kernels which gives us a chance to check the existence of phase transitions and to classify the set of Gibbs measures.

2. Special equation of Hammerstein type

Let Ω be a set. A nonlinear integral equation of Hammerstein type on Ω is one of the form

$$u(x) + \int_{\Omega} K(x, y) f(l(y)) dy = h(x) \quad (2.1)$$

where dy stands for a σ -finite measure on the measure space Ω ; the mappings l and K are measurable on Ω and $\Omega \times \Omega$ respectively, f is a real-valued function defined on \mathbb{R} and is in general nonlinear and h is given function on Ω . If we define the operator A by

$$Av(x) = \int_{\Omega} K(x, y) v(y) dy, \quad (2.2)$$

and N_f to be the Nemystkii operator associated with f :

$$\tilde{N}_f l(x) = f(l(x)) \quad (2.3)$$

then integral equation (2.1) can be transformed to functional equation form as follows:

$$l + A\tilde{N}_f l = 0, \quad (2.4)$$

where without the loss of generality, we have taken $h \equiv 0$ (see detail in [15]).

We consider a special equation of Hammerstein type, i.e.

$$\int_0^1 K(x, y) l^k(y) dy = l(x), \quad k \in \mathbb{N}. \quad (2.5)$$

Here and below, $K : [0, 1]^2 \rightarrow (0, +\infty)$.

Actually, the last equation is very sufficient in the Gibbs measure theory. In the present paper, we give short information about relation between the last equation and the Gibbs measures. Detailed information can be found in references [5, 8].

Let $\Gamma^k = (V, L)$ be a Cayley tree and we consider models where the spin takes values in the set $[0, 1]$, and is assigned to the vertices of the tree. For $A \subset V$ a configuration σ_A on A is an arbitrary function $\sigma_A : A \rightarrow [0, 1]$. For $J \in R \setminus \{0\}$ and $\xi : (u, v) \in [0, 1]^2 \rightarrow \xi_{uv} \in R$ we define a Hamiltonian

$$H(\sigma) = -J \sum_{\langle x, y \rangle \in L} \xi_{\sigma(x)\sigma(y)}, \quad (2.6)$$

which is the generalization of some classic models such as Ising, Potts, Here and below, the notation $\langle x, y \rangle$ means the nearest neighbor vertices.

Let $h(t, x) := h_{t,x}, (t, x) \in [0, 1] \times V$ be real mapping of $x \in V \setminus \{x^0\}$, where x^0 is a root of the tree. Now, we define the family of probability measures $\{\mu^{(n)}\}_{n \in \mathbb{N}}$ on Ω_{V_n} , i.e.,

$$\mu^{(n)}(\sigma_n) = Z_n^{-1} \exp \left(-\beta H(\sigma_n) + \sum_{x \in W_n} h_{\sigma(x), x} \right), \quad (2.7)$$

Here, as before, $\sigma_n : x \in V_n \mapsto \sigma(x)$ and Z_n is the partition function.

If the family of probability measures $\{\mu^{(n)}\}_{n \in \mathbb{N}}$ is compatible then by Kolmogorov's extension theorem, there exists a unique measure μ on Ω_V such that $\mu(\{\sigma|_{V_n} = \sigma_n\}) = \mu^{(n)}(\sigma_n)$ for all $n \in \mathbb{N}$. The measure μ is called *splitting Gibbs measure* corresponding to Hamiltonian (2.6)

The following result describes a new condition which is equivalent to the condition of compatibility.

Proposition 1. [5] The probability distributions $\mu^{(n)}(\sigma_n)$, $n = 1, 2, \dots$, in (2.7) are compatible iff for any $x \in V \setminus \{x^0\}$ the following equation holds:

$$f(t, x) = \prod_{y \in S(x)} \frac{\int_0^1 \exp(J\beta\xi_{tu})f(u, y)du}{\int_0^1 \exp(J\beta\xi_{0u})f(u, y)du}. \quad (2.8)$$

Here, and below $f(t, x) = \exp(h_{t,x} - h_{0,x})$, $t \in [0, 1]$ and $du = \lambda(du)$ is the Lebesgue measure.

Let $f(t, x)$ do not depend on the vertices of the Cayley tree. Then the last equation (2.8) has strongly positive solution if and only if the equation (2.5) has strongly positive solution in $\mathcal{M}_0 = \{f \in C^+[0, 1] : f(0) = 1\}$, where $C^+[0, 1]$ is the set of all positive continuous functions on $[0, 1]$ (see [6]).

Let $f\left(\frac{1}{3}\right) = g\left(\frac{2}{3}\right) = c$ and denote that

$$\varphi_1(t) = \begin{cases} f(t) & \text{if } t \in \left[0, \frac{1}{3}\right] \\ c & \text{if } t \in \left[\frac{1}{3}, \frac{2}{3}\right] \\ g(t) & \text{if } t \in \left[\frac{2}{3}, 1\right] \end{cases} \text{ and } \varphi_2(t) = \begin{cases} g(1-t) & \text{if } t \in \left[0, \frac{1}{3}\right] \\ c & \text{if } t \in \left[\frac{1}{3}, \frac{2}{3}\right] \\ f(1-t) & \text{if } t \in \left[\frac{2}{3}, 1\right] \end{cases}.$$

Also, for $f_1\left(\frac{1}{3}\right) = g_1\left(\frac{2}{3}\right) = c_1$, we define functions:

$$\psi_1(u) = \begin{cases} f_1(u) & \text{if } u \in \left[0, \frac{1}{3}\right] \\ c_1 & \text{if } u \in \left[\frac{1}{3}, \frac{2}{3}\right] \\ g_1(u) & \text{if } u \in \left[\frac{2}{3}, 1\right] \end{cases} \text{ and } \psi_2(u) = \begin{cases} g_1(1-u), & \text{if } u \in \left[0, \frac{1}{3}\right] \\ c_1, & \text{if } u \in \left[\frac{1}{3}, \frac{2}{3}\right] \\ f_1(1-u), & \text{if } u \in \left[\frac{2}{3}, 1\right] \end{cases}.$$

By using these functions, we define a degenerate kernel:

$$\tilde{K}(t, u) = \varphi_1(t)\psi_1(u) + \varphi_2(t)\psi_2(u). \quad (2.9)$$

Then equation (2.5) can be written as

$$f(t) = \int_0^1 (\varphi_1(t)\psi_1(u) + \varphi_2(t)\psi_2(u))f^k(u)du. \quad (2.10)$$

Namely,

$$f(t) = \varphi_1(t) \int_0^1 \psi_1(u)f^k(u)d(u) + \varphi_2(t) \int_0^1 \psi_2(u)f^k(u)d(u) = f(t).$$

Put

$$C_1 = \int_0^1 \psi_1(u)f^k(u)d(u), \quad C_2 = \int_0^1 \psi_2(u)f^k(u)du.$$

Consequently, by taking into account $f(t) = C_1\varphi_1(t) + C_2\varphi_2(t)$, we obtain

$$C_i = \int_0^1 \psi_i(u)(C_1\varphi_1(u) + C_2\varphi_2(u))^k du, \quad i \in \{1, 2\}.$$

The last equality is equivalent to

$$\begin{cases} C_1 = \binom{k}{0} C_1^k \alpha_1 + \binom{k}{1} C_1^{k-1} C_2 \alpha_2 + \dots + \binom{k}{k} C_2^k \alpha_{k+1} \\ C_2 = \binom{k}{0} C_2^k \alpha_1 + \binom{k}{1} C_2^{k-1} C_1 \alpha_2 + \dots + \binom{k}{k} C_1^k \alpha_{k+1}. \end{cases} \quad (2.11)$$

Here and below,

$$\begin{aligned}\alpha_1 &= \int_0^1 \psi_1(u) \varphi_1^k(u) du, & \alpha_2 &= \int_0^1 \psi_1(u) \varphi_1^{k-1}(u) \varphi_2(u) du, & \dots & \alpha_{k+1} = \int_0^1 \psi_1(u) \varphi_2^{k+1}(u) du, \\ \beta_1 &= \int_0^1 \psi_2(u) \varphi_1^k(u) du, & \beta_2 &= \int_0^1 \psi_2(u) \varphi_1^{k-1}(u) \varphi_2(u) du, & \dots & \beta_{k+1} = \int_0^1 \psi_2(u) \varphi_2^{k+1}(u) du.\end{aligned}\quad (2.12)$$

Let $x = \frac{C_1}{C_2}$, then the system of equations (2.11) can be written as

$$x = \frac{\binom{k}{0} \alpha_1 x^k + \binom{k}{1} \alpha_2 x^{k-1} + \binom{k}{2} \alpha_3 x^{k-2} + \dots + \binom{k}{k-1} \alpha_k x + \binom{k}{k} \alpha_{k+1}}{\binom{k}{0} \alpha_{k+1} x^k + \binom{k}{1} \alpha_k x^{k-1} + \binom{k}{2} \alpha_{k-1} x^{k-2} + \dots + \binom{k}{k-1} \alpha_2 x + \binom{k}{k} \alpha_1}.$$

Namely,

$$\begin{aligned}Q_k(x) &:= \binom{k}{0} \alpha_{k+1} x^{k+1} + \left(\binom{k}{1} \alpha_k - \binom{k}{0} \alpha_1 \right) x^k + \dots \\ &\dots + \left(\binom{k}{k} \alpha_1 - \binom{k}{k-1} \alpha_k \right) x - \binom{k}{k} \alpha_{k+1}.\end{aligned}\quad (2.13)$$

Now, we can conclude the following result:

Proposition 2. *Finding positive solutions of equation (2.5) with the kernel (2.9) is equivalent to finding positive roots of the polynomial $Q_k(x)$.*

In the next sections, we consider the positive roots of the polynomial $Q_k(x)$ in special cases.

3. Solutions to the equation (2.5) with the kernel (2.9) for the case $k = 2$.

In this section, we study positive solutions to equation (2.5) with the kernel (2.9) for the case $k = 2$.

Let $k = 2$ then the system of equations (2.11) can be rewritten as

$$\begin{cases} C_1 = C_1^2 \alpha_1 + 2C_1 C_2 \alpha_2 + C_2^2 \alpha_3 \\ C_2 = C_1^2 \beta_1 + 2C_1 C_2 \beta_2 + C_2^2 \beta_3. \end{cases}\quad (3.1)$$

By (2.12) and the construction of kernel one obtains:

$$\begin{aligned}\alpha_1 &= \int_0^1 \psi_1(u) \varphi_1^2(u) d(u) = \int_0^{\frac{1}{3}} f_1(u) f^2(u) d(u) + \int_{\frac{1}{3}}^{\frac{2}{3}} c_1 c^2 d(u) + \int_{\frac{2}{3}}^1 g_1(u) g^2(u) du = \\ &= \int_0^{\frac{1}{3}} g_1(1-u) g^2(1-u) d(u) + \int_{\frac{1}{3}}^{\frac{2}{3}} c_1 c^2 d(u) + \int_{\frac{2}{3}}^1 f_1(1-u) f^2(1-u) du = \int_0^1 \psi_2(u) \varphi_2^2(u) d(u) = \beta_3.\end{aligned}$$

Similarly,

$$\begin{aligned}\alpha_2 &= \int_0^1 \psi_1(u) \varphi_1(u) \varphi_2(u) d(u) = \int_0^{\frac{1}{3}} f_1(u) f(u) g(1-u) d(u) + \int_{\frac{1}{3}}^{\frac{2}{3}} c_1 c^2 d(u) + \int_{\frac{2}{3}}^1 g_1(u) g(u) f(1-u) du = \\ &= \int_0^{\frac{1}{3}} g_1(1-u) f(u) g(1-u) d(u) + \int_{\frac{1}{3}}^{\frac{2}{3}} c_1 c^2 d(u) + \int_{\frac{2}{3}}^1 f_1(1-u) g(u) f(1-u) d(u) = \int_0^1 \psi_2(u) \varphi_1(u) \varphi_2(u) d(u) = \beta_2\end{aligned}$$

and

$$\begin{aligned}\alpha_3 &= \int_0^1 \psi_1(u)\varphi_2^2(u)d(u) = \int_0^{\frac{1}{3}} f_1(u)g^2(1-u)d(u) + \int_{\frac{1}{3}}^{\frac{2}{3}} c_1c^2d(u) + \int_{\frac{2}{3}}^1 g_1(u)f^2(1-u)d(u) = \\ &= \int_0^{\frac{1}{3}} g_1(1-u)f^2(u)d(u) + \int_{\frac{1}{3}}^{\frac{2}{3}} c_1c^2d(u) + \int_{\frac{2}{3}}^1 f_1(1-u)g^2(u)d(u) = \int_0^1 \psi_2(u)\varphi_1^2(u)d(u) = \beta_1.\end{aligned}$$

Hence,

$$\alpha_1 = \beta_3, \quad \alpha_2 = \beta_2, \quad \alpha_3 = \beta_1. \tag{3.2}$$

By taking into account $x = \frac{C_1}{C_2}$ and the equality (2.13), we have

$$Q_2(x) = \alpha_3x^3 + (2\alpha_2 - \alpha_1)x^2 + (\alpha_1 - 2\alpha_2)x - \alpha_3 = 0.$$

Thus, we obtain

$$Q_2(x) = (x - 1)(a_3x^2 + (a_3 + 2a_2 - a_1)x + a_3) = 0.$$

Put

$$D := (2a_2 - a_1 - a_3)(2a_2 - a_1 + 3a_3).$$

It is easy to check $a_1 + a_3 \geq 2a_2$. Therefore, the sign of D is the same as the sign of the expression $a_1 - 2a_2 - 3a_3$.

Proposition 3. *Let $k = 2$ and $\tilde{K}(t, u)$ be the kernel which defined in (2.9). Then the following statements hold:*

- (1) *If $a_1 < 2a_2 + 3a_3$ then there is unique positive solution of (2.10);*
- (2) *If $a_1 = 2a_2 + 3a_3$ then there are exactly two positive solutions of (2.10);*
- (3) *If $a_1 > 2a_2 + 3a_3$ then there are exactly three positive solutions of (2.10).*

In the language of Gibbs measure theory, we obtain:

Theorem 1. *Let $k = 2$ and $\tilde{K}(t, u)$ be the function of the Hamiltonian (2.6). Then the following assignments hold:*

- (1) *If $a_1 < 2a_2 + 3a_3$ then there is unique translation-invariant Gibbs measure of the model (2.6);*
- (2) *If $a_1 = 2a_2 + 3a_3$ then there are exactly two translation-invariant Gibbs measures of the model (2.6);*
- (3) *If $a_1 > 2a_2 + 3a_3$ then there are exactly three translation-invariant Gibbs measures of the model (2.6).*

4. Solutions to the equation (2.5) with the kernel (2.9) for the case $k = 3$.

Now, we consider positive solutions to equation (2.5) with the kernel (2.9) for the case $k = 3$. Then the system of equations (2.11) can be written as

$$\begin{cases} C_1 = C_1^3\alpha_1 + 3C_1^2C_2\alpha_2 + 3C_1C_2^2\alpha_3 + C_2^3\alpha_4 \\ C_2 = C_1^3\beta_1 + 3C_1^2C_2\beta_2 + 3C_1C_2^2\beta_3 + C_2^3\beta_4 \end{cases} \tag{4.1}$$

and

$$\alpha_1 = \int_0^1 \psi_1(u)\varphi_1^3(u)d(u) = \int_0^{\frac{1}{3}} f_1(u)f^3(u)du + \int_{\frac{1}{3}}^{\frac{2}{3}} c_1c^3du + \int_{\frac{2}{3}}^1 g_1(u)g^3(u)du = \beta_4.$$

Analogously,

$$\alpha_2 = \int_0^1 \psi_1(u)\varphi_1^2(u)\varphi_2(u)du = \int_0^{\frac{1}{3}} f_1(u)f^2(u)g(1-u)du + \int_{\frac{1}{3}}^{\frac{2}{3}} c_1c^3du + \int_{\frac{2}{3}}^1 g_1(u)g^2(u)f(1-u)du = \beta_3,$$

$$\alpha_3 = \int_0^1 \psi_1(u)\varphi_1(u)\varphi_2^2(u)du = \int_0^{\frac{1}{3}} f_1(u)f(u)g^2(1-u)du + \int_{\frac{1}{3}}^{\frac{2}{3}} c_1c^3du + \int_{\frac{2}{3}}^1 g_1(u)g(u)f^2(1-u)du = \beta_2,$$

$$\alpha_4 = \int_0^1 \psi_1(u)\varphi_2^3(u)du = \int_0^{\frac{1}{3}} f_1(u)g^3(1-u)du + \int_{\frac{1}{3}}^{\frac{2}{3}} c_1c^3du + \int_{\frac{2}{3}}^1 g_1(u)f^3(1-u)du = \beta_1.$$

As a result, one obtains

$$\alpha_1 = \beta_4, \quad \alpha_2 = \beta_3, \quad \alpha_3 = \beta_2, \quad \alpha_4 = \beta_1. \quad (4.2)$$

Consequently, the polynomial, which is defined in (2.13), is

$$Q_3(x) = \alpha_4 x^4 + (3\alpha_3 - \alpha_1)x^3 + (\alpha_1 - 3\alpha_3)x - \alpha_4 = 0.$$

Namely,

$$Q_3(x) = (x-1)(x+1)(\alpha_4 x^2 + (3\alpha_3 - \alpha_1)x + \alpha_4) = 0.$$

The discriminant of the polynomial $\alpha_4 x^2 + (3\alpha_3 - \alpha_1)x + \alpha_4$ is

$$D := (3\alpha_3 - \alpha_1 - 2\alpha_4)(3\alpha_3 - \alpha_1 + 2\alpha_4).$$

Proposition 4. *Let $k = 3$ and $\tilde{K}(t, u)$ be the kernel which defined in (2.9). Then the following statements hold:*

- (1) *If $|3\alpha_3 - \alpha_1| > 2\alpha_4$ then there is unique positive solution of (2.10);*
- (2) *If $|3\alpha_3 - \alpha_1| = 2\alpha_4$ then there are exactly two positive solutions of (2.10);*
- (3) *If $|3\alpha_3 - \alpha_1| < 2\alpha_4$ then there are exactly three positive solutions of (2.10).*

In the language of Gibbs measure theory, we can conclude the following theorem.

Theorem 2. *Put $k = 3$ and $\tilde{K}(t, u)$ is the function of the Hamiltonian (2.6). Then the following assignments hold:*

- (1) *If $|3\alpha_3 - \alpha_1| > 2\alpha_4$ then there is unique translation-invariant Gibbs measure of the model (2.6);*
- (2) *If $|3\alpha_3 - \alpha_1| = 2\alpha_4$ then there are exactly two translation-invariant Gibbs measures of the model (2.6);*
- (3) *If $|3\alpha_3 - \alpha_1| < 2\alpha_4$ then there are exactly three translation-invariant Gibbs measures of the model (2.6).*

5. Solutions to the equation (2.5) with the kernel (2.9) for the case $k = 4$.

In the Gibbs measure theory, it is more interesting to construct Hamiltonian which has more than three translation-invariant Gibbs measures. In this section, we show that the Hamiltonian which corresponds to our kernel has more than three Gibbs measures. For the case $k = 4$, the system of equations (2.11) can be written as

$$\begin{cases} C_1 = C_1^4 \alpha_1 + 4C_1^3 C_2 \alpha_2 + 6C_1^2 C_2^2 \alpha_3 + 4C_1 C_2^3 \alpha_4 + C_2^4 \alpha_5 \\ C_2 = C_1^4 + 4C_1^3 C_2 \beta_2 + 6C_1^2 C_2^2 \beta_3 + 4C_1 C_2^3 \beta_4 + C_2^4 \beta_5 \end{cases}$$

and

$$\alpha_1 = \int_0^1 \psi_1(u) \varphi_1^4(u) du = \int_0^{\frac{1}{3}} f_1(u) f^4(u) du + \int_{\frac{1}{3}}^{\frac{2}{3}} c_1 c^4 du + \int_{\frac{2}{3}}^1 g_1(u) g^4(u) du = \beta_5,$$

$$\alpha_2 = \int_0^1 \psi_1(u) \varphi_1^3(u) \varphi_2(u) du = \int_0^{\frac{1}{3}} f_1(u) f^3(u) g(1-u) du + \int_{\frac{1}{3}}^{\frac{2}{3}} c_1 c^4 du + \int_{\frac{2}{3}}^1 g_1(u) g^3(u) f(1-u) du = \beta_4,$$

$$\alpha_3 = \int_0^1 \psi_1(u) \varphi_1^2(u) \varphi_2^2(u) du = \int_0^{\frac{1}{3}} f_1(u) f^2(u) g^2(1-u) du + \int_{\frac{1}{3}}^{\frac{2}{3}} c_1 c^4 du + \int_{\frac{2}{3}}^1 g_1(u) g^2(u) f^2(1-u) du = \beta_3,$$

$$\alpha_4 = \int_0^1 \psi_1(u) \varphi_1(u) \varphi_2^3(u) du = \int_0^{\frac{1}{3}} f_1(u) f(u) g^3(1-u) du + \int_{\frac{1}{3}}^{\frac{2}{3}} c_1 c^4 du + \int_{\frac{2}{3}}^1 g_1(u) g(u) f^3(1-u) du = \beta_2,$$

$$\alpha_5 = \int_0^1 \psi_1(u) \varphi_2^4(u) du = \int_0^{\frac{1}{3}} f_1(u) g^4(1-u) du + \int_{\frac{1}{3}}^{\frac{2}{3}} c_1 c^4 du + \int_{\frac{2}{3}}^1 g_1(u) f^4(1-u) du = \beta_1.$$

Hence,

$$\alpha_1 = \beta_5, \quad \alpha_2 = \beta_4, \quad \alpha_3 = \beta_3, \quad \alpha_4 = \beta_2, \quad \alpha_5 = \beta_1. \quad (5.1)$$

By taking into account $x = \frac{C_1}{C_2}$ and the equality (5.1), one obtains

$$Q_4(x) = \alpha_5 x^5 + (4\alpha_4 - \alpha_1)x^4 + (6\alpha_3 - 4\alpha_2)x^3 + (4\alpha_2 - 6\alpha_3)x^2 + (\alpha_1 - 4\alpha_4)x - \alpha_5 = 0.$$

Namely,

$$Q_4(x) = (x-1)(\alpha_5 x^4 + (\alpha_5 + 4\alpha_4 - \alpha_1)x^3 + (\alpha_5 + 4\alpha_4 - \alpha_1 + 6\alpha_3 - 4\alpha_2)x^2 + (\alpha_5 + 4\alpha_4 - \alpha_1)x + \alpha_5) = 0.$$

After short calculations, we have (for $x \neq 1$)

$$\frac{Q_4(x)}{x^2(x-1)} = \alpha_5 y^2 + (\alpha_5 + 4\alpha_4 - \alpha_1)y + (4\alpha_4 - \alpha_5 - \alpha_1 + 6\alpha_3 - 4\alpha_2),$$

where $y = x + \frac{1}{x}$. The discriminant of the right hand side of the last equality is

$$D = (\alpha_5 + 4\alpha_4 - \alpha_1)^2 - 4\alpha_5(4\alpha_4 - \alpha_5 - \alpha_1 + 6\alpha_3 - 4\alpha_2).$$

Thus, we can give the following result:

Proposition 5. *Let $k = 4$ and $\tilde{K}(t, u)$ be the kernel which defined in (2.9). Then the following statements hold:*

- (1) *If $(\alpha_5 + 4\alpha_4 - \alpha_1)^2 < 4\alpha_5(4\alpha_4 - \alpha_5 - \alpha_1 + 6\alpha_3 - 4\alpha_2)$ then there is unique positive solution of (2.10);*
- (2) *If $(\alpha_5 + 4\alpha_4 - \alpha_1)^2 = 4\alpha_5(4\alpha_4 - \alpha_5 - \alpha_1 + 6\alpha_3 - 4\alpha_2)$ then there are at most three positive solutions of (2.10);*
- (3) *If $(\alpha_5 + 4\alpha_4 - \alpha_1)^2 > 4\alpha_5(4\alpha_4 - \alpha_5 - \alpha_1 + 6\alpha_3 - 4\alpha_2)$ then there are at most five positive solutions of (2.10).*

In the Gibbs measure theory, we obtain the following theorem.

Theorem 3. *Put $k = 4$ and let $\tilde{K}(t, u)$ be the function of the Hamiltonian (2.6). Then the following assignments hold:*

- (1) *If $(\alpha_5 + 4\alpha_4 - \alpha_1)^2 < 4\alpha_5(4\alpha_4 - \alpha_5 - \alpha_1 + 6\alpha_3 - 4\alpha_2)$ then there is unique translation-invariant Gibbs measure of the model (2.6);*
- (2) *If $(\alpha_5 + 4\alpha_4 - \alpha_1)^2 = 4\alpha_5(4\alpha_4 - \alpha_5 - \alpha_1 + 6\alpha_3 - 4\alpha_2)$ then there are at most three translation-invariant Gibbs measures of the model (2.6);*
- (3) *If $(\alpha_5 + 4\alpha_4 - \alpha_1)^2 > 4\alpha_5(4\alpha_4 - \alpha_5 - \alpha_1 + 6\alpha_3 - 4\alpha_2)$ then there are at most five translation-invariant Gibbs measures of the model (2.6).*

6. Conclusion

The central concept in understanding phase transitions on the Cayley trees is the notion of cluster decomposition. In the absence of phase transitions, there is a unique Gibbs measure that describes the equilibrium behavior of the system. However, in the presence of a phase transition, multiple Gibbs measures can coexist. The existence of multiple Gibbs measures is often associated with the breaking of symmetry in the system. This symmetry breaking can manifest itself in different ways, such as the appearance of multiple stable states or the coexistence of different phases (e.g. [3]).

Mathematically, the presence of multiple Gibbs measures can be established by studying the behavior of the system under different boundary conditions or by considering the behavior of relevant observables. The occurrence of non-uniqueness in the limit of large system size indicates the existence of phase transitions and the coexistence of multiple Gibbs measures. Also, the properties of the different Gibbs measures can also provide insights into the nature of the phase transition. For example, the entropy of the Gibbs measures can exhibit non-analytic behavior or the correlation length may diverge at the critical point (see [2] and [4]).

In short, the existence of multiple Gibbs measures is closely related to the presence of phase transitions on the Cayley trees. These phase transitions are characterized by breaking of symmetry and the coexistence of different equilibrium states. The identification and characterization of different Gibbs measures play a crucial role in understanding the critical phenomenon and the behavior of the system near the phase transition point. In this paper, we showed that under certain conditions (see Theorems 1,2,3) there exist multiple Gibbs measures of the model (2.6) (this model is a generalization of Ising, Potts, SOS, ...) on the Cayley trees of order two, three and four.

Now, we will give short information about the novelty of our paper. Firstly, in [5], authors consider the model (2.6) on the Cayley trees and prove that there is not any phase transition on the Cayley tree of order $k = 1$. For the case $k \geq 2$, models in which phase transitions exist are constructed in [8] and the generalization of the constructed model is studied in [7, 9]. In [6], the problem of finding translation-invariant (periodic with period two) Gibbs measures of the model (2.6) was reduced to finding positive fixed points of the nonlinear operator of Hammerstein type and the problem of the existence of fixed points of this operator considered in [10, 15, 16] ([13, 14]). But, from the Gibbs measure theory, it is interesting to study fixed points of the nonlinear operator of the Hammerstein type with degenerate kernel and all the above works corresponding to non-degenerate kernels. Then works for degenerate kernels considered in [11] and [12] but in these papers, the fixed point of the operator with the degenerate kernel does not correspond to any Gibbs measure. In the present paper, each fixed point of the operator with a degenerate kernel is corresponding to one Gibbs measure.

References

- [1] Dolezale V. Monotone operators and its applications in automation and network theory, in: *Studies in Automation and Control. Elsevier Science Publ*, New York, 1979.
- [2] Friedli S., Velenik Y. *Statistical Mechanics of Lattice Systems. Cambridge University Press*, 2017.
- [3] Georgii H.O. *Gibbs Measures and Phase Transitions. de Gruyter Studies in Mathematics*, 2011.
- [4] Rozikov U.A. *Gibbs measures on Cayley trees, World Sci. Pub*, Singapore, 2013.
- [5] Rozikov U.A. and Eshkabilov Yu.Kh. On models with uncountable set of spin values on a Cayley tree: Integral equations. *Math. Phys. Anal. Geom.*, 2010, **13**, P. 275–286.
- [6] Eshkabilov Yu.Kh., Haydarov F.H., Rozikov U.A. Uniqueness of Gibbs measure for models with uncountable set of spin values on a Cayley tree. *Math. Phys. Anal. Geom.*, 2013, **16(1)**, P. 1-17.
- [7] Botirov G., Jahnel B. Phase transitions for a model with uncountable spin space on the Cayley tree: the general case. *Positivity*, 2019, **23**, P. 291–301.
- [8] Eshkabilov Yu.Kh., Haydarov F.H., Rozikov U.A. Non-uniqueness of Gibbs measure for models with uncountable set of spin values on a Cayley Tree. *J.Stat.Phys.*, 2012, **147**, P. 779–794.
- [9] Jahnel B., Christof K., Botirov G. Phase transition and critical value of nearest-neighbor system with uncountable local state space on Cayley tree. *Math. Phys. Anal. Geom.*, 2014, **17**, P. 323–331.
- [10] Eshkabilov Yu.Kh., Haydarov F.H. On positive solutions of the homogeneous Hammerstein integral equation. *Nanosystems: Phys. Chem. Math.*, 2015, **6(5)**, P. 618–627.
- [11] Eshkabilov Yu.Kh., Nodirov Sh.D., Haydarov F.H. Positive fixed points of quadratic operators and Gibbs Measures. *Positivity*, 2016.
- [12] Eshkabilov Yu.Kh., Nodirov Sh.D. Positive Fixed Points of Cubic Operators on R^2 and Gibbs Measures, *Jour.Sib.Fed. Univer.Math.Phys.*, 2019, **12(6)**, P. 663–673.
- [13] Haydarov F.H. Fixed points of Lyapunov integral operators and Gibbs measures. *Positivity*, 2018, **22(4)**, P. 1165–1172.
- [14] Eshkabilov Yu.Kh., Haydarov F.H. Lyapunov operator L with degenerate kernel and Gibbs measures. *Nanosystems: Phys. Chem. Math.*, 2017, **8(5)**, P. 553–558.
- [15] Haydarov F.H. Existence and uniqueness of fixed points of an integral operator of Hammerstein type. *Theor. Math. Phys.*, 2021, **208**, P. 1228–1238.
- [16] Ganikhodjaev N.N. Exact solution of an Ising model on the Cayley tree with competing ternary and binary interactions. *Theor. Math. Phys.*, 2002, **130**, P. 419–424.

Submitted 7 November 2023; revised 12 January 2024; accepted 14 January 2024

Information about the authors:

Ismoil M. Mavlonov – National University of Uzbekistan, University str., 4 Olmazor district, Tashkent, 100174, Uzbekistan; ORCID 0009-0009-4889-1889; mavlonovismoil16@gmail.com

Aloberdi M. Sattarov – University of Business and Science, Namangan region, Namangan city, 111 Beshkapa str., Namangan, 160100, Uzbekistan; ORCID 0009-0008-0115-3937; saloberdi90@mail.ru

Sevinchbonu A. Karimova – National University of Uzbekistan, University str., 4 Olmazor district, Tashkent, 100174, Uzbekistan; ORCID 0009-0006-3128-6605;

Farhod H. Haydarov – Institute of Mathematics, 9, University str., Tashkent, 100174, Uzbekistan; New Uzbekistan University, 54, Mustaqillik Ave., Tashkent, 100007, Uzbekistan; National University of Uzbekistan, University str., 4 Olmazor district, Tashkent, 100174, Uzbekistan; ORCID 0000-0001-9388-122X; haydarov imc@mail.ru

Conflict of interest: the authors declare no conflict of interest.

Non-compact perturbation of the spectrum of multipliers given by a special form

Ramziddin R. Kucharov^{1,2,a,b}, Tillohon M. Tuxtamurodova^{2,c}

¹Tashkent International University of Financial Management and Technology, Tashkent, Uzbekistan

²National University of Uzbekistan, Tashkent, Uzbekistan

^ar.kucharov@tift.uz, ^bramz3364647@yahoo.com, ^cmirzayevatilloxon13@gmail.com

Corresponding author: R. R. Kucharov, r.kucharov@tift.uz, ramz3364647@yahoo.com

ABSTRACT In this paper, the change of the spectrum of multiplier $H_0 f(x, y) = k_0(x, y) f(x, y)$ for perturbation with non-compact partially integral operators is studied. In addition, the existence of resonance is investigated in the model $H = H_0 - (\gamma_1 T_1 + \gamma_2 T_2)$.

KEYWORDS essential spectrum, discrete spectrum, lower bound of the essential spectrum, non-compact partial integral operator, resonance with zero energy.

FOR CITATION Kucharov R.R., Tuxtamurodova T.M. Non-compact perturbation of the spectrum of multipliers given by a special form. *Nanosystems: Phys. Chem. Math.*, 2024, **15** (1), 31–36.

1. Introduction

Self-adjoint partial integral operators appear in the theory of discrete Schrödinger operators. The study of the theory of elasticity [1], continuum mechanics [2–4], aerodynamics [5] and other problems leads to the problem of spectral analysis of the partial integral operators. In 1969, Uchiyama [6,7] obtained the first results on the finiteness of the discrete spectrum of N -particle Hamiltonians with $N > 2$. He found sufficient conditions for the finiteness of the number of discrete eigenvalues for the energy operators. In 1971, Zhislin [8] assumed the total charge of the system to be less than -1 and proved that the discrete spectrum of the energy operators is finite in the symmetry spaces of negative atomic ions of molecules with any mass of nucleus and infinitely heavy nuclei.

Let \mathcal{H} be a separable Hilbert space and the operator $H_0 : \mathcal{H} \rightarrow \mathcal{H}$ be self-adjoint and have only essential spectrum ($\sigma(H_0) = \sigma_{ess}(H_0)$), i.e. the operator H_0 lacks the discrete spectrum ($\sigma_{disc}(H_0) = \emptyset$). Let's assume that the operator H_0 is perturbed by the self-adjoint operator T , i.e. consider the operator $H_0 + \varepsilon T$, $\varepsilon > 0$. The main questions in the theory of perturbation of spectra are as follows:

1) How is the structure of the spectrum of the operator $H_0 + \varepsilon T$ related to the spectrum of the original (unperturbed) operator H_0 ?

2) What are the properties of the spectrum as a function of $\varepsilon > 0$?

Let H_0 be a multiplier in $L_2(\Omega)$ ($\Omega \subset \mathbb{R}^m$ – compact): $H_0 f(x) = u(x) f(x)$, where $u(x)$ is a given real valued continuous function on Ω , $T : L_2(\Omega) \rightarrow L_2(\Omega)$ is a linear self adjoint compact operator. The operator $H_0 + \varepsilon T$, $\varepsilon > 0$, is an operator in the Friedrichs model. It is known for such an operator that $\sigma_{ess}(H_0 + \varepsilon T) = \sigma(H_0)$ [9]. In addition, a number of methods have been developed [10–12] to investigate the existence of an eigenvalue in the discrete spectrum $\sigma_{disc}(H_0 + \varepsilon T)$ and to study the finiteness (infiniteness) of the discrete spectrum $\sigma_{disc}(H_0 + \varepsilon T)$. If the operator T is non-compact, then there is no general way to study the spectrum of the perturbed operator $H_0 + \varepsilon T$. In [13, 14], a method is proposed for studying the spectrum of the operator $H_0 + \varepsilon T : L_2(\Omega_1 \times \Omega_2) \rightarrow L_2(\Omega_1 \times \Omega_2)$ ($\Omega_1 \subset \mathbb{R}^{m_1}$, $\Omega_2 \subset \mathbb{R}^{m_2}$ are nonempty compact sets), when H_0 is a multiplier defined by a continuous function $k_0(x, y)$ on $\Omega_1 \times \Omega_2$ and $T = T_1 + T_2$ is a linear bounded self adjoint operator with partial integrals in $L_2(\Omega_1 \times \Omega_2)$, i.e. T_1, T_2 are partially integral operators (PIO). It should be stressed that T_1 and T_2 with a non-zero kernel are not compact. In [13] it is proved that $\sigma_{ess}(H_0 + \varepsilon T) = \sigma(H_0 + \varepsilon T_1) \cup \sigma(H_0 + \varepsilon T_2)$, in the case when the kernels of T_1 and T_2 are continuous functions.

Consider the multiplier H_0 , given by the function $h_0(x, y)$, having the following form: $h_0(x, y) = u(x) + \omega(x, y) + v(x)$, and PIO T_1, T_2 with kernels identically equal to one.

Let the multiplier H_0 be perturbed by a non-compact operator $T = \gamma_1 T_1 + \gamma_2 T_2$, where $\gamma_1 > 0$, $\gamma_2 > 0$. The purpose of the work is to apply the method from [13] to study the structure of the essential spectrum of the operator $H_0 - (\gamma_1 T_1 + \gamma_2 T_2)$ and to study the existence of resonance in the model $H = H_0 - (\gamma_1 T_1 + \gamma_2 T_2)$.

We denote by $\sigma(\cdot)$, $\sigma_{ess}(\cdot)$ and $\sigma_{disc}(\cdot)$, respectively, the spectrum, the essential spectrum and the discrete spectrum of the self-adjoint operators.

The number

$$E_{\min}(H) = \inf\{\lambda : \lambda \in \sigma_{ess}(H)\}$$

is called the bound edge (or the lower edge) of the essential spectrum of the operator H .

2. Non-compact perturbation of the essential spectrum

Let $\Omega_1 = [0, 1]^{\nu_1} \subset \mathbb{R}^{\nu_1}$ and $\Omega_2 = [0, 1]^{\nu_2} \subset \mathbb{R}^{\nu_2}$ ($\nu_1, \nu_2 \in \mathbb{N}$). In the space $L_2(\Omega_1 \times \Omega_2)$, let us consider a linear bounded self-adjoint operator H of the form

$$H = H_0 - (\gamma_1 T_1 + \gamma_2 T_2), \quad \gamma_1 > 0, \quad \gamma_2 > 0, \quad (1)$$

where H_0 is the multiplier given by the continuous real valued function $k_0(x, y)$, i.e. $H_0 f(x, y) = k_0(x, y) f(x, y)$, and the operators T_1, T_2 in the space $L_2(\Omega_1 \times \Omega_2)$ are defined by the following formulas:

$$T_1 f(x, y) = \int_{\Omega_1} f(s, y) d\mu_1(s), \quad T_2 f(x, y) = \int_{\Omega_2} f(x, t) d\mu_2(t),$$

where $\mu_j(\cdot)$ is the Lebesgue measure on Ω_j , $j = 1, 2$.

It is known that $\sigma(H_0) = [k_0^{\min}, k_0^{\max}] \subset \sigma_{ess}(H)$, where $k_0^{\min} = \min k_0(x, y)$, $k_0^{\max} = \max k_0(x, y)$, and $\sigma_{ess}(H) = \sigma(W_1) \cup \sigma(W_2)$, where $W_k = H_0 - \gamma_k T_k$, $k = 1, 2$ (see. [13]).

Assume that $k_0(x, y) = u(x) + v(y)$, where $u(x)$ and $v(y)$ are real valued continuous functions on Ω_1 and Ω_2 , respectively. Then the operator H (1) will be unitarily equivalent to the operator $H_1 \otimes E + E \otimes H_2$, where H_1, H_2 are operators in the Friedrichs model, E is the identity operator and “ \otimes ” means the tensor product of operators [13]. Using the spectral properties of the tensor product of operators [15, 16], it can be argued that for all positive values of the parameters γ_1 and γ_2 , the operator H has at most one eigenvalue outside the essential spectrum and $E_{\min}(H) \leq 0$. The eigenvalue $\lambda \in \sigma_{disc}(H)$ of the operator H is simple and $\lambda < E_{\min}(H)$.

Suppose that $k_0(x, y) = u(x)v(y)$, where $u(x)$ and $v(y)$ are non-negative continuous functions on Ω_1, Ω_2 , respectively, and $0 \in \text{Ran}(u) \cap \text{Ran}(v)$. Then $E_{\min}(H) < 0$ and the operator H has at most one eigenvalue below the lower edge of the essential spectrum. The eigenvalue $\lambda < E_{\min}(H)$ of the operator H is simple [9, 10].

Let $\omega(x, y)$ is a non-negative continuous function on $\Omega_1 \times \Omega_2$ and $0 \in \text{Ran}(\omega)$. Assume that $u(\theta) = v(\theta) = 0$ and $\omega(x, \theta) = \omega(\theta, y) = 0$, $x \in \Omega_1, y \in \Omega_2$, where the zero element in the corresponding linear space is denoted by θ .

Let the multiplier in (1) be given by the function

$$h_0(x, y) := k_0(x, y) = u(x) + \omega(x, y) + v(y).$$

Here, we study the spectral properties of the operator:

$$H = H_0 - (\gamma_1 T_1 + \gamma_2 T_2), \quad \gamma_1, \gamma_2 > 0, \quad (2)$$

in the case

$$H_0 f(x, y) = h_0(x, y) f(x, y)$$

and under the following assumptions: the following integrals exist and are finite

$$\int_{\Omega_1} \frac{ds}{u(s)}, \quad \int_{\Omega_2} \frac{dt}{v(t)}.$$

For each $\beta \in \Omega_2$, we define the self-adjoint operator $H_1(\beta) : L_2(\Omega_1) \rightarrow L_2(\Omega_1)$ in the Friedrichs model:

$$H_1(\beta)\varphi(x) = h_0(x, \beta)\varphi(x) - \gamma_1 \int_{\Omega_1} \varphi(s) ds.$$

Similarly, for each $\alpha \in \Omega_1$, we define the operator $H_2(\alpha) : L_2(\Omega_2) \rightarrow L_2(\Omega_2)$ in the Friedrichs model:

$$H_2(\alpha)\psi(y) = h_0(\alpha, y)\psi(y) - \gamma_2 \int_{\Omega_2} \psi(t) dt.$$

Let's put $M_1(\beta) = \max_{x \in \Omega_1} h_0(x, \beta)$, $M_2(\alpha) = \max_{y \in \Omega_2} h_0(\alpha, y)$.

By Weyl's theorem [1] on the compact perturbation of the essential spectrum, we have $\sigma_{ess}(H_k(\xi)) = [0, M_k(\xi)]$, $\xi \in \Omega_j$, $j \neq k$, $j, k = 1, 2$.

Lemma 2.1. [18] *The number $\lambda \in \mathbb{R} \setminus [0, M_1(\beta)]$ is the eigenvalue of the operator $H_1(\beta)$ if and only if $\Delta_1(\beta; \gamma_1, \lambda) = 0$, where*

$$\Delta_1(\beta; \gamma_1, \lambda) = 1 - \gamma_1 \int_{\Omega_1} \frac{ds}{h_0(s, \beta) - \lambda}.$$

Let's define the function $h_1(\beta)$ on Ω_2 by the formula

$$h_1(\beta) = \int_{\Omega_1} \frac{ds}{h_0(s, \beta)}.$$

The function $h_1(\beta)$ is continuous on the set of Ω_2 and $h_1(\beta) > 0$, $\beta \in \Omega_2$.

We define [20] non-positive and continuous functions $\pi_1(y)$ on Ω_2 and $\pi_2(x)$ on Ω_1 using the following equalities

$$\pi_1(y) = \inf_{\|\varphi\|=1} (H_1(y)\varphi, \varphi), \quad y \in \Omega_2, \quad \pi_2(x) = \inf_{\|\psi\|=1} (H_2(x)\psi, \psi), \quad x \in \Omega_1.$$

Let's put $\pi_j^{\min} = \min_{\xi \in \Omega_k} \pi_j(\xi)$, $\pi_j^{\max} = \max_{\xi \in \Omega_k} \pi_j(\xi)$, $j \neq k$, $j, k = 1, 2$, $h_0^{\max} = \max_{(x,y) \in \Omega_1 \times \Omega_2} h_0(x, y)$.

Proposition 2.1. *The following conditions hold for the operators W_1 and W_2*

- a) $\sigma(W_1) = [\pi_1^{\min}, \pi_1^{\max}] \cup \sigma(H_0)$;
- b) $\sigma(W_2) = [\pi_2^{\min}, \pi_2^{\max}] \cup \sigma(H_0)$.

Proof. a) In [13], the equality $\sigma(W_1) = \sigma(H_0) \cup \sigma_1$ is proven, where

$$\sigma_1 = \{\lambda \in \rho(H_0) : \Delta_1(\beta_0; \lambda, \gamma) = 0 \text{ for some } \beta_0 \in \Omega_2\}.$$

Let $\pi_1(\beta_0) < 0$ for some $\beta_0 \in \Omega_2$. Then, due to the minimax principle, solution $\lambda_0(\beta_0)$ of the equation $\Delta_1(\beta_0; \gamma_1, \lambda) = 0$, is defined using continuous function $\pi_1(\beta_0)$. i.e. $\lambda_0(\beta_0) = \pi_1(\beta_0)$. Therefore, $\pi_1(\beta_0) \in \sigma_1$. If $\pi_1(\beta) < 0$ for all $\beta \in \Omega_2$, then $\lambda(\beta) = \pi_1(\beta) \in \sigma_1$, $\sigma_1 = [\pi_1^{\min}, \pi_1^{\max}]$ and $\sigma(W_1) = \sigma(H_0) \cup \sigma_1 = [0, h_0^{\max}] \cup [\pi_1^{\min}, \pi_1^{\max}]$. If $\pi_1(\beta_0) = 0$ for some $\beta_0 \in \Omega_2$, then $\pi_1^{\max} = 0$. Hence, we obtain $\sigma(W_1) = \sigma(H_0) \cup \sigma_1 = [0, h_0^{\max}] \cup [\pi_1^{\min}, \pi_1^{\max}] = [\pi_1^{\min}, h_0^{\max}]$.

The equality $\sigma(W_2) = [0, h_0^{\max}] \cup [\pi_2^{\min}, \pi_2^{\max}]$ is proved similarly.

Proposition 2.2. *If $\gamma_1 \leq h_1^{-1}(\theta)$, then $\sigma(H_1(\beta)) = \sigma_{ess}(H_1(\beta))$ for all $\beta \in \Omega_2$.*

Proof. Since

$$h_0(x, y) = u(x) + \omega(x, y) + v(y) \geq u(x), \quad x \in \Omega_1, \quad y \in \Omega_2,$$

then

$$H_1(\beta) \geq H_1(\theta), \quad \beta \in \Omega_2. \tag{3}$$

However, $E_{\min}(H_1(\theta)) = 0$ and

$$\Delta_1(\theta; \gamma_1, \lambda) = 1 - \gamma_1 \int_{\Omega_1} \frac{ds}{u(s) - \lambda}.$$

The function $\Delta_1(\lambda) = \Delta_1(\theta; \gamma_1, \lambda)$ on $(-\infty, 0)$ is strictly decreasing, while $\lim_{\lambda \rightarrow -\infty} \Delta_1(\lambda) = 1$ and $\lim_{\lambda \rightarrow 0^-} \Delta_1(\lambda) = 1 - \gamma_1 h_1(\theta) \geq 0$. Hence, one obtains that $\Delta_1(\lambda) = \Delta_1(\theta; \gamma_1, \lambda) > 0$ for $\lambda \in (-\infty, 0)$. Then, according to Lemma 2.1, $\sigma_{disc}(H_1(\theta)) = \emptyset$, i.e. $\sigma(H_1(\theta)) = [0, M_1(\theta)]$. It follows from (3) that

$$\inf_{\|\varphi\|=1} (H_1(\beta)\varphi, \varphi) \geq \inf_{\|\varphi\|=1} (H_1(\theta)\varphi, \varphi) = 0, \quad \beta \in \Omega_2.$$

However, $0 \in \sigma(H_1(\beta))$, $\beta \in \Omega_2$ and consequently $\inf_{\|\varphi\|=1} (H_1(\beta)\varphi, \varphi) = E_{\min}(H_1(\beta)) = 0$, $\beta \in \Omega_2$. Hence, due to the minimax principle [1], it follows that $\sigma_{disc}(H_1(\beta)) = \emptyset$, for all $\beta \in \Omega_2$.

Now we define the function $h_2(\alpha)$ on Ω_1 by the following formula

$$h_2(\alpha) = \int_{\Omega_2} \frac{dt}{h_0(\alpha, t)}.$$

Obviously, the function $h_2(\alpha)$ is continuous in Ω_1 and $h_2(\alpha) > 0$, $\alpha \in \Omega_1$.

Just as in proposition 2.2, it is proved that if $\gamma_2 \leq h_2^{-1}(\theta)$, then $\sigma(H_2(\alpha)) = \sigma_{ess}(H_2(\alpha))$ for all $\beta \in \Omega_2$.

Hence, due to Proposition 2.2, the following theorem is proved:

- Theorem 2.1.** a) if $\gamma_1 \leq h_1^{-1}(\theta)$, then $\sigma(W_1) = \sigma(H_0) = [0, h_0^{\max}]$;
 b) if $\gamma_2 \leq h_2^{-1}(\theta)$, then $\sigma(W_2) = \sigma(H_0) = [0, h_0^{\max}]$.

We define the sets $\mathcal{D}_0 \subset \Omega_2$ and $\mathcal{D}_1 \subset \Omega_2$:

$$\mathcal{D}_0 = \{\beta \in \Omega_2 : \gamma_1 \leq h_1^{-1}(\beta)\}, \quad \mathcal{D}_1 = \Omega_2 \setminus \mathcal{D}_0.$$

Lemma 2.2. a) If $\mathcal{D}_0 = \Omega_2$ (i.e. $\mathcal{D}_1 = \emptyset$), then $\pi_1(t) \equiv 0$;

b) if $\mathcal{D}_0 \neq \emptyset$, $\mathcal{D}_1 \neq \emptyset$, then $\pi_1^{\min} < \pi_1^{\max} = 0$;

c) if $\mathcal{D}_0 = \emptyset$, then $\pi_1^{\min} < \pi_1^{\max} < 0$.

Proof. Obviously, for every fixed $\beta \in \Omega_2$ and $\gamma_1 > 0$, the function $\Delta_1(\lambda) = \Delta_1(\beta; \gamma_1, \lambda)$ is strictly decreasing on $(-\infty, 0)$ and

$$\lim_{\lambda \rightarrow -\infty} \Delta_1(\lambda) = 1 \quad \text{and} \quad \lim_{\lambda \rightarrow 0^-} \Delta_1(\lambda) = 1 - \gamma_1 h_1(\beta).$$

a) Let $\mathcal{D}_0 = \Omega_2$. Then $1 - \gamma_1 h_1(\beta) \geq 0$ for all $\beta \in \Omega_2$. Due to monotonicity of the function $\Delta_1(\lambda)$ for $(-\infty, 0)$ we have $\Delta_1(\beta; \gamma_1, \lambda) > 0$ for all $\lambda \in (-\infty, 0)$ for each $\beta \in \Omega_2$. Hence, by virtue of Lemma 2.1, we obtain $\sigma(H_1(\beta)) = \sigma_{ess}(H_1(\beta))$, $\beta \in \Omega_2$. Then, by the minimax principle $\pi_1(t) = 0$ for all $t \in \Omega_2$.

b) Let $\mathcal{D}_0 \neq \emptyset$. Then there exists a point $\beta_0 \in \mathcal{D}_0 \subset \Omega_2$, such that,

$$\lim_{\lambda \rightarrow 0^-} \Delta_1(\beta_0; \gamma_1, \lambda) = 1 - \gamma_1 h_1(\beta_0) \geq 0,$$

i.e. $\Delta_1(\beta_0; \gamma_1, \lambda) \geq 0$ on $(-\infty, 0)$. Hence, due to the lemma 2.1, we obtain that $\sigma(H_1(\beta_0)) = \sigma_{ess}(H_1(\beta_0))$. Therefore, we have $\pi_1(\beta_0) = 0$. Since $\pi_1(t) \leq 0$, $t \in \Omega_2$, we have $\pi_1^{\max} = \pi_1(\beta_0) = 0$. If $\mathcal{D}_1 \neq \emptyset$, then there exists $\beta_1 \in \mathcal{D}_1 \subset \Omega_2$ such that

$$\lim_{\lambda \rightarrow 0^-} \Delta_1(\beta_1; \gamma_1, \lambda) = 1 - \gamma_1 h_1(\beta_1) < 0.$$

Hence, the equation $\Delta_1(\beta_1; \gamma_1, \lambda) = 0$ on $(-\infty, 0)$ has unique solution $\lambda_0 < 0$. By Lemma 2.1, the number λ_0 is an eigenvalue of the operator $H_1(\beta_1)$. Hence, following the minimax principle, we obtain that $\pi_1(\beta_1) = \lambda_0 < 0$, i.e. $\pi_1^{\min} \leq \pi_1(\beta_1) < 0$.

c) Let $\mathcal{D}_0 = \emptyset$. Then $\mathcal{D}_1 = \Omega_2$ and therefore for each $\beta \in \Omega_2$, we have

$$\lim_{\lambda \rightarrow 0^-} \Delta_1(\beta; \gamma_1, \lambda) = 1 - \gamma_1 h_1(\beta) < 0.$$

Due to the monotonicity of the function $\Delta_1(\beta; \gamma_1, \lambda)$ on $(-\infty, 0)$ there is a negative number $\lambda = \lambda(\beta)$ such that $\Delta_1(\beta; \gamma_1, \lambda(\beta)) = 0$, i.e. the number $\lambda(\beta)$ is the eigenvalue of the operator $H_1(\beta)$. Then, by the minimax principle, we obtain that $\pi_1(\beta) = \lambda(\beta)$, $\beta \in \Omega_2$. It follows from the continuity of the function $\pi_1(t)$ on Ω_2 that $\pi_1^{\max} < 0$.

We prove that $\pi_1^{\min} < \pi_1^{\max}$. Let's assume the opposite: let $\pi_1^{\min} = \pi_1^{\max}$. Then the solutions $\lambda_0, \lambda_0 < 0$, and $\lambda_1, \lambda_1 < 0$ of the equations $\Delta_1(\theta; \gamma_1, \lambda) = 0$ and $\Delta_1(\beta; \gamma_1, \lambda) = 0$, $\beta \in \Omega_2, \beta \neq \theta$ coincide, i.e.

$$\Delta_1(\theta; \gamma_1, \lambda_0) = \Delta_1(\beta; \gamma_1, \lambda_0) = 0.$$

Therefore, we obtain

$$\int_{\Omega_1} \frac{h_0(s, \beta) - u(s)}{(u(s) - \lambda_0)(h_0(s, \beta) - \lambda_0)} ds = 0. \quad (4)$$

However, $h_0(s, \beta) - u(s) \geq 0$, $s \in \Omega_2$ and the function

$$F_1(s, \beta) = \frac{h_0(s, \beta) - u(s)}{(u(s) - \lambda_0)(h_0(s, \beta) - \lambda_0)}$$

is non-negative continuous on Ω_2 and distinct from a constant. Hence, in accordance with the property of the Lebesgue integral, we obtain that $\int_{\Omega_2} F_1(s, \beta) ds > 0$. This contradicts equality (4). Therefore, $\pi_1^{\min} \neq \pi_2^{\max}$.

We put:

$$h_j^{\min} = \min_{\xi \in \Omega_k} h_j(\xi) \text{ and } h_j^{\max} = \max_{\xi \in \Omega_k} h_j(\xi), \quad j = 1, 2, \quad k = 1, 2, \quad j \neq k.$$

Lemma 2.2 implies the proof the theorem

- Theorem 2.2.** a) if $\gamma_1 > (h_1^{\min})^{-1}$, then $\pi_1^{\max} < 0$;
 b) if $(h_1^{\max})^{-1} < \gamma_1 \leq (h_1^{\min})^{-1}$, then $\pi_1^{\min} < 0$, $\pi_1^{\max} = 0$;
 c) if $\gamma_1 \leq (h_1^{\max})^{-1}$, then $\pi_1(t) = 0$.

A similar theorem is true for the function $\pi_2(x)$.

Corollary 2.1. If $\gamma_1 \leq (h_1^{\max})^{-1}$, $\gamma_2 \leq (h_2^{\max})^{-1}$, then $\sigma_{ess}(H) = \sigma(H_0)$.

Proof. For the essential spectrum of the operator H , the equality holds (see. [13])

$$\sigma_{ess}(H) = \sigma(W_1) \cup \sigma(W_2),$$

where $W_k = H_0 - \gamma_k T_k$, $k = 1, 2$. Hence, by Theorem 2.2 and Proposition 2.1, we obtain

$$\sigma_{ess}(H) = \sigma(H_0) = [0, h_0^{\max}].$$

Corollary 2.2 Let in (1) $\gamma_1 = h_1^{-1}(\theta)$ and $\gamma_2 = h_2^{-1}(\theta)$. Then $\sigma_{ess}(H) = \sigma(H_0)$.

Proof. Consider PIO V , defined by the equality

$$V = H_0 - (h_1^{-1}(\theta)T_1 + h_2^{-1}(\theta)T_2).$$

For $\gamma_1 = h_1^{-1}(\theta)$, one has

$$\lim_{\lambda \rightarrow 0^-} \Delta_1(\theta; \gamma_1, \lambda) = 1 - h_1^{-1}(\theta) \lim_{\lambda \rightarrow 0^-} \int_{\Omega_1} \frac{ds}{h_0(s, \theta) - \lambda} = 0.$$

From the monotonicity of the function $\Delta_1(\theta; h_1^{-1}(\theta), \lambda)$ on $(-\infty, 0)$ we obtain that $\Delta_1(\theta; h_1^{-1}(\theta), \lambda) > 0$ on $(-\infty, 0)$, i.e. $\sigma(H_0 - h_1^{-1}(\theta)T_1) = \sigma(H_0)$. Similarly, it is shown that $\sigma(W_2) = \sigma(H_0)$. Hence, $\sigma_{ess}(V) = \sigma(W_1) \cup \sigma(W_2) = \sigma(H_0)$.

3. Zero-energy resonance of the operator H

It is said that, the operator $H_1(\theta)$ (operator $H_2(\theta)$) has a resonance with zero energy [19] if the number 1 is the eigenvalue of the integral operator $H_1 : L_2(\Omega_1) \rightarrow L_2(\Omega_1)$ ($H_2 : L_2(\Omega_2) \rightarrow L_2(\Omega_2)$), where

$$H_1\varphi(x) = \gamma_1 \int_{\Omega_1} \frac{\varphi(s)ds}{u(s)}, \quad H_2\psi(y) = \gamma_2 \int_{\Omega_1} \frac{\psi(t)dt}{v(t)}$$

and at least one corresponding eigenfunction $\varphi_0(x)$ (eigenfunction $\psi_0(y)$) satisfies the condition $\varphi_0(\theta) \neq 0$ ($\psi_0(\theta) \neq 0$).

Theorem 3.1. Let $\gamma_1 = h_1^{-1}(\theta)$. Then:

a) operator $H_1(\theta)$ has a resonance with zero energy;

b) for all $\beta \in \Omega_2$, $\beta \neq 0$ operator $H_1(\beta)$ has no negative eigenvalue..

Proof. a) Let $\varphi_0(x) \equiv 1$. Then $V_1\varphi_0 = \gamma_1 h_1(\theta) = \varphi_0(x)$, i.e. the equation $V_1\varphi = \varphi$ has a solution φ_0 from $C(\Omega_1)$ and $\varphi_0(0) \neq 0$.

b) If $\gamma_1 = h_1^{-1}(\theta)$, then the condition of Proposition 2.2 is satisfied, and therefore $\sigma(H_1(\beta)) = \sigma_{ess}(H_1(\beta))$ for all $\beta \in \Omega_2$, i.e. there is no negative eigenvalue for the operators $H_1(\beta)$, $\beta \in \Omega_2$.

Example. Let $\Omega_1 = \Omega_2 = [0, 1]$ and

$$u(x) = v(x) = x^{1/2}, \quad \omega(x, y) = \left(1 - \cos \frac{\pi}{2}x\right) \left(1 - \cos \frac{\pi}{2}y\right).$$

We have

$$\int_0^1 \frac{ds}{u(s)} = \int_0^1 \frac{dt}{v(t)} = 2.$$

The function $h_1(x)$ strictly decreases on $[0, 1]$, and hence, $h_1^{\min} = h_1(1)$ and $h_1^{\max} = h_1(0) = 2$. It is obvious that $\frac{1}{u(x)} \notin L_2(\Omega_1)$, i.e. $\frac{1}{u(x)} \in L_1(\Omega_1) \setminus L_2(\Omega_1)$. Hence, for $\gamma_1 = \frac{1}{2}$ the operator $H_1(0)$ has a resonance with zero energy and for all $\beta \in (0, 1]$ operator $H_1(\beta)$ has no negative eigenvalue.

4. Conclusion

Our main goals are the description of the essential spectrum of the operator H and studying its spectral properties. This work differs from the work of other scientists because we choose the special form of the multiplier H_0 and the non-compactness of the partial integral operators T_1 and T_2 takes place. To summarize, we applied the method of [13] for the description of the essential spectrum. Additionally, we mainly used the minimax principle from [9] to prove the theorems and found the exact description of the essential spectrum proved by conditioning the parameters γ_1 and γ_2 .

References

- [1] Vekua I.N., *New Methods for Solving Elliptic Equations*. OGIZ, Moscow Leningrad, 1948 [inRussian].
- [2] Aleksandrov V.M. and Kovalenko E.V. A class of integral equations of mixed problems of continuum mechanics. *Sov. Phys., Dokl.*, 1980, **25**, P. 354.
- [3] Aleksandrov V.M. and Kovalenko E.V. Contact interaction between coated bodies with wear. *Sov. Phys., Dokl.*, 1984, **29**, P. 340.
- [4] Manzhairov A.V. On a method of solving two-dimensional integral equations of axisymmetric contact problems for bodies with complex rheology, *J. Appl. Math. Mech.*, 1985, **49**, P. 777.
- [5] Kalitvin A.S. *Linear Operators with Partial Integrals* Izd. Voronezh. Gos. Univ., Voronezh, 2000 [in Russian].
- [6] Uchiyama J. Finiteness of the number of discrete eigenvalues of the Schrödinger operator for a three particle system. *Publ. Res. Inst., Math. Sci.*, 1969, **5**(1), P. 51–63.
- [7] Uchiyama J. Corrections to finiteness of the number of discrete eigenvalues of the Schrödinger operator for a three particle system. *Publ. Res. Inst. Math. Sci.*, 1970, **6**(1), P. 189–192.
- [8] Zhislin G.M. On the finiteness of the discrete spectrum of the energy operator of negative atomic and molecular ions. *Theor. Math. Phys.*, 1971, **7**, P. 571–578.
- [9] Reed M., Simon B. *Methods of Modern Mathematical Physics. Analysis of Operators*, Acad. Press, New York, 1982, **4**.
- [10] Friedrichs K.O. "Über die Spectralzerlegung eines Integral Operators. *Math. Ann.*, 1938, **115**, P. 249–272.
- [11] Ladyzhenskaya O.A. and Faddeev L.D. To the theory of perturbations of the continuous spectrum. *Dokl. Akad. Nauk SSSR*, 1958, **6**(120), P. 1187–1190.
- [12] Eshkabilov Yu.Kh. On infinity of the discrete spectrum of operators in the Friedrichs model. *Siberian Adv. Math.*, 2012, **22**, P. –12.
- [13] Eshkabilov Yu.Kh. On a discrete three-particle Schrödinger operator in the Hubbard model. *Theor. Math. Phys.*, 2006, **149**(2), P. 1497–1511.
- [14] Eshkabilov Yu.Kh. On the discrete spectrum of partially integral operators. *Siberian Adv. Math.*, 2013, **23**, P. 227–233.
- [15] Ichinose T. Spectral properties of tensor products of linear operators:I. *Trans.Amer.Math.Soc.*, 1978, **235**, P. 75–113.
- [16] Ichinose T. Spectral properties of tensor products of linear operators:II. *Trans.Amer.Math.Soc.*, 1978, **237**, P. 223–254.
- [17] Eshkabilov Yu.Kh., Kucharov R.R. On the finiteness of negative eigenvalues of a partially integral operator. *Siberian Adv. Math.*. 2015, **25**(3), P. 179–190.
- [18] Eshkabilov Yu.Kh., Kucharov R.R. Essential and discrete spectra of the three-particle Schrodinger operator on a lattice. *Theor.Math.Phys.*, 2012, **170**(3), P. 341–353.

- [19] Albeverio S., Lakaev S.N., Muminov Z.I. On the number of eigenvalues of a model operator associated to a system of three-particles on lattices. *Russ. J. of Math. Phys.*, 2007, **14**(4), P. 377–387.
- [20] Kucharov R.R., Tuxtamurodova T.M., Arzikulov G.P. Essential spectrum of one partial integral operator with degenerate kernel. *Vestnik NUUz*, 2023, **1**, P. 85–96.

Submitted 30 December 2023; revised 13 January 2024; accepted 15 January 2024

Information about the authors:

Ramziddin R. Kucharov – Tashkent International University of Financial Management and Technology; National University of Uzbekistan, Mathematics, Tashkent, 4, 100174, Uzbekistan; ORCID 0000-0002-0728-9340; r.kucharov@tift.uz; ramz3364647@yahoo.com

Tillohon M. Tuxtamurodova – National University of Uzbekistan, Mathematics, Tashkent, 4, 100174, Uzbekistan; ORCID 0009-0002-1721-880X; mirzayevatilloxon13@gmail.com

Conflict of interest: the authors declare no conflict of interest.

Molecular dynamics study of nanofluids viscosity with carbon tubes

Valery Ya. Rudyak^a, Sergey L. Krasnolutskii^b, Evgeniy V. Lezhnev^c

Novosibirsk State University of Architecture and Civil Engineering, Novosibirsk, Russia

^avalery.rudyak@mail.ru, ^bsergius-l@mail.ru, ^clionlev@yandex.ru

Corresponding author: Valery Ya. Rudyak, valery.rudyak@mail.ru

PACS 61.20.Ja, 61.48.De, 66.20.Cy

ABSTRACT The purpose of this paper is molecular dynamics simulation of viscosity of benzene-based nanofluids with carbon nanotubes, and carbon or copper nanoparticles. The nanotubes diameter and lengths were 1.1 nm and 1.1, 3.5, 7.2, 14.6 nm, respectively. The size of spherical nanoparticle was 1.39, 2.5, and 3.2 nm. The viscosity is calculated using the fluctuation-dissipation theorem (the Green–Kubo formula). It was shown that the viscosity coefficient of all the studied nanofluids with carbon nanotubes increases with their concentration and length. This increase is significantly higher than predicted by the corresponding theories for coarse dispersed fluids. At given weight concentrations, the viscosity coefficient of nanofluids with carbon nanotubes is higher than that of nanofluids with spherical particles. The increase in viscosity of nanofluids compared to that of the base fluid is explained by the structuring of the base fluid molecules in the vicinity of nanoparticles or carbon nanotubes.

KEYWORDS viscosity, molecular dynamics method, nanofluid, nanoparticles, carbon nanotubes

ACKNOWLEDGEMENTS This research was financially supported by the Russian Science Foundation (Agreement No. 20-19-00043). The authors thank A. A. Belkin and T. A. Rafalskaya for the multiple discussions of the results obtained.

FOR CITATION Rudyak V.Ya., Krasnolutskii S.L., Lezhnev E.V. Molecular dynamics study of nanofluids viscosity with carbon tubes. *Nanosystems: Phys. Chem. Math.*, 2024, **15** (1), 37–45.

1. Introduction

Nanofluids have unique properties that have been studied for over 25 years. They are currently being used or targeted on for use in various biomedical, cosmetic, and thermophysical technologies, as well as in the creation of advanced materials, in tribology, pharmacology, etc. [1–7]. Since the viscosity is a crucial factor for the potential applications of nanofluids, it has been extensively investigated. It has been experimentally established that the viscosity of nanofluids is significantly higher than that of conventional coarse dispersed fluids [1, 8–11]. Additionally, the viscosity of nanofluids depends not only on the concentration but also on size and material of the nanoparticles [1, 8–12]. With increasing the size of nanoparticles, the viscosity of the nanofluid decreases. An increase in temperature of the nanofluid results in a decrease in viscosity. This decrease is determined by the corresponding viscosity dependence of the base fluid, especially at low particle concentrations [13–16].

The dependence on both size and material was first established by the molecular dynamics (MD) method and later confirmed experimentally [17–20]. In general, the MD method has been widely used to investigate the viscosity of nanofluids. The relevant bibliography for nanofluids with conventional spherical particles can be found in the reviews [20, 21]. In addition to the fact that the use of the MD method has revealed new factors affecting the viscosity of nanofluids, it is absolutely indispensable when studying the corresponding mechanisms. It is due to this method that it was revealed that the greatest contribution to momentum transfer in nanofluids is related to the interaction of fluid molecules with nanoparticles [18, 20] and the structuring of the base fluid [20, 22].

Today, dispersed fluids with carbon nanotubes (CNTs) are also referred to as nanofluids. The viscosity and rheology of nanofluids with CNTs have been studied for about twenty years. However, studying such nanofluids is complicated due to the fact that CNTs can be single-walled (SWCNTs) or multi-walled (MWCNTs), which results in different their rheology and viscosity. This has been systematically shown in a recent work [23]. CNTs are unique particles, their diameters ranging from 1–2 nm for SWCNTs to 100 nm for MWCNTs. Their lengths also vary, with SWCNTs typically around 4–5 μm and MWCNTs reaching tens of micrometers. Strictly speaking, one of the CNT sizes turns out to be significantly larger than the limit size of spherical nanoparticles (100 nm). Such a complex morphology of CNTs makes them a difficult object for MD modeling. So far, only a few papers have been published.

The viscosity of a water-based nanofluid with 0.95 nm diameter of SWCNTs was simulated in one of the first papers [24]. The interaction of carbon atoms in CNTs was described using the Tersoff potential and their interaction with water molecules was described by the Lennard–Jones potential. A single CNT was used in the simulation cell, so that

the possible effect of CNT interaction on the viscosity of the nanofluid was excluded. Another disadvantage of this paper was that the increase in CNT concentration from 0.125 to 1 % was achieved simply by the corresponding elongation of the nanotubes. The length of the CNTs varied from 0.22 to 1.78 nm. However, it is clear that in this case, the viscosity of completely different nanofluids is actually compared and it is simply impossible to draw a meaningful conclusion about the dependence of the viscosity of a nanofluid with given CNTs on their concentration. Here a nanofluid simply with nanoparticles of a non-spherical shape, and of a very small size is actually considered. However, the authors also analyzed the effect of temperature on the viscosity of these nanofluids. The calculations seem reasonable when the CNT concentration is constant. The study revealed that the viscosity of nanofluids decreases monotonically at a fixed CNT concentration (i.e., at a fixed CNT length). At the same time, it is indicated that the relative viscosity (the ratio of the viscosity of nanofluid to the viscosity of the base fluid) increases with increasing temperature, starting from the nanotube length of 0.88 nm, and this growth is greater the longer the CNTs. In contrast, the relative viscosity of nanofluids with particles of shorter length decreases with increasing temperature.

In another series of calculations, the length of the tubes was fixed and equal to 2.5 nm (the volume concentration was 0.734 %), but the diameter varied from 1.11 to 1.59 nm. The results have shown that the variation in diameter had almost no noticeable impact on the viscosity of the studied nanofluids.

In the following paper of the same authors [25], viscosity calculations of similar nanofluids were performed. The diameter of CNTs was 0.951 nm, and their length varied from 0.22 to 1.3 nm, allowing for CNT concentrations to be varied in the range of 0.125 – 0.734 %. The results obtained were qualitatively the same as in the previous work. It should be noted that according to the authors, the viscosity of the nanofluids is significantly higher than that predicted by classical theories [26–28].

In another set of studies [29, 30], nanofluids were simulated using water and armchair-type (6, 6) CNTs with a length of 3 nm at temperature range of 298 – 313 K. The volume concentration of CNTs was varied from 0.557 to 3 %. The simulation cell contained only one CNT again. The results have shown that the viscosity of nanofluids was significantly higher than that of the base fluid and increased with increasing CNT concentration. It was noted that the viscosity of the nanofluid decreased as the temperature increased. It is worth noting that the viscosity of the nanofluid was significantly higher than that predicted by classical theories. In this case, a comparison was made with Brinkman's theory [27]. Finally, this work proposes a correlation for the viscosity coefficient based on temperature and CNT concentration, derived from numerical analysis of MD data. However, caution should be exercised when interpreting the obtained correlation for two reasons. Firstly, it is difficult to classify CNTs as proper nanotubes due to their length being of the same order as their diameter. Secondly, the viscosity coefficient, calculated using Green–Kubo formulas, has not reached the plateau values.

To conclude this forcedly very brief review of MD simulation of viscosity of nanofluids with CNTs it should be noted that still a number of fundamental issues remain unexplained. This concerns the following issues. (i) How does the viscosity of nanofluids vary with the aspect ratio (length-to-diameter ratio) of CNTs? (ii) How does the nanofluid viscosity depend on CNTs length? (iii) How does the viscosity of nanofluids with CNTs depend on their concentration? (iv) How does the viscosity of nanofluids with CNTs relate to that of conventional spherical particles? This article is devoted to answering these questions.

The immediate purpose of this paper is MD modeling of the viscosity coefficient of several benzene-based nanofluids with CNTs and carbon or copper nanoparticles. Benzene was chosen as the base fluid due to the hydrophobic nature of CNTs, which makes it impossible to create a water-based nanofluid without the use of any surfactants. From this viewpoint, the above referred data [24, 25, 29, 30], which use water as the base fluid in their calculations are model-based and cannot accurately simulate a real nanofluid. Alternately, carbon nanotubes (CNTs) are lyophilic to benzene and various alcohols (isopropanol, ethylene glycol, and etc).

Armchair-type CNTs with chirality (8, 8) were used as nanotubes, their diameter was 1.1 nm and lengths were 1.1, 3.5, 7.2, and 14.6 nm. Respectively, the CNTs were composed of 160, 480, 960, and 1920 carbon atoms. The number of benzene molecules in the simulation cell varied from 6700 to 38000, so that the weight concentrations of CNTs were 3, 9, and 15 %, which roughly corresponded to the volume concentrations of 1, 3, and 5 %. The number of CNTs in the calculations varied from 4 to 48, and the number of nanoparticles varied from 6 to 24.

To compare, the viscosity of nanofluids with spherical carbon and copper particles with diameters of 1.39, 2.5, and 3.2 nm was studied simultaneously. The mass of the carbon nanoparticles was equal to the mass of the corresponding CNTs. Given this, the size of the nanoparticles was determined. Thus, the indicated diameters of carbon nanoparticles corresponded to CNT lengths of 1.1, 7.2, and 14.6 nm. The weight concentrations of carbon particles were equal to those of CNTs. The volume concentrations of copper and carbon nanoparticles coincided and were equal to 1.16, 3.5, and 5.8 %.

2. Simulation technique

The simulation of nanofluid viscosity was performed based on MD method [31] using free LAMMPS package [32]. The shear viscosity coefficient was determined by the fluctuation-dissipation theorem, known in the literature as the

Green-Kubo formula [33–35]:

$$\eta = \frac{V}{3k_B T} \int_0^{\tau_p} \langle \mathbf{J}(0) : \mathbf{J}(t) \rangle dt = \frac{V}{k_B T} \int_0^{\tau_p} \chi_\eta(0, t) dt, \quad (1)$$

where the microscopic stress tensor for the considered binary mixture has the following form

$$\mathbf{J} = \frac{1}{V} \sum_{\alpha=1}^2 \sum_{i=1}^{N_\alpha} \left(m_\alpha \mathbf{v}_i \mathbf{v}_j + \frac{1}{2} \sum_{\alpha=1,2}^{N_\alpha} \sum_{i \neq j} \mathbf{F}_{ij} \mathbf{r}_{ij} \right).$$

Here the index $\alpha = 1$ refers to the carrier fluid molecules, and 2 refers to the CNT atoms or nanoparticles, m_i is the mass of the corresponding particle (molecule or nanoparticle), V is the volume of the system, T is the temperature of the medium, τ_p is the time to reach the plateau value, \mathbf{F}_{ij} is the force acting on the particle (molecule or nanoparticle), \mathbf{r}_{ij} is the radius-vector between the centers of the interacting particles, and k_B is the Boltzmann constant. N_1 and N_2 are the number of molecules of the carrier fluid and atoms of the nanotubes or nanoparticles, respectively. The angular brackets in (1) denote averaging over the equilibrium ensemble.

The simulation was conducted in cubic cells with periodic boundary conditions. To determine the viscosity coefficient, the simulated system needed to be brought to an equilibrium state due to the fluctuation-dissipation theorem (1), according to which the coefficient is determined by the equilibrium thermal fluctuations of the stress tensor. To investigate a nanofluid with CNTs, the following procedure was followed: initially, benzene molecules were uniformly placed in the simulation cell, based on the given density $\rho_f = 0.8765 \text{ g}\cdot\text{cm}^{-3}$ (corresponding to atmospheric pressure and a temperature of 25 °C), except for the volume occupied by CNTs. The initial velocities of molecules were set according to the Maxwell distribution at a given temperature. The calculation began after a relaxation period of 1 – 1.5 ns, during which the entire system reached equilibrium. The initial state of the nanofluid with nanoparticles was also reached using the same method.

To calculate the viscosity coefficient (1) using MD method, it is necessary to first calculate the corresponding two-time correlation function χ_η . This calculation requires information about all dynamic variables of the system at successive instants, for which the corresponding system of Newton's equations is solved sequentially. Newton's equations were integrated using the Verlet scheme. The NPT Nose–Hoover thermostat [36,37] was used to maintain atmospheric pressure and a temperature of 25 °C. The interaction between benzene and carbon molecules was determined using the Lennard–Jones potential

$$\Phi_{LJ}(r) = 4\varepsilon_{ij} \left[(\sigma_{ij}/r)^{12} - (\sigma_{ij}/r)^6 \right], \quad (2)$$

where σ_{ij} is the effective diameter of molecules (atoms), ε_{ij} is the depth of the potential well, $r = |\mathbf{r}_i - \mathbf{r}_j|$ is the distance between the centers of molecules i and j .

The potential parameters (1) for benzene molecules are $\sigma_1 = 0.5034 \text{ nm}$, $\varepsilon_1/k_B = 544.3 \text{ K}$, for carbon atoms – $\sigma_2 = 3.4157 \text{ \AA}$, $\varepsilon_2/k_B = 27.70 \text{ K}$, and for copper atoms – $\sigma_2 = 2.2268 \text{ \AA}$, $\varepsilon_2/k_B = 2255.3 \text{ K}$. The density of carbon was taken equal to $\rho_G = 2267 \text{ kg}\cdot\text{m}^{-3}$, and that of copper was $\rho_{Cu} = 7998 \text{ kg}\cdot\text{m}^{-3}$. The interaction potential parameters (2) between the carrier fluid molecule and carbon atoms of CNT or nanoparticle were calculated using simple combination relations [38]: $\sigma_{12} = \sqrt{\sigma_1 \sigma_2}$, $\varepsilon_{12} = \sqrt{\varepsilon_1 \varepsilon_2}$. Since the potential (2) has an infinite action radius, it needs to be cut-off in the simulation process, the cut-off radius was $2.5 \sigma_1$. The CNT was simulated by a set of carbon atoms interacting using the AIREBO potential [39].

The interaction of benzene molecules with carbon or copper nanoparticles was described by the Rudyak–Krasnolutskiï potential [40,41]:

$$\Psi(r) = \Psi_9(r) - \Psi_3(r), \quad (3)$$

$$\Psi_i = C_i \left\{ \left[\frac{1}{(r-R)^i} - \frac{1}{(r+R)^i} \right] - \frac{a_i}{r} \left[\frac{1}{(r-R)^{i-1}} - \frac{1}{(r+R)^{i-1}} \right] \right\},$$

where $i = 9, 3$, $a_9 = 9/8$, $a_3 = 3/2$, $C_9 = (4\pi\varepsilon_{12}\sigma_{12}^{12})/45V_p$, $C_3 = (2\pi\varepsilon_{12}\sigma_{12}^6)/3V_p$, $V_p^{-1} = \rho_p/m_p$. Here ρ_p is the density of the nanoparticle material, m_p is the mass of an atom (molecule) of the nanoparticle material, R is the nanoparticle radius, σ_{ij} , ε_{ij} are the parameters of the potential (2) between the carrier fluid molecule and the nanoparticle atom.

The Rudyak–Krasnolutskiï–Ivanov potential [42] is used to describe the interaction between carbon or copper nanoparticles. This potential has the following form:

$$U(r, R) = U_7(r, R) - U_1(r, R), \quad (4)$$

$$\begin{aligned}
U_7(r, R) &= \frac{\pi^2 \varepsilon_2 \sigma_2^{12}}{315 V_p^2} \left\{ \frac{R^2}{r} \left[\frac{1}{(r-2R)^7} + \frac{2}{r^7} + \frac{1}{(r+2R)^7} \right] - \right. \\
&\quad \left. - \frac{R}{3r} \left[\frac{1}{(r-2R)^6} - \frac{1}{(r+2R)^6} \right] - \frac{1}{30r} \left[\frac{1}{(r-2R)^5} - \frac{2}{r^5} + \frac{1}{(r+2R)^5} \right] \right\}, \\
U_1(r, R) &= \frac{2\pi^2 \varepsilon_2 \sigma_2^6}{3 V_p^2} \left[\ln \left(\frac{r^2 - 4R^2}{r^2} \right) + 2R^2 \left(\frac{1}{r^2 - 4R^2} + \frac{1}{r^2} \right) \right].
\end{aligned}$$

Here R is the radius of nanoparticles, σ_2 and ε_2 are parameters of the Lennard–Jones potential (2) of the interaction between nanoparticle atoms.

The potential (3) was constructed based on the assumption that the interaction between the carrier fluid molecules and nanoparticle atoms, as well as between nanoparticle atoms themselves, can be described by potentials (2) with parameters σ_{12} , ε_{12} , and σ_2 , ε_2 , respectively. The adequacy of this potential was experimentally verified by simulating the diffusion of nanoparticles in nitrogen [43]. Potential (4) was constructed in a similar manner. Later, both potentials were used to simulate various transport coefficients in nanofluids [20].

For potential (3), the cut-off radius was $(R + b\sigma_{12})$. The value of parameter b was selected to ensure that the force exerted on the molecule from the nanoparticle was equal to the interaction force between two molecules at the cut-off radius for potential (1). The parameter b is dependent on the nanoparticle size and material, as well as the properties of the carrier fluid molecules. For instance, for 1.39 nm diameter carbon nanoparticles in benzene, $b = 3.0$, while for 3.2 nm diameter nanoparticles, b equals $b = 3.34$. The nanoparticle potential (4) was cut off at a distance of two particle diameters between the centers of the nanoparticles.

Because of the local instability and mixing of the system's phase trajectories during MD simulation [44–46], the obtained data must be averaged over an ensemble of independently constructed phase trajectories. In this paper, averaging was performed over at least 1000 independent phase trajectories.

In the simulation, the dependence of the nanofluid viscosity on the weight concentration w of CNTs or nanoparticles was studied. The relationship between weight concentration and volume concentration ϕ is determined by the following equation

$$\phi = w [w + (1 - w)\rho_p/\rho_f]^{-1}, \quad (5)$$

where ρ_f and ρ_p are mass densities of fluid and nanoparticles, respectively.

3. Simulation of the nanofluid viscosity

The nanofluids studied in this paper were prepared using benzene. Therefore, the first step was to simulate the viscosity of benzene and compare it with experimental data. It was found that at atmospheric pressure and a temperature of 25 °C, the calculated benzene viscosity coefficient was 0.6 mPa·s, which closely matched the measured value [47].

The viscosity coefficient of nanofluid with CNTs was calculated by varying both their length and concentration. In all cases, the viscosity coefficient $\eta(t)$ (1) was considered calculated when it reached the plateau value. An example of this is shown in Fig. 1, which displays the evolution of the viscosity coefficient of a nanofluid with CNTs with length of 1.1 nm at a nanotube weight concentration of 3 %. The simulation cell contained 9 CNTs and 7184 benzene molecules. The graph displays the benzene viscosity coefficient as a dashed line and the plateau value of the nanofluid viscosity coefficient as a solid line. Time is measured in femtoseconds, and the plateau is reached in approximately 30 picoseconds. The calculated viscosity coefficient of the nanofluid is 9.5 % higher than that of the base fluid (benzene).

The dependence of the relative viscosity coefficient $\eta_r = \eta/\eta_{bf}$ (where η_{bf} is the viscosity coefficient of benzene) of nanofluids with CNTs of different lengths on their volume concentration is shown in Fig. 2. The nanotubes have lengths of 1.1, 3.5, 7.2, and 14.6 nm. The corresponding data and solid curves are depicted from bottom to top, and the dashed line corresponds to Batchelor's theory [28]. Based on the obtained data, several conclusions can be drawn. The first conclusion is that the viscosity coefficient of all nanofluids is significantly higher than that of coarse dispersed fluids, as concluded particularly in [28].

The second conclusion is that the viscosity coefficient increases with the length of CNTs at a given weight concentration. More precisely, viscosity depends on the aspect ratio of CNTs, since in this case the diameter of all CNTs was the same. The viscosity of nanofluids with ordinary spherical particles also depends on their radius, and it is the greater the smaller the size of the nanoparticles. This fact was established both experimentally [1, 8, 9] and by the MD simulation [17, 20]. Such dependence is primarily determined by the structuring of the base fluid in the vicinity of the nanoparticles [20]. This structuring is determined by the surface area of the nanoparticles at given values of the interaction potential parameters. Since the surface area of CNTs of the same diameter is proportional to their length, the viscosities of nanofluids with CNTs will be increased proportionally to the length of CNT. For suspensions with solid ellipsoidal particles, the corresponding viscosity coefficient was obtained by G. B. Jeffrey [48]. The viscosity coefficient of a dispersed medium grows as the particle shape deviates from spherical. This is expected due to the shorter Brownian rotation time compared to the hydrodynamic times considered. Therefore, particle rotation leads to an increase in the effective volume they occupy. The prolate spheroidal ellipsoid models a solid CNT quite well. Later, in [49] it was shown that

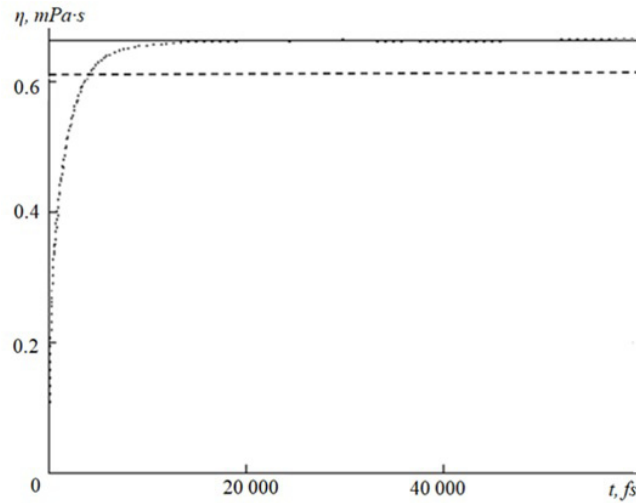


FIG. 1. Evolution of the viscosity coefficient of benzene-based nanofluid with CNTs

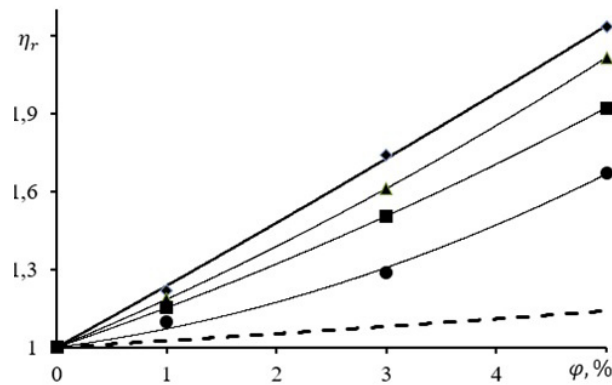


FIG. 2. Dependence of relative viscosity coefficient of nanofluids on CNT volume concentration

suspensions with ellipsoidal particles should have viscoelastic properties. For nanofluids with CNTs, this was established experimentally in [23].

The third conclusion is that the dependence of the viscosity coefficient of both coarse dispersed fluids and nanofluids with spherical particles on the volume concentration of particles is described by the square law dependence [9, 20]:

$$\eta_r = 1 + a_1\phi + a_2\phi^2. \quad (6)$$

The volume concentration dependence of the viscosity coefficient of the CNT nanofluids is also described by this formula. The coefficients in this formula are dependent on the length of the CNT and are presented in Table 1. The solid lines in Fig. 2 correspond to the dependences (6).

TABLE 1. Coefficients in formula (6) for benzene-based nanofluids with CNTs

L , nm	1.1	3.6	7.4	14.6
a_1	7.38	16.36	19.59	24.36
a_2	144.23	38.39	45.14	11.27

CNTs have a complex morphology and differ significantly from ordinary spherical nanoparticles. Comparing the viscosity of the both types of nanofluids is crucial. Moreover, this is of independent interest due to the active investigation of thermophysical properties of hybrid nanofluids, in which both CNTs and nanoparticles act as dispersed elements (see, for example, [50, 51] and references therein). For comparison, the viscosity of benzene-based nanofluids containing carbon and copper particles have been calculated. In all cases, the viscosity of these nanofluids was described by the square dependence (6). The corresponding data are summarized in Table 2 (d – is the diameter of nanoparticles). The viscosity of the nanofluids increased as the nanoparticle size decreased, consistent with both experimental data and MD

simulations [1, 8–12]. The comparison of the obtained data is presented in Fig. 3. Here, dark points indicate nanofluids with copper particles, while light points indicate those with carbon particles. In all cases, the size of nanoparticles increases from bottom to top. The viscosity of both nanofluids increases as the nanoparticle size decreases. Additionally, the nanofluid with copper particles has higher viscosity than the one with carbon particles.

TABLE 2. Coefficients in formula (6) for benzene-based nanofluids with CNTs

d , nm	1.4, Cu	2.6, Cu	3.2, Cu	1.4, C	2.6, C	3.2, C
a_1	8.78	4.76	3.92	5.52	4.02	3.40
a_2	573.7	469.8	241.3	134.0	23.2	11.97

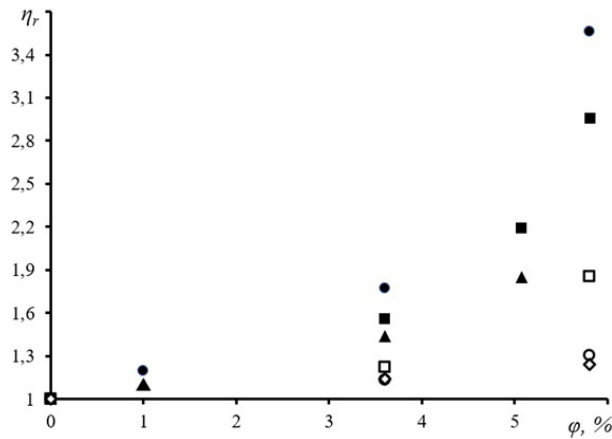


FIG. 3. Dependence of viscosity of benzene-based nanofluids with carbon and copper nanoparticles on their volume concentration

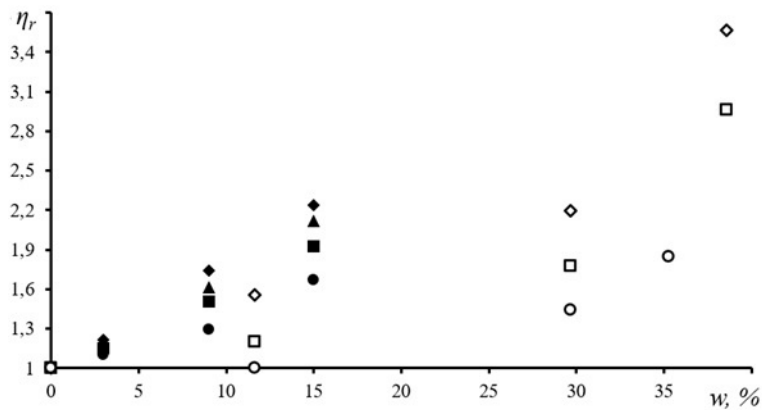


FIG. 4. Comparison of relative viscosity coefficients of nanofluids with CNTs, carbon and copper nanoparticles depending on weight concentration

Nanofluids are typically prepared using a two-step method [1, 8]. First, an appropriate powder of carbon nanotubes (CNTs) or nanoparticles is added to the base fluid to achieve a desired weight concentration. It is important to note that the density of SWCNTs is typically much lower (1.8 g/sm^3) than that of metallic particles. For instance, copper has a density about four times greater. As a general rule, the weight concentration of nanoparticles is typically much higher than that of the corresponding CNT concentrations, even if their volume concentrations are comparable or equal. From this standpoint, it is useful to compare the dependence of viscosity of nanofluids with CNTs and copper particles on weight concentration. Such a comparison is presented in Fig. 4. Here, the dark points correspond to CNTs with lengths of 1.1, 3.6, 7.2 and 14.6 nm (from bottom to top), and the light points correspond to copper nanoparticles with diameters of 1.4, 2.6 and 3.6 nm (from bottom to top). As shown in Fig. 4, the nanofluid with CNTs has higher viscosity than the nanofluid with copper particles at the same weight concentrations. However, while comparing the viscosity at the same volume concentrations, the viscosity of nanofluid with copper particles is higher (see Figs. 3 and 2).

4. Results and discussion

The simulation data, obtained based on MD method require some comments. The viscosity of nanofluids, as well as basic fluids, is determined by the fluctuation-dissipation theorem (1). This theorem states that the momentum redistribution in the system is determined by the dynamics of thermal equilibrium fluctuations of the microscopic stress tensor. The dynamics of the stress tensor and the evolution of the two-time correlation function χ_{η} depend on the structure of the fluid's short-range order. The dissipation of momentum in the fluid is associated with a permanent local rearrangement of the short-range order structure. In nanofluids, the molecules of the base fluid are structured near the nanoparticles. The nature of this structuring is well represented by the radial distribution function (RDF), which determines the average local density of the base fluid molecules around each nanoparticle. As an example, Fig. 5 demonstrates the radial distribution functions of benzene molecules in the vicinity of carbon nanoparticles. The dashed line represents the RDF of pure benzene molecules, while the dotted, dash-dotted, and solid lines correspond to the benzene molecules in the nanofluids surrounding carbon nanoparticles with diameters of 1.4, 2.6, and 3.2 nm, respectively. In all cases, the volume concentration of nanoparticles was the same and equal to 5 %.

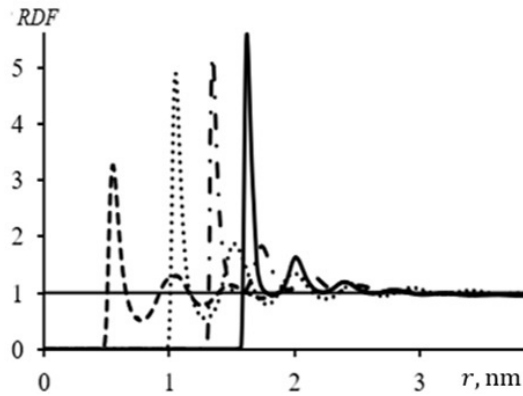


FIG. 5. Radial distribution functions of pure benzene molecules (dashed line) and benzene molecules in nanofluids around graphite nanoparticles with diameters of 1.4 nm (dotted line), 2.6 nm (dash-dotted line), and 3.2 nm (solid line)

The RDFs of benzene molecules surrounding the nanoparticles have significantly higher maxima compared to the corresponding values of the pure liquid. This indicates greater ordering of benzene molecules. As the molecule diameter increases, the degree of ordering of the molecules around the nanoparticles slightly increases, which is due to the decrease in their surface curvature. This effect is observed for particle sizes up to approximately 10 nm, and further the character of the wall layer of molecules remains practically unchanged. However, the viscosity of the nanofluid is not only determined by the magnitude of these maxima, but also by the total number of structured fragments of the base fluid. The total volume of structured regions in the base fluid molecules decreases as nanoparticle size increases at a given volume concentration.

Thus, the increase in viscosity of the nanofluid is due to the sharp intensification of the short-range order of the base fluid molecules. The structuring of the based-fluid molecules is proportional to the surface area of the nanoparticles. The ratio of the surface area of a spherical particle to its volume is inversely proportional to the radius of the particle. Therefore, for given nanoparticle volume concentration, the structuring of the base fluid will be the more effective the smaller the particle radius. Therefore the viscosity of nanofluids with spherical particles will increase with decreasing nanoparticle size.

The structuring of the base fluid molecules also occurs in nanofluids containing CNTs. The surface area of CNTs increases proportionally with their length, resulting in an increase in viscosity of the nanofluid as the length of the CNTs increases.

The ratio of the surface area S_{sp} of a spherical nanoparticle of radius R to that of a CNT S_{cnt} of radius R_{cnt} and length L is given by the relation

$$\frac{S_{sp}}{S_{cnt}} = \frac{2R^2}{R_{cnt}^2 + R_{cnt}L}. \quad (7)$$

Here the following situations are possible: $R \sim R_{cnt}$. This ratio for SWCNTs is fulfilled if the diameter of nanoparticles does not exceed 1 – 3 nm, that is, the spherical particles are very small. In this case, $S_{sp}/S_{cnt} \sim R/L \ll 1$. The viscosity of nanofluids with spherical particles will be smaller than that of nanofluids with CNTs, and only for the smallest CNTs ($L \sim R$) will it be almost the same in both cases. This is confirmed by the data presented in Figs. 2 and 3.

For large SWCNT particles the condition $R > R_{cnt} \ll L$ is met. In this case,

$$\frac{S_{sp}}{S_{cnt}} \sim \frac{R^2}{R_{cnt}L} < 1.$$

Again, the viscosity of nanofluid with CNTs will be higher than that of nanofluid with spherical particles. It is easy to see that these two cases exhaust all possible situations for nanofluids with SWCNTs.

5. Conclusions

In this paper, the viscosity coefficient of benzene-based nanofluids with SWCNTs has been simulated by the MD method. The dependence of the viscosity coefficient of the concentration of SWCNTs and their length was investigated. Simultaneously, the viscosity coefficients of nanofluids with spherical carbon and copper particles were calculated. All the obtained data were systematically compared and it is shown that:

- The viscosity coefficient of all studied nanofluids with SWCNTs increases with their concentration. This increase is significantly higher than predicted by the corresponding theories for coarse dispersed fluids.
- At given concentration, the viscosity coefficient of nanofluids with SWCNTs increases with their length (aspect ratio).
- At given weight concentrations, the viscosity coefficient of nanofluids with SWCNTs is higher than that of nanofluids with spherical particles.
- At the same volume concentrations, the viscosity coefficient of nanofluid with copper particles is higher than that of nanofluid with carbon particles.
- One of the main reasons for the increase in viscosity of nanofluids compared to that of the base fluid is the structuring of the base fluid molecules in the vicinity of nanoparticles or CNTs. This structuring is determined by the parameters of the interaction potential between the molecules of the base fluid and atoms of nanoparticles or CNTs and their surface area.

References

- [1] Murshed S.M.S., de Castro C.A.N. *Nanofluids: synthesis, properties and applications*. Nova Science Publishers, New York, 2014, 296 p.
- [2] Li J., Zhang X., Xu B., Yuan V. Nanofluid research and applications: A review. *Int. Communications Heat and Mass Transfer*, 2021, **127**, 105543.
- [3] Yaqoob S.B., Adnan R., Rameez Khan R.M., Rashid M. Gold, silver, and palladium nanoparticles: A chemical tool for biomedical applications. *Front. Chem.*, 2020, **8**, P. 376–392.
- [4] Rubbi F., Das L., Habib K., Aslfattahi N., Saidur R., Ul Alam S. A comprehensive review on advances of oil-based nanofluids for concentrating solar thermal collector application. *J. Mol. Liq.*, 2021, **338**, 116771.
- [5] Hajiabadi S.H., Aghaei H., Kalateh-Aghamohammadi M., Shorgasthi M. An overview on the significance of carbon-based nanomaterials in upstream oil and gas industry. *J. Petrol. Sci. & Eng.*, 2020, **186**, 106783.
- [6] Zhao J., Huang Y., He Y., Shi Y. Nanolubricant additives: A review. *Friction*, 2021, **9** (5), P. 891–917.
- [7] Pordanjani A.H., Aghakhani S., Afrand M., Mahmoudi B., Mahian O., Wongwise S. An updated review on application of nanofluids in heat exchangers for saving energy. *Energy Convers. Manag.*, 2019, **198**, 111886.
- [8] Rudyak V.Ya. Thermophysical characteristics of nanofluids and transport process mechanisms. *J. Nanofluids*, 2019, **8**, P. 1–16.
- [9] Minakov A.V., Rudyak V.Ya., Pryazhnikov M.I. Systematic experimental study of the viscosity of nanofluids. *Heat Transfer Eng.*, 2021, **42** (12), P. 1024–1040.
- [10] Patra A.K., Nayak M.K., Misra A. Viscosity of nanofluids-A Review. *Int. J. Thermofluid Sci. and Technology*, 2020, **7** (2), 070202.
- [11] Said Z., Sundar L.S., Tiwari A.K., Ali H., Sheikholeslami M., Bellos E., Babar H. Recent advances on the fundamental physical phenomena behind stability, dynamic motion, thermophysical properties, heat transport, applications, and challenges of nanofluids. *Phys. Reports*, 2022, **946**, P. 1–94.
- [12] Koca H.D., Doganay S., Turgut A., Tavman I.H., Saidur R., Mahbulul I.M. Effect of particle size on the viscosity of nanofluids: A review. *Renewable and Sustainable Energy Rev.*, 2018, **82**, P. 1664–1674.
- [13] Namburu P.K., Kulkarni D.P., Dandekar A., Das D.K. Experimental investigation of viscosity and specific heat and silicon dioxide nanofluids. *Micro & Nano Lett.*, 2007, **2** (3), P. 67–71.
- [14] Nguyen C.T., Desgranges F., Galanis N., Roy G., Maré T., Boucher S., Angue Mintsa H. Viscosity data for Al₂O₃-water nanofluid – hysteresis: is heat transfer enhancement using nanofluids reliable? *Int. J. Thermal Sci.*, 2008, **47** (2), P. 103–111.
- [15] Chen H., Ding Y., Tan C. Rheological behavior of nanofluids. *New J. Phys.*, 2007, **9** (10), 367.
- [16] Rudyak V.Ya., Dimov S.V., Kuznetsov V.V. On the dependence of the viscosity coefficient of nanofluids on particle size and temperature. *Tech. Phys. Lett.*, 2013, **39** (9), P. 779–782.
- [17] Rudyak V.Ya., Krasnolutski S.L. Dependence of the viscosity of nanofluids on nanoparticle size and material. *Phys. Lett. A*, 2014, **378**, P. 1845–1849.
- [18] Rudyak V.Ya., Krasnolutski S.L. Simulation of the nanofluid viscosity coefficient by the molecular dynamics method. *Tech. Phys.*, 2015, **60** (6), P. 798–804.
- [19] Rudyak V.Ya., Minakov A.V., Smetanina M.S., Pryazhnikov M.I. Experimental data on the dependence of the viscosity of water- and ethylene glycol-based nanofluids on the size and material of particles. *Dokl. Phys.*, 2016, **61** (3), P. 152–154.
- [20] Rudyak V.Ya., Belkin A.A., Krasnolutski S.L. Molecular dynamics modeling transport processes of fluids and nanofluids in bulk and nanochannels. In: S. Köhler, editor. *Advances in Molecular Dynamics Simulations Research*. Nova science publisher, New York, 2021, P. 1–86.
- [21] Jabbari F., Rajabpour A., Saedodin S. Thermal conductivity and viscosity of nanofluids: A review of recent molecular dynamics studies. *Chem. Eng. Sci.*, 2017, **174**, P. 67–81.
- [22] Rudyak V.Ya., Belkin A.A. On the effect of nanoparticles on fluid structure. *Colloid J.*, 2019, **81** (4), P. 487–490.
- [23] Rudyak V.Ya., Dashapilov G.R., Minakov A.V., Pryazhnikov M.I. Comparative characteristics of viscosity and rheology of nanofluids with multi-walled and single-walled carbon nanotubes. *Diamond & Related Mat.*, 2023, **132**, 109616.
- [24] Jabbari F., Saedodin S., Rajabpour A. Experimental investigation and molecular dynamics simulations of viscosity of CNT-water nanofluid at different temperatures and volume fractions of nanoparticles. *J. Chem. Eng. Data*, 2018, **64** (1), P. 262–272.
- [25] Jabbari F., Rajabpour A., Saedodin S. Viscosity of carbon nanotube/water nanofluid. *J. Therm. Anal. Calorim.*, 2019, **135**, P. 1787–1796.
- [26] Einstein A. Eine neue Bestimmung der Moleküldimensionen. *Ann. Phys.*, 1906, **19**, P. 289–306.
- [27] Brinkman H.C. The viscosity of concentrated suspensions and solutions. *J. Chem. Phys.*, 1952, **20**, P. 571.

- [28] Batchelor G.K. The effect of Brownian motion on the bulk stress in a suspension of spherical particles. *J. Fluid. Mech.*, 1977, **83**, P. 97–117.
- [29] Razmara N., Namarvari H., Meneghini J.R. A new correlation for viscosity of model water-carbon nanotube nanofluids: Molecular dynamics simulation. *J. Mol. Liq.*, 2019, **293**, 111438.
- [30] Namarvari H., Razmara N., Miranda C.R., Hashemi M.Y. Effect of SWCNT volume fraction on the viscosity of water based nanofluids. *J. Mol. Model.*, 2021, **27**, P. 253.
- [31] Rapaport D.C. *The Art of Molecular Dynamics Simulation*. Cambridge University Press, Cambridge, 2004, 564 p.
- [32] Thompson A.P., et al. LAMMPS – a flexible simulation tool for particle-based materials modeling at the atomic, meso, and continuum scales. *Comp. Phys. Comm.*, 2022, **271**, 108171.
- [33] Zubarev D.N. *Nonequilibrium statistical thermodynamics*. Consultants Bureau, New York, 1974, 243 p.
- [34] Allen M.P., Tildesley D.J. *Computer Simulation of Liquids*. Oxford University Press, Oxford, 1987, 385 p.
- [35] Rudyak V.Ya. Fluctuation-dissipation theorems and transport coefficients of the gases, liquids and nanofluids. *J. Phys.: Conf. Ser.*, 2020, **1560**, 012002.
- [36] Nosé S. A unified formulation of the constant temperature molecular-dynamics methods. *J. Chem. Phys.*, 1984, **81**, P. 511–519.
- [37] Hoover W.G. Canonical dynamics: Equilibrium phase-space distributions. *Phys. Rev. A*, 1985, **31** (3), P. 1695–1697.
- [38] Hirschfelder J.O., Curtiss C.F., Bird R.B. *Molecular theory of gases and liquids*. Revised Edition. Wiley-Interscience, New York, 1964, 1280 p.
- [39] Stuart S.J., Tutein A.B., Harrison J.A. A reactive potential for hydrocarbons with intermolecular interactions. *J. Chem. Phys.*, 2000, **112**, P. 6472–6486.
- [40] Rudyak V.Ya., Krasnolutski S.L. The interaction potential of dispersed particles with carrier gas molecules. In: Proceedings of the 21st international symposium on Rarefied Gas Dynamics. Cepadues-Editions, Toulouse, 1999, **1**, P. 263–270.
- [41] Rudyak V.Ya., Krasnolutski S.L. Diffusion of nanoparticles in a rarefied gas. *Tech. Phys.*, 2002, **47**, P. 807–813.
- [42] Rudyak V.Ya., Krasnolutski S.L., Ivanov D.A. The interaction potential of nanoparticles. *Dokl. Phys.*, 2012, **57**, P. 33–35.
- [43] Rudyak V.Ya., Krasnolutski S.L., Nasibulin A.G., Kauppinen E.I. Methods of measuring the diffusion coefficient and sizes of nanoparticles in rarefied gas. *Dokl. Phys.*, 2002, **47**, P. 758–761.
- [44] Norman G.E., Stegailov V.V. Stochastic and dynamic properties of molecular dynamics systems: simple liquids, plasma and electrolytes, polymers. *Comput. Phys. Commun.*, 2002, **147** (4), P. 678–683.
- [45] Norman G.E., Stegailov V.V. Stochastic theory of the classical molecular dynamics method. *Math. Models Comput. Simul.*, 2013, **5** (4), P. 305–333.
- [46] Rudyak V.Ya. *Statistical aerohydrodynamics of homogeneous and heterogeneous media*. Vol. 2, Hydromechanics. NSUACE, Novosibirsk, 2005, 469 p.
- [47] Lide D.R., ed. *Handbook of chemistry and physics*. 90th edition. CRC, 2010, 2760 p.
- [48] Jeffery G.B. The motion of ellipsoidal particles immersed a viscous fluid. *Proc. R. Soc. London A*, 1922, **102**, P. 161–179.
- [49] Pokrovskii V. Stresses, viscosity, and optical anisotropy of a moving suspension of rigid ellipsoids. *Sov. Phys. Usp.*, 1972, **14**, P. 737–746.
- [50] Sajid M.U., Ali H.M. Thermal conductivity of hybrid nanofluids: A critical review. *Int. J. Heat and Mass Transfer A*, 2018, **126**, P. 211–234.
- [51] Yasmin H., Giwa S.O., Noor S., Sharifpur M. Experimental exploration of hybrid nanofluids as energy-efficient fluids in solar and thermal energy storage application. *Nanomaterials*, 2023, **13** (2), 278.

Submitted 15 January 2024; accepted 2 February 2024

Information about the authors:

Valery Ya. Rudyak – Novosibirsk State University of Architecture and Civil Engineering, Novosibirsk, Russia;
ORCID 0000-0003-1335-4548; valery.rudyak@mail.ru

Sergey L. Krasnolutski – Novosibirsk State University of Architecture and Civil Engineering, Novosibirsk, Russia;
ORCID 0000-0002-9495-7326; sergius-l@mail.ru

Evgeniy V. Lezhnev – Novosibirsk State University of Architecture and Civil Engineering, Novosibirsk, Russia;
ORCID 0000-0003-3347-0781; lionlev@yandex.ru

Conflict of interest: the authors declare no conflict of interest.

Features of surface Bessel plasmon-polaritons in optical anisotropic hyperbolic metamaterials

Nguyen Van Vinh^{1,a}, Nguyen Pham Quynh Anh^{2,b}

¹Ho Chi Minh City University of Economics and Finance, Ho Chi Minh City, Vietnam

²Faculty of Electrical, Electronics and Materials Technology, University of Sciences, Hue University, Hue 530000, Vietnam

^avinhmv@uef.edu.vn, ^bnpqanh.dhkh@hueuni.edu.vn

Corresponding author: Nguyen Pham Quynh Anh, npqanh.dhkh@hueuni.edu.vn

ABSTRACT The features of generation and properties of surface Bessel Plasmon-polaritons (SBPPs) in optical anisotropic hyperbolic metamaterials formed by a periodic lattice of metal nanowires made of gold and silver embedded into pores of aluminum oxide is studied. We investigate the influence of the thickness of the porous material matrix on the generated plasmon-polaritons. Calculation of energy flows in the structure is made.

KEYWORDS surface plasmons, Bessel light beam, surface Bessel plasmon-polaritons, hyperbolic metamaterials

FOR CITATION Nguyen Van Vinh, Nguyen Pham Quynh Anh Features of surface Bessel plasmon-polaritons in optical anisotropic hyperbolic metamaterials. *Nanosystems: Phys. Chem. Math.*, 2024, **15** (1), 46–54.

1. Introduction

In recent years, surface plasmon-polaritons (SPPs) that arise at the interface between a dielectric and a conducting medium have been actively studied. Surface plasmon-polaritons are coupled oscillations of the electromagnetic wave and the density of free oscillations of the electron gas [1]. SPPs propagate along the interface between dielectric and metal. The metal in this system is necessary for the existence of electronic plasma, and the dielectric is necessary to bind the electronic plasma to the electromagnetic field [2]. Surface plasmon-polaritons are two-dimensional objects: they propagate along the interface and decay on the both sides of it [3–6]. This leads to unique properties of SPPs: high spatial localization and the ability to significantly enhance the intensity of the field near the boundary [7–9]. Due to these properties, it is promising to use surface plasmon-polaritons for creation of photonic and electronic devices of the nanometer scale, plasmonic modulators and switches, and for transmitting information over metallic wires in plasmonic microcircuits [10–13].

Currently, interest in the study of nanostructures that excite surface plasmon-polaritons is associated with the need of creation a new class of devices characterized by small dimension and a significantly lower resolution threshold that meets the challenges of nanotechnology. The use of metamaterials (MM), new artificial materials with electromagnetic properties that do not occur in nature, is one of the approaches to this problem [14–20].

Among anisotropic metamaterials, the most simple in technological implementation are uniaxial hyperbolic metamaterials (HMMs), which have isofrequency surfaces in the space of wave vectors in the form of a hyperboloid [21]. These metamaterials are of significant interest due to their ability to be used for obtaining an image with sub-wavelength (up to 15 nm or less) resolution, amplifying spontaneous emission, and increasing the density of photon states. A number of important practical applications of HMMs are associated with the possibility of exciting plasmon-polaritons (PP), which represent coupled oscillations of an electro-magnetic wave and the density of free oscillations of the electron gas. Tasks related to the study of the excitation and localization of plasmon-polaritons at the boundary (in the layer) of HMMs are of interest for optical manipulation of micro- and nano-particles, quantum informatics, photonics, and astrophysics [21–23]. The use of plasmon-polariton light fields in HMMs is one of the ways to solve the problem of creating new optical devices characterized by significantly lower resolution thresholds and smaller sizes.

At present, the attention of many researchers is turned to quasi-nondiffracting light fields. Among them, the Bessel light beams (BLBs) occupy a special place, having a divergence in the axial region significantly smaller than that of traditional (e.g., Gaussian) beams, as well as the ability to self-reconstruct the wavefront [24–29]. However, the evanescent BLBs investigated in works [24–29] have a significant disadvantage: they are weak. This leads to the need for strong laser fields to generate them. One of the possibilities of using BSPs for microscopy is to form Bessel plasmon-polaritons (BPPs) – quasi-nondiffracting light fields formed at the boundary of media with different dielectric permittivities.

This paper investigates the interaction of Bessel light beams with hyperbolic metamaterials and studies the possibility of generating quasi-nondiffracting SBPPs in hyperbolic metamaterial.

2. Conditions for the formation of Bessel plasmon-polariton in hyperbolic metamaterials

Let's consider a structure created using nanoporous aluminum oxide with pores filled with metal (Fig. 1). Thus, we obtain a medium that represents a set of periodically arranged metallic nanorods in a dielectric matrix. The controlled parameters are the radius of the metallic nanocylinders, the dielectric permittivity of the metal, and the average distance between the centers of two adjacent nanocylinders .

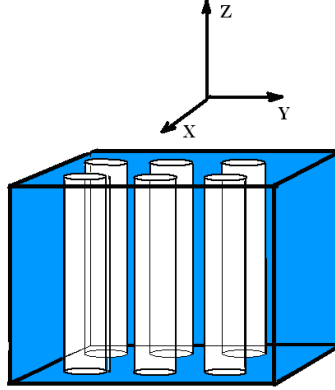


FIG. 1. Matrix of nanoporous aluminum oxide with pores filled with metal

In the effective medium approximation, the structure shown in Fig. 1 can be regarded as a uniaxial medium with effective dielectric parameters [30].

$$\begin{aligned}\varepsilon_x = \varepsilon_y = \varepsilon_o &= \frac{\beta\varepsilon_m N + \varepsilon_d(1 - N)}{\beta N + (1 - N)}, \\ \varepsilon_e &= \varepsilon_m N + \varepsilon_d(1 - N),\end{aligned}\quad (1)$$

where $N = \pi r^2/D^2$ is the filling ratio, $\beta = 2\varepsilon_d/(\varepsilon_m + \varepsilon_d)$, ε_d is the dielectric permittivity of the dielectric. It is assumed that $N \ll 1$ and $D, r \ll \lambda_0$, λ_0 is the wavelength of radiation incident on the structure. As known, the dielectric permittivity of gold and silver within the Drude model can be described by the following formulas:

$$\begin{aligned}\varepsilon_m^{Au}(\omega) &\approx \varepsilon_\infty^{Au} - \frac{(\omega_p^{Au})^2}{\omega^2 \left(1 + i\frac{\Gamma^{Au}}{\omega}\right)}, \\ \varepsilon_m^{Ag}(\omega) &\approx \varepsilon_\infty^{Ag} - \frac{(\omega_p^{Ag})^2}{\omega^2} + i\frac{(\omega_p^{Ag})^2 \Gamma^{Ag}}{\omega^3},\end{aligned}\quad (2)$$

with parameters $\varepsilon_\infty^{Au} = 9$; $\omega_p^{Au} = 13.8 \cdot 10^{15}$ Hz; $\Gamma^{Au} = 0.11 \cdot 10^{15} s^{-1}$, $\varepsilon_\infty^{Ag} = 5$; $\omega_p^{Ag} = 14 \cdot 10^{15} s^{-1}$; $\Gamma^{Ag} = 0.032 \cdot 10^{15} s^{-1}$ [30].

From Eqs. (1) and (2), we can obtain the spectral dependences of the permittivities of metamaterials samples. Fig. 2 shows our calculated results for the dependence of the real parts of transverse and longitudinal permittivities of Al_2O_3/Au and Al_2O_3/Ag on the wavelength. From Fig. 2, we can see that, at a wavelength of $\lambda = 633$ nm, for the filling ratio $f = 0.3$ the real part of the transverse permittivity has a positive value and longitudinal permittivity has a negative value, then metamaterial structure Al_2O_3/Au displays the properties of the hyperbolic metamaterial. Similarly, for the metamaterial sample Al_2O_3/Ag properties of hyperbolic metamaterial are achieved when the wavelength is 589.3 nm.

Let's assume that the hyperbolic metamaterial with thickness h , depicted in Fig. 1, separates a dielectric substrate with dielectric permittivity ε_0 and an external dielectric medium with permittivity ε_1 . We will use a cylindrical coordinate system, choosing it such that its origin is located at the boundary between the substrate and hyperbolic metamaterial.

Let's first consider the case when a TM-polarized m -order Bessel light beam falls on the interface between two semi-infinite media: an isotropic medium and an anisotropic uniaxial medium with its optical axis perpendicular to the interface. The electric $\vec{E}(R)$ and magnetic $\vec{H}(R)$ vectors of the Bessel light beam propagating along the z -axis in a medium with refractive index n_i can be represented as:

$$\begin{aligned}\vec{E}(R) &= A\vec{E}^{TM}(\rho) \exp i(k_{zi}z + m\varphi), \\ \vec{H}(R) &= A\vec{H}^{TM}(\rho) \exp i(k_{zi}z + m\varphi),\end{aligned}\quad (3)$$

where k_{zi} is the z -component of the wave vector, A is a complex constant, the common factor $\exp[i(qx - \omega t)]$ is omitted, and $q = \sqrt{k_0^2 n_i^2 - k_{zi}^2}$ is the transverse component of the wave vector.

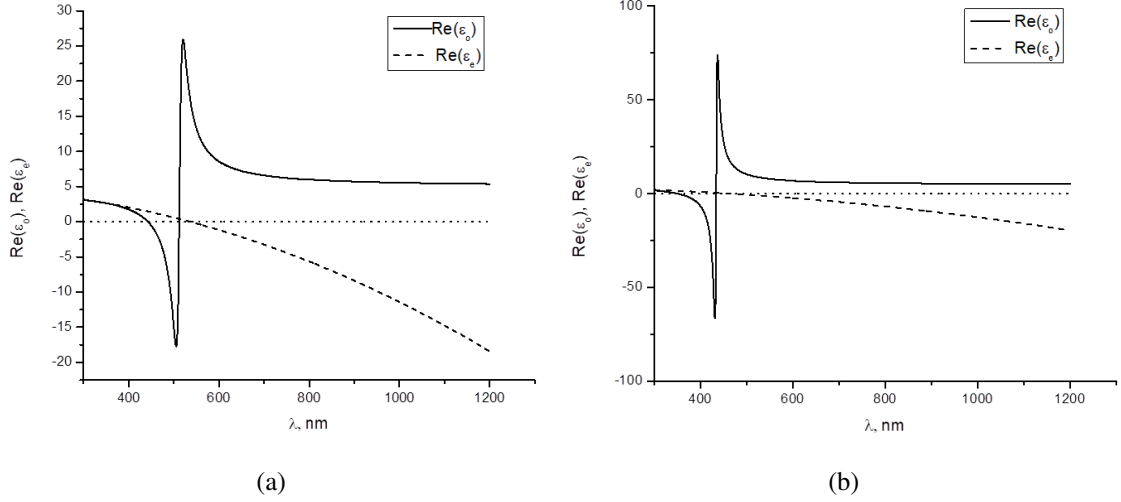


FIG. 2. Spectral dependences of the real parts of transverse ε_o and longitudinal ε_e permittivities of metamaterials made of gold (a) and silver (b) cylinders periodically with radius $r = 30$ nm embedded into aluminum oxide matrix.

From the solution of the boundary value problem, it follows that the electric $\vec{E}_t(R)$ and magnetic $\vec{H}_t(R)$ vectors of the refracted Bessel beam can be represented as:

$$\begin{aligned}\vec{E}_t(R) &= \vec{E}_t^{tr}(R) + \vec{E}_t^l(R), \\ \vec{E}_t^l(R) &= A_{inc} t_{ij}^{TM} \exp i[m\varphi + k_{zj}z] \frac{q}{k_0 n_j} J_m(q\rho) \vec{e}_z,\end{aligned}\quad (4)$$

$$\begin{aligned}\vec{E}_t^{tr}(R) &= \frac{iA_{inc}}{\sqrt{2}} \exp i[(m-1)\varphi + k_{zj}z] t_{ij}^{TM} [J_{m-1}(q\rho) \vec{e}_+ - J_{m+1}(q\rho) \exp(2i\varphi) \vec{e}_-], \\ \vec{H}_t(R) &= \frac{n_j A_{inc}}{\sqrt{2}} \exp i[(m-1)\varphi + k_{zj}z] t_{ij}^{TM} [J_{m-1}(q\rho) \vec{e}_+ + J_{m+1}(q\rho) \exp(2i\varphi) \vec{e}_-].\end{aligned}\quad (5)$$

Here $\cos \gamma_j = k_{zj}/k_0 n_j$, $k_0 = \omega/c$, ω is the frequency of the BLB; the symbols “tr” and “l” denote the transverse and longitudinal components of the electric (magnetic) vector, respectively; A_t^{TM} is the amplitude coefficient; $\vec{e}_\pm = (\vec{e}_1 \pm i\vec{e}_2)/\sqrt{2}$.

Similarly for the reflected field, we obtain:

$$\begin{aligned}\vec{E}_r(R) &= \vec{E}_r^{tr}(R) + \vec{E}_r^l(R), \\ \vec{E}_r^l(R) &= A_{inc} r_{ij}^{TM} \exp i[m\varphi - k_{zi}z] \sin \gamma_i J_m(q\rho) \vec{e}_z, \\ \vec{E}_r^{tr}(R) &= -\frac{iA_{inc}}{\sqrt{2}} \exp i[(m-1)\varphi - k_{zi}z] r_{ij}^{TM} \cos \gamma_i [J_{m-1}(q\rho) \vec{e}_+ - J_{m+1}(q\rho) \exp(2i\varphi) \vec{e}_-],\end{aligned}\quad (6)$$

$$\vec{H}_r(R) = \frac{n_i A_{inc}}{\sqrt{2}} \exp i[(m-1)\varphi - k_{zi}z] r_{ij}^{TM} [J_{m-1}(q\rho) \vec{e}_+ + J_{m+1}(q\rho) \exp(2i\varphi) \vec{e}_-].\quad (7)$$

Here $r_{ij}^{TM} = A_r^{TM}/A_{inc}$ is the reflection coefficient; A_r^{TM} is the amplitude coefficient.

In this case, for the refractive and reflective coefficients of Bessel light beams at the boundary between an isotropic medium and a hyperbolic metamaterial, we have the following expressions:

$$\begin{aligned}t_{ic}^e &= \frac{2\sqrt{\varepsilon_0 \varepsilon_e} \sqrt{1 - \frac{q^2}{k_0^2 \varepsilon_0}}}{\sqrt{\varepsilon_0 \varepsilon_e} \sqrt{1 - \frac{q^2}{k_0^2 \varepsilon_e}} + \varepsilon_o \sqrt{1 - \frac{q^2}{k_0^2 \varepsilon_0}}}, \\ r_{ic}^{TE} &= \frac{\varepsilon_o \sqrt{1 - \frac{q^2}{k_0^2 \varepsilon_0}} - \sqrt{\varepsilon_0} \sqrt{\varepsilon_e - \varepsilon_o q^2 / k_0^2 \varepsilon_e}}{\varepsilon_o \sqrt{1 - \frac{q^2}{k_0^2 \varepsilon_0}} + \sqrt{\varepsilon_0} \sqrt{\varepsilon_e - \varepsilon_o q^2 / k_0^2 \varepsilon_e}}.\end{aligned}\quad (8)$$

For the refractive and reflective coefficients of the Bessel light beams at the boundary between the hyperbolic metamaterial and the isotropic medium, we obtain:

$$\begin{aligned} t_{ci}^{TE} &= \frac{2\varepsilon_o \sqrt{1 - \frac{q^2}{k_0^2 \varepsilon_e(q)}}}{\sqrt{\varepsilon_1} \sqrt{\varepsilon_e - \varepsilon_o q^2 / k_0^2 \varepsilon_e} + \varepsilon_o \sqrt{1 - \frac{q^2}{k_0^2 \varepsilon_1}}}, \\ r_{ci}^e &= -\frac{\varepsilon_o \sqrt{1 - \frac{q^2}{k_0^2 \varepsilon_1}} - \sqrt{\varepsilon_1} \sqrt{\varepsilon_e - \varepsilon_o q^2 / k_0^2 \varepsilon_e}}{\varepsilon_o \sqrt{1 - \frac{q^2}{k_0^2 \varepsilon_1}} + \sqrt{\varepsilon_1} \sqrt{\varepsilon_e - \varepsilon_o q^2 / k_0^2 \varepsilon_e}}. \end{aligned} \quad (9)$$

Taking into account the limited thickness of the metamaterial structure, we obtain for the electric field vector inside the hyperbolic metamaterial (HMM) and outside it:

$$\begin{aligned} \vec{E}_0(R) &= \vec{E}_0^{tr}(R) + \vec{E}_0^l(R), \\ \vec{E}_0^l(R) &= A_{inc} \frac{q}{k_0 \sqrt{\varepsilon_0}} \exp i[m\varphi - k_{z0}z] J_m(q\rho) \vec{e}_z, \\ \vec{E}_0^{tr}(R) &= -\frac{iA_{inc}}{\sqrt{2}} \exp i[(m-1)\varphi - k_{z0}z] \sqrt{1 - \frac{q^2}{k_0^2 \varepsilon_0}} [J_{m-1}(q\rho) \vec{e}_+ - J_{m+1}(q\rho) \exp(2i\varphi) \vec{e}_-], \\ \vec{E}_1(R) &= \vec{E}_1^{tr}(R) + \vec{E}_1^l(R), \\ \vec{E}_1^l(R) &= A_{inc} \frac{q}{k_0 \sqrt{\varepsilon_1}} t \exp i[m\varphi + k_{z1}(z-h)] J_m(q\rho) \vec{e}_z, \\ \vec{E}_1^{tr}(R) &= \frac{iA_{inc}}{\sqrt{2}} \exp i[(m-1)\varphi + k_{z1}(z-h)] t \sqrt{1 - \frac{q^2}{k_0^2 \varepsilon_1}} [J_{m-1}(q\rho) \vec{e}_+ - J_{m+1}(q\rho) \exp(2i\varphi) \vec{e}_-], \\ \vec{E}_{HMM}(R) &= \vec{E}_{HMM}^{tr}(R) + \vec{E}_{HMM}^l(R), \\ \vec{E}_{HMM}^l(R) &= (\vec{E}_{HMM}^l)^f + (\vec{E}_{HMM}^l)^b, \\ \vec{E}_{HMM}^{tr}(R) &= (\vec{E}_{HMM}^{tr})^f + (\vec{E}_{HMM}^{tr})^b, \\ (\vec{E}_{HMM}^l)^{f,b} &= A_{inc} \frac{q}{k_0 \sqrt{\varepsilon_e(q)}} s^{f,b} \exp i[m\varphi \pm k_{zHMM}z] J_m(q\rho) \vec{e}_z, \\ (\vec{E}_{HMM}^{tr})^{f,b} &= \pm \frac{iA_{inc}}{\sqrt{2}} s^{f,b} \exp i[(m-1)\varphi \pm k_{zHMM}z] \times \\ &\quad \times \sqrt{1 - \frac{q^2}{k_0^2 \varepsilon_e(q)}} [J_{m-1}(q\rho) \vec{e}_+ - J_{m+1}(q\rho) \exp(2i\varphi) \vec{e}_-]. \end{aligned} \quad (10)$$

Here $s^f = A_f/A_{inc}$, $s^b = A_b/A_{inc}$ are the amplitude coefficients for the BLB propagating in the forward (along the z axis) and counter-direction to it, and t is the transmittance of the metamaterial layer. Similarly, we can obtain expressions for the magnetic field vector.

In this case, it follows from the boundary conditions that:

$$t = \frac{t_{ic}^e t_{ci}^{TM} \exp(ik_{zHMM}h)}{1 + r_{ic}^{TM} r_{ci}^e \exp(2ik_{zHMM}h)}, \quad (12)$$

$$s^f = \frac{t_{ic}^e}{1 + r_{ic}^{TM} r_{ci}^e \exp(2ik_{zHMM}h)}, \quad s^b = \frac{t_{ic}^e r_{ci}^{TM} \exp(2ik_{zHMM}h)}{1 + r_{ic}^{TM} r_{ci}^e \exp(2ik_{zHMM}h)}. \quad (13)$$

In addition, the boundary conditions allow us to determine the form of the dispersion equation, which defines the condition for generating Bessel plasmon-polaritons:

$$F = 1 + r_{ic}^{TM} r_{ci}^e \exp 2i(k_{zHMM}h) = 0. \quad (14)$$

3. Features of the generation and energetic characteristics of surface Bessel plasmon-polaritons in metamaterial structure.

The determination of roots for equation (14) (with the parameter of conicity q) is rather complex task, as this equation is complex. The method of reflection coefficient poles allows one to solve this problem. The essence of the method can be summarized as follows: The function F can be represented as $F = |F| \exp(if)$, where f is the phase of this function. It is evident that $f = f(q)$ corresponds to the maximum change in the phase of the function. Therefore, to determine the roots, it is necessary to construct dependencies $f(q)$ (more precisely, $f(\text{Re } q)$). The peaks of this dependency correspond to the real part of the roots, and the full width at half maximum of each peak corresponds to the imaginary part of the corresponding root.

Let's consider a practically important scenario where the environment of the hyperbolic metamaterial is the same medium. Suppose the hyperbolic metamaterial separates semi-infinite identical dielectric media with a dielectric permittivity $\varepsilon_0 = \varepsilon_2 = (1.723)^2$ (SF10 glass). The thickness of the porous structure filled with gold is 500 nm.

The derivative of the phase of function $f(\text{Re } q)$ versus the real part of the Bessel plasmon mode effective index is shown in Fig. 3.

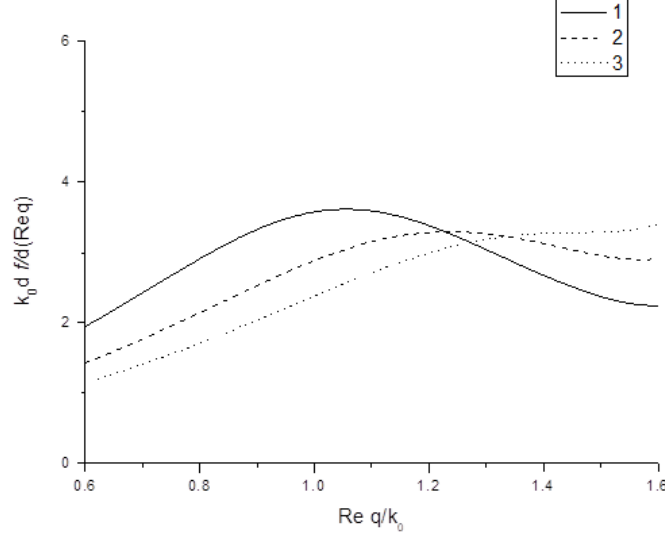


FIG. 3. Dependency of the function $k_0 df(\text{Re } q)/d(\text{Re } q)$ on the dimensionless parameter $\text{Re } q/k_0$: 1 – $N = 0.3$; 2 – $N = 0.35$; 3 – $N = 0.4$. The wavelength of the incident light is 633 nm. The case of surrounding a nanoporous structure with gold nanorods by SF10 glass.

From Fig. 2, we find that: $q = (1.030 + 0.538i) \cdot 10^7 \text{ m}^{-1}$ for $N = 0.3$; $q = (1.187 + 0.614i) \cdot 10^7 \text{ m}^{-1}$ for $N = 0.35$; $q = (1.325 + 0.658i) \cdot 10^7 \text{ m}^{-1}$ for $N = 0.4$. It follows that, the Bessel plasmon-polaritons are generated when a Bessel light beam with cone angles of 37° , 44° , and 51° falls on a hyperbolic metamaterial based on aluminum oxide with gold-filled pores. As can be seen, the cone angle of the BLB for excitation of the surface Bessel plasmon exhibits high sensitivity to the filling ratio.

Let us now consider the dependence of the excitation conditions of plasmon polaritons on the thickness of the hyperbolic metamaterial (see Fig. 4). As can be seen from Fig. 4, $q/k_0 = 1.037 + 0.542i$ for $h = 500 \text{ nm}$; $q/k_0 = 1.04 + 0.563i$ for $h = 250 \text{ nm}$; $q/k_0 = 1.128 + 0.804i$ for $h = 100 \text{ nm}$ and $q/k_0 = 1.357 + 0.837i$ for $h = 70 \text{ nm}$. Thus, as the thickness of the nanoporous structure decreases, the cone angle of the BLB for excitation of the surface Bessel plasmon-polariton increases.

Let's consider the case when a hyperbolic metamaterial is created using porous aluminum oxide with silver metallic nanowires. At a wavelength of $\lambda = 589.3 \text{ nm}$ and filling ratio $N=0.3$ one has $\varepsilon_m = -11.8736 + i1.376$. The calculation shows that $q/k_0 = 0.908 + 0.1i$ for $h = 200 \text{ nm}$; $q/k_0 = 1.084 + 0.605i$ for $h = 100 \text{ nm}$; $q/k_0 = 1.1253 + 0.566i$ for $h = 70 \text{ nm}$. Thus, as the thickness of the nanoporous structure decreases, the parameter of the cone-shaped surface plasmon (Bessel surface plasmon) for exciting the surface Bessel plasmon-polaritons increases. Consequently, the overall nature of the established dependencies remains unchanged. However, it should be noted that the low absorption of silver, described by the imaginary part of the dielectric permittivity, leads to a reduction in the damping of Bessel plasmon-polaritons in the transverse direction.

Let us now consider the distribution of energy flows (the behavior of the Poynting vector $\vec{S} = \frac{c}{8\pi} \text{Re}[\vec{E}\vec{H}^*]$). In this case, we will neglect the finiteness of the thickness of the metamaterial film. As estimated, this assumption is valid as $h \geq 500 \text{ nm}$, which fully corresponds to the conditions for obtaining a hyperbolic metamaterial based on nanoporous aluminum oxide with pores filled with metal. Consider a transverse magnetic TM-polarized Bessel light beam incident on the hyperbolic metamaterial. Then, using expressions (4) and (5), where we set $t_{ij}^{\text{TM}} = t_{ic}^e$, we obtain the following result for the longitudinal and radial components of the Poynting vector within the metamaterial:

$$S_z = S_\rho = 0. \quad (15)$$

The azimuthal component of this vector is determined by the expression:

$$S_\varphi = \frac{cq}{8\pi k_0} |A_{inc}|^2 |t_{ic}^e|^2 F_2(\rho) \exp(-2\chi_{\text{HMM}}z), \quad (16)$$

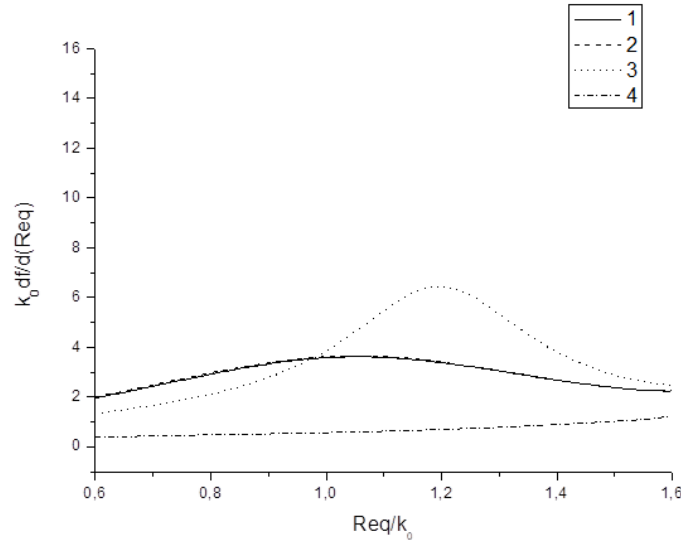


FIG. 4. Dependence $k_0 df(\text{Re } q)/d(\text{Re } q)$ on the dimensionless parameter $\text{Re } q/k_0$: 1 — $h = 500$ nm; 2 — $h = 250$ nm; 3 — $h = 100$ nm; 4 — $h = 70$ nm. The wavelength of the incident light is 633 nm. Filling ratio 0.3. The case of symmetric environment of the hyperbolic metamaterial.

where $\chi_{\text{HMM}} = \text{Re} \left[k_0 \sqrt{\varepsilon_e^{\text{eff}}(q)} [q^2 / (k_0^2 \varepsilon_e^{\text{eff}}(q)) - 1]^{1/2} \right]$, $F_2(\rho) = \frac{m}{|q|\rho} (J_m(|q|\rho))^2$.

Thus, in the metamaterial, only the azimuthal energy flow is presented.

Figures 5 and 6 illustrate the 2D and 3D distribution for energy flow of the azimuthal component of the Bessel plasmon inside the hyperbolic metamaterial based on nanoporous aluminum oxide with pores filled with metal (gold and silver) at the distance $z = \lambda/3$ from the boundary with metamaterial layer. Figs. 4 and 5 show that the central peak of the distribution for energy flow of the azimuthal component of the Bessel plasmon generated in the structure decays exponentially when the cone angle of the BLB for excitation of the Bessel plasmon-polariton increases. The low absorption of silver leads to the reduction in the damping for azimuthal energy flow of the Bessel plasmon-polaritons. Besides it the field for azimuthal energy flow is characterized by more narrow near axial maxima and essential suppression of lateral maxima while moving off the field axis to its periphery.

4. Conclusion

In this paper, we have found the dispersion equation that determines the condition for exciting the Bessel plasmon-polaritons in a confined hyperbolic metamaterial based on dielectric with periodically embedded metallic nanowires. A method for solving this dispersion equation has been developed. Values for the cone-shaped parameters of the Bessel plasmons generated within the matrix of nanoporous aluminum oxide, with pores filled with gold and silver, have been obtained. Remarkably, there is a super-sensitivity of the plasmon generation conditions in this structure to the filling factor.

We have also examined the energy flows formed in the hyperbolic metamaterial when the surface Bessel plasmons are excited within it. It is demonstrated that the sole non-zero energy flow is the azimuthal flow, whose magnitude exponentially decreases as one moves away from the boundary between the isotropic medium and the hyperbolic metamaterial.

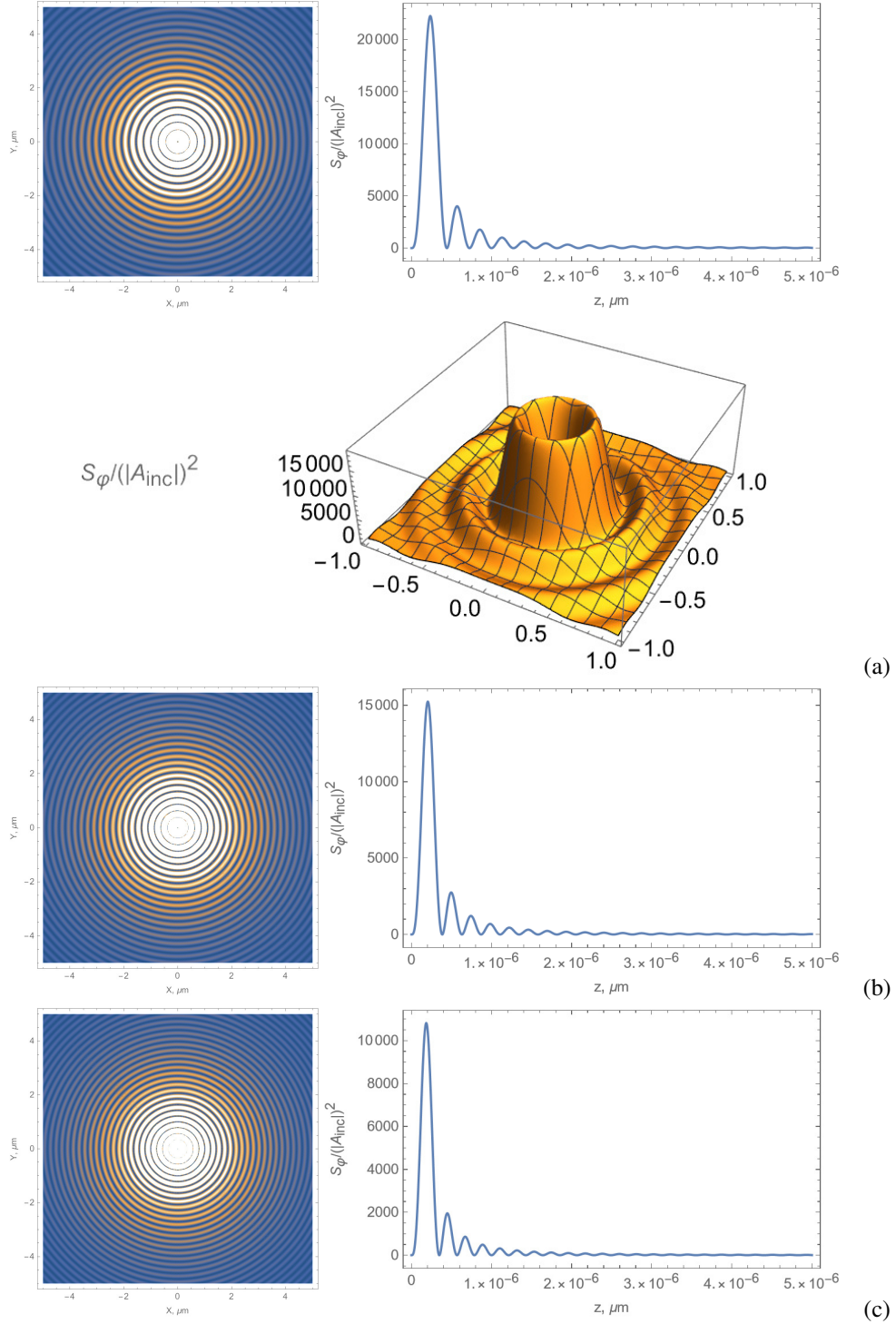


FIG. 5. 2D- and 3D- distribution for energy flow of azimuthal component of the Bessel plasmon field formed inside the hyperbolic metamaterial based on nanoporous aluminum oxide with pores filled with gold when (a) $q = (1.030 + 0.538i) \cdot 10^7 \text{ m}^{-1}$, (b) $q = (1.187 + 0.614i) \cdot 10^7 \text{ m}^{-1}$, (c) $q = (1.325 + 0.658i) \cdot 10^7 \text{ m}^{-1}$ and the wavelength $\lambda = 633 \mu\text{m}$. The distance from the boundary with metamaterial layer is $z = \lambda/3$.

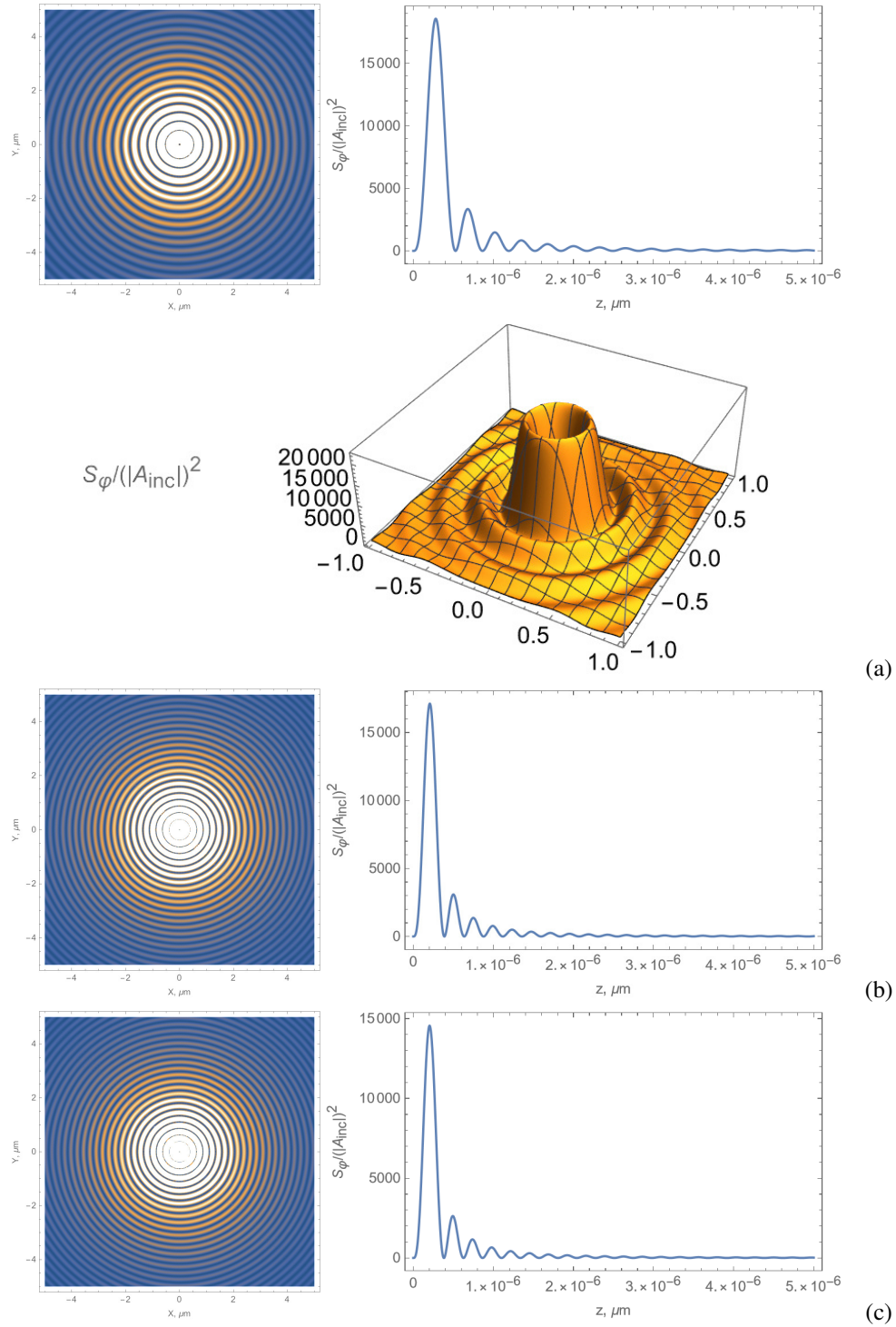


FIG. 6. 2D- and 3D- distribution for energy flow of azimuthal component of the Bessel plasmon field formed inside the hyperbolic metamaterial based on nanoporous aluminum oxide with pores filled with silver when (a) $q/k_0 = 0.908 + 0.1i$, (b) $q/k_0 = 1.084 + 0.605i$, (c) $q/k_0 = 1.1253 + 0.566i$ and the wavelength $\lambda = 589.3$ nm. The distance from the boundary with metamaterial layer $z = \lambda/3$.

References

- [1] Gaponenko S.V. *Introduction to Nanophotonics*. Cambridge, Cambridge University Press, 2010, 458 p.
- [2] Maier S.A. *Plasmonics Theory and Applications*. Moscow, Research Center “Regular and Chaotic Dynamics”, 2011, 292 p. (in Russian)
- [3] Libeson M.N. Surface electromagnetic waves in the optical range. *Soros Educational J.*, 1996, **10**, P. 92–98. (in Russian)
- [4] Agranovich V.M., Mills D.L. *Surface Polaritons: Electromagnetic Waves at Surfaces and Interfaces*. Amsterdam: North-Holland, 1982, 734 p.
- [5] Reather H. *Surface plasmon on Smooth and Rough Surfaces and on Gratings*. Berlin, Springer-Verlag, 1988, 140 p.
- [6] Boardman A.D. *Electromagnetic Surface Modes*. New York, John Wiley & Sons, 1982, 786 p.
- [7] Klimov V.V. *Nanoplasmonics*. Fizmatlit, Moscow, 2009, 480 p. (in Russian)
- [8] Klyuchnik A.V., Kurganov S.Yu., Lozovik Yu.E. Plasma optics of nanostructures. *Physics of the Solid State*, 2003, **45** (7), P. 1327–1331.
- [9] Ebbesen T.W., et al. Extraordinary optical transmission through sub-wavelength hole arrays. *Nature*, 1998, **391**, P. 667–669.
- [10] Ozbay E. Plasmonics: Merging Photonics and Electronics at Nanoscale Dimensions. *Science*, 2006, **311**, P. 189–193.
- [11] Krasavin V., Zheludev N.I. Active plasmonics: Controlling signals in Au/Ga waveguide using nanoscale structural transformations. *Applied Physics Letters*, 2004, **84**, P. 1416–1419.
- [12] Bozhevolnyi S.I. *Plasmonics Nanoguides and Circuits*. Singapore, Pan Stanford Publishing, 2008, 449 p.
- [13] Maier S.A., et al. Experimental demonstration of fiberaccessible metal nanoparticle plasmon waveguides for planar energy guiding and sensing. *Applied Physics Letters*, 2005, **86** (7), 071103.
- [14] Rayleigh L. *The Theory of Sound*. New York, Dover, 1954, 507 p.
- [15] Ritchie R. Plasma losses by fast electrons in thin films. *Physical Review*, 1957, **106**, P. 874–881.
- [16] Powell C., Swan J. Origin of the characteristic electron energy losses in aluminum. *Physical Review*, 1959, **115**, P. 869–875.
- [17] Liu Y., Zhang X. Metamaterials: a new frontier of science and technology. *Chemical Society Reviews*, 2011, **40** (5), P. 2494–2507.
- [18] Kshetrimayum R.S. A brief Intro to Metamaterials. *IEEE Potentials*, 2004, **23** (5), P. 44–46.
- [19] Soukoulis C.M. *Photonic Band Gap Materials*. Dordrecht: Springer Netherlands, 1996, 744 p.
- [20] Poddubny A.N., et al. Hyperbolic metamaterials. *Nature Photonics*, 2013, **7**, P. 958–967.
- [21] Jacob Z., Alekseyev L.V., Narimanov E. Optical hyperlens: far-field imaging beyond the diffraction limit. *Optics Express*, 2006, **14**, P. 8247–8256.
- [22] Lu D., Liu Z. Hyperlenses and metalenses for far-field super-resolution imaging. *Nature Communications*, 2012, **3**, 1205.
- [23] Poddubny A.N., et al. Microscopic model of Purcell enhancement in hyperbolic metamaterials. *Physical Review B*, 2012, **86**, 035148.
- [24] Kurilkina S.N., Belyi V.N., Kazak N.S. Features of evanescent Bessel light beams formed in structures containing a dielectric layer. *Optics Communications*, 2010, **283**, P. 3860–3868.
- [25] Goncharenko A.M., Khilo N.A., Petrova E.S. Evanescent Bessel light. *Proceedings of SPIE – The Int. Society for Optical Engineering*, 2001, **4517**, P. 95–99.
- [26] Zhan Q. Evanescent Bessel beam generation via surface plasmon resonance excitation by a radially polarized beam. *Optics Letters*, 2006, **31**, P. 1726–1728.
- [27] Jiefeng X., Quing L., Jia W. Numerical simulation of evanescent Bessel beams and apodization of evanescent field in near-field optical virtual probe. *Proceedings of the SPIE*, 2005, **5635**, P. 42–47.
- [28] Novitsky A.V., Barkovsky L.M. Total internal reflection of vector Bessel beams: Imbert–Fedorov shift and intensity transformation. *J. of Optics A Pure and Applied Optics*, 2008, **10**, 075006.
- [29] Al-Muhanna M.K., et al. Energy flow patterns in an optical field formed by a superposition of evanescent Bessel light beams. *J. of Optics*, 2011, **13** (10), 105703.
- [30] Cai W., Shalaev V.M. *Optical Metamaterials – Fundamentals and Applications*. Springer, Berlin, 2010.

Submitted 5 December 2023; revised 29 December 2023; accepted 1 January 2024

Information about the authors:

Nguyen Van Vinh – Ho Chi Minh City University of Economics and Finance, Ho Chi Minh City, Vietnam;
ORCID 0009-0003-6732-0789; vinhnv@uef.edu.vn

Nguyen Pham Quynh Anh – Faculty of Electrical, Electronics and Materials Technology, University of Sciences, Hue University, Hue 530000, Vietnam; ORCID 0009-0009-4001-4873; npqanh.dhkh@hueuni.edu.vn

Conflict of interest: the authors declare no conflict of interest.

The structure of magnetic domain walls in cylindrical nano- and microwires with inhomogeneous anisotropy

Ksenia A. Chichay^{1,a}, Igor S. Lobanov^{1,b}, Valery M. Uzdin^{1,c}

¹Department of Physics, ITMO University, St. Petersburg, Russia

^aks.chichay@gmail.com, ^blobanov.igor@gmail.com, ^cv.uzdin@mail.ru

Corresponding author: K. A. Chichay, ks.chichay@gmail.com

PACS 75.60.Ch, 75.30.Gw

ABSTRACT The structure of domain walls in cylindrical nano- and microwires with a non-uniform anisotropy distribution in the transverse-radial direction has been studied. This distribution can be controlled by mechanical stresses associated with specific wire manufacturing methods as well as with the glass coating in some types of microwires. Our calculations have shown that in the presence of axial anisotropy in the core of the wire and radial anisotropy near its surface, various configurations of domain walls can be stabilized. A diagram of magnetic states has been calculated depending on the radial anisotropy values. The stability of various types of domain walls and their possible transformation under the excitation of thermal fluctuations and external perturbations are discussed.

KEYWORDS Domain wall, cylindrical systems, amorphous ferromagnetic microwires, mechanical stress, micro-magnetics.

ACKNOWLEDGEMENTS This work was funded by Russian Science Foundation (project No. 23-72-10028, <https://rscf.ru/en/project/23-72-10028/>). K.A.Ch. acknowledges the support of ITMO Fellowship Program.

FOR CITATION Chichay K.A., Lobanov I.S., Uzdin V.M. The structure of magnetic domain walls in cylindrical nano- and microwires with inhomogeneous anisotropy. *Nanosystems: Phys. Chem. Math.*, 2024, **15** (1), 55–59.

1. Introduction

Magnetic domains in nano- and microwires are of great interest in relation with the concept of racetrack magnetic memory [1–3]. In these memory devices, information is stored in the form of a sequence of domain walls (DW) that can be moved by an electric current. The absence of mechanical motion of reading and writing tools relative to the magnetic medium, the high density of domain walls, and their ability to move at high speed under the action of low currents make this technology very promising. Low-dimensional magnetic systems with cylindrical symmetry (such as nano- and microwires) are of particular interest from this point of view [4, 5]. The cylindrical shape determines a number of useful properties and advantages compared to low-dimensional planar structures. The combination of strong shape anisotropy and cylindrical symmetry makes it possible to stabilize axisymmetric states [6]. Moreover, due to the absence of edges in cylindrical wires, the DW can rotate along the axis of the wire without loss of energy, thereby preventing changes in the structure of the DW (that is, blocking nucleation of anti-vortex states, as occurs in planar wires) [4, 7]. In this way, the so-called Walker breakdown [7, 8] is suppressed, which promises higher DW speed [9, 10].

To date, three types of DWs have been discovered that can be stabilized in nano- micrometer-sized cylindrical systems with uniform magnetic parameters [6]. These are a transverse DW (which is the ground state for thin wires), a Bloch point DW (which is the ground state for thicker wires) and an asymmetric transverse DW, which can only be a metastable state.

In addition to the properties associated with cylindrical symmetry, the small spatial size of micro- and nanowires increases the role of surface and interface effects, and also allows one to significantly change the magnetic characteristics when exposed to mechanical stresses during sample manufacturing or induced anisotropy. This makes it possible to obtain media with parameters unattainable in bulk materials, which turns out to be quite useful for energy-efficient applications [11]. Examples of such cylindrical magnetic systems are amorphous ferromagnetic microwires in a glass shell, obtained by drawing from a melt [12–14]. As a consequence of the fabrication method (drawing and rapid quenching) [15], such systems, in addition to being amorphous, have internal stresses, that lead to a non-uniform distribution of anisotropy in the transverse-radial direction [16–18]. The microwires with a positive magnetostriction acquire an easy magnetization axis oriented along its axis. Such microwires are magnetically bistable (they have only two stable states corresponding to two directions of the magnetization vector along the wire), and magnetization reversal occurs by extremely fast DW movement (single Barkhausen jump) [19].

Presently, there are a lot of experimental data on the dynamics of the DW in such wires. DW velocity and mobility, critical values of external magnetic field and current required for the DW movement as well as the range of fields and

currents at which magnetization reversal occurs through the DW movement are being studied very intensively [20–22]. However, there is still no complete understanding of the types and internal structure of the DW in such systems. In experiments, only the width and approximate shape of the DW can be estimated by analyzing the emf peaks induced by the traveling DW (and, therefore, the change in magnetization) in the pick-up coils [21, 23, 24]. This is due to the “inconvenient size” of such microwires: their lateral dimensions, on the one hand, are very small, and on the other hand they are too bulky to use transmission electron microscopy or tools that can only provide information about the magnetic structure on the surface.

Presumably, in such cylindrical systems with non-uniform magnetic parameters as amorphous ferromagnetic microwires in glass shell [16] the DW structure can be more complex than that of known types of DWs in nanowires. This is due to the micrometer diameter of such wire and inhomogeneity of anisotropy along the radius, which can significantly change the configuration of DW. In this case micromagnetic simulations can play a decisive role in revealing existing magnetic configurations.

In our work, we investigated the stability and internal structure of domain walls stabilized in cylindrical wires with inhomogeneous anisotropy. We considered wires with fixed geometric parameters, but different ratios of the anisotropy values in the core and on the surface of the wire. We have shown stabilization of radial domain wall by the radial anisotropy. According to our simulations radial DW has larger stability region than the transverse DW, while their energy are close in the domain of coexistence.

2. Method

We consider a ferromagnetic wire of radius R and length L shown in Fig. 1. The total micromagnetic energy of the system in cylindrical coordinates is given by:

$$\mathcal{E} = \iiint \left(\frac{A}{2} \left[\left(\frac{\partial \mathbf{S}}{\partial \rho} \right)^2 + \frac{1}{\rho^2} \left(\frac{\partial \mathbf{S}}{\partial \phi} \right)^2 + \left(\frac{\partial \mathbf{S}}{\partial z} \right)^2 \right] - \sum_i K_i(\rho) (\mathbf{S} \cdot \mathbf{e}_i)^2 - B (\mathbf{S} \cdot \mathbf{e}_z) \right) \rho \cdot d\rho \cdot d\phi \cdot dz \quad (1)$$

where \mathbf{S} is the magnetization vector field. The first term in (1) is the exchange energy with exchange stiffness $A = 2 \cdot 10^{-11}$ J/m. The second term describes the easy-axis/easy-plane anisotropy $K_i(\rho)$, which is non-uniform along the radius ρ of the wire, and the third term is the interaction with an external magnetic field B , which is applied along the z direction. The anisotropy axis \mathbf{e}_i is assumed to be different in the core of the wire, where it coincides with the z axis \mathbf{e}_z , and near the surface, where it is assumed to be radial.

For simulations, we use the type and value of anisotropy corresponding to the anisotropy distribution in amorphous ferromagnetic microwires, but in a simplified form. Thus, according to the anisotropy distribution given in [15], starting from the center of the wire to $0.9R$, we used the average value of axial anisotropy $K_{ax} = 1 \cdot 10^4$ J/m³ (easy axis). On the periphery the radial type of anisotropy, K_r , prevails (easy axis). To investigate the influence of the anisotropy on the periphery on the type and structure of the domain wall, we vary the value of K_r from 0 to $10 \cdot 10^4$ J/m³. In addition to stress-induced anisotropy, we include an effective shape anisotropy for cylinder $K_{eff} = 1/4\mu_0 M_s^2$ due to the demagnetization field, where $M_s = 500$ kA/m is saturation magnetization.

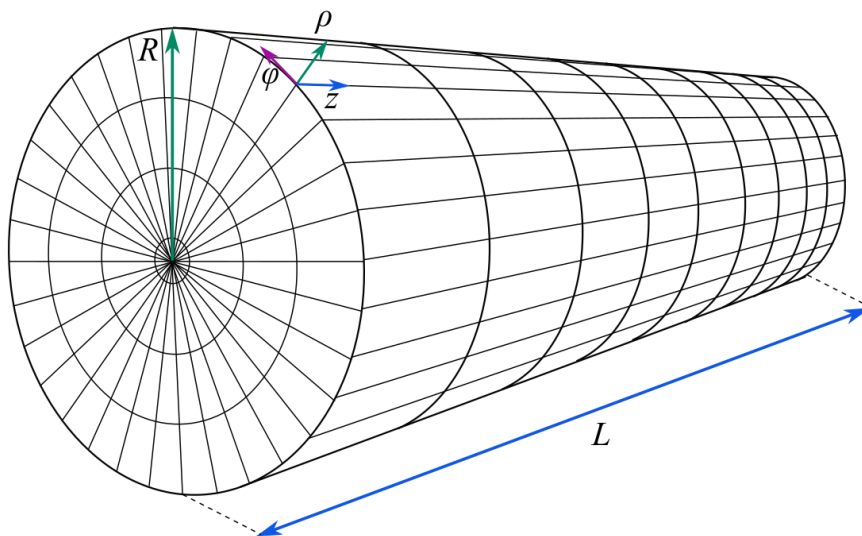


FIG. 1. Schematic representation of a wire in cylindrical coordinate system. R is the wire radius, L is the length of the wire.

The calculations were made using the original code developed by the authors, which implements a finite-difference discretization scheme. Since discretization in this way results in unit cells of different sizes, we took into account the cell volume to calculate the local magnetic moment. For simulations, we use a wire with radius $R = 0.1 \cdot 10^{-6}$ m and length $L = 1 \cdot 10^{-6}$ m with periodic boundary conditions in the z direction. The number of discretization nodes along each axes was: $N_\rho = 30$ (from the center of wire to the periphery), $N_\phi = 100$, $N_z = 400$.

3. Results

For wires with inhomogeneous anisotropy, we found two configurations of the DWs. Fig. 3 shows a 3D view and $\rho-\phi$ cross section of each of the two head-to-head DW configurations. The first configuration (Fig. 3a) is the transverse DW, similar to that found for planar and cylindrical nanowires. In this case, the transition from an axially ordered magnetization parallel to the e_z axis in one direction to ordering in the opposite direction occurs by rotating the magnetization about an axis perpendicular to the wire axis, breaking the axial symmetry. Due to the cylindrical symmetry of the wire and the absence of a preferred transverse direction, such a DW can be formed at any angle ϕ . Black and grey colors on the 3D view in Fig. 3 represent the magnetization being parallel and antiparallel to the z -axis ($+z$ and $-z$), while colors indicate the transverse component of magnetization for different ϕ angles.

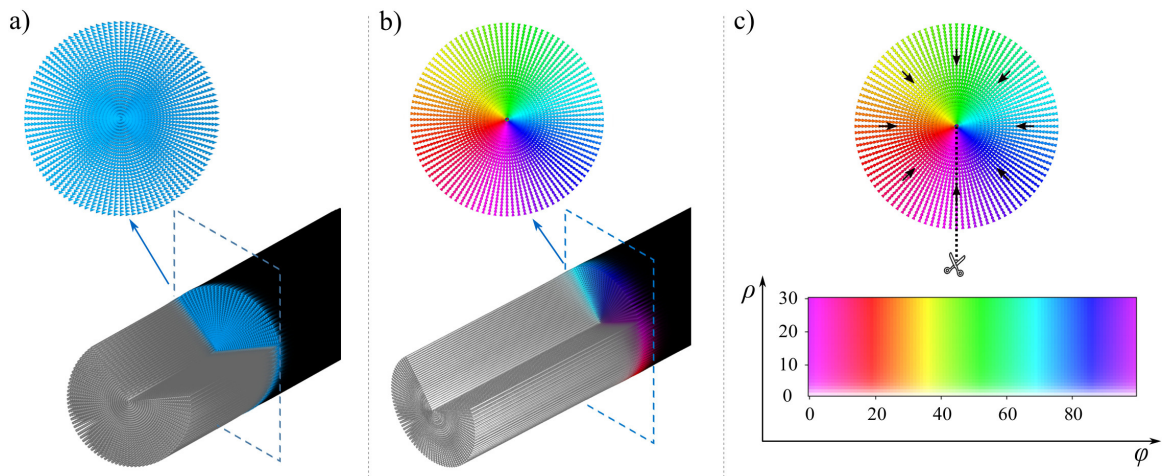


FIG. 2. 3D view and cross section of the cylindrical wire representing magnetic configuration of a) transverse DW, b) radial DW. The cross sections indicate the structure of the DWs at the marked position. Both cross sections are given for the value $K_r = 0$; c) the unrolled view of the $\rho-\phi$ cross section. Direction of magnetization is indicated by color. Black arrows in panel (c) set correspondence between direction and color.

Another type of DW corresponds to the magnetization ordered radially from or towards the center of the wire. In this case, a Bloch point is formed on the axis of symmetry, see Fig. 3b. We refer to this type of a magnetic configuration as a radial domain wall. The bottom panel of Fig. 3c shows the “unrolled” spin structures of the $\rho-\phi$ cross section for radial DW. The magnetization direction is color-encoded as indicated in upper panel in Fig. 3c.

Having discovered two DW configurations, we investigated their stability depending on the value of radial anisotropy at the near surface region of the wire. Fig. 3 summarizes our results as a phase diagram that shows the magnetic energy as a function of radial anisotropy value for both stable DW configurations. Fig. 3a represents the distribution of anisotropy types (axial and radial) along the wire radius. Almost the entire volume of the wire is dominated by the axial anisotropy, corresponding to the realistic case of amorphous ferromagnetic microwires [15]. The radial anisotropy prevails in the outermost 10% of the wire radius forming a layer with a thickness of 10 nm in the considered case.

To study the phase diagram of the obtained DW configurations depending on the anisotropy parameters, each of the DW types obtained at certain anisotropy values was taken as the initial state and relaxed to a local minimum at other anisotropy values. The phase diagram (Fig. 3b) shows that in the case of zero radial anisotropy, only the transverse DW is stable and is an ordinary transverse DW in cylindrical wires. Further, at low values of radial anisotropy, both DW configurations have very similar energy values, although the energy of the transverse DW is somewhat lower in the range of radial anisotropy values from 0 to $4.3 \cdot 10^4$ J/m. At values of K_r above $4.3 \cdot 10^4$ J/m, only the radial DW is stable, and the energy of the system decreases with increasing the radial anisotropy value.

Figure 3c shows the transverse DW for various values of radial anisotropy at the nearsurface region. A more visual representation of the magnetic structure can be obtained by unrolling the $\rho-\phi$ magnetization cross section. It can be seen that at zero radial anisotropy the DW is a conventional transverse DW, when all spins are ordered perpendicular to the wire axis with the same angle ϕ . At non-zero values of radial anisotropy, one can observe a deviation of magnetization

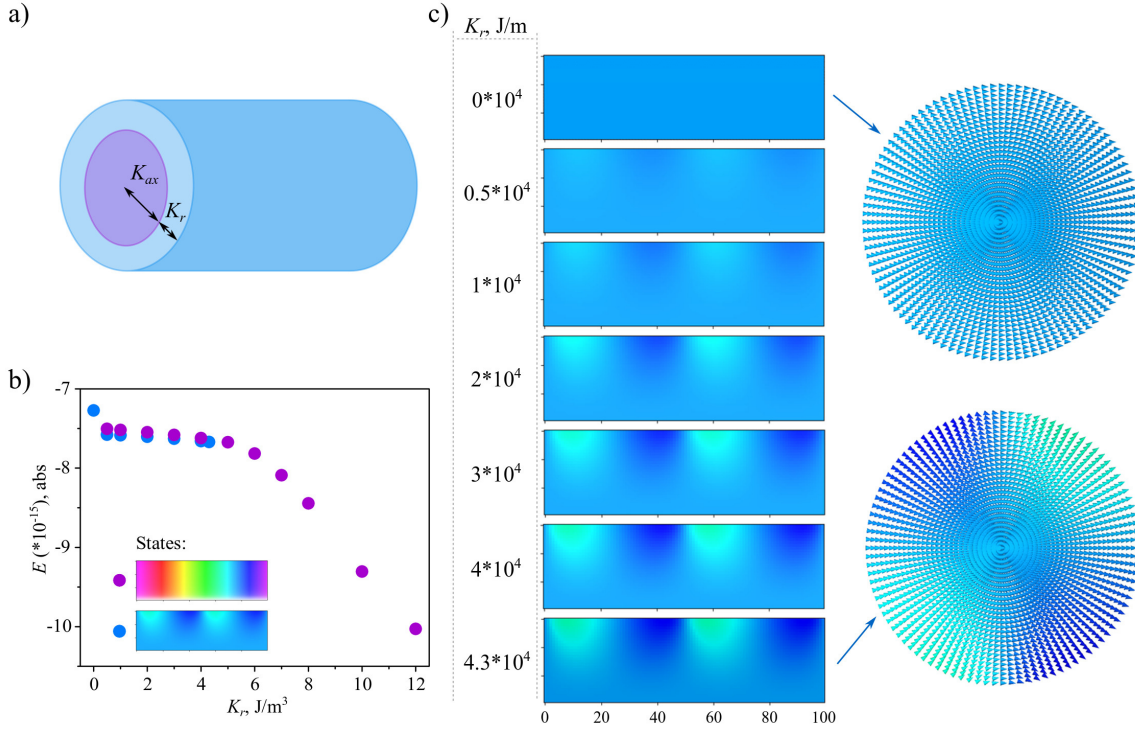


FIG. 3. a) Schematic representation of a cylindrical wire showing the distribution of various types of anisotropy, K_{ax} is axial anisotropy (purple part), K_r is radial anisotropy (blue part). Black arrows show the area (volume) of the wire occupied by each type of anisotropy; b) Dependence of wire energy on the magnitude of radial anisotropy for two configurations of DW. Radial DW exists in the entire range of considered anisotropy values except $K_r = 0$, while transverse DW only exists in the range from 0 to $4.3 \cdot 10^4$ J/m for the wire parameters considered in the work; c) Evolution of the magnetic configuration of the transverse DW with a change of the radial anisotropy value. For each radial anisotropy value, an unrolled view of the $\rho - \phi$ DW cross section is given.

from the original direction near the wire surface, which becomes more pronounced as the radial anisotropy increases. For the limiting case, when $K_r = 4.3 \cdot 10^4$ J/m, the angle of rotation of the magnetization at the periphery from the initial one (at $K_r = 0$ J/m) is almost $+90^\circ$ and -90° , while in the center the direction of magnetization remains original. A further increase in radial anisotropy leads to stabilization of the radial DW.

4. Conclusion

We found two different domain wall configurations in cylindrical wires with inhomogeneous anisotropy. One of them is a transverse domain wall, the other is a so-called radial domain wall, where the magnetization has a Bloch point in the wire center. Phase diagrams of stable configurations of domain walls for wires with different radial anisotropy in the near-surface region have been constructed. A change in the internal structure of the transverse domain wall was found in the presence of nonzero radial anisotropy in the near-surface region of the wire.

There is a certain range of parameter values in which both types of DW are locally stable and have close energy. Transitions between these states are possible due to thermal fluctuations and random perturbations. The rate of such transitions can be estimated based on transition state theory (TST) for magnetic degrees of freedom [25]. In harmonic approximation of TST the temperature dependence of transition rate is given by the Arrhenius law. Activation barrier for transition between different type of DW can be found after building the minimal energy path between correspondent locally stable states on the multidimensional energy surface of the system. The maximum along the path corresponds to the saddle point on the multidimensional energy surface. The difference between the energies in saddle point and initial state determines the activation energy for transition whereas the preexponential factor depend on the shape of the energy surface near these points [26].

References

- [1] Parkin S.S.P., Hayashi M. and Thomas L. Magnetic Domain-Wall Racetrack Memory. *Science*, 2008, **320**, 5873, P. 190–194.
- [2] Parkin S., Yang S.H. Memory on the racetrack. *Nature nanotechnology*, 2015, 10(3), P. 195–198.
- [3] Blasing R. et al. Magnetic Racetrack Memory: From Physics to the Cusp of Applications Within a Decade. *Proc. IEEE*, 2020, **108**, P. 1303–1321.
- [4] Alam J., et.al. Cylindrical micro and nanowires: Fabrication, properties and applications. *J. Magn. Magn. Mater.*, 2020, **513**, P. 167074.

- [5] Hertel R., Computational micromagnetism of magnetization processes in nickel nanowires. *J. Magn. Magn. Mater.*, 2002, **249**(1-2), P. 251–256.
- [6] Ferguson C.A., MacLaren D.A., McVitie S. Metastable magnetic domain walls in cylindrical nanowires. *J. Magn. Magn. Mater.*, 2015, **381**, P. 457–462.
- [7] Yan M. Beating the Walker limit with massless domain walls in cylindrical nanowires. *Phys. Rev. Lett.*, 2010, **104**, P. 057201.
- [8] Mougín A., Cormier M., Adam J. P., Metaxas P. J. and Ferre J. Domain wall mobility, stability and Walker breakdown in magnetic nanowires. *EPL*, 2007, **78**, P. 57007.
- [9] Hertel R. Ultrafast domain wall dynamics in magnetic nanotubes and nanowires. *J. Phys.: Condens. Matter*, 2016, **28**, P. 483002.
- [10] Yan M., Andreas C., Kakay A., Garcia-Sanchez F., Hertel R. Fast domain wall dynamics in magnetic nanotubes: Suppression of Walker breakdown and Cherenkov-like spin wave emission. *Appl. Phys. Lett.*, 2011, **99**, P. 122505.
- [11] Bukharaev A.A., Zvezdin A.K., Pyatakov A.P., Fetisov Y.K. Straintronics: a new trend in micro- and nanoelectronics and materials science. *Physics-Uspekhi*, 2018, **61**(12), P. 1175.
- [12] Larin V.S., Torcunov A.V., Zhukov A., Gonzalez J., Vazquez M., Panina L. Preparation and properties of glass-coated microwires. *J. Magn. Magn. Mater.*, 2002, **249**(1-2), P. 39-45.
- [13] Zhukov A., Gonzalez J., Blanco J.M., Vazquez M., Larin V. Microwires coated by glass: a new family of soft and hard magnetic materials. *J. Mater. Res.*, 2000, **15**, P. 2107-2113
- [14] Zhukova V., Ipatov M., Zhukov A. Thin magnetically soft wires for magnetic microsensors. *Sensors*, 2009, **9**, P. 9216-2940.
- [15] Baranov S.A., Larin V.S., Torcunov A.V. Technology, Preparation and Properties of the Cast Glass-Coated Magnetic Microwires. *Crystals*, 2017, **7**(6), P. 136.
- [16] Chiriac H., Ovari T.A., Pop Gh. Internal stress distribution in glass-covered amorphous magnetic wires. *Phys. Rev. B.*, 1995, **52**(14), P. 10104.
- [17] Chiriac H., Ovari T.A., Zhukov A. Magnetoelastic anisotropy of amorphous microwires. *J. Magn. Magn. Mater.*, 2003, **496**, P. 254-255.
- [18] Zhukova V., Blanco J.M., Ipatov M., Zhukov A. Magnetoelastic contribution in domain wall dynamics of amorphous microwires. *Physica B*, 2012, **407**, P. 1450–1454.
- [19] Corte-León P., Gonzalez-Legarreta L., Zhukova V., Ipatov M., Blanco J. M., Churyukanova M., Taskaev S. and Zhukov A. Controlling the domain wall dynamics in Fe-, Ni- and Co- based magnetic microwires. *J. Alloys Compound.*, 2020, **834**, P. 155170.
- [20] Zhukova, V., Corte-Leon, P., González-Legarreta, L., Talaat, A., Blanco, J.M., Ipatov, M., Olivera, J. and Zhukov, A. Review of domain wall dynamics engineering in magnetic microwires. *Nanomaterials*, 2020, **10**(12), P. 2407.
- [21] Corte-León, P., Zhukova V., Blanco J.M., Chizhik A., Ipatov M., Gonzalez J., Fert A., Alonso A. and Zhukov A. Engineering of domain wall propagation in magnetic microwires with graded magnetic anisotropy. *Applied Materials Today*, 2022, **26**, P. 101263.
- [22] Chichay K., et. al. Tunable domain wall dynamics in amorphous ferromagnetic microwires. *J. Alloys Compound.*, 2020, **835**, P. 154843.
- [23] Gudoshnikov S.A., Grebenshchikov Yu.B., Ljubimov B.Ya., Palvanov P.S., Usov N.A., Ipatov M., Zhukov A., Gonzalez J. Ground state magnetization distribution and characteristic width of head to head domain wall in Fe-rich amorphous microwire. *Phys. Stat. Sol. A*, 2009, **206**(4), P. 613-617.
- [24] Panina L.V., Ipatov M., Zhukova V., Zhukov A. Domain wall propagation in Fe-rich amorphous microwires. *Physica B*, 2012, **407**(4), P. 1442–1445.
- [25] Lobanov I.S., Potkina M.N., Uzdin V.M. Stability and Lifetimes of Magnetic States of Nano- and Microstructures (Brief Review). *JETP Letters*, 2021, **113**(12), P. 801–813.
- [26] Lobanov I.S., Uzdin V.M. The lifetime of micron scale topological chiral magnetic states with atomic resolution. *Comp. Phys. Commun.*, 2021, **269**, P. 108136.

Submitted 11 November 2023; revised 1 December 2023; accepted 7 December 2023

Information about the authors:

Ksenia A. Chichay – Department of Physics, ITMO University, St. Petersburg, 197101, Russia; ORCID 0000-0002-6921-6075; ks.chichay@gmail.com

Igor S. Lobanov – Department of Physics, ITMO University, St. Petersburg, 197101, Russia; ORCID 0000-0001-8789-3267; lobanov.igor@gmail.com

Valery M. Uzdin – Department of Physics, ITMO University, St. Petersburg, 197101, Russia; ORCID 0000-0002-9505-0996; v.uzdin@mail.ru

Conflict of interest: the authors declare no conflict of interest.

Extremely short optical pulses in a thin polymer film with carbon nanotubes

Sergey V. Belibikhin, Natalia N. Konobeeva

Volgograd State University, Volgograd, Russia

^abelibihin@gmail.com, ^byana_nn@volsu.ru

Corresponding author: Sergey V. Belibikhin, belibihin@gmail.com

PACS 42.65.-k, 42.70.Jk, 73.63.Fg

ABSTRACT In this work, we study the dynamics of electromagnetic radiation in a thin polymer film containing carbon nanotubes. Maxwell's equations are supplemented with a term that takes into account the presence of polymers in the medium. The dependence of the spatial-energy characteristics of the optical pulse on the polymer concentration is revealed.

KEYWORDS optical pulses, polymer film, carbon nanotubes

ACKNOWLEDGEMENTS This research was funded by the Ministry of Science and Higher Education of the Russian Federation the government task "FZUU-2023-0001".

FOR CITATION Belibikhin S.V., Konobeeva N.N. Extremely short optical pulses in a thin polymer film with carbon nanotubes. *Nanosystems: Phys. Chem. Math.*, 2024, **15** (1), 60–64.

1. Introduction

Propagation of multidimensional localized structures in optical and waveguide media is of great interest to researchers from the point of view of both fundamental and applied science [1–5]. The first work on the extremely short pulses propagation in a medium with carbon nanotubes (CNTs) [6] was published in 2006 [7]. Since that time the number of publications on this topic has been steadily growing. Many interesting patterns and effects were discovered. Among them, the stabilizing properties of nanotubes, the influence of external electric and magnetic fields, as well as the acoustic field, are presented. The dependence of the pulse characteristics on the properties of the medium, including the anisotropic optical medium, was analyzed [8, 9].

In the present paper, we study the evolution of an extremely short optical pulse during its scattering on a thin film, which is a composite of a polymer with CNTs [10]. We use previously developed model [11], which was modified taking into account the polymer in the medium.

When the pulse is scattered by a thin film (i.e., with a thickness comparable to the characteristic size of the pulse), there are many new effects. As shown in Ref. [12, 13], even in the case of weak fields, analog of differentiation and integration of the extremely short optical pulse is possible. Of course, it is necessary to generalize such effects to the case of strong fields. We consider this case in the present work.

2. Basic equations

We consider the interaction of an extremely short pulse with a thin polymer film containing semiconductor carbon nanotubes of the zigzag type. We place the film in the path of the pulse in such a way that the electric field of the pulse is directed along the axis of the nanotubes (y -axis). We assume that all nanotubes are oriented in the same way and are located at the same distance from each other, forming a homogeneous bulk. The distances between neighboring nanotubes are large compared to their diameter. This specific assumption allows us to neglect the interaction between CNTs.

It is known that the electron dispersion law for carbon nanotubes of type $(m, 0)$ can be written as [14]:

$$\varepsilon(p, s) = \pm \gamma_0 \sqrt{1 + 4 \cos(ap) \cos\left(\frac{\pi s}{m}\right) + 4 \cos^2\left(\frac{\pi s}{m}\right)}, \quad (1)$$

where $\gamma \approx 2.7$ eV, p is the electron quasi-momentum, $a = 3b/2\hbar$, $b = 0.142$ nm is the distance between adjacent carbon atoms.

The wave equation for vector-potential \mathbf{A} has the following form:

$$\frac{1}{c^2} \frac{\partial^2 \mathbf{A}}{\partial t^2} = \frac{\partial^2 \mathbf{A}}{\partial x^2} + \frac{\partial^2 \mathbf{A}}{\partial y^2} + \frac{\partial^2 \mathbf{A}}{\partial z^2} + \frac{4\pi}{c} \mathbf{j}(\mathbf{A}) \left(\Phi(z_0 - z) - \Phi(z_0 + h - z) \right), \quad (2)$$

here Φ is the Heaviside function, h is the thickness of the polymer film with CNTs, z_0 is the location of the edge of the thin film from the side of the traveling pulse, \mathbf{j} is the electric current density.

Since the thin film is a composite of a polymer with carbon nanotubes, the current density consists of two components: \mathbf{j}_1 , \mathbf{j}_2 – contributions to the electric current of carbon nanotubes and polymers, respectively.

Let us take into account that the field is directed along the y axis, then the vector potential has the form: $\mathbf{A} = (0, A(x^2 + y^2, z, t), 0)$. The expression for the projection of the current density \mathbf{j}_1 onto CNT axis can be written as follows:

$$j_1(A) = -en_0\gamma_0a \sum_q B_q \sin\left(\frac{aeA}{c}q\right),$$

$$B_q = \sum_s \frac{q}{\gamma_0} a_{sq} \int_{BZ} \frac{\exp(-\varepsilon(p, s)/k_B T)}{1 + \exp(-\varepsilon(p, s)/k_B T)} \cos(q \cdot p') dp', \quad (3)$$

where n_0 is the electron concentration in CNT array, $k_B = 1.380649 \cdot 10^{-23} \text{ J}\cdot\text{K}^{-1}$, T is the temperature, BZ is the first Brillouin zone, a_{sq} are the coefficients of spectrum expansion (1) in the Fourier series. The calculation of the current j_2 is carried out similarly to the calculation of the current for a system of quantum dots with hopping conductivity [15]. This model is described in details and justified in [16].

Finally, the equation for the vector potential of the electric field component takes the following form in the cylindrical coordinate system:

$$\frac{1}{c^2} \frac{\partial^2 A}{\partial t^2} = \frac{1}{r} \frac{\partial}{\partial r} \left(r \frac{\partial A}{\partial r} \right) + \frac{\partial^2 A}{\partial z^2} + \frac{1}{r^2} \frac{\partial^2 A}{\partial \phi^2} + \frac{4\pi}{c} \left(j_1(A) + j_2(A) \right) \left(\Phi(z_0 - z) - \Phi(z_0 + h - z) \right). \quad (4)$$

Here (r, z, φ) are the coordinates in the cylindrical system, so that $r^2 = x^2 + y^2$, $\tan \varphi = y/x$.

In the general case, when the extremely short pulse propagates through a CNT array, due to the inhomogeneity of the pulse field, current inhomogeneity may arise. So, it can lead to charge accumulation in some area. However, previous calculations [17] showed that this effect for femtosecond pulses can be neglected. As a result, we can assume that cylindrical symmetry in the field distribution is preserved. Based on this, we believe that, due to the cylindrical symmetry, the derivative with respect to angle is equal to zero. In this case, we obtain an effective equation for the components of the vector potential in the cylindrical coordinate system:

$$\frac{1}{r} \frac{\partial}{\partial r} \left(r \frac{\partial A_1}{\partial r} \right) + \frac{\partial^2 A_1}{\partial z^2} - \frac{1}{c^2} \frac{\partial^2 A_1}{\partial t^2} + \frac{4en_0\gamma_0a}{c} \times$$

$$\times \left[\sum_{q=1}^{\infty} B_q \sin\left(\frac{aeq}{c}A\right) + \chi \cdot \sin\left(\frac{a_{POL}e}{c}A\right) \right] \cdot \left(\Phi(z_0 - z) - \Phi(z_0 + h - z) \right) = 0. \quad (5)$$

Here $\chi \cdot n_0$ is the electron concentration in polymer, a_{POL} is the polymer C-C bond length.

3. Numerical modeling and discussion

To solve the resulting equation (5), we use a cross-type numerical scheme with standard stability conditions [18]. The initial condition is chosen in the Gaussian form:

$$A(r^2, z, 0) = A_0 \cdot \exp\left(-\frac{z^2}{l_z^2}\right) \exp\left(-\frac{r^2}{l_r^2}\right),$$

$$\frac{dA(r^2, z, 0)}{dt} = 2 \cdot u \cdot \frac{z}{l_z} \cdot A_0 \cdot \exp\left(-\frac{z^2}{l_z^2}\right) \exp\left(-\frac{r^2}{l_r^2}\right). \quad (6)$$

Here A_0 is the pulse amplitude, l_r, l_z are the pulse width along the directions r and z , correspondingly, u is the initial pulse velocity along z -axis.

The evolution of the pulse is shown in Fig. 1.

Note that the pulse is divided into several peaks of different amplitudes when scattered by a thin polymer film with carbon nanotubes, while maintaining the region of its localization.

The pulse intensity for different film thicknesses h and different initial velocity is shown in Fig. 2. According to Fig. 2, we can conclude that the shape of the extremely short optical pulse is greatly influenced by both the pulse velocity and the thickness of the composite film. Note that the greater the initial pulse velocity, the more local maxima are formed. For a better understanding of what exactly happens to the spatial-energy characteristics of an electromagnetic wave, let us construct slices at $r = 0$, which are shown in Fig. 3.

It can be seen from Fig. 3 that for the initial velocity of the pulse $u = 0.95$, there is a larger number of additional peaks compared to the case of $u = 0.9$. The lower the speed, the longer the pulse interacts with the polymer film and stronger localization is observed. That is, the effects of nonlinearity of the medium act for a longer time and a balance between dispersion and nonlinearity has time to be established, which leads to conservation of the pulse energy in a smaller region of space, i.e. its stabilization. The film thickness has the greatest influence on the pulse intensity.

The dependence of the shape of an extremely short optical pulse on the polymer concentration is shown in Fig. 4.

The polymer concentration in a thin film does not affect the spatial localization of the pulse, but manifests itself in a change in its shape and amplitude.

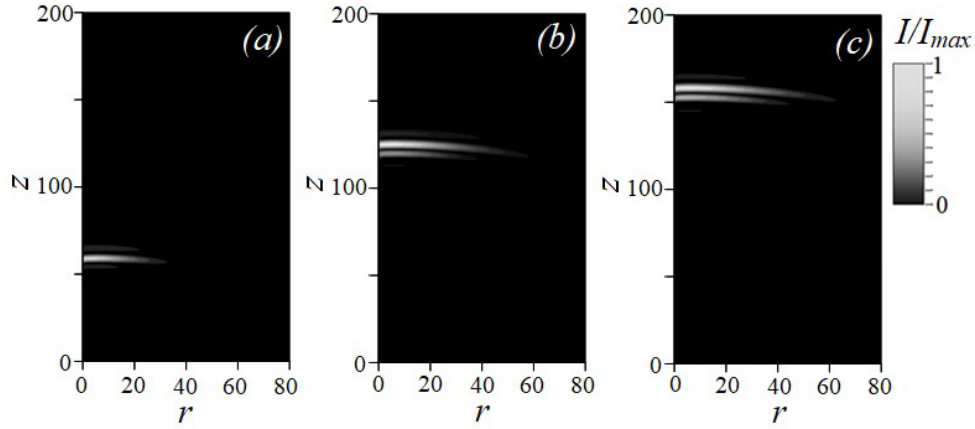


FIG. 1. Dynamics of the pulse propagation after passing through a thin polymer film with CNTs: a) $t = 7$; b) $t = 11$; c) $t = 13$. The film is located between $z = 0$ and $z = 50$. The time unit corresponds to 10^{-13} s, the unit corresponds to coordinates $r, z - 1.2 \mu\text{m}$. I_{max} is the maximum intensity value for each moment of time.

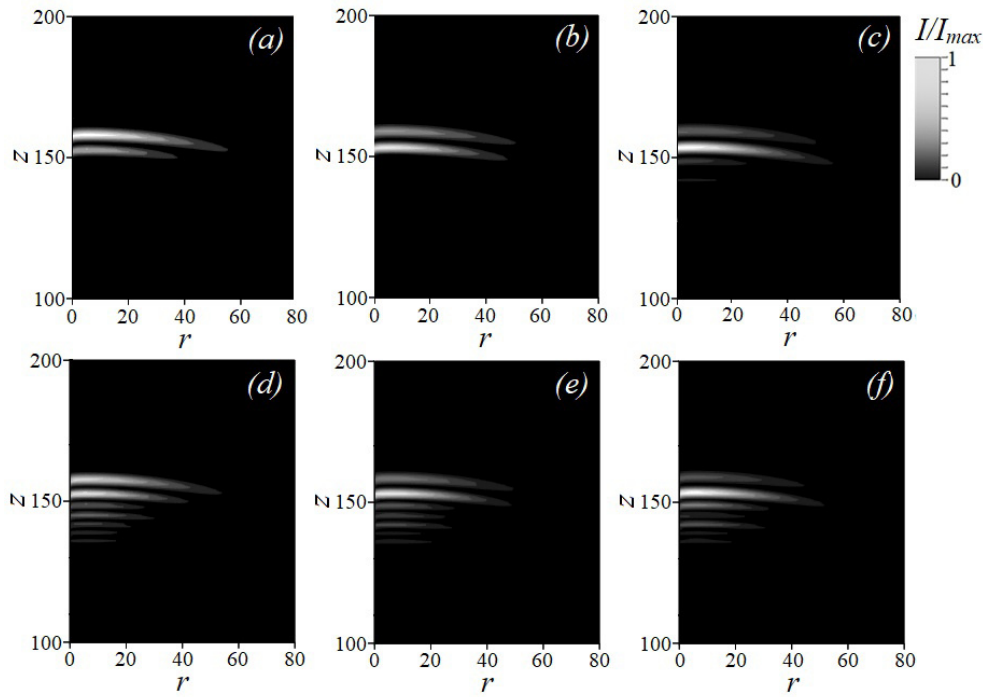


FIG. 2. Pulse intensity after passing through thin polymer film with CNTs at $t = 13$ for different film thickness: (a, d) 50; (b, e) 80; (c, f) 100. The film starts at position $z = 0$. Figures (a-c) $u = 0.9$; (d-f) $u = 0.95$ (in units of the speed of light). The time unit corresponds to 10^{-13} s, the unit corresponds to coordinates $r, z - 1.2 \mu\text{m}$. I_{max} is the maximum intensity value for each row of patterns (for each velocity value).

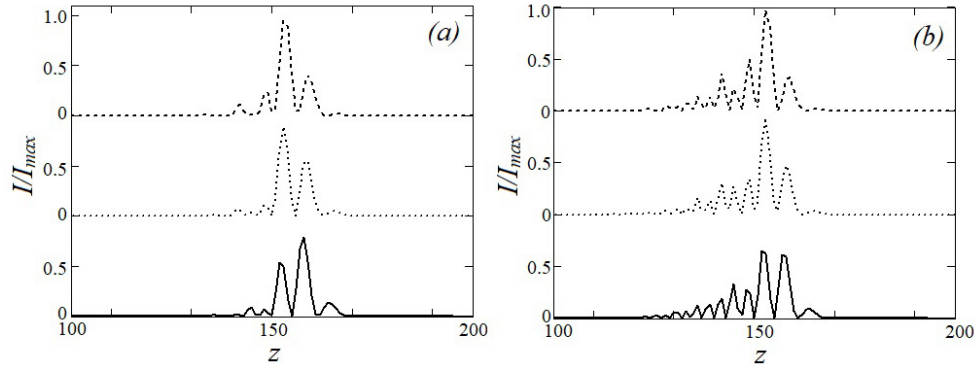


FIG. 3. Pulse intensity after passing through thin polymer film with CNTs at $t = 13$ for different film thickness (slices at $r = 0$): a) $u = 0.9$; b) $u = 0.95$. The solid curve corresponds to $h = 50$; the dotted curve – $h = 80$; the dashed curve – $h = 100$. The film starts at position $z = 0$. The time unit corresponds to 10^{-13} s, the unit along z -axis corresponds to $1.2 \mu\text{m}$. I_{max} is the maximum intensity value for velocity value.

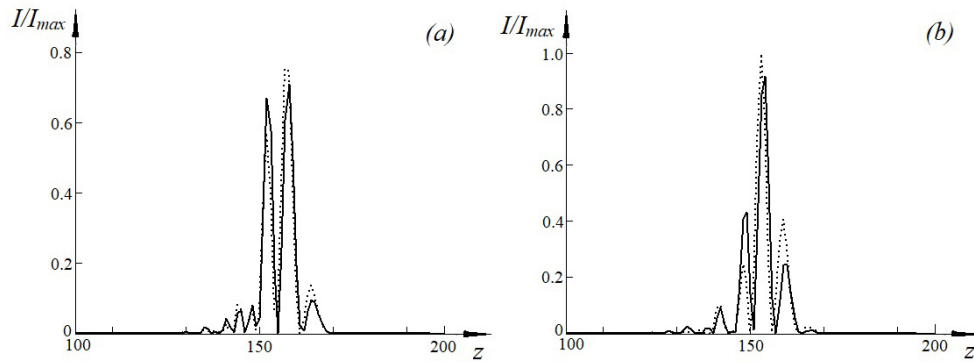


FIG. 4. Pulse intensity after passing through thin polymer film with CNTs at $t = 13$ for different film thickness (slices at $r = 0, u = 0.9$): a) $h = 50$; b) $h = 100$. The solid curved corresponds to $\chi = 0.1$; the dotted curve – $\chi = 0.8$. The time unit corresponds to 10^{-13} s, the unit along z -axis corresponds to $1.2 \mu\text{m}$. I_{max} is the maximum intensity value for all figures.

4. Conclusion

- (1) The model for the passage of an extremely short optical pulse through a thin polymer film with carbon nanotubes has been constructed.
- (2) The thickness of the polymer film with CNTs allows one to control the shape and intensity of the pulse.
- (3) The localization area of an extremely short optical pulse when passing through a polymer film can be controlled using the initial velocity of the pulse.
- (4) When a short-duration electromagnetic pulse is scattered by a composite film, the generation of higher harmonics is possible.

References

- [1] Mihalache D. Multidimensional localized structures in optical and matter-wave media: a topical survey of recent literature. *Rom. Rep. Phys.*, 2021, **73** (2), 403.
- [2] Younas U., Ren J. Investigation of exact soliton solutions in magneto-optic waveguides and its stability analysis. *Results in Physics*, 2021, **21**, 103816.
- [3] Leblond H., Kremer D., Mihalache D. Few-cycle spatiotemporal optical solitons in waveguide arrays. *Phys Rev. A*, 2017, **95**, 043839.
- [4] Barland S., Coen S., Erkintalo M., Giudici M., Javaloyes J., Murdoch S. Temporal localized structures in optical resonators. *Advances in Physics: X*, 2017, **2** (3), P. 496–517.
- [5] Zhang J., Lin Q., Piredda G., Boyd R.W., Agrawal G.P., Fauchet P.M. Optical solitons in a silicon waveguide. *Optics Express*, 2007, **15** (12), P. 7682–7688.
- [6] Hassan M.Th., Luu T.T., Moulet A., Raskazovskaya O., Zhokhov P., Garg M., Karpowicz N., Zheltikov A.M., Pervak V., Krausz F., Goulielmakis E. Optical attosecond pulses and tracking the nonlinear response of bound electrons. *Nature*, 2016, **530** (7588), P. 66–70.
- [7] Belonenko M.B., Demushkina E.V., Lebedev N.G. Electromagnetic solitons in a system of carbon nanotubes. *J. Russ. Las. Research*, 2006, **27**, P. 457–465.

- [8] Konobeeva N.N., Belonenko M.B. Propagation of ultrashort optical pulses in anisotropic optical media with carbon nanotubes. *Int. J. Mod.Phys. B*, 2021, **35** (19), 2150197.
- [9] Konobeeva N.N., Belonenko M.B. Influence of a magnetic field on the propagation of ultrashort optical pulses in anisotropic optical media with carbon nanotubes. *Nanosystems: Physics, Chemistry, Mathematics*, 2021, **12** (4), P. 407–538.
- [10] Zaidi B., Smida N., Althobaiti M.G. Polymer/Carbon nanotube based nanocomposites for photovoltaic application: functionalization, structural and optical properties. *Polymers*, 2022, **14** (6), 1093.
- [11] Almohammad Alhousen G., Konobeeva N.N., Belonenko M.B. Rectification of extremely short pulses in thin films of chiral nanotubes. *Modern Physics Letters B*, 2023, **37** (29), 2350134.
- [12] Arkhipov R.M., Rosanov N.N., Arkhipov M.V., Tolmachev Y.A., Pakhomov A.V., Babushkin I. Generation of unipolar pulses in nonlinear media. *JETP Letters*, 2017, **105** (6), P. 408–418.
- [13] Pakhomov A.V., Arkhipov R.M., Arkhipov M.V., Rosanov N.N. Time integration and differentiation of extremely short pulses in thin conducting films. *Proceedings of the XXXIII All-Russian school-seminar “Wave phenomena: physics and applications” named after Professor A.P. Sukhorukov*, Mozhaisk, June 5–10, 2022, P. 19–21.
- [14] Harris P.J. *Carbon nanotubes and related structures. New materials for the twenty-first century*. Cambridge University press, Cambridge, 1999, 277 p.
- [15] Bass F.G., Bulgakov A.A., Teterov A.P. *High frequency properties of semiconductors with superlattices*. Nauka, Moscow, 1989, 288 p.
- [16] Osipov V.A., Fedyanin V.K. *Light scattering by solitons in polyacetylene*. JINR, Dubna, 1984.
- [17] Zhukov A.V., Bouffanais R., Fedorov E.G., Belonenko M.B. Three-dimensional electromagnetic breathers in carbon nanotubes with the field inhomogeneity along their axes Three-dimensional electromagnetic breathers in carbon nanotubes with the field inhomogeneity along their axes. *J. Appl. Phys.*, 2013, **114**, 143106.
- [18] Thomas J.W. *Numerical partial differential equations – finite difference methods*. Springer-Verlag, New-York, 1995, 426 p.

Submitted 31 October 2023; revised 12 January 2024; accepted 17 January 2024

Information about the authors:

Sergey V. Belibikhin – Volgograd State University, University avenue, 100, Volgograd, 400062, Russia;
ORCID 0009-0007-2201-9959; belibihin@gmail.com

Natalia N. Konobeeva – Volgograd State University, University avenue, 100, Volgograd, 400062, Russia;
ORCID 0000-0002-6043-9555; yana_nn@volsu.ru

Conflict of interest: the authors declare no conflict of interest.

Equilibrium of intrinsic and impurity point defects in Ca-doped $\text{Sm}_2\text{Zr}_2\text{O}_7$

Vladimir A. Vorotnikov^{1,2}, Semyon A. Belyakov³, Alexey V. Ivanov^{1,2}, Yulia V. Novikova³, Anna Yu. Stroeva¹, Vadim V. Grebenev⁴, Dmitry N. Khmelenin⁴, Olga V. Emelyanova⁴, Maksim S. Plekhanov⁵, Anton V. Kuzmin^{1,2}

¹Institute of Chemistry and Ecology, Vyatka State University, Kirov, Russia

²Institute of Solid-State Chemistry and Mechanochemistry SB RAS, Novosibirsk, Russia

³Institute of High-Temperature Electrochemistry UB RAS, Yekaterinburg, Russia

⁴Shubnikov Institute of Crystallography of Federal Scientific Research Centre "Crystallography and Photonics" of the RAS, Moscow, Russia

⁵Institute of Crystallography, RWTH Aachen University, Aachen, Germany

Corresponding author: Anton V. Kuzmin, a.v.kuzmin@yandex.ru

PACS 82.45.Gj, 82.33.Pt

ABSTRACT In this work, a doping strategy was used to achieve a good conductivity in samarium zirconate which crystallizes in the pyrochlore. The production of nanopowders made it possible to form high-density ceramics with an optimal microstructure. It is shown that intrinsic and impurity defects coexist in $\text{Sm}_{2-x}\text{Ca}_x\text{Zr}_2\text{O}_{7-\delta}$, impairing ion transport at high doping levels. Despite this, $\text{Sm}_{1.95}\text{Ca}_{0.05}\text{Zr}_2\text{O}_{7-\delta}$ maintains low activation energy of the parent and has good ionic conductivity ($10^{-3} \text{ S}\cdot\text{cm}^{-1}$ at 600 °C) which is one of the largest among oxide pyrochlores. It has been shown to have a good chemical stability. The material has a thermal expansion coefficient (TEC) of 12 ppm K^{-1} which is higher than YSZ and provides better compatibility with electrode materials. The above makes it possible to successfully use it as a highly stable oxygen electrolyte or an intermediate thin layer at the electrolyte-electrode interface in electrochemical devices.

KEYWORDS solid oxide electrolyte, pyrochlores, grain boundary conductivity, nanoscale powders, combustion method

ACKNOWLEDGEMENTS The research was partially supported by the Russian Science Foundation (Grant No. 22-23-01121).

FOR CITATION Vorotnikov V.A., Belyakov S.A., Ivanov A.V., Novikova Yu.V., Stroeva A.Yu., Grebenev V.V., Khmelenin D.N., Emelyanova O.V., Plekhanov M.S., Kuzmin A.V. Equilibrium of intrinsic and impurity point defects in Ca-doped $\text{Sm}_2\text{Zr}_2\text{O}_7$. *Nanosystems: Phys. Chem. Math.*, 2024, **15** (1), 65–79.

1. Introduction

In recent years, high thermal, chemical and radiation stability has led to great interest in lanthanide zirconates $\text{Ln}_2\text{Zr}_2\text{O}_7$ with a pyrochlore structure. Due to their good thermomechanical characteristics, compositions such as $\text{Gd}_2\text{Zr}_2\text{O}_7$, and $(\text{La}_{1-x}\text{Gd}_x)_2\text{Zr}_2\text{O}_7$ are recommended as thermal barrier coating materials [1–6], which is one of the promising applications of pyrochlores. Having high chemical stability, pyrochlores are used as electrolytes for oxygen sensors for aggressive environments, such as Li-based melts [7–9]. High radiation resistance allows pyrochlores to be used as materials for the encapsulation of nuclear waste [10, 11]. Pyrochlores are also considered as promising oxygen-ion conductors for solid oxide fuel cells (SOFCs), so a large amount of work is aimed at studying the relationship between structure and transport properties [12–14].

The mechanism of disorder in pyrochlores is based on its own oxygen deficiency. Partially disordered pyrochlore phases are better ionic conductors than highly disordered fluorite materials of the same composition due to lower activation energies (E_A) for the migration of oxygen ions. For example, E_A is significantly lower in the pyrochlore-type defective gadolinium zirconate $\text{Gd}_2\text{Zr}_2\text{O}_7$ than in its fluorite-type analogue [15]. The pyrochlore crystal structure can be derived from the fluorite structure by doubling the unit cell, removing one out of every eight anions, and placing the cations and anions at four crystallographically nonequivalent positions. Using the setup of Tabira et al. [16], the A cation is in the 8-coordinated 16c positions and the B cation is in the 6-coordinated 16d positions (Wyckoff notation). The anions are distributed between two 4-coordinated positions O(48f) and O(8b). One 4-coordinate position O(8b) is free. A decrease in the lanthanide radius in $\text{Ln}_2\text{Zr}_2\text{O}_7$ leads to a gradual occupation of this position [17–19].

Previously, using atomistic modeling, it was proposed that the most stable intrinsic defect in pyrochlores is the oxygen Frenkel pair, consisting of a vacant O(48f) site and an interstitial ion located at the O(8a) position, and that the diffusion of

oxygen ions occurs due to hopping between O(48f) sites [20–24]. Thus, the oxygen conductivity in disordered pyrochlores depends significantly on the energy of formation of this type of defect. The presence of disorder in the cationic sublattice leads to a decrease in this energy value, since cationic disorder increases the similarity between nonequivalent oxygen sites and thereby contributes to the formation of defects in the oxygen sublattice [21, 24–28].

Among the zirconate pyrochlore series, $\text{Gd}_2\text{Zr}_2\text{O}_7$ has the greatest internal disorder [29], demonstrating high conductivity values of about $0.01 \text{ S}\cdot\text{cm}^{-1}$ at fairly high temperatures $\sim 900 \text{ }^\circ\text{C}$ [30–34]. However, the most disordered pyrochlores are not necessarily the best conductors of oxygen ions and exhibit systematically higher E_A for oxygen ion migration. Due to the increase in E_A , the conductivity at lower temperatures drops significantly. Thus, the highest conductivity values are usually achieved in partially disordered pyrochlores. This statement can be traced using the example of isovalent doping, when disorder is regulated by varying the ratio of the ionic radii of A and B cations. Doping Gd in $\text{Gd}_{2-x}\text{M}_x\text{Zr}_2\text{O}_7$ with larger La or Nd leads to a decrease in the E_A and the peak conductivity value reaches $\text{Gd}_{1.7}\text{La}_{0.3}\text{Zr}_2\text{O}_7$ and equimolar $\text{GdNdZr}_2\text{O}_7$, respectively [30, 31]. In $\text{Gd}_2\text{Sn}_{2-x}\text{Zr}_x\text{O}_7$, the conductivity increases with the concentration of Zr which is slightly larger than Sn although the E_A changes slightly [32]. For $\text{Gd}_2\text{Zr}_{2-x}\text{Ti}_x\text{O}_7$ pyrochlores, a decrease in the E_A is observed with increasing content of smaller Ti as the structure becomes more ordered [33]. A decrease in the average size of cations in the A-position, the replacement of Gd by smaller lanthanides such as Dy, Y or Er, increases the intrinsic structural disorder of $\text{Gd}_2\text{Zr}_2\text{O}_7$ and induces the pyrochlore-fluorite phase transition [34]. In this case, the replacement of Gd with larger cations, such as Sm, Nd or La, orders the pyrochlore structure.

Heterovalent acceptor-type doping is a strategy to significantly increase oxygen deficiency, as well as cationic disorder. Those dopants that cause the least deformation of the crystal lattice of the base material have the lowest dissolution energy and give the highest conductivity of materials, therefore the replacement of lanthanides with Ca in $\text{Ln}_2\text{Zr}_2\text{O}_7$ pyrochlores is usually most advantageous [21, 23, 35]. Against the background of the fairly well-studied mechanism of acceptor doping in both ordered $\text{La}_2\text{Zr}_2\text{O}_7$ [23, 36–43] and noticeably disordered $\text{Gd}_2\text{Zr}_2\text{O}_7$ [7–9, 44–46, 48], moderately disordered $\text{Sm}_2\text{Zr}_2\text{O}_7$ has been less studied, although it should combine the advantages of the previous two. Liu et al. [49–51] even made attempts to take advantage of equimolar $\text{GdSm}_{1-x}\text{M}_x\text{Zr}_2\text{O}_{7-\delta}$ ($\text{M} = \text{Ca}, \text{Mg}$) compositions. Without the dopant, the conductivity reaches $0.001 \text{ S}\cdot\text{cm}^{-1}$ at $600 \text{ }^\circ\text{C}$, but decreases for both dopants due to the increasing E_A . Sm and Ca have very similar ionic radii [52]. Despite this, it was reported that the solubility of Ca in $\text{Sm}_2\text{Zr}_2\text{O}_7$ is low [46, 53], although the mentioned authors used a solid-phase synthesis method. The conductivity of the materials at $600 \text{ }^\circ\text{C}$ is about $4\cdot 10^{-4} \text{ S}\cdot\text{cm}^{-1}$ and decreases slightly with increasing concentration of Ca dopant, and E_A also increase. Our study reveals a noticeable increase in conductivity at low (2.5 at. %) Ca dopant concentrations in $\text{Sm}_{2-x}\text{Ca}_x\text{Zr}_2\text{O}_{7-\delta}$ without a significant effect on the E_A .

The microstructure of the samples also affects the level of conductivity; the electrolyte materials must be of high density and approximately equal grain sizes so that the processes occurring in the bulk and at the grain boundary are more understandable. For example, in [46], $\text{Sm}_{2-x}\text{Ca}_x\text{Zr}_2\text{O}_{7-\delta}$ ceramics obtained by mechanical activation have a relative density of 89 – 92.6 % and a strong variation in grain sizes from 100–300 nm to several microns is recorded. In work [47], we synthesized the proton conductor $\text{La}_{1-x}\text{Sr}_x\text{ScO}_{3-\delta}$ by the following methods: solid state reaction, combustion and co-deposition. It has been shown that only the combustion method leads to the production of highly dispersed powders with particle sizes up to 100 nm. As a result, this method proved to be the most effective in obtaining a given microstructure of ceramic samples. Hence, a high density relative to the theoretical one ($> 95 \%$) and a uniform size distribution of ceramic grains have been achieved. The influence of the defect formation model and grain boundary effects on the conductivity of materials is also discussed in detail. This work is devoted to the synthesis of nanostructured samarium zirconate powders, the production of dense ceramics and the study of its physico-chemical properties.

2. Experimental

2.1. Sample preparation

The citrate-nitrate combustion technique was used for the preparation of $\text{Sm}_{2-x}\text{Ca}_x\text{Zr}_2\text{O}_{7-\delta}$ (where $x = 0; 0.05; 0.075; 0.01; 0.125$ and 0.15 , then SZ; SCZ5, SCZ7.5, SCZ10, SCZ12.5 SCZ15, total – SCZ) samples. Samarium oxide Sm_2O_3 , calcium carbonate CaCO_3 and zirconium oxynitrate $\text{ZrO}(\text{NO}_3)_2$, all high purity reagents, were used as precursors. To achieve high homogenization of oxide-forming cations, a solution mixing stage was carried out. For this purpose, a solution of $\text{ZrO}(\text{NO}_3)_2$ with the precise concentration was prepared. The calculated Sm_2O_3 weights, taking into account the mass loss coefficient during calcination and the drained CaCO_3 in a proportional amount of CaO, were transferred to a nitrate solution when interacting with nitric acid (high purity reagent) and an aliquot of zirconium oxynitrate solution was added. Further, citric acid (high purity reagent) was added to the solution in a ratio of 3/1 to the mass of the resulting oxide and evaporated at a temperature of $130 \text{ }^\circ\text{C}$ until the combustion reaction took place. The obtained powders were annealed at a temperature of $800 \text{ }^\circ\text{C}$ (1 hours) to remove the organic residues and carbon black. After this, additional homogenization of the powdered mixture was carried out in an isopropyl alcohol medium using a PM 100 (Retch GmbH, Haan, Germany) planetary ball mill for 1 hour (350 rpm). The dried powders of all compositions

were subjected to preliminary synthesis at a temperature of 1100 °C for 2 hours. After that, the samples were formed by isostatic pressing at 600 MPa and then sintered in air at 1600 °C for 5 hours in a backfill of the appropriate composition.

2.2. Exposure to various atmospheres

The humidity of gas passing through the samples was set using a thermostated vessel with water of a room temperature. The dry atmosphere was reached by a gas passage through synthetic zeolites.

The samples were calcined before analyzes at 1000 °C for 20 hours when blown with dry air, and also at 600 °C without holding when blown in laboratory air. The stability to reduction was checked by holding samples at 850 °C for 250 hours in a flow of dry hydrogen.

2.3. X-ray diffraction

The phase composition of the samples was characterized by a X-ray diffractometer TDM-20 (Tongda, Hong Kong, China) with $\text{Cu K}\alpha$ ($\lambda = 1.5418 \text{ \AA}$) radiation with step scan 0.0095° ($2\theta = 12 - 135^\circ$, exposure 1.3 s). The cubic lattice parameters were refined from XRD patterns by Le Bail method. The initial symmetry group and lattice parameters were taken for $\text{Sm}_2\text{Zr}_2\text{O}_7$ (ICSD 261415).

2.4. Electron microscopy

The surface morphology and cross section of the ceramics were studied by scanning electron microscopy (SEM). The cross sections were performed by grinding and polishing samples with water-based diamond abrasives. SEM images of the cross sections were obtained on a microscope JSM-6510 LV (JEOL, Tokyo, Japan), and the elemental distribution was studied by energy-dispersive X-ray (EDX) spectroscopy using an Inca X-MAX spectrometer system (Oxford Instruments, Abingdon, UK).

In order to investigate microstructure and elemental content of selected samples at subgrain scale, transmission electron microscopy (TEM) study was carried out using OSIRIS TEM (Thermo Fisher Scientific, Waltham, USA) equipped by high-angle annular dark-field (HAADF) detector (Fischione, Corporate Circle, Export, USA) and energy-dispersive spectrometer Super-X EDXS (Bruker, Billerica, USA). TEM data processing was performed in Digital Micrograph 3.4 (Gatan Inc., Pleasanton, USA) and Esprit (Bruker, Billerica, USA) software. The cross-sectional TEM samples were prepared by means of focused ion beam FIB lift-out technique using Scios Dual Beam (Thermo Fisher Scientific, Waltham, USA).

2.5. Dilatometry

Measurements of the thermal expansion were carried out in a quartz cell using the Tesatronic TT-80 (TESA, Renens, Switzerland) meter with a high-precision measuring probe GT 21HP (TESA, Renens, Switzerland). Before the experiment, the cell was calibrated to deduct the contribution of quartz's own expansion. Thermal expansion measurements were implemented during heating/cooling (speed 120 °C/hour) in the temperature range of 50 – 900 °C in moist ($\text{pH}_2\text{O} = 2.8 \text{ kPa}$) and dry ($\text{pH}_2\text{O} < 0.1 \text{ kPa}$) air. Thermal expansion coefficients (TEC) were calculated from the linear sections of the $\Delta L/L_0 - T$ dependencies. Humidity induced chemical expansion was measured during the transition from dry atmosphere ($\text{pH}_2\text{O} < 0.1 \text{ kPa}$) to humidified atmospheres ($\text{pH}_2\text{O} = 0.6$ and 2.8 kPa) at isothermal exposure ($T = 600 \text{ }^\circ\text{C}$).

2.6. DC and AC conductivity

The total electrical conductivity of ceramic samples was measured by a four-probe DC method using a RM3545-02 (Hioki, Nagano, Japan) ohmmeter. The prepared samples had the geometry of rectangular bars with dimensions of about $12 \times 3 \times 3 \text{ mm}$. Pt paste and wires were used as electrodes, which was baked to the faces of the samples at a temperature of 1100 °C during 1 hour. The measurements were carried out in the temperature range of 400 – 900 °C in heating/cooling modes in increments of 20 °C. An isothermal exposure at each temperature until the equilibrium resistance values were reached.

The electrochemical impedance spectroscopy (EIS) was applied in a two-probe mode. The samples were tablets with a diameter of 10 mm and a thickness of 1 mm. Ag paste was applied by painting in the form of a 5 by 5 mm area and baked at 800 °C for 2 hours. In order to reduce the polarization resistance of the electrodes, they were impregnated with a solution of cerium and terbium nitrates and slowly heated to 800 °C at a rate of 20 °C/hour, according to the method of [54]. The measurements were implemented on a SP-200 (Bio-Logic, Seyssinet-Pariset, France) equipment in the temperature range 300 – 400 °C with the step of 25 °C, and in the frequency range 3 MHz – 0.1 Hz at an AC voltage amplitude of 100 mV. The distribution of relaxation times (DRT) technique was employed for the analysis of the spectra [55]. The Tikhonov regularization method was applied [56]. The accuracy of the selection of the regularization coefficient was based on a comparison of the DRT functions of the experimental spectrum and the simulated DRT spectrum from the equivalent circuit [57].

3. Results and discussion

3.1. Crystal structure and morphology

Figure A1 shows typical XRD patterns for SCZ samples. Fig. 1 shows the values of unit cell parameters for samples of two series, as well as literature data. Samples of the first series were calcined in dry air at 1000 °C for 20 hours. Samples of the second series were calcined in laboratory air at 600 °C without holding. One can see a noticeable scatter of parameters for the two series, as well as for the literature data. Thus, heat treatment conditions affect the value of the unit cell parameter. It is known that the formation of the pyrochlore phase passes through the fluorite phase, therefore the unit cell parameter depends on the annealing temperature [58]. First, the synthesis method influences. In all the cited literature references, except for [59], the materials were obtained by the solid-phase synthesis method. Further, the maximum annealing temperature, cooling rate and atmosphere influence. One can compare the annealing conditions using the example of SZ material: in [60], double calcination was used at 1400 °C for 10 hours; in [61], samples were sintered at 1400 – 1600 °C for 8 hours; in [53], there was annealing at 1700 °C for 10 hours; and in [46], there was annealing at 1600 °C for 4 – 10 hours. In [59], a solution citrate synthesis method was used with final calcination only at 800 °C, although one should expect a much higher combustion temperature for a mixture of citrates and ethylene glycol.

In this work, we chose the method of slow combustion (about 12 hours at a temperature of 130 °C) with the addition of three times the amount of citric acid in relation to the mass of the resulting oxide. This method allows us to obtain powders having the specific surface area of after annealing at 800 °C amounted to 80.000 – 85.000 cm²/cm³ which defines their nano-dimensional character even at this stage of synthesis. At the same time, the powders have already been heat treated, which inevitably led to particle agglomeration. It should be borne in mind that the granulometric composition of powders without heat treatment does not make sense to evaluate due to the presence of additional components, organic residues, and/or the presence of an oxide-forming mixture still in the salt state. The obtained highly dispersed powders led to the production of high-density ceramics (more than 95 % relative to the theoretical one) with a uniform grain size distribution. The final sintering was implemented at 1600 °C for 5 hours. Synthesis and heat treatment conditions primarily affect the concentration of antistructural defects such as Zr in the Sm sublattice and, conversely, Sm in the Zr sublattice [24, 26, 27]. This can also affect the distribution of the dopant over both sublattices.

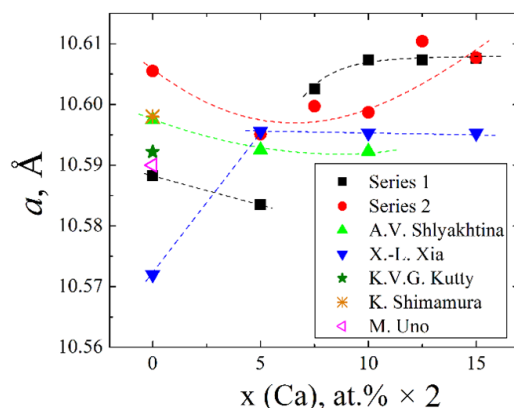


FIG. 1. Cubic unit cell parameter of SCZ as a function of dopant concentration. Series 1 means samples pre-calcined at 1000 °C for 20 hours in dry air, Series 2 means samples pre-calcined at 600 °C in laboratory air without holding. Literature results from papers by Shlyakhtina et al. [46], Xia et al. [53], Govindan Kutty et al. [60], Shimamura et al. [61] and Uno et al. [59] are also given.

Figure 2 shows cross sectional images of SCZ ceramic samples. The relative density of SCZ5-SCZ7.5-SCZ10 ceramics varies about 94 %, whereas in samples SCZ12.5 and SCZ15 the density slightly decreases to 91 %. According to the EDX data analysis, all elements in SCZ5-SCZ12.5 are distributed uniformly. Whereas, a clear Ca enrichment is observed in the local areas of SCZ15 sample (Fig. 2c). The presence of such areas indicates the formation of second phase Ca-enriched precipitates. These precipitates have apparently low number density, which is below the detection limit of XRD.

3.2. Thermal expansion

The results of dilatometric measurements of SCZ ceramic samples are presented in Fig. 3. The initial dilatometric dependences are shown in Fig. A2. Average TEC values for Ca-doped samarium zirconates is about $11.5 \cdot 10^{-6} \text{ K}^{-1}$, which is higher than for the conventional oxide-ion electrolyte – YSZ ($10.4 \cdot 10^{-6} \text{ K}^{-1}$ [62]). It is known that with a decrease in the ionic radius of the lanthanide in Ln₂Zr₂O₇, the TEC values increase [60, 61]. A higher TEC values make it possible to use samarium zirconates as materials of thermal barrier coatings (TBCs) [1–6] which is not available for

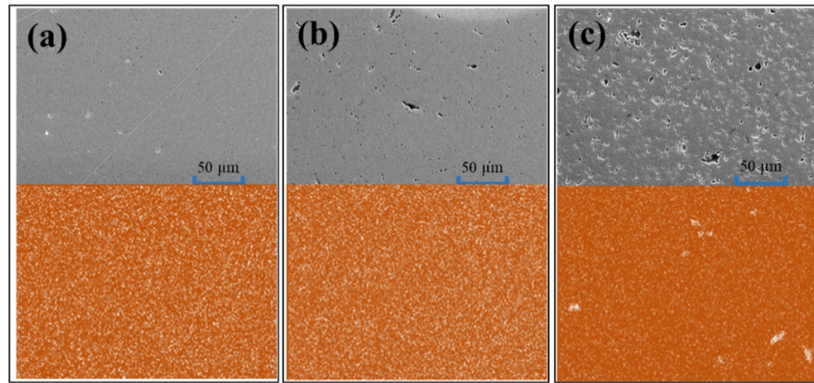


FIG. 2. Cross-sectional SEM images of SCZ5 (a), SCZ10 (b) and SCZ15 (c) along with EDX maps of Ca distribution

some other rare earth element zirconates [63]. Also, higher TEC values make the materials more compatible with SOFC electrode materials and similar electrochemical devices [64].

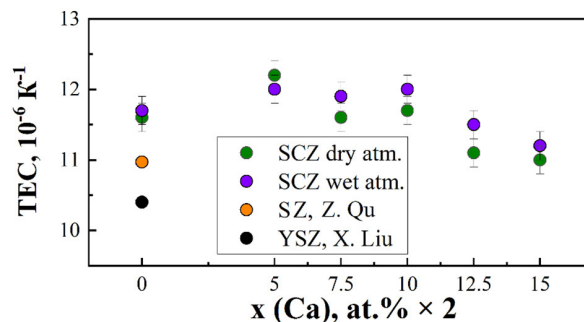


FIG. 3. Average thermal expansion coefficients (TEC) for SCZ ceramic samples obtained from dilatometry in dry ($p_{\text{H}_2\text{O}} < 0.1$ kPa) and wet ($p_{\text{H}_2\text{O}} = 2.8$ kPa) atmospheres. Our experimental data are compared with literature data for $\text{Sm}_2\text{Zr}_2\text{O}_7$ (SZ) [63] and yttria stabilized zirconia (YSZ) [62].

According to dilatometry data, thermal expansion of SCZ materials does not depend practically on air humidity, and the difference in the TEC in two atmospheres is at the error level. Under stepwise hydration, SCZ5 and SCZ10 samples experience a weak response to a change in humidity, because oxygen vacancies in samarium zirconates are stable to hydration (Fig. A3). Relaxation of chemical expansion occurs abruptly and quickly. It is possible that only partial surface hydration occurs.

3.3. Total conductivity and defects equilibrium

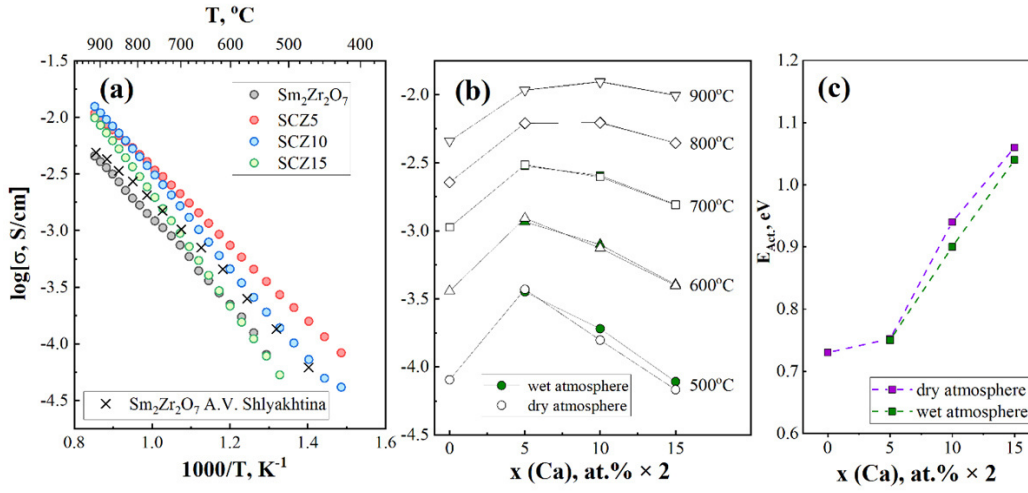
Figure 4 shows the temperature dependencies of the total conductivity for SCZ samples. SCZ5 has a systematically higher conductivity than SZ, while a further increase in Ca concentration generally leads to a decrease in conductivity. Only the conductivity of SCZ10 dominates the others in the temperature range of 800 – 900 °C. The conductivity of all doped SCZ samples is higher than that of undoped SZ at temperatures above 500 °C. Table 1 lists the apparent activation energies (E_A). SZ and SCZ5 have comparable E_A , while at higher Ca concentrations, the E_A increases markedly. In general, the increase in the E_A of materials with Ca concentration in $\text{Sm}_{2-x}\text{Ca}_x\text{Zr}_2\text{O}_{7-\delta}$ is consistent with literature results [46,53]. In our case, the conductivity of SCZ5 at relatively low temperatures of about 600 °C reaches 10^{-3} S·cm⁻¹ which is a record value in the series of oxide pyrochlores, even exceeding the conductivity of the most conducting phases based on doped $\text{Gd}_2\text{Zr}_2\text{O}_7$ [30–34,49–51].

We did not find a noticeable effect of air humidity on the conductivity of the materials studied, although some researchers have considered these materials as potential proton conductors [46,65]. The air humidity has a slightly visible effect on the conductivity only at temperatures below 700 °C (Fig. 4b). It is difficult to estimate the level of proton conductivity in samarium zirconates according to our data, while we assume that the bulk proton conductivity is very small, and these materials can be successfully considered as oxygen-ion conductors.

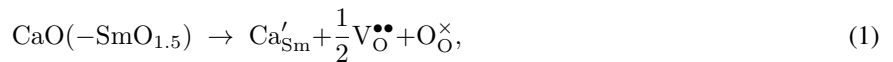
Figure 5 shows the conductivity versus p_{O_2} dependence for $\text{Sm}_{2-x}\text{Ca}_x\text{Zr}_2\text{O}_{7-\delta}$ ($x = 0.05, 0.1, 0.15$). A small effect of p_{O_2} on the conductivity is seen at all temperatures studied. Analogous dependencies can be found in the literature for $\text{Gd}_{2-x}\text{M}_x\text{Zr}_2\text{O}_{7-\delta}$ ($M = \text{Li}, \text{Mg}$) systems [8,9]. Taken into account the specifics of disorder in the studied pyrochlore-like

TABLE 1. Apparent activation energies of total conductivity (E_{Tot}) for $\text{Sm}_{2-x}\text{Ca}_x\text{Zr}_2\text{O}_{7-\delta}$ ($x = 0, 0.05, 0.1, 0.15$)

Composition	Activation energy of total conductivity (E_{Tot}), eV	
	Dry air, $p_{\text{H}_2\text{O}} < 0.1$ kPa	Wet air, $p_{\text{H}_2\text{O}} = 2.8$ kPa
$\text{Sm}_2\text{Zr}_2\text{O}_{7-\delta}$	0.73	—
$\text{Sm}_{1.95}\text{Ca}_{0.05}\text{Zr}_2\text{O}_{6.975}$	0.75	0.75
$\text{Sm}_{1.9}\text{Ca}_{0.1}\text{Zr}_2\text{O}_{6.95}$	0.94	0.90
$\text{Sm}_{1.85}\text{Ca}_{0.15}\text{Zr}_2\text{O}_{6.925}$	1.06	1.04

FIG. 4. The Arrhenius plot of total conductivity for SCZ samples in dry air (a), isothermal dependences of total conductivity on Ca dopant concentration at different temperatures in dry and wet air (b) and apparent activation energies of total conductivity (c). Conductivity values for $\text{Sm}_2\text{Zr}_2\text{O}_7$ according to Shlyakhtina et al. [46] data are also given.

materials [22,25], several processes affecting the concentration of defects can take place. First, there are oxygen vacancies formed due to doping:



where Ca'_{Sm} are Ca atoms in Sm positions, $\text{V}_{\text{O}}^{\bullet\bullet}$ are oxygen vacancies, and $\text{O}_{\text{O}}^{\times}$ are oxygen atoms in regular lattice sites. With an increase in temperature, the probability of the formation of anti-Frenkel defects increases according to the equation:



where O_{O}'' is the interstitial positions of oxygen. Oxygen vacancies formed by both (1) and (2) reactions can interact with the molecular oxygen:



This creates two electron holes h^{\bullet} . In the case of the dominance of reaction (3), the conductivity should be a linear function of $p\text{O}_2^{1/4}$. However, at 800 and 700 °C, the conductivity is linearized only in the plots $\sigma = f(p\text{O}_2^{-1/6})$ (Fig. 5d), while the $\sigma = f(p\text{O}_2^{1/4})$ dependence can be found only below 600 °C (Fig. 5e). This indicates the occurrence of several competing processes at temperatures above 700 °C. One of the side processes can be a change in the number of oxygen vacancies, for example, during reaction (2). However, Hagiwara et al. [66] showed by XRD that the occupancy of the O(8a) position in $\text{Eu}_2\text{Zr}_2\text{O}_7$ at 900 °C is even less than that at room temperature. Shehu [67] also showed by ND method a slight decrease in the occupancy of the O(8a) position at a temperature of 800 °C relative to room temperature for $\text{Nd}_{2-x}\text{Ca}_x\text{Zr}_2\text{O}_{7-\delta}$.

In fact, the O(8a) site in the pyrochlore structure is often called interstitial, although this is not exactly like that. This position is free in ideal pyrochlore, for example in $\text{La}_2\text{Zr}_2\text{O}_7$ [66]. With a decrease in the ionic radius of the lanthanide, the probability of the formation of a split oxygen vacancy increases, when the oxygen atom is displaced from the O(48f)

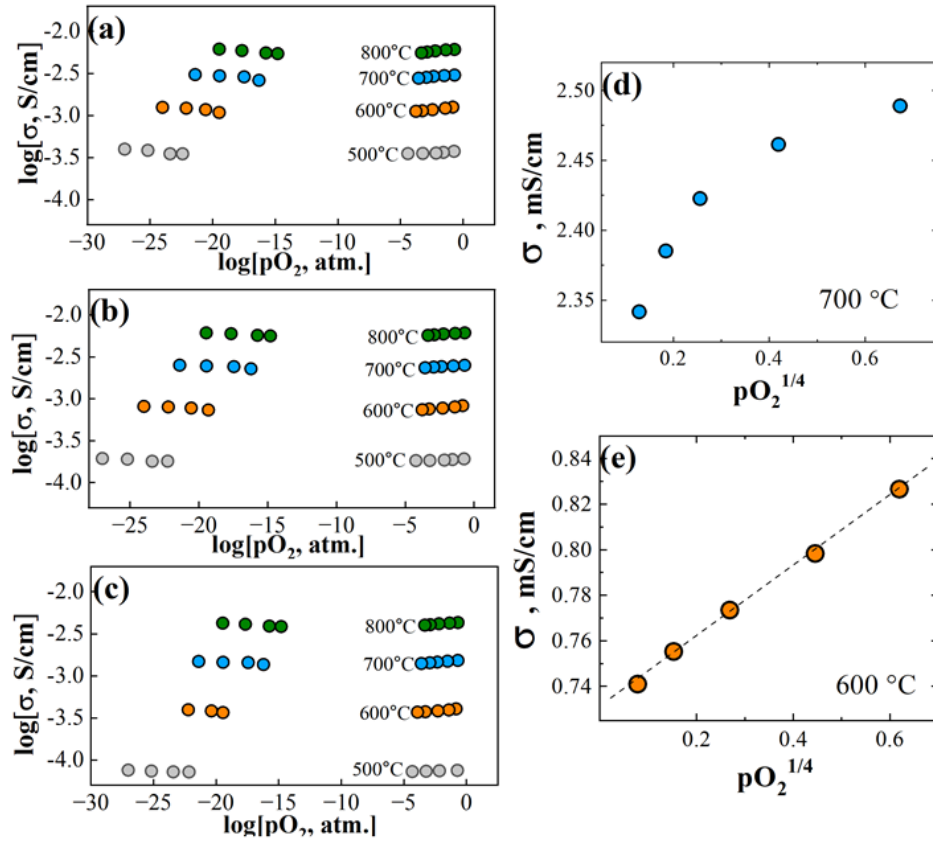


FIG. 5. Total conductivities of SCZ as a functions of the $p\text{O}_2$ in wet atmosphere for SCZ5 (a), SCZ10 (b), SCZ15 (c). Dependences of total conductivity as a function of $p\text{O}_2^{1/4}$ for SCZ10 at 700 °C (d) and 600 °C (e).

site towards the O(8a) site, and as a result, the interstitial oxygen atom is between two vacancies in the O(48f) sites [22]. Thus, the oxygen atom never occupies O(8a) site, but only approaches it. If the migration of an “ordinary” oxygen vacancy (at O(48f) or O(8b) sites) is preferable in the crystallographic direction (100), then the split vacancy migrates on average in the direction [111] [22]. In fact, hole migration is also anisotropic and passes along the [110] direction through the Zr and O(48f) positions [19]. This migration direction is perpendicular to the migration direction of ordinary oxygen vacancies. We can assume that the dependence of the total conductivity of SCZ on $p\text{O}_2$ at temperatures above 600 °C is a function not only of the concentration of electron holes but also of the concentration ratio between ordinary and split oxygen vacancies as well as the difference in their mobility due to anisotropic migration.

In contrast to the O(48f) sites, oxygen vacancies in the O(8b) site have a high energy of both formation and migration, as indicated by a number of theoretical studies [20–23]. The oxygen atom O(8b) is surrounded exclusively by A cations. It is to be expected that when the Ca dopant occupies a position in the A sublattice it contributes to the formation of an oxygen vacancy in its immediate environment, including in the O(8b) position. It is worth noting that Shehu [67] did not observe an appreciable deviation from 1 in the occupancy of O(8b) positions in $\text{Nd}_{2-x}\text{Ca}_x\text{Zr}_2\text{O}_{7-\delta}$ by ND even at a very high dopant concentration ($x = 0.5$). The pair distribution function (PDF) analysis showed a decrease in the average coordination number in the Nd sublattice, but its increase for the Zr sublattice [67]. Thus, the coordination environment of all cations changes [28, 67].

It can be seen that the Ca dopant concentration has a progressive effect on disordering in SCZ, in accordance with the ideas developed by van Dijk et al. [15, 20]. Formally, the total number of oxygen vacancies increases with increasing Ca concentration which increases the pre-exponential factor of conductivity, but the vacancies are localized in unfavorable crystallographic positions which complicates their migration and increases the activation energy of conductivity.

The presence of a weak but noticeable dependence of conductivity on $p\text{O}_2$ in reducing atmospheres confirms the evolution of the number of oxygen vacancies in materials when oxygen leaves the interstitial positions of the material lattice, interacting with hydrogen:



As a result, electrons e' are generated for charge compensation, which leads to a slight increase in conductivity. These electrons are probably localized and may be the reason for the partial reduction of Sm^{3+} to Sm^{2+} . This behavior

is typical for both undoped [68] and Ca-doped samarium zirconate [46]. We additionally tested the stability of SCZ5 sample to reduction through long-term calcination in an H_2 atmosphere (Fig. A4). No signs of new phases were found, but the unit cell parameter increases noticeably from 10.583 Å after calcination in dry air at 1000 °C for 20 hours to 10.618 Å after calcination in dry hydrogen at 850 °C for 250 hours. This may be caused by an increase in the ionic radius of samarium from Sm^{3+} ($r = 1.08$ Å, CN = 8) to Sm^{2+} ($r = 1.27$ Å, CN = 8) [52].

The question remains for our case: why does a low concentration of Ca dopant (2.5 %) in $Sm_2Zr_2O_7$ increase the conductivity of the material and does not influence on the E_A . It differs from the results of Xia et al. [53], who received a clear negative reaction? We exclude the influence of sample density, since high-density samples were obtained in both our and Xia et al. [53] works. It is more likely that the difference is due to the specific features of the local structure of pyrochlores where disorder in the anion and cation sublattices is closely related [21, 24–28]. The dopant causes a change in the coordination environment in both A and B sublattices [28, 67]. Van Dijk et al. [15, 20] argue that the oxygen vacancy has the lowest energy when passing between O(48f) positions near the O(8a) position which is essentially identical to the mechanism of migration of a split vacancy. Probably, disruption of such optimal pathways causes a decrease in the mobility of oxygen ions. Unlike the works [46, 53], where the SCZ materials were obtained by a solid-phase reaction, in our case, a solution synthesis method with a precursor combustion stage was used. This condition affects the proportion of antistructural defects, as well as the distribution of Ca dopant over the A and B sublattices. It should be expected that the stages of high-temperature combustion and subsequent high-temperature annealing contribute to greater pyrochlore ordering and the formation of a smaller number of antisite pairs, and the solution stage of synthesis promotes the localization of the Ca dopant in the A sublattice. The effect of annealing temperature on the degree of ordering of the pyrochlore structure was shown in the paper [58]. Thus, a small dopant concentration apparently promotes the formation of an increased number of “free” oxygen vacancies and the favorable migration paths are not interrupted. An increased concentration of the dopant causes a violation of the optimal coordination of A and B cations which leads to high energy consumption for the migration of oxygen ions. We believe that an ND study could directly show the occupancy of oxygen positions, unfortunately, ND is difficult for Sm due to its high neutron absorption cross sections. According to ND data for $Nd_{2-x}Ca_xZr_2O_{7-\delta}$ [67], the occupancy of the O(8a) position increases noticeably with the dopant concentration and slightly decreases when the material is heated to 800 °C. In addition, Shehu [67] also found a clear increase in the activation energy of conductivity with increasing dopant concentration.

The above allows us to make two general assumptions:

- (1) The migration of a split oxygen vacancy, despite the low energy barrier, is disrupted at high defect concentrations. This should also be related to the occupancy of O(8a) positions. A significant change in the coordination environment of cations disrupts the optimal migration routes of oxygen ions.
- (2) If the localization of the Ca dopant is preferable in the A position of $Sm_2Zr_2O_7$, and accordingly, the effect only on coordination in the A sublattice occurs, then this contributes to the formation of energetically favorable oxygen vacancies with low migration activation energy. If part of the dopant ends up in the B position, this will lead to a more significant mismatch of ionic radii between Ca and Zr. The oxygen ion, when migrating, will need to overcome a higher energy barrier in order to change the local coordination of the B cation.

3.4. Grains boundaries state

Since polycrystalline ceramics are under study, one might suspect that the trends in material conductivity discussed above are not related to the equilibrium model of defects in the grain volume, but to the contribution of grain boundary (GB) conductivity. EIS was used to clarify this. Unfortunately, EIS measurements were carried out at lower temperatures compared to the 4-probe method in order to be able to observe the high-frequency response of the impedance spectrum. Fig. 6a shows typical impedance spectra at 350 °C for ceramic samples SCZ5 and SCZ10. A large semicircle emerging from the origin, as well as an additional semicircle, are clearly visible. It should be noted that the analysis may complicate the response from the electrode, so we achieved the lowest resistance of the electrodes by activating them, as was indicated in the experimental section. DRT analysis was used to separate the contributions of relaxation processes on the impedance spectra. Fig. 6b shows the results of DRT analysis at 350 °C. High-frequency processes with characteristic relaxation times of $\sim 10^{-5.5}$ s and capacitances of $\sim 10^{-11}$ F correspond to the bulk resistance. Low-frequency processes with relaxation times of about 10^{-4} s and capacitances of $\sim 10^{-9}$ F can correspond to the GB resistance. The relaxation times of the GB process for SCZ10 are systematically slightly longer than for SCZ5 for all temperatures studied. At the same time, the relaxation times of the bulk process are close for the two samples.

It is worth noting that the resistance of the GB process observed from the impedance spectra is apparent and, before calculating the specific values, it is lower than the bulk one for the both samples. Under the approximation of equality of dielectric constants of bulk and GB [69], the specific GB resistance can be expressed through the ratio of process capacitances:

$$R_{gb}^* = R_{gb} \cdot \frac{C_{gb}}{C_{bulk}}. \quad (5)$$

After recalculation, the specific GB conductivity turns out to be noticeably lower than the bulk resistance.

Figure 6c shows the temperature dependences of the bulk and GB conductivity. The dependences of the bulk conductivity are in good agreement with the higher temperature region of conductivity determined by the 4-probe method (Fig. 4a). More importantly, the apparent activation energies of grain volume conductivity are in agreement with higher temperature data which makes our previous discussions about the equilibrium model of defects in the materials under study valid.

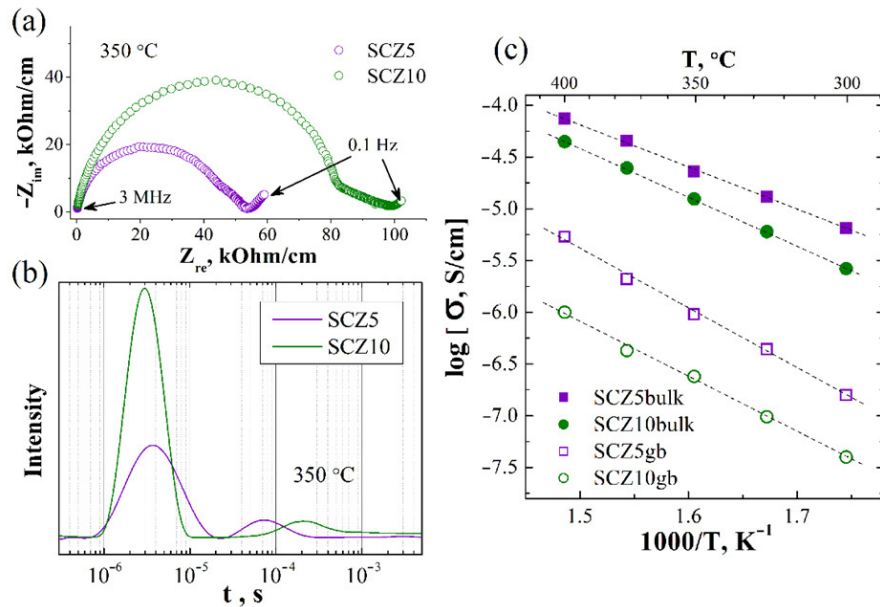


FIG. 6. (a) EIS results, (b) DRT spectra and (c) temperature dependencies of bulk and grain boundaries conductivities of SCZ5 and SCZ10 ceramics

To directly confirm or deny formation of single pyrochlore structure at sub-grain scale, we investigate the GB chemistry for SCZ5 and SCZ10 samples. Fig. 7 shows typical bright-field TEM (BF TEM) images and corresponding selected area diffraction (SAED) patterns of SCZ5 and SCZ10 samples. Both samples contained no visible precipitates. In addition, SAED patterns of the SCZ5 and the SCZ10 samples, clearly demonstrate that the local crystal structure of both samples fully matches the cubic phase of $\text{Sm}_2\text{Zr}_2\text{O}_7$, in the PDF-2 database (ICSD 261415) as follows: the space group $Fd\bar{3}m$ (227).

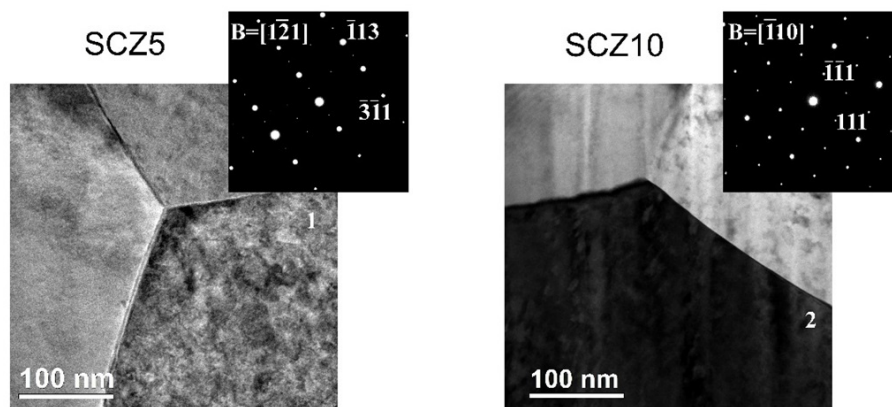


FIG. 7. BF TEM images and corresponding SAED patterns of SCZ5 and SCZ10 ceramics cross-sections in the triple junction area

Figure 8 shows the element concentration profiles across the GB for samples SCZ5 and SCZ10 which indicate a uniform distribution of all elements. This contrasts with the results for $\text{La}_{2-x}\text{Ca}_x\text{Zr}_2\text{O}_{7-\delta}$ which show clear segregation of the Ca dopant to the GB [43]. Fig. A5 provides the EDX compositional maps of SCZ5 and SCZ10 samples obtained in the triple junction region using the scanning transmission electron microscopy regime (STEM-EDX). Based on the analysis of STEM-EDX compositional maps, both samples under study contain homogeneously distributed Sm, Ca, Zr and O; neither Ca precipitates inside grains, nor Ca segregation at the GB were formed in these samples.

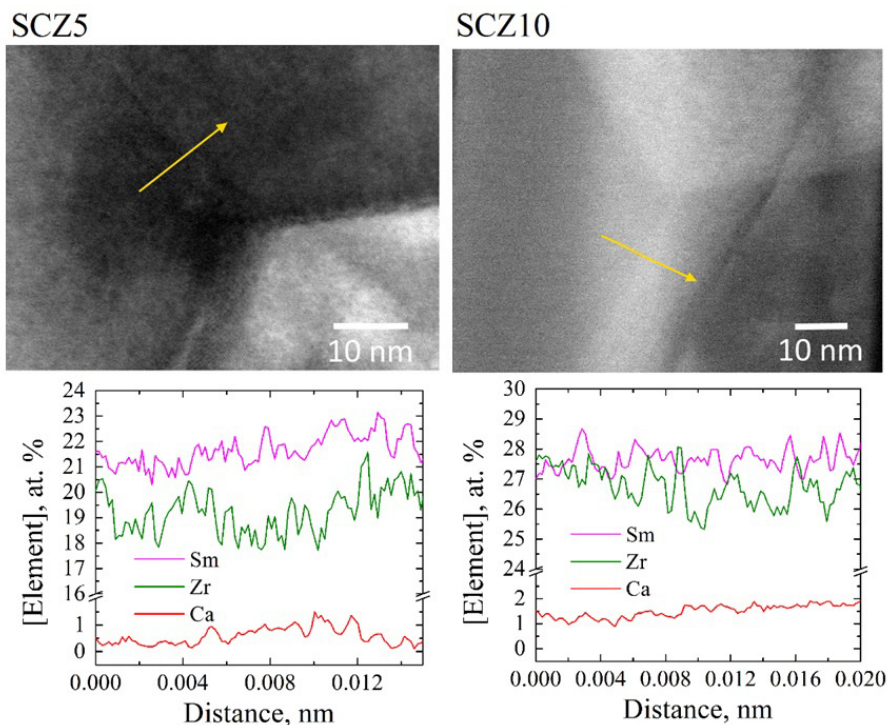


FIG. 8. HAADF images of SCZ ceramics cross-sections of in the region of the triple junction of grains with EDX-profiles across the grain boundaries

Thus, from the totality of the results, it can be expected that the conductivity trends at high temperatures are observed for both bulk and GB. Disorder at GB in pyrochlores is known to occur due to an increased number of antisite pairs, although this effect becomes less significant as cationic disorder in the bulk increases [70]. Apparently, GB, having a similar structure and composition to the bulk, exhibits a similar model of defect equilibrium and only the usual space charge is realized [69].

4. Conclusion

In this work, we obtained high-density ($> 95\%$) ceramic materials based on $\text{Sm}_2\text{Zr}_2\text{O}_7$ by combustion method. It was the use of nanoscale pre-ceramic powders that ensured the formation of a given microstructure of the studied samples. We investigated the effect of acceptor doping in $\text{Sm}_2\text{Zr}_2\text{O}_7$ with a pyrochlore structure on the model of defect formation and conductivity. The low concentration of Ca dopant in the Sm sublattice increases ionic conductivity and almost does not reduce the activation energy (E_A), which makes $\text{Sm}_{1.95}\text{Ca}_{0.05}\text{Zr}_2\text{O}_{7-\delta}$ one of the most highly conductive oxide pyrochlores. The coexistence of intrinsic and impurity defects in $\text{Sm}_{2-x}\text{Ca}_x\text{Zr}_2\text{O}_{7-\delta}$ gradually impairs ion transport at high doping levels. This leads to high E_A due to disruption of the optimal route of the oxygen ions migration which is typical for pyrochlore-type materials. Apparently, the localization of Ca predominantly in the Sm sublattice, which is a consequence of the solution synthesis of materials used, contributes to less distortion of the coordination environment of cations and an increased number of oxygen vacancies, simultaneously. This leads to an increase in conductivity without negatively affecting the E_A . Also, the influence of grain boundaries (GB) on the conductivity was tested using impedance spectroscopy. Transmission electron microscopy (TEM) shows the purity of the GB, so it is only the space charge that causes the reduced conductivity of the GB. $\text{Sm}_{1.95}\text{Ca}_{0.05}\text{Zr}_2\text{O}_{7-\delta}$ has been shown to have good chemical stability and a coefficient of thermal expansion (TEC) of 12 ppm K^{-1} which is higher than YSZ and provides better compatibility with electrode materials. This allows it to be used as a highly stable oxygen electrolyte in electrochemical devices.

Appendix

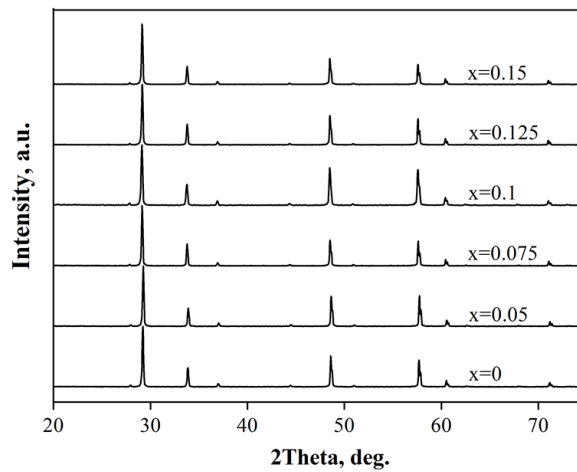


FIG. A1. XRD patterns for $\text{Sm}_{2-x}\text{Ca}_x\text{Zr}_2\text{O}_{7-\delta}$ ($x = 0; 0.05; 0.075; 0.1; 0.125; 0.15$) powders calcined at 1000°C for 20 hours in dry air

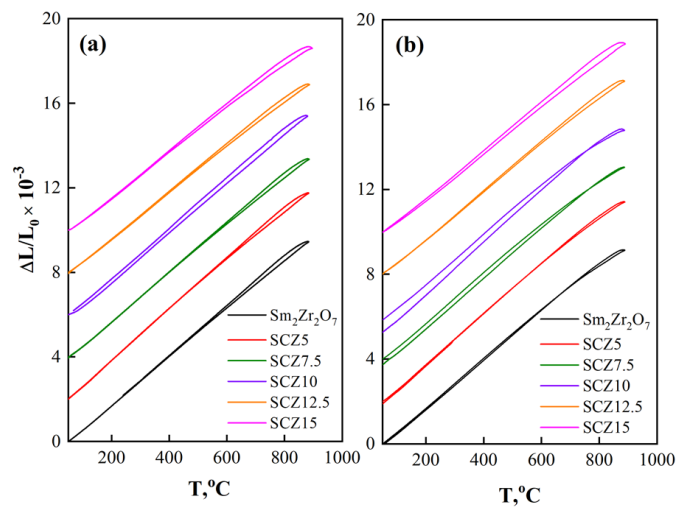


FIG. A2. Temperature dependencies of relative linear expansion and narrowing for $\text{Sm}_{2-x}\text{Ca}_x\text{Zr}_2\text{O}_{7-\delta}$ ($x = 0; 0.05; 0.075; 0.1; 0.125; 0.15$) dry (a) and wet (b) atmospheres

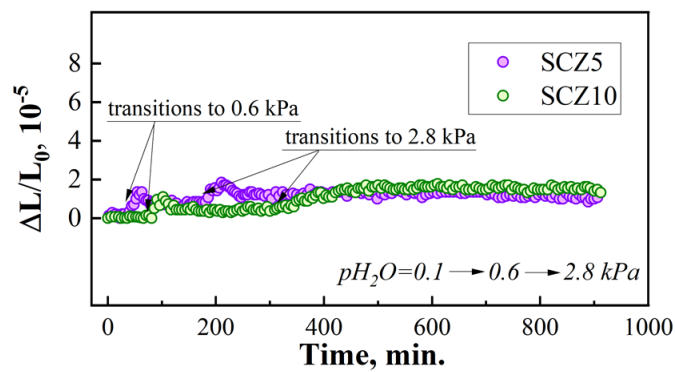


FIG. A3. Chemical expansion of SCZ5 and SCZ10 samples during the transition from a dry atmosphere ($p_{\text{H}_2\text{O}} \approx 0.1$ kPa) to humidified atmospheres ($p_{\text{H}_2\text{O}} = 0.6, 2.8$ kPa) at a constant temperature $T = 600^\circ\text{C}$

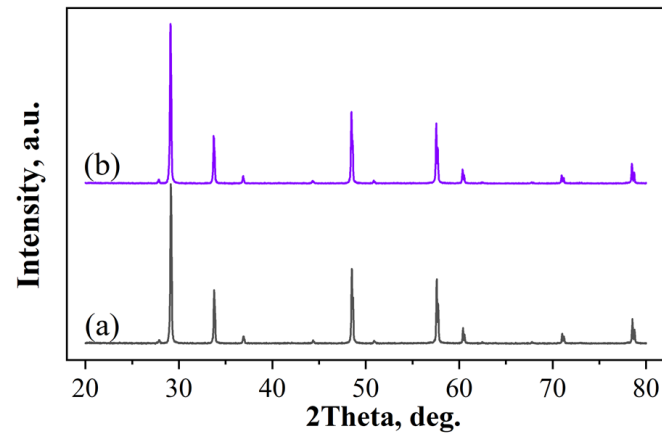


FIG. A4. XRD patterns of the SCZ5 sample before (a) and after (b) exposure in hydrogen (250 hours) at 850 °C

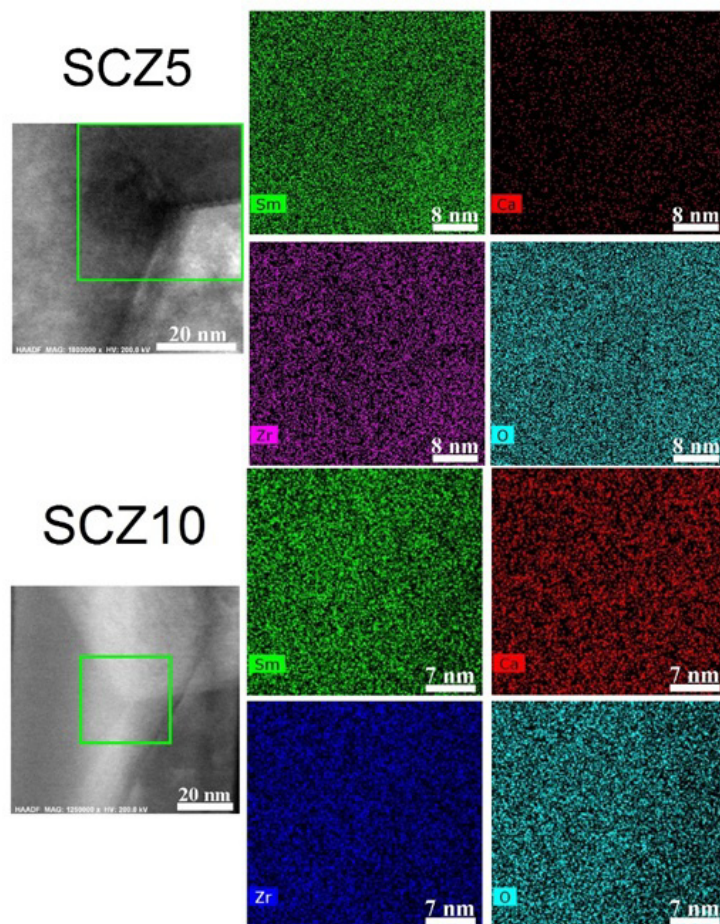


FIG. A5. HAADF and SAED cross-sectional images of SCZ5 and SCZ10 samples in the region of the triple junction of grains with STEM-EDX maps of elements distribution

References

- [1] Wu J., Wei X., Padture N.P., Klemens P.G., Gell M., Garcia E., Miranzo P., Osendi M.I. Low-Thermal-Conductivity Rare-Earth Zirconates for Potential Thermal-Barrier-Coating Applications. *J. Am. Ceram. Soc.*, 2002, **85** (12), P. 3031–3035.
- [2] Wan C.L., Pan W., Xu Q., Qin Y.X., Wang J.D., Qu Z.X., Fang M.H. Effect of point defects on the thermal transport properties of $(\text{La}_x\text{Gd}_{1-x})_2\text{Zr}_2\text{O}_7$: Experiment and theoretical model. *Phys. Rev. B*, 2006, **74** (14), 144109.
- [3] Shin D., Shin H.G., Lee H., Thermodynamic investigation of the $(\text{La}_{1-x}\text{Gd}_x)_2\text{Zr}_2\text{O}_7$ pyrochlore phase. *Calphad*, 2014, **45**, P. 27–32.
- [4] Schmitt M.P., Rai A.K., Bhattacharya R., Zhu D., Wolfe D.E. Multilayer thermal barrier coating (TBC) architectures utilizing rare earth doped YSZ and rare earth pyrochlores. *Surf. Coat. Technol.*, 2014, **251**, P. 56–63.
- [5] Zhang J., Guo X., Jung Y.G., Li L., Knapp J. Lanthanum zirconate based thermal barrier coatings: A review. *Surf. Coat. Technol.*, 2017, **323**, P. 18–29.
- [6] Mathanbabu M., Thirumalaikumarasamy D., Thirumal P., Ashokkumar M. Study on thermal, mechanical, microstructural properties and failure analyses of lanthanum zirconate based thermal barrier coatings: A review. *Mater. Today Proc.*, 2021, **46** (17), P. 7948–7954.
- [7] Anokhina I.A., Animitsa I.E., Buzina A.F., Nokhrin S.S., Zaikov Y.P., Voronin V.I., Vykhodets, V.B. Kurennykh, T.E. Kazakova, V.N. Electrical properties of Li+-substituted solid solutions based on $\text{Gd}_2\text{Zr}_2\text{O}_7$. *Russ. J. Phys. Chem. A*, 2021, **95**, P. 2426–2431.
- [8] Anokhina I.A., Animitsa I.E., Voronin V.I., Vykhodets V.B., Kurennykh T.E., Molchanova N.G., Vylkov A.I., Dedyukhin A.E., Zaikov Y.P. The structure and electrical properties of lithium doped pyrochlore $\text{Gd}_2\text{Zr}_2\text{O}_7$. *Ceram. Int.*, 2021, **47**, P. 1949–1961.
- [9] Anokhina I., Pavlenko O., Proskurnina N., Dedyukhin A., Animitsa I. The $\text{Gd}_{2-x}\text{Mg}_x\text{Zr}_2\text{O}_{7-x/2}$ Solid Solution: Ionic Conductivity and Chemical Stability in the Melt of $\text{LiCl-Li}_2\text{O}$. *Materials*, 2022, **15**, 4079.
- [10] Sickafus K.E., Mimervini L., Grimes R.W., Valdez J.A., Ishimaru M., Li F., McClellan K.J., Hartmann, T. Radiation tolerance of complex oxides. *Science*, 2000, **289** (5480), P. 748–751.
- [11] Wang S.X., Begg B.D., Wang L.M., Ewing R.C., Weber W.J., Govidan Kutty K.V. Radiation stability of gadolinium zirconate: a waste form for plutonium disposition, *J. Mater. Res.*, 1999, **14**, P. 4470–4473.
- [12] Wuensch B.J., Eberman K.W., Heremans C., Ku E.M., Onnerud P., Yeo E.M.E., Haile S.M., Stalick J.K., Jorgensen J.D. Connection between oxygen-ion conductivity of pyrochlore fuel-cell materials and structural change with composition and temperature. *Solid State Ion*, 2000, **129**, P. 111–133.
- [13] Anantharaman A.P., Dasari H.P. Potential of pyrochlore structure materials in solid oxide fuel cell applications. *Ceram. Int.*, 2021, **47**, P. 4367–4388.
- [14] Mandal B.P., Tyagi A.K. Ionic conductivity in materials with a pyrochlore structure. In *Pyrochlore Ceramics: Properties, Processing, and Applications, Elsevier Series on Advanced Ceramic Materials*, Chowdhury A., Ed., Elsevier: Amsterdam, Netherlands, 2022, **7**, P. 277–294.
- [15] Van Dijk M.P., Burggraaf A.J., Cormack A.N., Catlow C.R.A. Defect structures and migration mechanisms in oxide pyrochlores. *Solid State Ion*, 1985, **17** (2), P. 159–167.
- [16] Tabira Y., Withers R., Thompson J., Schmid S. Structured diffuse scattering as an indicator of inherent cristobalite-like displacive flexibility in the rare earth zirconate pyrochlore $\text{La}_\delta\text{Zr}_{1-\delta}\text{O}_{2-\delta/2}$, $0.49 < \delta < 0.51$. *J. Solid State Chem.*, 1999, **142**, P. 393–399.
- [17] Whittle K.R., Cranswick L.M.D., Redfern S.A.T., Swainson I.P., Lumpkin G.R. Lanthanum pyrochlores and the effect of yttrium addition in the systems $\text{La}_{2-x}\text{Y}_x\text{Zr}_2\text{O}_7$ and $\text{La}_{2-x}\text{Y}_x\text{Hf}_2\text{O}_7$. *J. Solid State Chem.*, 2009, **182**, P. 442–450.
- [18] Blanchard P.E.R., Clements R., Kennedy B.J., Ling C.D., Reynolds E., Avdeev M., Stampfl A.P.J., Zhang Z., Jang L.Y. Does local disorder occur in the pyrochlore zirconates? *Inorg. Chem.*, 2012, **51**, P. 13237–13244.
- [19] Hagiwara T., Yamamura H., Nishino H. Relationship between oxide-ion conductivity and ordering of oxygen vacancy in the $\text{Ln}_2\text{Zr}_2\text{O}_7$ (Ln = La, Nd, Eu) system having a pyrochlore composition. *IOP Conf. Series: Materials Science and Engineering*, 2011, **18**, 132003.
- [20] Van Dijk M.P., de Vries K.J., Burggraaf A.J. Oxygen ion and mixed conductivity in compounds with the fluorite and pyrochlore structure. *Solid State Ion*, 1983, **9&10**, P. 913–920.
- [21] Wilde P.J., Catlow C.R.A. Defects and diffusion in pyrochlore structured oxides. *Solid State Ion*, 1998, **112**, P. 173–183.
- [22] Pirzada M., Grimes R.W., Minervini L., Maguire J.F., Sickafus K.E. Oxygen migration in $\text{A}_2\text{B}_2\text{O}_7$ pyrochlores. *Solid State Ion*, 2001, **140**, P. 201–208.
- [23] Nyman B.J., Björketun M.E., Wahnström G. Substitutional doping and oxygen vacancies in $\text{La}_2\text{Zr}_2\text{O}_7$ pyrochlore oxide. *Solid State Ion*, 2011, **189**, P. 19–28.
- [24] Li Y., Kowalski P.M. Energetics of defects formation and oxygen migration in pyrochlore compounds from first principles calculations, *J. Nucl. Mater.*, 2018, **505**, P. 255–261.
- [25] Minervini L., Grimes R.W., Sickafus K.E. Disorder in pyrochlore oxides. *J. Am. Ceram. Soc.*, 2000, **83**, P. 1873–1878.
- [26] Shlyakhtina A.V., Savvin S.N., Levchenko A.V., Knotko A.V., Fedtke P., Busch A., Barfels T., Wienecke M., Shcherbakova L.G. Study of bulk and grain-boundary conductivity of $\text{Ln}_{2+x}\text{Hf}_{2-x}\text{O}_{7-\delta}$ (Ln = Sm–Gd, $x = 0, 0.096$) pyrochlores. *J. Electroceram.*, 2010, **24**, P. 300–307.
- [27] Li Y., Kowalski P.M., Beridze G., Birnie A.R., Finkeldei S., Bosbach D. Defect formation energies in $\text{A}_2\text{B}_2\text{O}_7$ pyrochlores. *Scr. Mater.*, 2015, **107**, P. 18–21.
- [28] Marlton F.P., Zhang Z., Zhang Y., Proffen T.E., Ling C.D., Kennedy B.J. Lattice Disorder and Oxygen Migration Pathways in Pyrochlore and Defect-Fluorite Oxides. *Chem. Mater.*, 2021, **33**, P. 1407–1415.
- [29] Zhang F.X., Lang M., Ewing R.C. Atomic disorder in $\text{Gd}_2\text{Zr}_2\text{O}_7$ pyrochlore. *Appl. Phys. Lett.*, 2015, **106**, 191902.
- [30] Díaz-Guillén J.A., Díaz-Guillén M.R., Padmasree K.P., Fuentes A.F., Santamaría J., León C. High ionic conductivity in the pyrochlore-type $\text{Gd}_{2-y}\text{La}_y\text{Zr}_2\text{O}_7$ solid solution ($0 \leq y \leq 1$). *Solid State Ion*, 2008, **179**, P. 2160–2164.
- [31] Mandal B.P., Deshpande S.K., Tyagi A.K. Ionic conductivity enhancement in $\text{Gd}_2\text{Zr}_2\text{O}_7$ pyrochlore by Nd doping. *J. Mater. Res.*, 2008, **23**, P. 911–916.
- [32] Moreno K.J., Fuentes A.F., García-Barriocanal J., León C., Santamaría J. Mechanochemical synthesis and ionic conductivity in the $\text{Gd}_2(\text{Sn}_{1-y}\text{Zr}_y)_2\text{O}_7$ ($0 \leq y \leq 1$) solid solution. *J. Solid State Chem.*, 2006, **179**, P. 323–330.
- [33] Díaz-Guillén M.R., Moreno K.J., Díaz-Guillén J.A., Fuentes A.F., García-Barriocanal J., Santamaría J., León C. Dynamics of mobile oxygen ions in disordered pyrochlore-type oxide-ion conductors. *Defect and Diffusion Forum*, 2009, **289–292**, P. 347–354.
- [34] Díaz-Guillén J.A., Fuentes A.F., Díaz-Guillén M.R., Almanza J.M., Santamaría J., León C. The effect of homovalent A-site substitutions on the ionic conductivity of pyrochlore-type $\text{Gd}_2\text{Zr}_2\text{O}_7$. *J. Power Sources*, 2009, **186**, P. 349–352.
- [35] Tuller H.L. Oxygen ion conduction and structural disorder in conductive oxides. *J. Phys. Chem. Solids*, 1994, **55** (12), P. 1393–1404.
- [36] Omata T., Otsuka-Yao-Matsuo S. Electrical properties of proton-conducting Ca^{2+} -doped $\text{La}_2\text{Zr}_2\text{O}_7$ with a pyrochlore-type structure. *J. Electrochem. Soc.*, 2001, **148** (6), P. 252–261.

- [37] Omata T., Ikeda K., Tokashiki R., Otsuka-Yao-Matsuo S. Proton solubility for $\text{La}_2\text{Zr}_2\text{O}_7$ with a pyrochlore structure doped with a series of alkaline-earth ions. *Solid State Ion*, 2004, **167**, P. 389–397.
- [38] Huo D., Gosset D., Siméone D., Baldinozzi G., Khodja H., Villeroz B., Surblé S. Influence of sintering methods on microstructure and ionic conductivity of $\text{La}_{1.95}\text{Sr}_{0.05}\text{Zr}_2\text{O}_{6.975}$ synthesized by co-precipitation. *Solid State Ion*, 2015, **278**, P. 181–185.
- [39] Huo D., Baldinozzi G., Siméone D., Khodja H., Surblé S. Grain size-dependent electrical properties of $\text{La}_{1.95}\text{Sr}_{0.05}\text{Zr}_2\text{O}_{7-\delta}$ as potential Proton Ceramic Fuel Cell electrolyte. *Solid State Ion*, 2016, **298**, P. 35–43.
- [40] Antonova E.P., Ananyev M.V., Farlenkov A.S., Tropin E.S., Khodimchuk A.V., Porotnikova N.M. Phase equilibria, water dissolution, and peculiarities of charge transfer in Ca-doped $\text{La}_2\text{Zr}_2\text{O}_{7-\alpha}$. *Russ. J. Electrochem.*, 2017, **53**, P. 651–657.
- [41] Antonova E.P., Farlenkov A.S., Tropin E.S., Eremin V.A., Khodimchuk A.V., Ananyev M.V. Oxygen isotope exchange, water uptake and electrical conductivity of Ca-doped lanthanum zirconate. *Solid State Ion*, 2017, **306**, P. 112–117.
- [42] Farlenkov A.S., Khodimchuk A.V., Eremin V.A., Tropin E.S., Fetisov A.V., Shevyrev N.A., Leonidov I.I., Ananyev M.V. Oxygen isotope exchange in doped lanthanum zirconates. *J. Solid State Chem.*, 2018, **268**, P. 45–54.
- [43] Vorotnikov V.A., Belyakov S.A., Plekhanov M.S., Stroeva A.Yu., Lesnichyova A.S., Zhigalina O.M., Khmelenin D.N., Àtanovà A.V., Basu V.G., Kuzmin A.V. Proton transfer in $\text{La}_{2-x}\text{Ca}_x\text{Zr}_2\text{O}_{7-\delta}$ pyrochlores: Reasons for limited water uptake and high grain boundary conductivity. *Ceram. Int.*, 2022, **48**, P. 35166–35175.
- [44] Fournier T., Nots J.Y., Muller J., Joubert J.C. Conductive ionique des phases de type pyrochlore $\text{Gd}_{2-x}\text{Ca}_x\text{Zr}_2\text{O}_{7-x/2}$ and $\text{Gd}_2\text{Zr}_{2-x}\text{Sc}_x\text{O}_{7-x/2}$. *Solid State Ion*, 1985, **15**, P. 71–74.
- [45] Zhong F., Zhao J., Shi L., Xiao Y., Cai G., Zheng Y., Long J. Alkaline-earth metals-doped pyrochlore $\text{Gd}_2\text{Zr}_2\text{O}_7$ as oxygen conductors for improved NO_2 sensing performance. *Sci. Rep.*, 2017, **7**, 4684.
- [46] Shlyakhtina A.V., Abrantes J.C.C., Gomes E., Lyskov N.V., Konyshva E.Y., Chernyak S.A., Kharitonova E.P., Karyagina O.K., Kolbanev I.V., Shcherbakova L.G. Evolution of Oxygen–Ion and Proton Conductivity in Ca-Doped $\text{Ln}_2\text{Zr}_2\text{O}_7$ ($\text{Ln} = \text{Sm}, \text{Gd}$), Located Near Pyrochlore–Fluorite Phase Boundary. *Materials*, 2019, **12**, 2452.
- [47] Kuzmin A.V., Stroeva A.Yu., Gorelov V.P., Novikova Yu.V., Lesnichyova A.S., Farlenkov A.S., Khodimchuk A.V. Synthesis and characterization of dense proton-conducting $\text{La}_{1-x}\text{Sr}_x\text{ScO}_{3-\delta}$ ceramics. *Hydrogen Energy*, 2019, **44**, P. 1130–1138.
- [48] Jiang L., Wang C., Wang J., Liu F., You R., Lv S., Zeng G., Yang Z., He J., Liu A., et al. Pyrochlore Ca-doped $\text{Gd}_2\text{Zr}_2\text{O}_7$ solid state electrolyte type sensor coupled with ZnO sensing electrode for sensitive detection of HCHO. *Sens. Actuators B Chem.*, 2020, **309**, 127768.
- [49] Liu Z.G., Ouyang J.H., Zhou Y., Xia X.L. Effect of Sm substitution for Gd on the electrical conductivity of fluorite-type $\text{Gd}_2\text{Zr}_2\text{O}_7$. *J. Power Sources*, 2008, **185** (2), P. 876–880.
- [50] Liu Z., Ouyang J., Sun K., Zhou Y. Effect of CaO addition on the structure and electrical conductivity of the pyrochlore-type $\text{GdSmZr}_2\text{O}_7$. *Ceram. Int.*, 2012, **38**, P. 2935–2941.
- [51] Liu Z.-G., Ouyang J.-H., Sun K.-N., Zhou Y. Influence of magnesia doping on structure and electrical conductivity of pyrochlore type $\text{GdSmZr}_2\text{O}_7$. *Adv. Appl. Ceram.*, 2012, **111**, P. 214–219.
- [52] Shannon R.D. Revised effective ionic radii and systematic studies of interatomic distances in halides and chalcogenides. *Acta Cryst. A*, 1976, **32**, P. 751–767.
- [53] Xia X.-L., Ouyang J.-H., Liu Z.-G. Influence of CaO on structure and electrical conductivity of pyrochlore-type $\text{Sm}_2\text{Zr}_2\text{O}_7$. *J. Power Sources*, 2009, **189**, P. 888–893.
- [54] Kovrova A.I., Gorelov V.P. Characteristics of Pt electrode activated by $\text{Tb}_{1-x}\text{Ce}_x\text{O}_{2-\alpha}$ films in contact with $\text{ZrO}_2 + 10 \text{ mol } \% \text{ Y}_2\text{O}_3$ electrolyte. *Russ. J. Electrochem.*, 2019, **55**, P. 132–136.
- [55] Wan T.H., Saccoccio M., Chen C., Ciucci F. Influence of the discretization methods on the distribution of relaxation times deconvolution: implementing radial basis functions with DRTtools. *Electrochim. Acta*, 2015, **184**, P. 483–499.
- [56] Gavriljuk A.L., Osinkin D.A., Bronin D.I. The use of Tikhonov regularization method for calculating the distribution function of relaxation times in impedance spectroscopy. *Russ. J. Electrochem.*, 2017, **53**, P. 575–588.
- [57] Schlüter N., Ernst S., Schröder U. Finding the Optimal Regularization Parameter in Distribution of Relaxation Times Analysis. *ChemElectroChem*, 2019, **6** (24), P. 6027–6037.
- [58] Yastrebtev A.A., Popov V.V., Menushenkov A.P., Beskrovnyi A.I., Neov D.S., Shchetin I.V., Ponkratov K.V. Comparative neutron and X-ray diffraction analysis of anionic and cationic ordering in rare-earth zirconates ($\text{Ln} = \text{La}, \text{Nd}, \text{Tb}, \text{Yb}, \text{Y}$). *J. Alloys Compd.*, 2020, **832**, 154863.
- [59] Uno M., Kosuga A., Okui M., Horisaka K., Muta H., Kurosaki K., Yamanaka S. Photoelectrochemical study of lanthanide zirconium oxides, $\text{Ln}_2\text{Zr}_2\text{O}_7$ ($\text{Ln} = \text{La}, \text{Ce}, \text{Nd}$ and Sm). *J. Alloys Compd.*, 2006, **420**, P. 291–297.
- [60] Govindan Kutty, K.V., Rajagopalan, S., Mathews, C.K., Varadaraju, U.V. Thermal expansion behavior of some rare earth oxide pyrochlores. *Mater. Res. Bull.*, 1994, **29** (7), P. 759–766.
- [61] Shimamura K., Arima T., Idemitsu K., Inagaki Y. Thermophysical Properties of Rare-Earth-Stabilized Zirconia and Zirconate Pyrochlores as Surrogates for Actinide-Doped Zirconia. *Int. J. Thermophys.*, 2007, **28**, P. 1074–1084.
- [62] Liu X.Y., Xu Z.H., Liang G.Y. Comparative study of the sintering behaviors between YSZ and LZ/YSZ composite. *Mater. Lett.*, 2017, **191**, P. 108–111.
- [63] Qu Z., Wan C., Pan W. Thermal expansion and defect chemistry of MgO-doped $\text{Sm}_2\text{Zr}_2\text{O}_7$. *Chem. Mater.*, 2007, **19**, P. 4913–4918.
- [64] Nikonov A.V., Kuterbekov K.A., Bekmyrza K.Z., Pavzderin N.B. A brief review of conductivity and thermal expansion of perovskite-related oxides for SOFC cathode. *Eurasian J. Phys. Funct. Mater.*, 2018, **2** (3), P. 274–292.
- [65] Eurenus K.E.J., Ahlberg E., Kneen C.S. Role of B-site ion on proton conduction in acceptor-doped $\text{Sm}_2\text{B}_2\text{O}_{7-\delta}$ ($\text{B} = \text{Ti}, \text{Sn}, \text{Zr}$ and Ce) pyrochlores and C-type compounds. *Dalton Trans.*, 2011, **40**, P. 3946–3954.
- [66] Hagiwara T., Nomura K., Kageyama H. Crystal structure analysis of $\text{Ln}_2\text{Zr}_2\text{O}_7$ ($\text{Ln} = \text{Eu}$ and La) with a pyrochlore composition by high-temperature powder X-ray diffraction. *J. Ceram. Soc. Jpn.*, 2017, **125**, P. 65–70.
- [67] Shenu A. Structural Analysis and Its Implications for Oxide ion Conductivity of Lanthanide Zirconate Pyrochlores. PhD Thesis, School of Biological and Chemical Sciences, Queen Mary University of London, London, UK, 2018.
- [68] Shlyakhtina A.V., Belov D.A., Knotko A.V., Kolbanev I.V., Streletskii A.N., Karyagina O.K., Shcherbakova L.G. Oxygen Interstitial and Vacancy Conduction in Symmetric $\text{Ln}_{2\pm x}\text{Zr}_{2\pm x}\text{O}_{7\pm x/2}$ ($\text{Ln} = \text{Nd}, \text{Sm}$) Solid Solutions. *Inorg. Mater.*, 2014, **50** (10), P. 1035–1049.
- [69] Guo X., Maier J. Grain Boundary Blocking Effect in Zirconia: A Schottky Barrier Analysis. *J. Electrochem. Soc.*, 2001, **148**, E121–E126.
- [70] Perriot R., Dholabhai P.P., Ueberuaga B.P. Disorder-induced transition from grain boundary to bulk dominated ionic diffusion in pyrochlores. *Nanoscale*, 2017, **9**, P. 6826–6836.

Information about the authors:

Vladimir A. Vorotnikov – Institute of Chemistry and Ecology, Vyatka State University, Kirov 610000, Russia; Institute of Solid-State Chemistry and Mechanochemistry SB RAS, Novosibirsk, 630090, Russia; ORCID 0000-0002-0247-6198; vorotnikov130@mail.ru

Semyon A. Belyakov – Institute of High-Temperature Electrochemistry UB RAS, Yekaterinburg 620137, Russia; ORCID 0000-0001-9237-8307; bca2@mail.ru

Alexey V. Ivanov – Institute of Chemistry and Ecology, Vyatka State University, Kirov 610000, Russia; Institute of Solid-State Chemistry and Mechanochemistry SB RAS, Novosibirsk, 630090, Russia; ORCID 0000-0002-7666-831X; alehaww@gmail.com

Yulia V. Novikova – Institute of High-Temperature Electrochemistry UB RAS, Yekaterinburg 620137, Russia; ORCID 0000-0002-0369-3274; mery118@mail.ru

Anna Yu. Stroeva – Institute of Chemistry and Ecology, Vyatka State University, Kirov 610000, Russia; ORCID 0000-0002-6772-3321; stroevaanna@yandex.ru

Vadim V. Grebenev – Shubnikov Institute of Crystallography of Federal Scientific Research Centre “Crystallography and Photonics” of the RAS, Moscow 119333, Russia; ORCID 0000-0002-5484-4642; vadim_grebenev@mail.ru

Dmitry N. Khmelenin – Shubnikov Institute of Crystallography of Federal Scientific Research Centre “Crystallography and Photonics” of the RAS, Moscow 119333, Russia; ORCID 0000-0003-0894-5087; xorrunn@gmail.com

Olga V. Emelyanova – Shubnikov Institute of Crystallography of Federal Scientific Research Centre “Crystallography and Photonics” of the RAS, Moscow 119333, Russia; ORCID 0000-0003-3951-8985; eolga@bk.ru

Maksim S. Plekhanov – Institute of Crystallography, RWTH Aachen University, Aachen 52066, Germany; ORCID 0000-0002-2701-4619; plexanovmax@mail.ru

Anton V. Kuzmin – Institute of Chemistry and Ecology, Vyatka State University, Kirov 610000, Russia; Institute of Solid-State Chemistry and Mechanochemistry SB RAS, Novosibirsk, 630090, Russia; ORCID 0000-0002-0700-662X; a.v.kuzmin@yandex.ru

Conflict of interest: the authors declare no conflict of interest.

Single-domain particles of manganese-for-iron substituted M-type barium hexaferrite: synthesis, crystal structure, and magnetic properties

Pavel E. Kazin¹, Anastasia E. Sleptsova², Alexander V. Vasiliev¹, Artem A. Eliseev¹, Robert E. Dinnebier², Sebastian Bette²

¹Department of Chemistry, Lomonosov Moscow State University, Moscow, Russia

²Max Planck Institute for Solid State Research, Stuttgart, Germany

Corresponding author: Pavel E. Kazin, kazin@inorg.chem.msu.ru

PACS 75.47.Lx; 61.90.+d

ABSTRACT Single-phase barium hexaferrite powders with crystallite sizes in a single-domain region and with the general composition $\text{BaFe}_{12-x}\text{Mn}_x\text{O}_{19}$, where $x = 0, 2, 4, 6$, were synthesized applying a citric sol-gel auto-combustion technique with final annealing temperatures of 900 – 1200 °C. The crystal structures were refined, and the magnetic properties were studied. The observed variations in atomic positions with the Mn-for-Fe substitution revealed presence of Mn in three oxidation state +2, +3, and +4, with a preference of Mn^{2+} to the tetrahedral $4f_1$ site and Mn^{4+} to the octahedral 2a and 12k sites. With the Mn-doping, the samples' magnetization decreased, while coercivity increased and reached 8.4 kOe for $x = 6$. The rise of the annealing temperature resulted in a slight growth of magnetization with a general tendency of the coercivity to decrease. A Curie temperature decreased with the Mn-doping remaining above room temperature for the maximal doping.

KEYWORDS magnetic materials, ferrites, crystal structure, magnetization, coercivity

ACKNOWLEDGEMENTS The reported study was funded by RFBR, project number 21-53-12002.

FOR CITATION Kazin P.E., Sleptsova A.E., Vasiliev A.V., Eliseev A.A., Dinnebier R.E., Bette S. Single-domain particles of manganese-for-iron substituted M-type barium hexaferrite: synthesis, crystal structure, and magnetic properties. *Nanosystems: Phys. Chem. Math.*, 2024, **15** (1), 80–97.

1. Introduction

M-type hexaferrites are widely used to produce permanent magnets due to their excellent chemical and thermal stability and due to the low production costs, despite their moderate magnetic parameters such as magnetic energy and coercivity [1]. Besides that, there are very good prospectives for their application in ultra-high frequency devices functioning up to THz frequencies as well as in medium for high-density magnetic recording [2, 3]. Variation in the chemical composition of hexaferrite has proven to be an excellent instrument to adjust and optimize the material magnetic properties [4, 5]. This way, e.g., a giant coercivity and a sub-terahertz resonance have been achieved for an Al–Ca co-doped strontium hexaferrite [6, 7]. However, in many cases the results of the hexaferrite doping are hard to predict because of the complex crystal structure in which the dopant atoms may prefer different crystallographic sites. In particular, partial substitution of Fe^{3+} by Mn^{3+} in $\text{MFe}_{12}\text{O}_{19}$ ($\text{M} = \text{Ba}, \text{Sr}$) resulted not only in the non-uniform site occupancies but also in the variation of the dopant atom oxidation state [8–11]. Using neutron diffraction, it was shown that in $\text{BaFe}_{12-x}\text{Mn}_x\text{O}_{19}$, Mn preferred 2a, $4f_1$, 12k, and to a less extent $4f_2$ sites, whereas it was not found in 4e site [9]. The authors observed that the (Fe,Mn)–O distance in the tetrahedral $4f_1$ site tended to increase with the Mn-doping suggesting that Fe^{3+} was replaced by Mn^{2+} cations. Because of the limited accuracy of the crystal structure parameters determination, the authors did not observe distinct regularities in other (Fe,Mn)–O distances and offered only a tentative picture of the Mn ions distribution in different oxidation states in the crystal structure. The magnetic properties of such deep Mn-substituted hexaferrites were studied only for coarsely grained samples prepared by a standard ceramic technology. Whereas maximum coercivity values may be obtained for single-domain particles which possess sizes in nanometer and submicron regions. Possibly smaller particles, with the size in a nanometer scale, are especially attractive candidates for high-density magnetic recording [3]. For a small Mn-for-Fe substitution the study of submicron particles revealed certain enhancement in coercivity [12, 13]. Since an above-room-temperature ferrimagnetic order remains even in highly Fe-for-Mn substituted compounds, it looks useful to extend the study to deep Mn-doped hexaferrite samples representing ensembles of single-domain particles. In the present paper, we consider the synthesis of such $\text{BaFe}_{12-x}\text{Mn}_x\text{O}_{19}$ samples and investigate in detail their crystal structure and magnetic properties.

2. Experimental

2.1. Samples preparation

The preparation method was similar to that described in [14]. The starting compounds, chemically grade BaCO_3 , $\text{Fe}(\text{NO}_3)_3 \cdot 9\text{H}_2\text{O}$, and $\text{Mn}(\text{NO}_3)_2 \cdot 4\text{H}_2\text{O}$, were taken in stoichiometric quantities corresponding to nominal compositions $\text{BaFe}_{12-x}\text{Mn}_x\text{O}_{19}$, where $x = 0, 2, 4, 6$. BaCO_3 was dissolved in an excess of 5 % nitric acid using magnetic stirring. Nitrates of iron and manganese were dissolved in the obtained solution. Solid citric acid was added to the solution in a stoichiometric quantity corresponding to 3 mol of acid per 1 mol of all metal cations, and the solution pH was adjusted to 7 by adding dropwise a 25 % ammonia solution. The resulting solution was slowly evaporated on a heated sand bath to a viscous state with consequent initiation of a self-propagating exothermal reaction. The obtained highly porous product was heated in a furnace in air for 2 hours to a certain annealing temperature T_{an} , dwelled for 2 hours at this temperature, and quenched in air. The annealing temperatures were 900, 1000, 1100, and 1200 °C.

2.2. Samples characterization

High-precision X-ray powder diffraction (XRD) was conducted on a STOE STADI/P powder diffractometer in the Debye–Scherer geometry using $\text{MoK}_{\alpha 1}$ radiation in the 2θ range $2 - 110^\circ$ with the 2θ step of 0.015° . The crystal structure was refined in the space group $\text{P6}_3/\text{mmc}$ using the Jana 2006 computer program [15]. The reflection's profile parameters, unit cell parameters, positional and isotropic atomic displacement parameters were refined. Occupancies of Fe and Mn were fixed assuming a uniform distribution of the elements at 3d metal atom sites admitting full occupancies of the sites. Crystallite sizes (diameter d and thickness h of platelike particles in ab plain and c direction, respectively) were estimated by fitting a full XRD pattern profile taking into account broadening of the XRD reflections caused by instrumental parameters, crystallite sizes, and effects of crystal strain. Because of correlations between the crystallite size parameters and the strain parameters, only smaller size h is reliably estimated with a large uncertainty though. To suppress the correlations, the strain parameters were assumed to be negligibly small and were set to zero. This allowed us to estimate both d and h . The latter parameter after this procedure was reduced by 20 – 30 %. The parameters obtained this way may be regarded as lower boundary values for average crystallite sizes. These values have to approach real crystallite dimensions for crystals without defects. The parameters were estimated for the samples annealed at temperatures up to 1100 °C. For $T_{an} = 1200$ °C, the lines broadening due to a crystal size was too small to be reliably determined.

Measurements of magnetization were performed on an original Faraday Balance magnetometer at the room temperature in the field range $-17 - +17$ kOe. A powder sample was fixed with glue on a small piece of paper to prevent rotation of the particles in magnetic field.

Measurements of the Curie temperatures were carried out using a Perkin–Elmer Pyris Diamond TG/DTA with a permanent Fe–Nd–B magnet fixed outside the sample chamber. A transition from paramagnetic to ferrimagnetic state was registered by monitoring an effective weight of the sample on the sample cooling with a rate of $10 \text{ K}\cdot\text{min}^{-1}$.

Scanning electron microscopy observations were performed on a Carl Zeiss Leo Supra VP50 electron microscope.

3. Results and discussion

3.1. Crystal structure features and morphology

As evidenced from the XRD analysis all the samples comprise pure hexaferrite phases with a hexagonal crystallographic symmetry. According to the scanning electron microscopy, samples annealed at 900 °C consist of grains looking like thick plates with a typical diameter of 100 – 200 nm and thickness of 50 – 100 nm (Fig. A1, Appendix). With the increasing of the annealing temperature, the grains grow reaching a diameter of 300 – 400 nm and thickness of 100 – 200 nm for $T_{an} = 1100$ °C. For $T_{an} = 1200$ °C, a further and considerable increase in the grain size takes place. The crystallites become more anisotropic in shape and represent rounded plates with an average diameter of 0.7 micron in the undoped sample and 1 – 2 microns in the doped samples. The XRD peaks profile analysis provides values for the crystallites diameter and thickness (Table 1) corresponding well to the SEM results. This implies that the observed grains are single crystals. They have to be perfect enough since the line broadening connected to crystal defects and strains was considered as a negligible one in the XRD analysis. In general, undoped samples contain somewhat thicker platelike particles than Mn-doped ones. For the lowest annealing temperature, Mn-doped samples have slightly finer grains. With the T_{an} increase, a stronger growth of grains takes place in Mn-doped samples, and the most pronounced effect is observed in the sample with the maximum Mn content.

The critical diameter d_c for a $\text{BaFe}_{12}\text{O}_{19}$ grain to represent a single magnetic domain is of 0.8 micron [4]. The Mn-doping usually leads to reduction of saturation magnetization M_s [8, 9], and d_c is expected to grow with the doping since it is inversely proportional to M_s^2 . Therefore, we regard that all the samples obtained represent ensembles of mostly monodomain grains. It especially concerns the samples annealed at lower temperatures.

The XRD patterns of all the samples are shown in Figs. A2–A17. The major results of the crystal structure refinement are collected in Table A1. Complete lists of atomic parameters are presented in Tables A2 and A3 for two limiting compositions, $\text{BaFe}_{12}\text{O}_{19}$ and $\text{BaFe}_6\text{Mn}_6\text{O}_{19}$, for the samples annealed at 1200 °C. The dependencies of the crystal cell

TABLE 1. Crystallite diameter d (nm) and thickness h (nm) estimated from the full-profile XRD powder pattern analysis for $\text{BaFe}_{12-x}\text{Mn}_x\text{O}_{19}$. Standard deviation values are presented in parentheses.

x	$T_{an} = 900\text{ }^\circ\text{C}$		$T_{an} = 1000\text{ }^\circ\text{C}$		$T_{an} = 1100\text{ }^\circ\text{C}$	
	d	h	d	h	d	h
0	184(4)	77(1)	244(5)	130(2)	282(6)	175(4)
2	177(4)	63(1)	244(6)	106(2)	263(6)	107(2)
4	144(2)	69(1)	226(6)	76(1)	285(7)	104(2)
6	152(3)	63(1)	280(9)	78(1)	399(17)	131(3)

parameters on the Mn doping level and the annealing temperature are depicted in Fig. 1. The atomic radii of Fe^{3+} and Mn^{3+} are practically equal and amount to 0.645 \AA for coordination number 6 [16]. One could expect a negligible influence of the Mn doping, but it is not the case. The cell parameters distinctly depend on x . There is also a detectable, but smaller variation of the cell parameters with the annealing temperature. On going from $x = 0$ to $x = 6$, almost independently from T_{an} , a increases by 0.2% , c drops by 0.3% , so that c/a decreases by 0.5% . As a result, cell volume V grows only slightly, by 0.2% . The data correspond well to those obtained earlier for coarsely grained hexaferrites with similar composition [8].

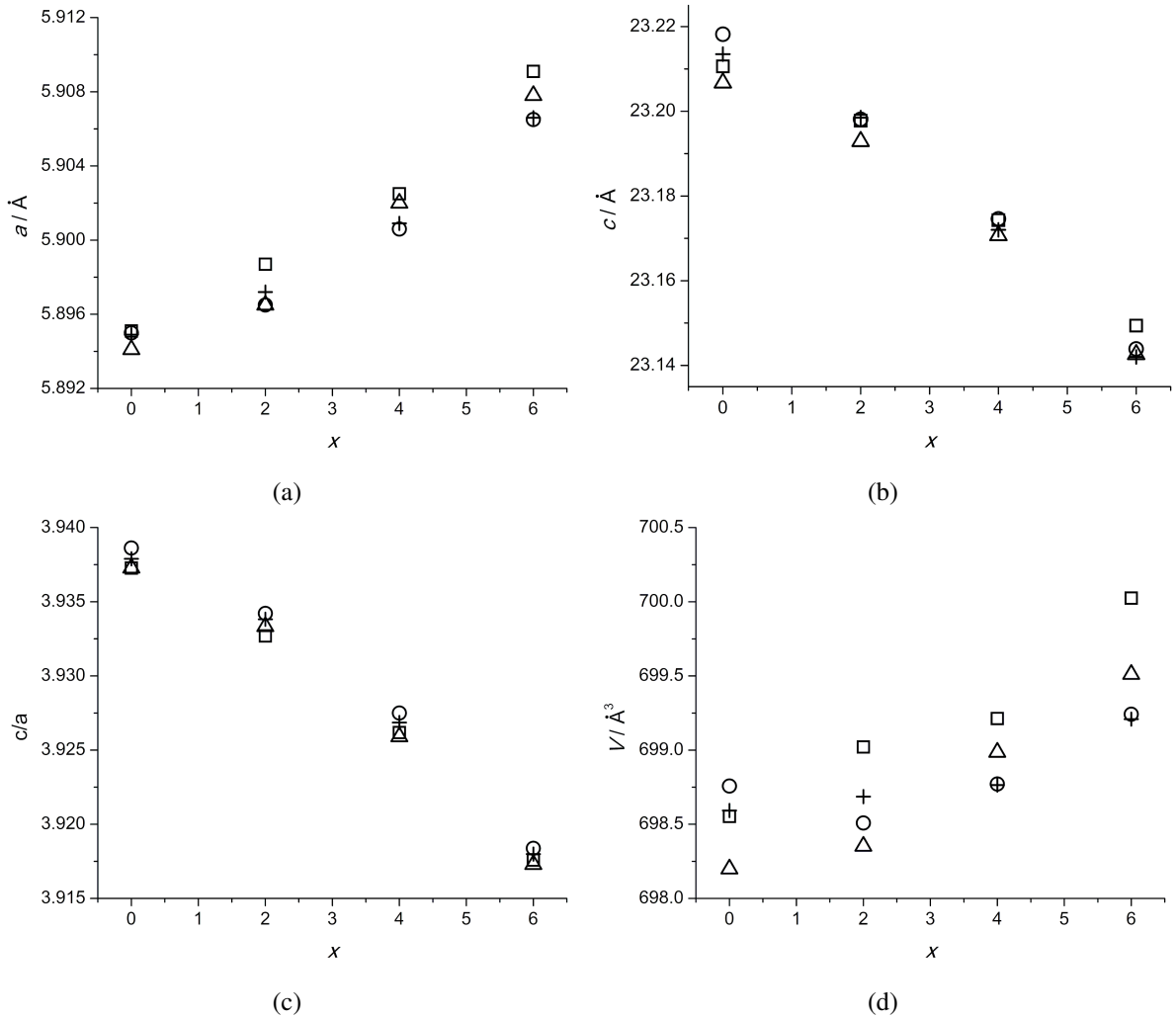


FIG. 1. The dependence of crystal cell parameters on Mn content x in the $\text{BaFe}_{12-x}\text{Mn}_x\text{O}_{19}$ samples annealed at temperatures of 900 (circles), 1000 (crosses), 1100 (triangles), and 1200 °C (squares): (a) parameter a (Å), (b) parameter c (Å), (c) parameters' ratio a/c , (d) unit cell volume V (Å³).

Despite the observed small variation of the cell parameters and the volume, some of interatomic distances change much stronger with the doping. It should be noted that by the X-ray diffraction it is virtually impossible to distinguish Mn from Fe, therefore, we did not determine the distribution of Mn and Fe between the transition metal (M) sites. However, the changes in certain M–O distances may indicate that Mn substitute Fe at the corresponding sites acquiring an oxidation state different from +3.

The crystal structure of barium hexaferrite may be considered as a distorted close packing of oxygen atoms forming a five layers' set with a thickness of $c/2$. The set includes S-block with a spinel structure and R-block containing Ba atoms. 1st oxygen layer includes Ba atoms replacing oxygen atoms and in addition Fe2 atoms at a split 2b site (resulting in a half-filled 4e site, M2). Fe2 shifts from the center of trigonal bipyramid of oxygen atoms along z and acquires tetrahedral coordination. Fe4 atoms ($4f_2$ site, M4) are found between 1st and 2nd as well as between 5th and 1st oxygen layers in an octahedral coordination. Fe5 atoms (12k site, M5) are found between 2nd and 3rd as well as between 4th and 5th oxygen layers in an octahedral coordination. Fe1 (2a site, M1) and Fe3 ($4f_1$ site, M3) atoms are found between 3rd and 4th oxygen layers in octahedral and tetrahedral coordination, respectively.

The changes in the interatomic distances are more pronounced for the samples, annealed at a maximum temperature of 1200 °C. Hence, we will analyze such distances for these samples. The dependence of average M–O distances on the Mn content is shown in Fig. 2. The strongest change takes place for the tetrahedral $4f_1$ site: $d(M3-O)$ linearly grows from 1.887 to 1.980 Å (by ca. 5 %) on increasing x from 0 to 6. For the M1 atom, found in the same layer, the corresponding distance, just in opposite, decreases from 2.014 to 1.977 Å (by ca. 2 %). A smaller decrease, from 2.032 to 2.008 Å (by ca. 1.2%), is observed for $d(M5-O)$. Distances $d(M2-O)$ and $d(M4-O)$ are not appreciably affected by the Mn doping. Taking into account equal radii (R) of Mn^{3+} and Fe^{3+} and admitting that Mn cannot occupy the same site as Mn^{2+} and Mn^{4+} (due to very large difference in their sizes) we may estimate content of Mn^{2+} and Mn^{4+} for every site. For a tetrahedral coordination, $R(Fe^{3+}) = 0.49$ Å and $R(Mn^{2+}) = 0.66$ Å [15]. Then the change of $d(M3-O)$ corresponds to 55(5) % of Mn^{2+} at $4f_1$ site in $BaFe_6Mn_6O_{19}$. For an octahedral coordination, $R(Fe^{3+}) = 0.645$ Å and $R(Mn^{4+}) = 0.53$ Å [16]. That corresponds to 32(7) % of Mn^{4+} at 2a site and 21(6) % of Mn^{4+} at 12k site. Due to comparable quantities of Mn^{4+} and Mn^{2+} ions found in the structure the average oxidation state of Mn approaches +3.

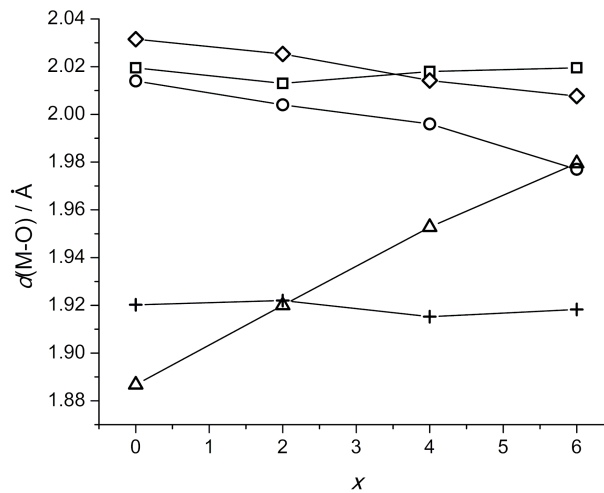


FIG. 2. The dependence of average distances $d(M-O)$ between 3d metal atom M (Fe, Mn) and oxygen atoms of the coordination sphere on Mn content x in the $BaFe_{12-x}Mn_xO_{19}$ samples annealed at 1200 °C: M1 (2a) – circles, M2 (4e) – crosses, M3 ($4f_1$) – triangles, M4 ($4f_2$) – squares, M5 (12k) – diamonds.

Occupancies of the M sites by Mn were estimated earlier for $BaFe_{12-x}Mn_xO_{19}$ ceramics using neutron powder diffraction [9]. For $BaFe_6Mn_6O_{19}$ they corresponded to 0.73, 0.73, 0.27, and 0.54 for M1, M3, M4, and M5 sites, respectively. No Mn was found at M2 site. We expect that a similar distribution of Mn ions takes place in our finely-grained samples. While the direct determination of Mn occupancies is not possible, the observed atomic displacement parameters U_{eq} of M sites reflect such occupancies (see Tables A2 and A3). In $BaFe_{12}O_{19}$, U_{eq} values for all 3d metal sites are close, while in $BaFe_6Mn_6O_{19}$, U_{eq} correlates with the reported site occupancies, growing with the increase of the Mn occupancy. Combining the data [9] and our results we may suggest that (i) at $4f_1$ site, major part of Mn is in oxidation state +2, (ii) at 2a site, approximately half of Mn is in oxidation state +4, (iii) at 12k site, from one third to half of Mn is present as Mn^{4+} , and (iv) at $4f_2$ site, Mn is mostly in oxidation state +3. It is interesting that, while $d(M2-O)$ does not vary with the Mn content (which is in accordance with the reported absence of Mn at 4e site [9]), the distances to apical oxygen (O1) and to those (O3) at the trigonal base of the distorted tetrahedron vary strongly. $d(M2-O1)$ decreases from 2.138 to 2.072 Å and $d(M2-O3)$ increases from 1.847 to 1.867 Å on going from $BaFe_{12}O_{19}$ to $BaFe_6Mn_6O_{19}$. Most

probably, the observed changes are determined by a local structure distortion due to Mn incorporation in other M sites. Fe^{3+} at the M2 site provides the major magnetic anisotropy [17]. Our modelling of the Fe^{3+} electronic structure using the CONDON program [18] shows that such lengthening of $d(\text{Fe2-O3})$ reduces the axial magnetic anisotropy.

Apparently, strong variations in interatomic distances on the Mn doping compensate each other so that the change in the crystal cell parameters and volume becomes approximately one order of magnitude smaller. Such a compensation phenomenon is convenient to discuss considering variation in weighted average distances (along z axis) between the oxygen atomic layers, which we denote as $h(n, m) = \Delta z/c$, where n and m are the numbers of oxygen layers (see Tables A2 and A3 for reference). Due to the crystal symmetry $h(5, 1) = h(1, 2)$ and $h(4, 5) = h(2, 3)$. In the undoped $\text{BaFe}_{12}\text{O}_{19}$ sample, $h(1, 2) = 0.10047$, $h(2, 3) = 0.09687$, $h(3, 4) = 0.10532$. In the maximally doped $\text{BaFe}_6\text{Mn}_6\text{O}_{19}$ sample, $h(1, 2) = 0.09993$, $h(2, 3) = 0.09499$, $h(3, 4) = 0.11016$. Thus, $h(3, 4)$ reveals an increase with the biggest absolute value, apparently, due to a large quantity of Mn^{2+} at $4f_1$ site, which effect is not fully compensated by Mn^{4+} at 2a site. $h(2, 3)$ decreases moderately and $h(1, 2)$ diminishes only slightly in consistence with the estimated Mn^{4+} occupancies. The changes in the interlayer distances for 5 consecutive oxygen layers are listed as follows: -0.5 , -1.9 , 4.8 , -1.9 , -0.5 %. This compensates the alteration of the crystal cell parameter c . Situated between the 3rd and 4th oxygen layers, the M3 ($4f_1$) coordination tetrahedron expands both, in the c direction and in the ab plain, while the M1 (2a) coordination octahedron, expanding in the c direction, shrinks in the ab plain. As a result, the cell parameter a increases only slightly. The observed small multidirectional deformation of the hexaferrite crystal lattice was commonly attributed to the Jahn–Teller effect of Mn^{3+} [8, 9]. In contrast to this, our study suggests that the stronger distortions affecting the net values of a and c are connected to simultaneous presence of non-Jahn–Teller Mn^{2+} and Mn^{4+} ions, rather than to the Jahn–Teller distortion of the Mn^{3+} polyhedron.

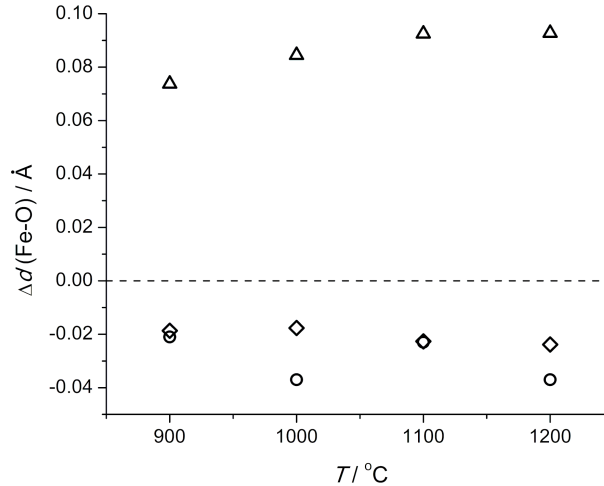


FIG. 3. The dependence of difference $\Delta d(\text{M-O})$ between average distances $d(\text{M-O})$ in $\text{BaFe}_6\text{Mn}_6\text{O}_{19}$ and $\text{BaFe}_{12}\text{O}_{19}$ on samples annealing temperature T_{an} : M1 (2a) – circles, M3 ($4f_1$) – triangles, M5 (12k) – diamonds.

Another interesting issue is possible dependence of Mn^{4+} and Mn^{2+} content on the sample annealing temperature and thus on the hexaferrite grain size. In Fig. 3, the differences $\Delta d(\text{M-O})$ between average distances $d(\text{M-O})$ in $\text{BaFe}_6\text{Mn}_6\text{O}_{19}$ and $\text{BaFe}_{12}\text{O}_{19}$ are shown for the samples annealed at different temperatures. In general, $\Delta d(\text{M1-O})$, $\Delta d(\text{M3-O})$, and $\Delta d(\text{M5-O})$ values are non-zero for the whole annealing temperature range, designating presence of Mn^{4+} and Mn^{2+} in all the samples. Determined with a better accuracy, $\Delta d(\text{M3-O})$ and $\Delta d(\text{M5-O})$ tend to decrease with decreasing T_{an} and drop by ca. 20 % on the T_{an} changing from 1200 to 900 °C. This implies that the degree of the Mn^{3+} disproportionation to Mn^{2+} and Mn^{4+} in the hexaferrite structure slightly decreases with lowering the sample annealing temperature and hence the grain size.

3.2. Magnetic properties

The dependence of the Curie temperature on the Mn content in the samples annealed at different temperatures is shown in Fig. 4. T_C depends strongly on x and very little on T_{an} . T_C decreases with increasing the Mn content almost linearly, approximately 48 K per 1 Mn in the formula unit. Undoped samples show identical T_C of 737 K for all the annealing temperatures. In Mn-doped samples T_C decreases by 7 K with increasing T_{an} from 900 to 1200 °C. This suggests that on the atomic scale, the changes in the undoped compound are negligible, whereas in the doped compounds, certain variations in the crystal structure may take place. Such variations may be connected to the disproportionation character of Mn^{3+} : the suggested above increase of the Mn^{3+} disproportionation degree with the elevating annealing

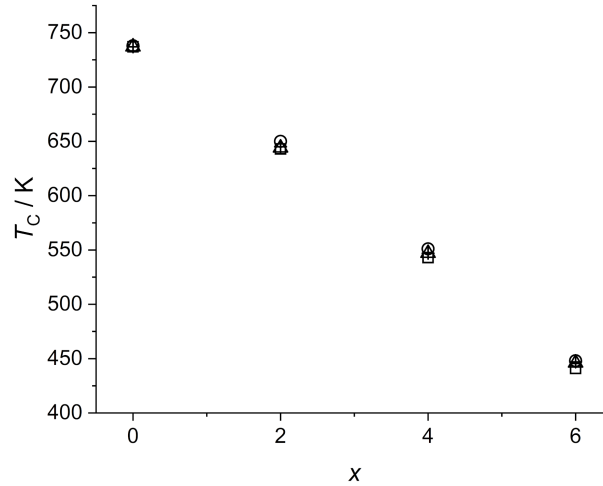


FIG. 4. The dependence of Curie temperature T_C on Mn content x in the $\text{BaFe}_{12-x}\text{Mn}_x\text{O}_{19}$ samples annealed at temperatures of 900 (circles), 1000 (crosses), 1100 (triangles), and 1200 °C (squares).

temperature may cause decrease of T_C . This is reasonable since the arising Mn^{4+} ions in octahedral sites cannot efficiently take part in the antiferromagnetic exchange interaction because of the absence of electrons on the e_g orbitals.

Magnetization and coercivity of the samples depend both, on the compound composition and the annealing temperature. To visualize better the latter dependence, in Fig. 5, magnetization and coercivity are displayed as a function of T_{an} . We analyze the magnetization of samples M taken at the highest applied field of 17 kOe. As the magnetization curves approach to saturation, this magnetization value is assumed to be close to saturation magnetization. The magnetization considerably decreases with increasing the Mn content in the compound. This agrees well with the fact that Mn^{3+} and Mn^{4+} , possessing lower magnetic moments than Fe^{3+} , occupy mostly sites of the major spin sublattice. In the undoped compound, M tends to increase with increasing T_{an} . This may be related to healing the crystal structure defects. In the Mn-doped samples the effect is smaller, and in $\text{BaFe}_6\text{Mn}_6\text{O}_{19}$, the magnetization is nearly the same for all T_{an} . Possibly, the expected growth of magnetization is suppressed by the overlapped magnetization decrease owing to increase of the Mn^{3+} disproportionation degree.

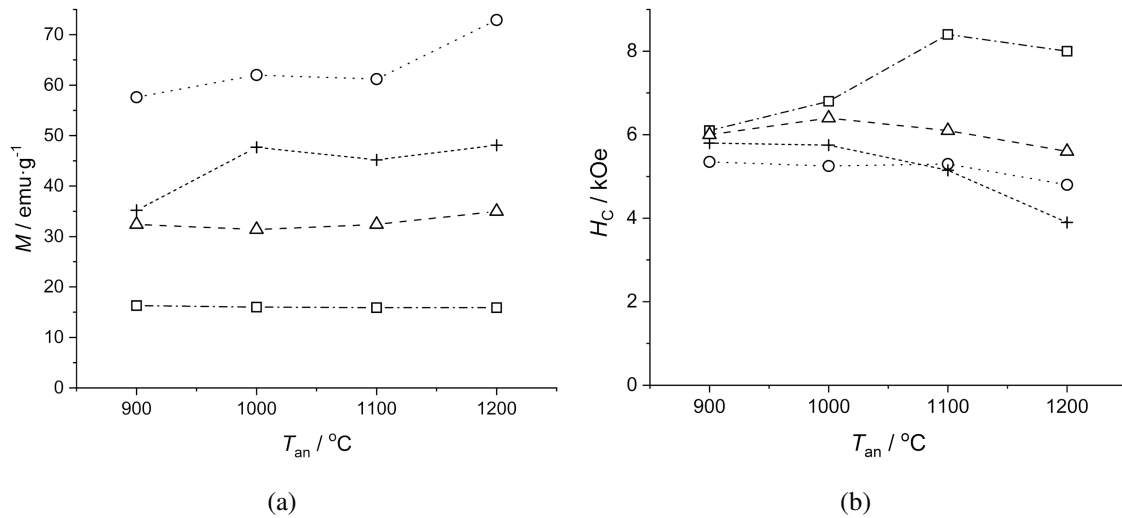


FIG. 5. The dependence of magnetization M under a field of 17 kOe (a) and coercivity H_c (b) on samples' annealing temperature T_{an} in $\text{BaFe}_{12-x}\text{Mn}_x\text{O}_{19}$, where $x = 0$ (circles), 2 (crosses), 4 (triangles), 6 (squares).

Coercivities of the samples are high and, in most cases, exceed 5 kOe, which conforms with predominantly single-domain nature of the grains (crystallites). Coercivity of the undoped compound is nearly constant (~ 5.3 kOe) for lower T_{an} , decreasing to 4.8 kOe only for $T_{an} = 1200$ °C. The latter may be related to growth of the grains so that the size of some of them exceeds a monodomain critical size. The compound with a low Mn content $x = 2$ shows somewhat increased coercivity of 5.8 kOe for $T_{an} = 900$ °C, which decreases to 3.9 kOe for $T_{an} = 1200$ °C. Probably, due to a larger grain size for $T_{an} = 1200$ °C and still substantial M_s , a higher fraction of grains is found in a multidomain

state. For the compounds with higher Mn content, the coercivity exhibits a maximum vs. T_{an} . The highest coercivity of 8.4 kOe is achieved for $\text{BaFe}_6\text{Mn}_6\text{O}_{19}$ annealed at 1100 °C. An analysis of interatomic distances sheds some light on the observed increase of H_c . The distance Fe2–O3 becomes shorter with increasing T_{an} , changing from 1.902 to 1.867 Å. And in accordance with the mentioned above theoretical calculations, such distance shortening should lead to a substantial raise of easy-axis magnetic anisotropy. The distance shortening may be in turn explained by rearrangement of other atoms because of increase of the Mn^{3+} disproportionation degree. A small drop of coercivity for $T_{an} = 1200$ °C may be related to an enlargement of the crystallite size.

4. Conclusions

Pure phase manganese for iron substituted barium hexaferrite samples $\text{BaFe}_{12-x}\text{Mn}_x\text{O}_{19}$ ($x = 0, 2, 4, 6$) were prepared by a sol-gel citrate method in the form of powders with crystallite sizes from tens of nanometers to about a micron, which ensured single domain nature of the compound grains. The variation in the grain size was achieved by the precursor annealing at temperatures 900 – 1200 °C. Detailed analysis of the crystal structure using powder X-ray diffraction data reveals small variations in the crystal cell parameters with the Mn substitution and the sample annealing temperature, and along with this, demonstrates an order of magnitude larger changes in interatomic distances. It is shown that Mn^{3+} replacing Fe^{3+} partially disproportionates to larger Mn^{2+} ions occupying tetrahedral $4f_1$ sites and smaller Mn^{4+} ions, occupying 2a and to a less extent 12k sites. The degree of disproportionation slightly grows with increasing the annealing temperature. The Curie temperature decreases almost linearly with x from 737 to 448 K and, for Mn doped samples, drops other several degrees with increasing the annealing temperature in accordance with the change in the relative content of Mn^{2+} and Mn^{4+} . The magnetization decreases with x , while coercivity tends to increase, reaching 8.4 kOe for the sample with $x = 6$ annealed at 1100 °C. To our knowledge, the obtained maximum value of coercivity is one of the highest among Mn doped hexaferrites conceding only to a coercivity of 9.7 kOe registered in a submicron-grained $\text{SrFe}_{12-x}\text{Mn}_x\text{O}_{19}$ prepared by a mechano-chemical route [19].

Appendix

TABLE A1. Crystal cell parameters a and c , R -factors, and average M–O distances d (M = Fe, Mn) in $\text{BaFe}_{12-x}\text{Mn}_x\text{O}_{19}$, where $x = 0, 2, 4, 6$ (samples 1, 2, 3, 4, respectively), annealed at 900, 1000, 1100, 1200 °C (samples' second symbol **a, b, c, d**, respectively). Values of a , c , and d are in Å.

Sample	a (Å)	c (Å)	R_{wp}, R_{all}	$d(\text{M1-O})$	$d(\text{M2-O})$	$d(\text{M3-O})$	$d(\text{M4-O})$	$d(\text{M5-O})$
1a	5.8950(1)	23.2182(3)	0.031, 0.019	2.013(5)	1.914(9)	1.887(6)	2.023(6)	2.032(4)
1b	5.8949(1)	23.2135(2)	0.029, 0.019	2.020(5)	1.916(7)	1.883(5)	2.020(5)	2.032(3)
1c	5.8941(1)	23.2067(2)	0.036, 0.015	2.008(4)	1.920(6)	1.888(4)	2.020(4)	2.031(3)
1d	5.8951(1)	23.2106(2)	0.038, 0.017	2.014(4)	1.920(6)	1.887(4)	2.020(4)	2.032(3)
2a	5.8965(1)	23.1981(3)	0.031, 0.016	2.016(5)	1.921(8)	1.913(6)	2.016(6)	2.024(3)
2b	5.8972(1)	23.1985(3)	0.028, 0.023	2.008(5)	1.909(9)	1.914(6)	2.025(6)	2.024(4)
2c	5.8965(1)	23.1929(2)	0.035, 0.015	2.003(4)	1.922(6)	1.914(4)	2.015(4)	2.027(3)
2d	5.8987(1)	23.1978(2)	0.039, 0.016	2.004(4)	1.922(6)	1.920(4)	2.013(4)	2.025(3)
3a	5.9006(1)	23.1746(3)	0.028, 0.016	2.010(5)	1.928(7)	1.936(5)	2.014(5)	2.018(4)
3b	5.9009(1)	23.1720(3)	0.028, 0.022	2.011(5)	1.941(8)	1.939(6)	2.009(6)	2.016(4)
3c	5.9020(1)	23.1707(2)	0.030, 0.018	2.002(5)	1.919(7)	1.945(5)	2.015(5)	2.019(3)
3d	5.9025(1)	23.1743(2)	0.042, 0.016	1.996(4)	1.915(6)	1.953(4)	2.018(4)	2.014(3)
4a	5.9065(1)	23.1439(3)	0.027, 0.017	1.992(5)	1.950(7)	1.961(5)	2.003(6)	2.014(4)
4b	5.9066(1)	23.1420(3)	0.028, 0.021	1.983(5)	1.935(8)	1.967(6)	2.007(6)	2.015(4)
4c	5.9078(1)	23.1426(3)	0.029, 0.028	1.985(5)	1.921(8)	1.981(6)	2.016(6)	2.009(4)
4d	5.9091(1)	23.1494(2)	0.042, 0.023	1.977(4)	1.918(6)	1.980(4)	2.020(4)	2.008(3)

TABLE A2. Atomic parameters in the crystal structure of BaFe₁₂O₁₉ annealed at 1200 °C

Atom	Occupancy	x/a	y/a	z/c	U_{iso} (Å ²)
Ba	1	2/3	1/3	1/4	0.0065(2)
Fe1	1	0	0	0	0.0048(4)
Fe2	0.5	0	0	0.25869(14)	0.0039(6)
Fe3	1	1/3	2/3	0.02733(6)	0.0045(3)
Fe4	1	1/3	2/3	0.19032(5)	0.0047(3)
Fe5	1	0.16853(9)	0.33706(19)	0.89168(3)	0.0048(2)
O1	1	0	0	0.1492(2)	0.0063(4)
O2	1	2/3	1/3	0.0540(2)	0.0063(4)
O3	1	0.1799(5)	0.3597(11)	1/4	0.0063(4)
O4	1	0.1575(4)	0.3150(8)	0.05221(12)	0.0063(4)
O5	1	0.5002(4)	0.0003(8)	0.14964(13)	0.0063(4)

TABLE A3. Atomic parameters in the crystal structure of BaFe₆Mn₆O₁₉ annealed at 1200 °C

Atom	Occupancy	x/a	y/a	z/c	U_{iso} (Å ²)
Ba	1	2/3	1/3	1/4	0.0093(2)
M1	1	0	0	0	0.0095(5)
M2	0.5	0	0	0.25908(14)	0.0022(7)
M3	1	1/3	2/3	0.02768(7)	0.0103(3)
M4	1	1/3	2/3	0.19062(6)	0.0069(3)
M5	1	0.16737(11)	0.3347(2)	0.89196(3)	0.0082(2)
O1	1	0	0	0.1514(3)	0.0154(5)
O2	1	2/3	1/3	0.0587(2)	0.0154(5)
O3	1	0.1813(6)	0.3626(12)	1/4	0.0154(5)
O4	1	0.1499(4)	0.2998(8)	0.05387(14)	0.0154(5)
O5	1	0.5012(4)	0.0023(9)	0.14962(16)	0.0154(5)

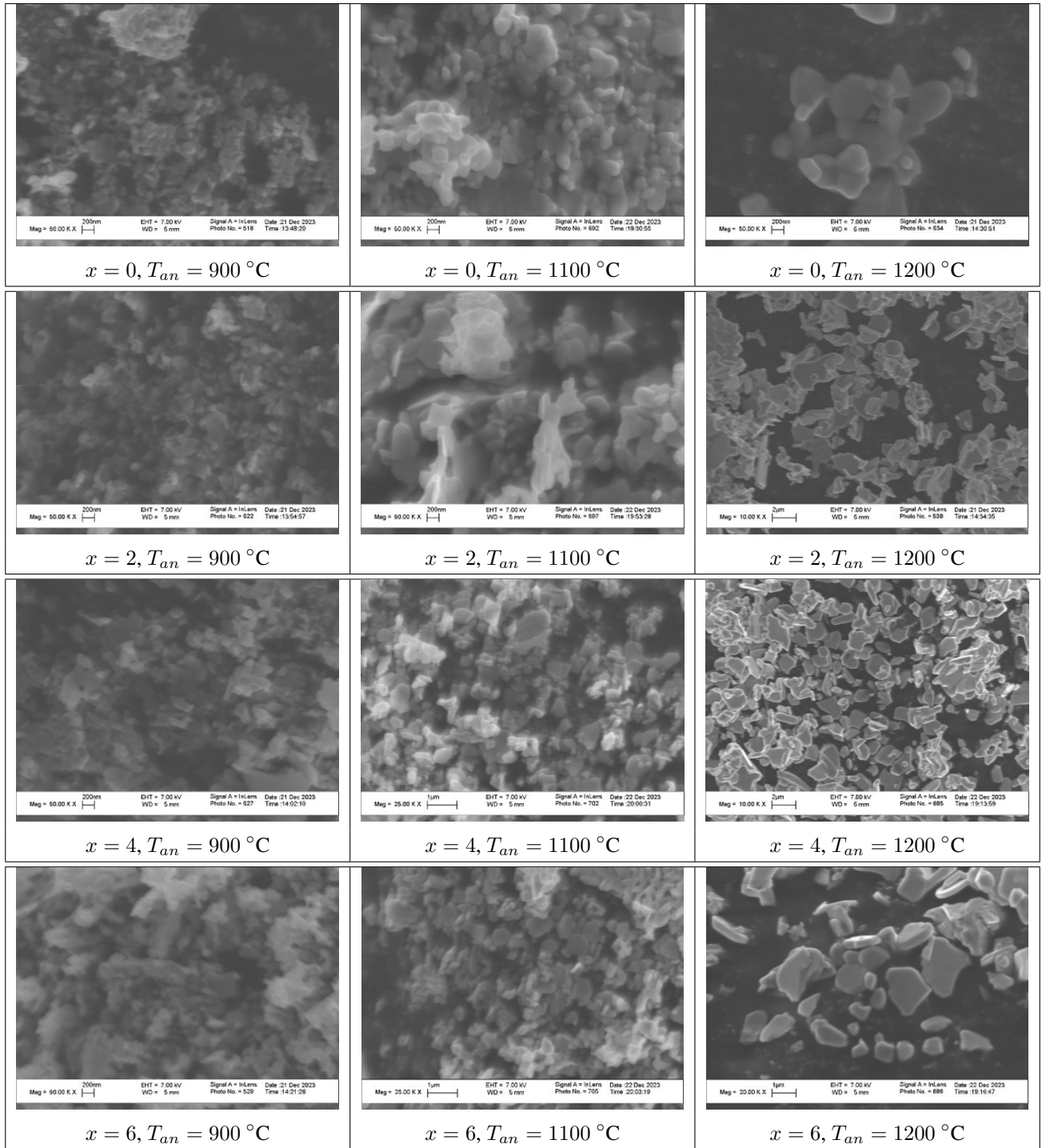


FIG. A1. Scanning electron microscopy images of $\text{BaFe}_{12-x}\text{Mn}_x\text{O}_{19}$ samples annealed at T_{an}

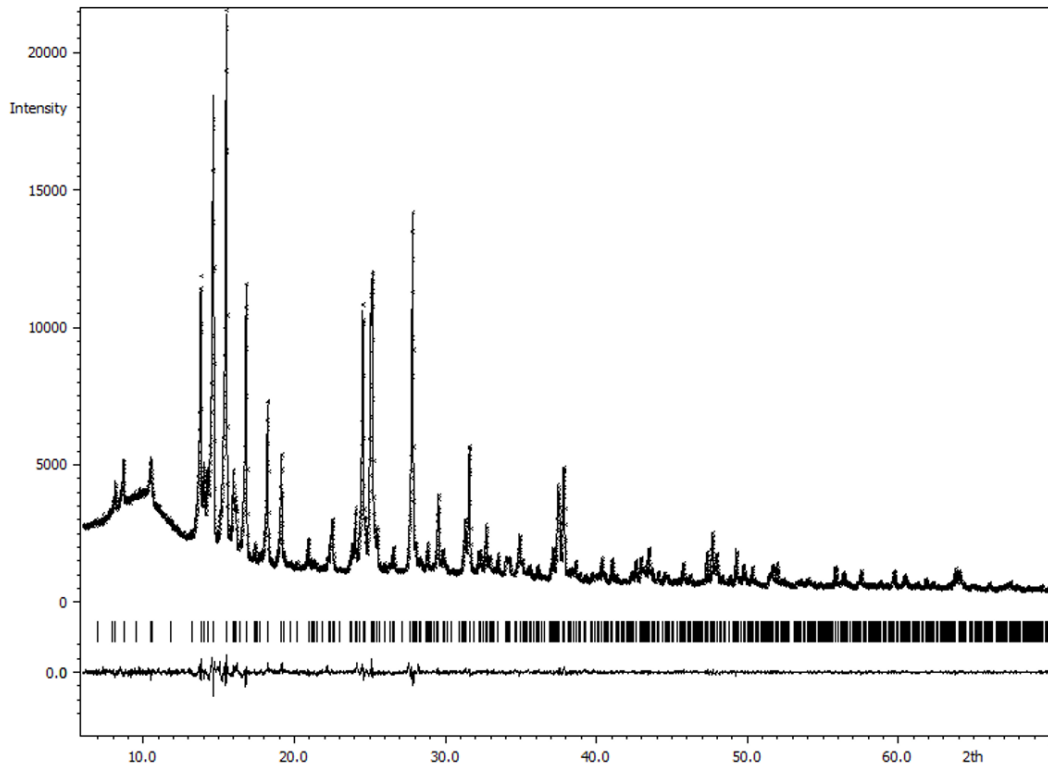


FIG. A2. Observed (crosses), calculated (line), and difference (line underneath) XRD patterns of $\text{BaFe}_{12-x}\text{Mn}_x\text{O}_{19}$, $x = 0$, $T_{an} = 900\text{ }^\circ\text{C}$

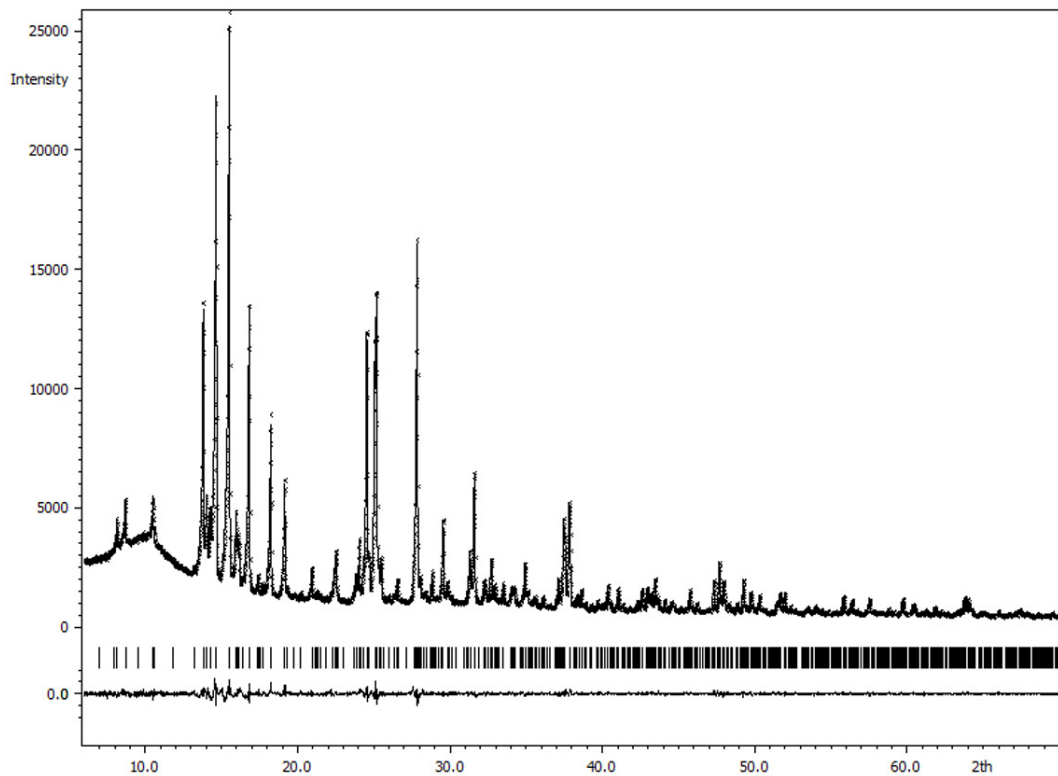


FIG. A3. Observed (crosses), calculated (line), and difference (line underneath) XRD patterns of $\text{BaFe}_{12-x}\text{Mn}_x\text{O}_{19}$, $x = 0$, $T_{an} = 1000\text{ }^\circ\text{C}$

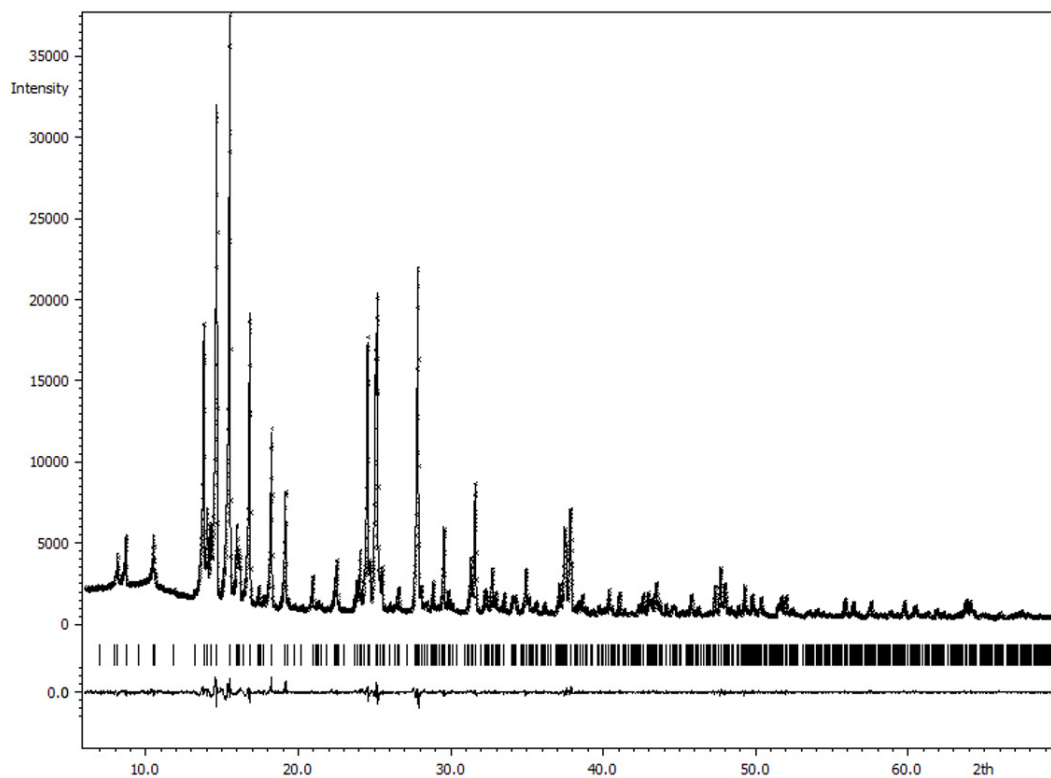


FIG. A4. Observed (crosses), calculated (line), and difference (line underneath) XRD patterns of $\text{BaFe}_{12-x}\text{Mn}_x\text{O}_{19}$, $x = 0$, $T_{an} = 1100\text{ °C}$

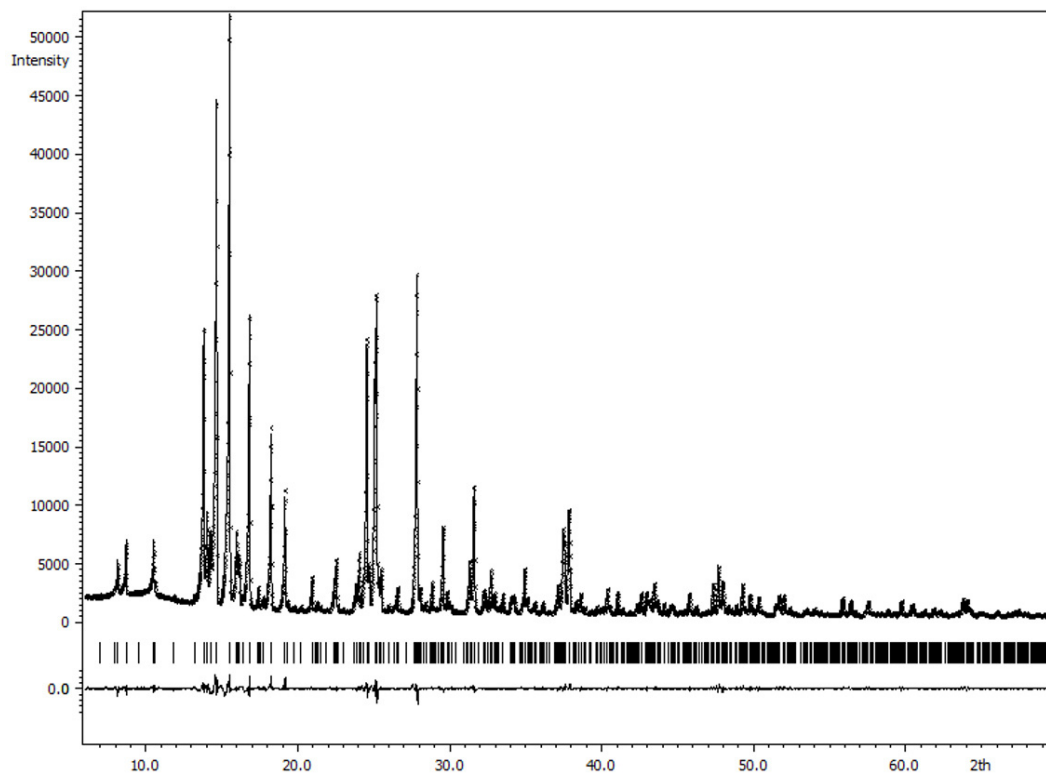


FIG. A5. Observed (crosses), calculated (line), and difference (line underneath) XRD patterns of $\text{BaFe}_{12-x}\text{Mn}_x\text{O}_{19}$, $x = 0$, $T_{an} = 1200\text{ °C}$

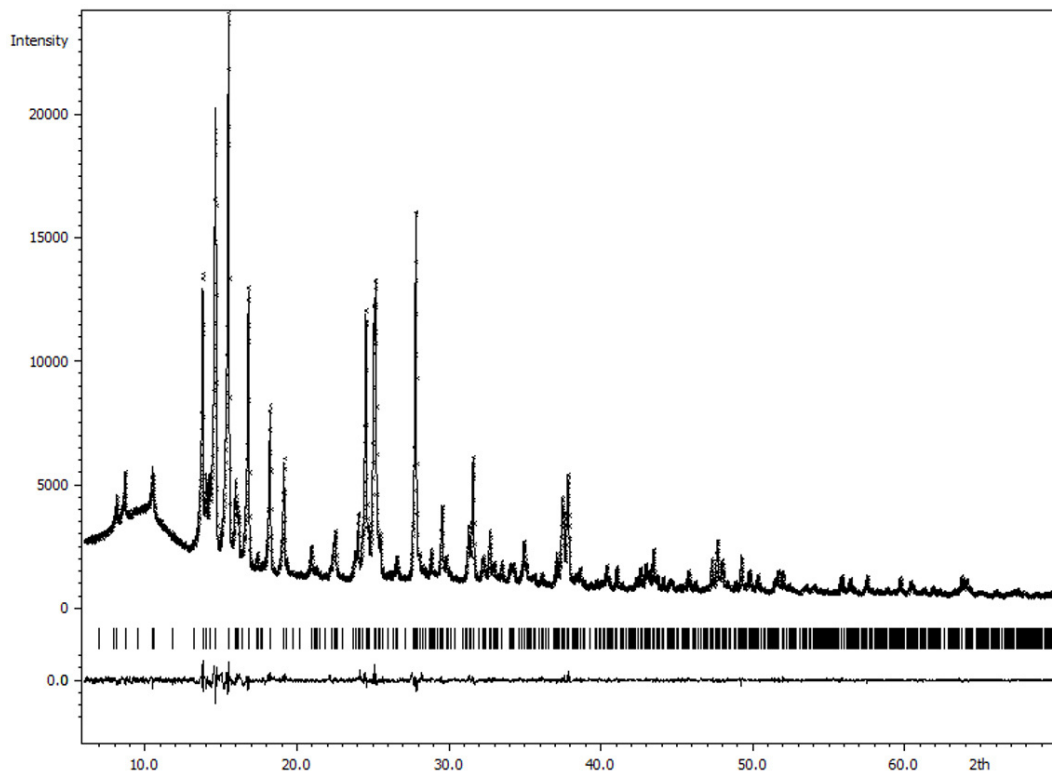


FIG. A6. Observed (crosses), calculated (line), and difference (line underneath) XRD patterns of BaFe_{12-x}Mn_xO₁₉, $x = 2$, $T_{an} = 900$ °C

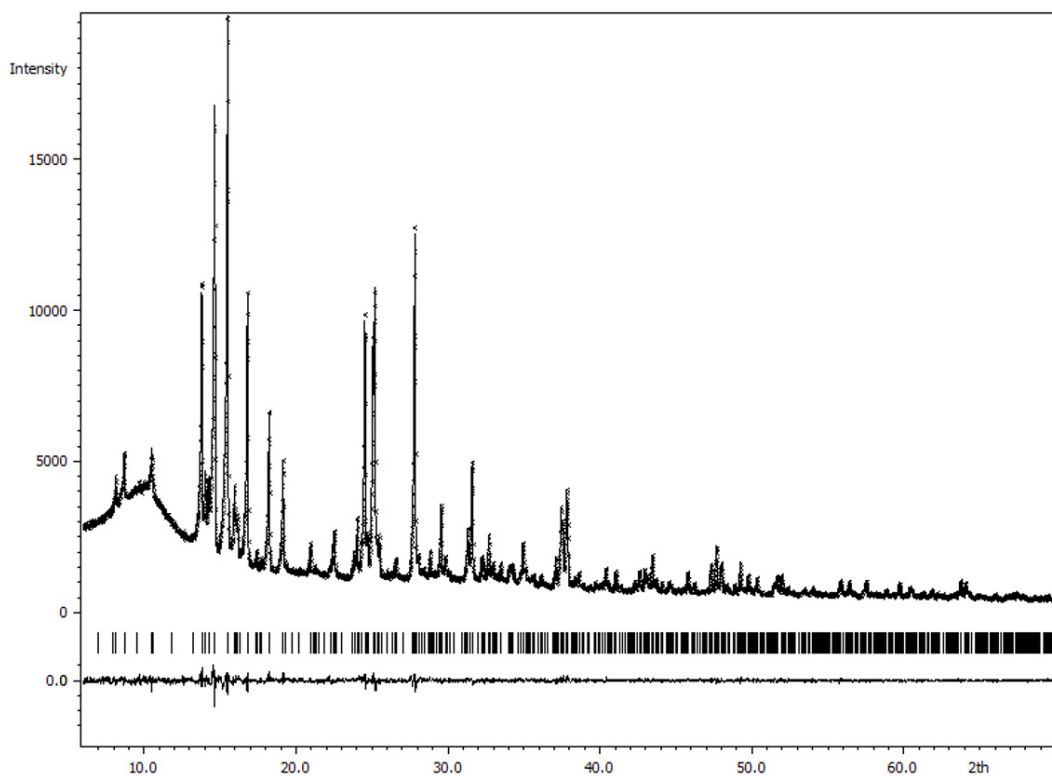


FIG. A7. Observed (crosses), calculated (line), and difference (line underneath) XRD patterns of BaFe_{12-x}Mn_xO₁₉, $x = 2$, $T_{an} = 1000$ °C

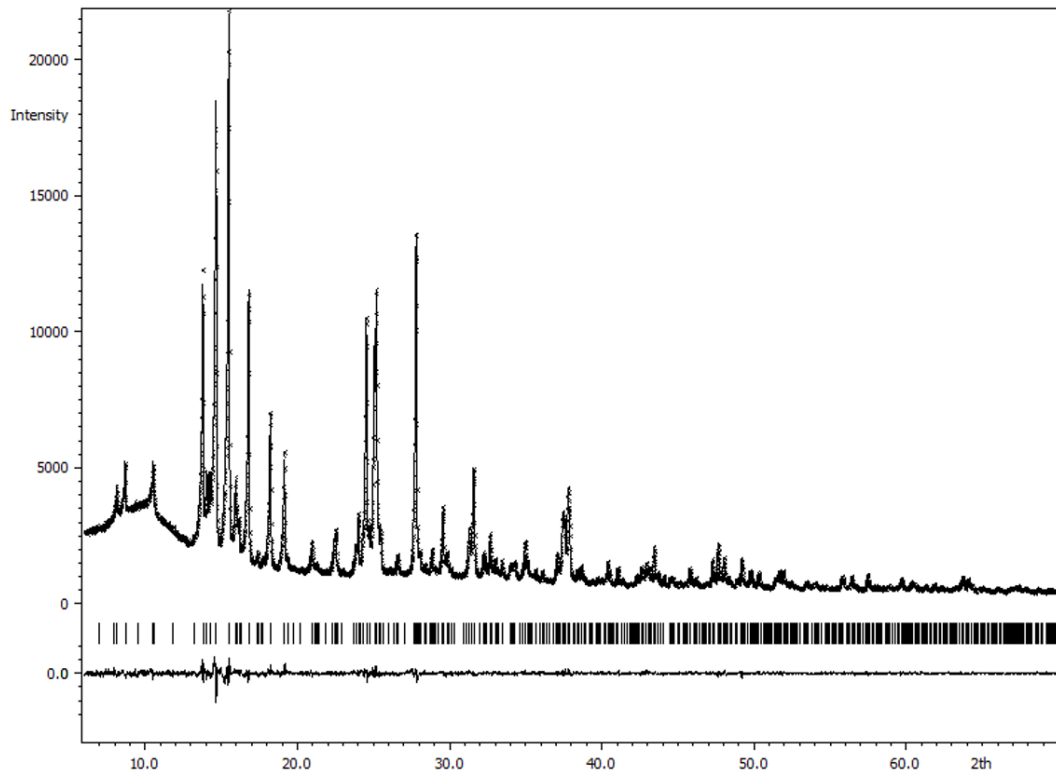


FIG. A10. Observed (crosses), calculated (line), and difference (line underneath) XRD patterns of $\text{BaFe}_{12-x}\text{Mn}_x\text{O}_{19}$, $x = 4$, $T_{an} = 900\text{ }^\circ\text{C}$

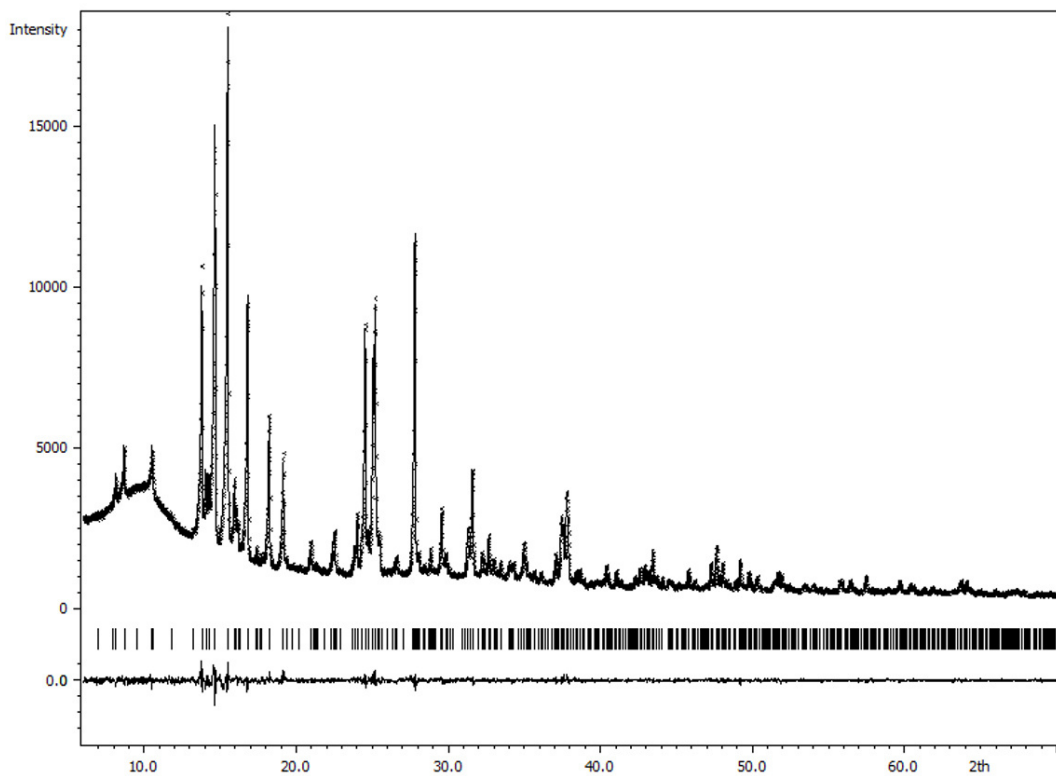


FIG. A11. Observed (crosses), calculated (line), and difference (line underneath) XRD patterns of $\text{BaFe}_{12-x}\text{Mn}_x\text{O}_{19}$, $x = 4$, $T_{an} = 1000\text{ }^\circ\text{C}$

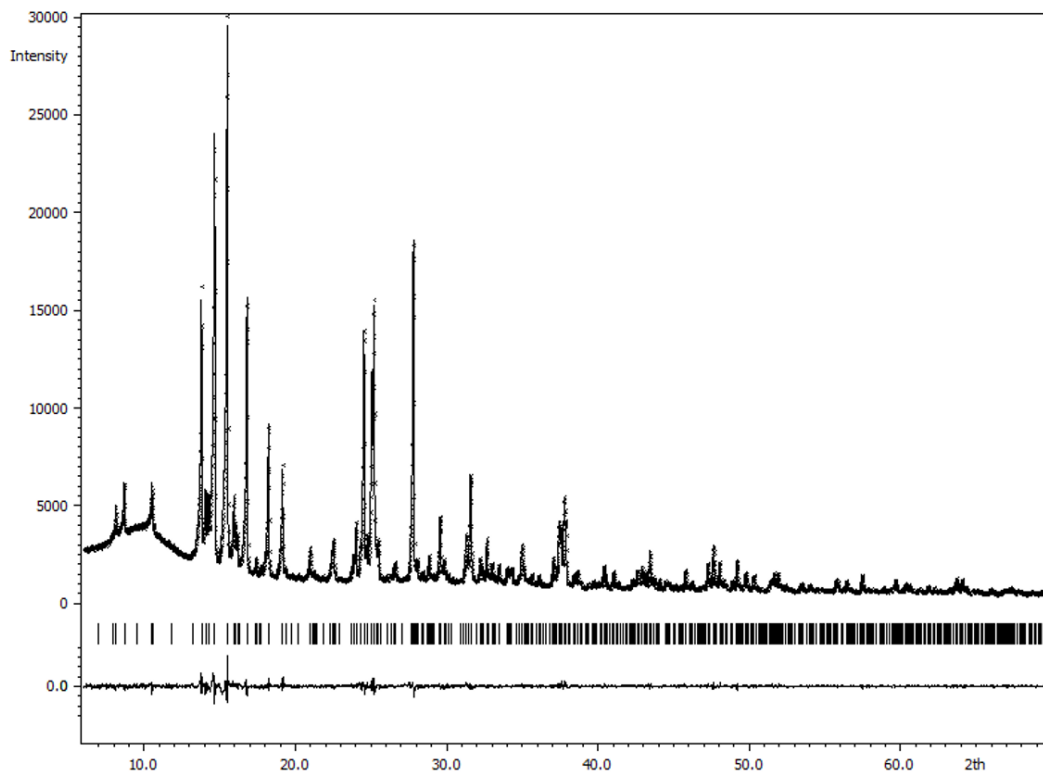


FIG. A12. Observed (crosses), calculated (line), and difference (line underneath) XRD patterns of $\text{BaFe}_{12-x}\text{Mn}_x\text{O}_{19}$, $x = 4$, $T_{an} = 1100\text{ °C}$

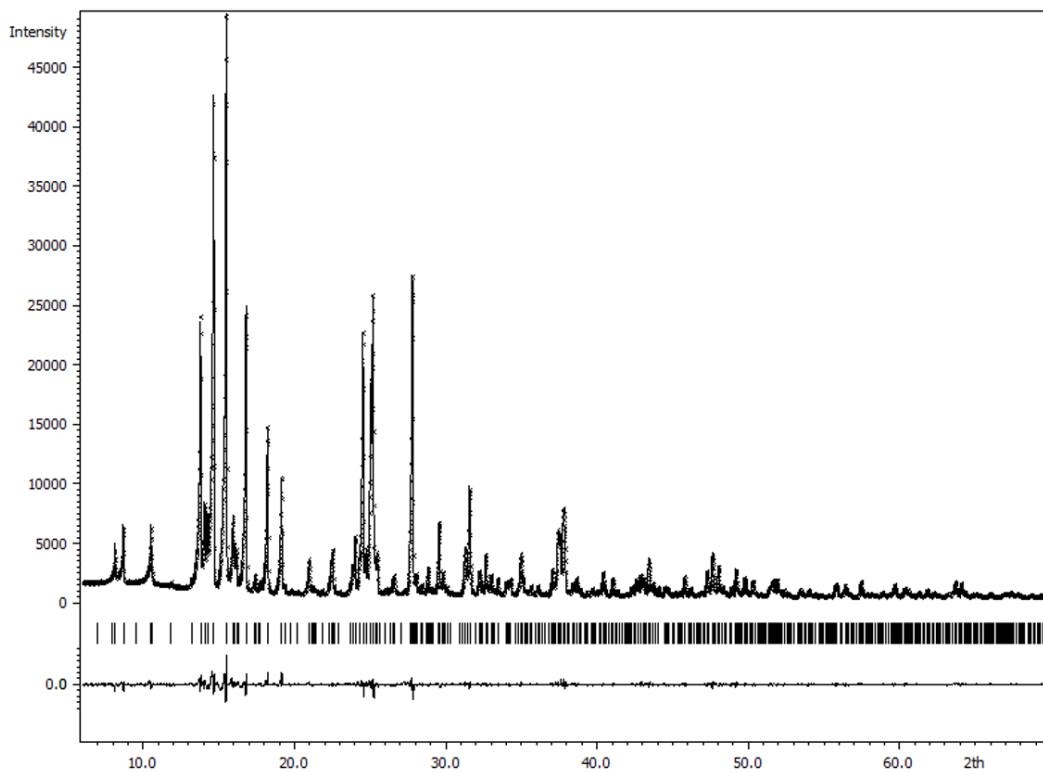


FIG. A13. Observed (crosses), calculated (line), and difference (line underneath) XRD patterns of $\text{BaFe}_{12-x}\text{Mn}_x\text{O}_{19}$, $x = 4$, $T_{an} = 1200\text{ °C}$

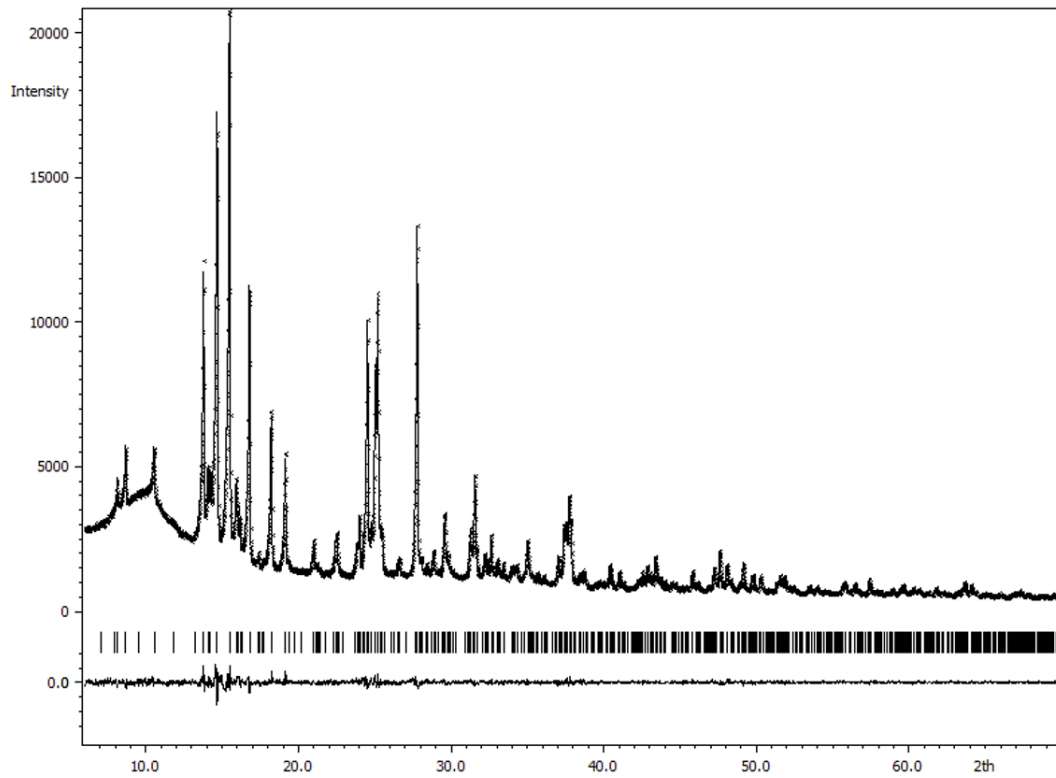


FIG. A14. Observed (crosses), calculated (line), and difference (line underneath) XRD patterns of $\text{BaFe}_{12-x}\text{Mn}_x\text{O}_{19}$, $x = 6$, $T_{an} = 900\text{ }^\circ\text{C}$

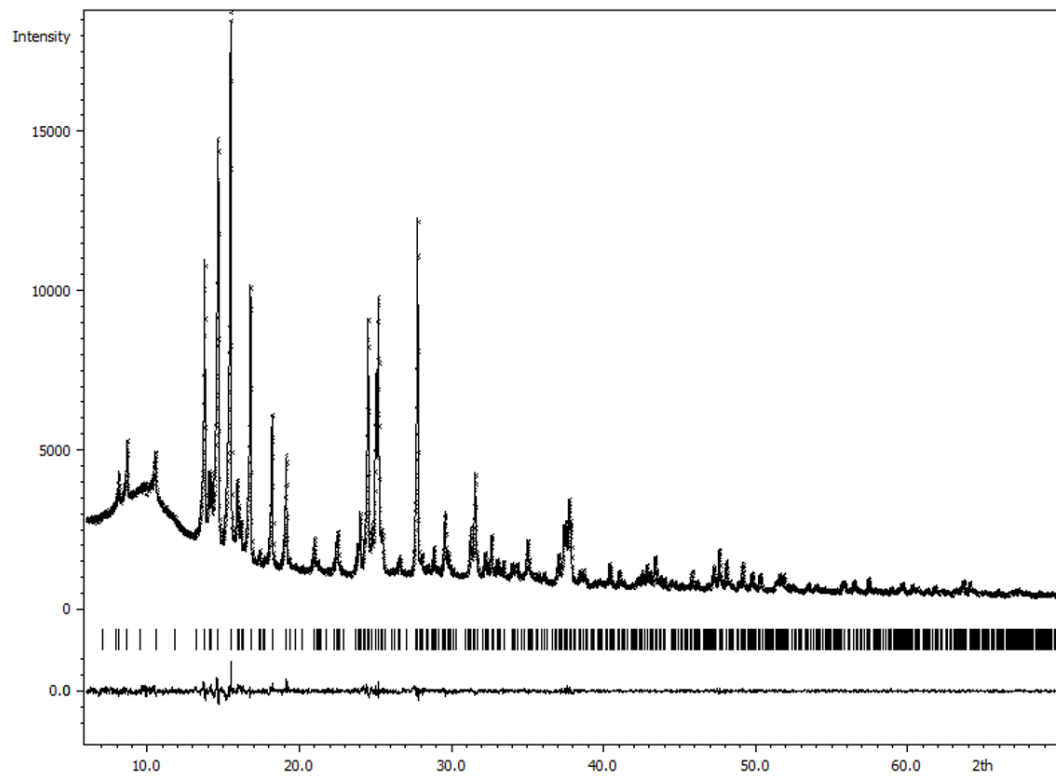


FIG. A15. Observed (crosses), calculated (line), and difference (line underneath) XRD patterns of $\text{BaFe}_{12-x}\text{Mn}_x\text{O}_{19}$, $x = 6$, $T_{an} = 1000\text{ }^\circ\text{C}$

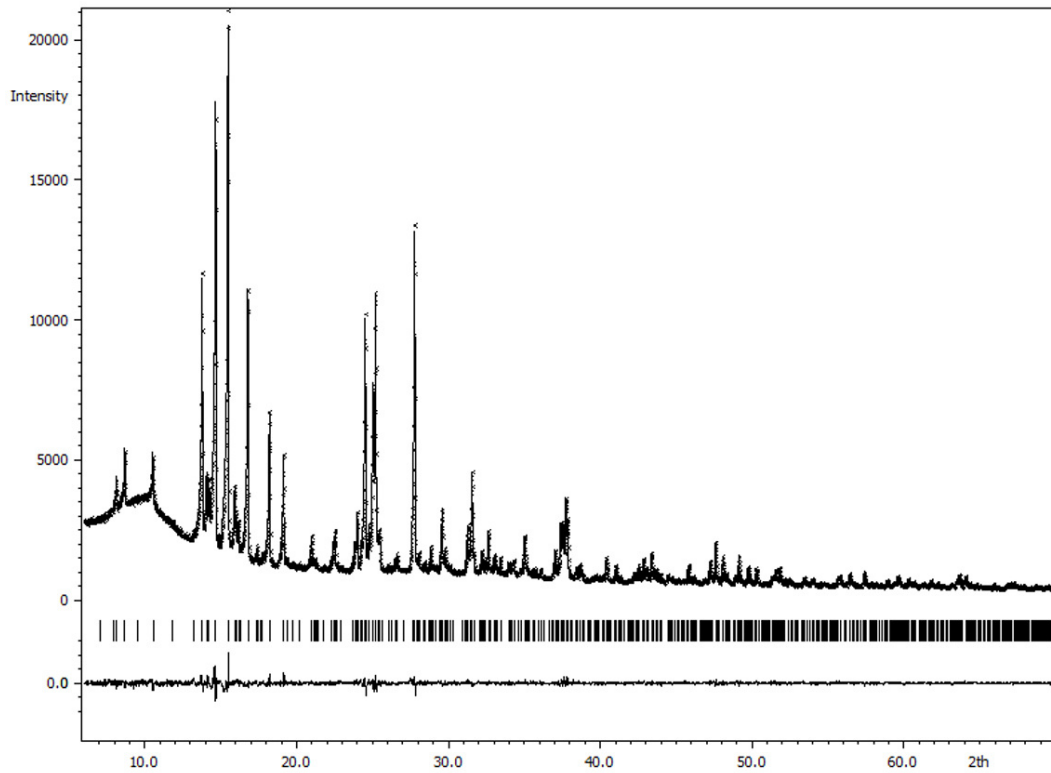


FIG. A16. Observed (crosses), calculated (line), and difference (line underneath) XRD patterns of BaFe_{12-x}Mn_xO₁₉, $x = 6$, $T_{an} = 1100$ °C

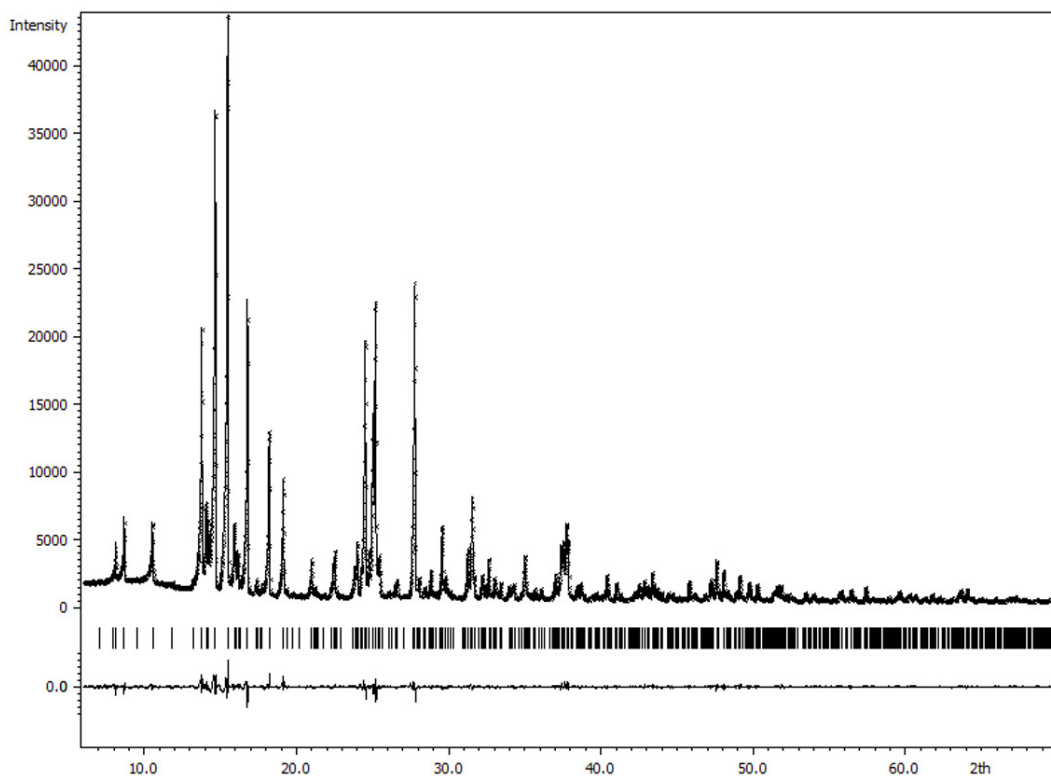


FIG. A17. Observed (crosses), calculated (line), and difference (line underneath) XRD patterns of BaFe_{12-x}Mn_xO₁₉, $x = 6$, $T_{an} = 1200$ °C

References

- [1] Buschow K.H.J., de Boer F.R. *Physics of Magnetism and Magnetic Materials*, Kluwer Academic/Plenum Publishers, New York, 2003, 182 p.
- [2] Harris V.G., Geiler A., Chen Y., Yoon S. D., Wu M., Yang A., Chen Z., He P., Parimi P. V., Zuo X., Patton C.E., Abe M., Acher O., Vittoria C. Recent advances in processing and applications of microwave ferrites. *J. Magn. Magn. Mater.*, 2009, **321**, P. 2035–2047.
- [3] Shimizu O., Oyanagi M., Morooka A., Mori M., Kurihashi Y., Tada T., Suzuki H., Harasawa T. Development of advanced barium ferrite tape media. *J. Magn. Magn. Mater.*, 2016, **400**, P. 365–369.
- [4] Pullar R.C. Hexagonal ferrites: A review of the synthesis, properties and applications of hexaferrite ceramics. *Prog. Mater. Sci.*, 2012, **57**, P. 1191–1334.
- [5] Banihashemi V., Ghazi M.E., Izadifard M., Dinnebier R.E. A study of Ca-doped hexaferrite $\text{Sr}_{1-x}\text{Ca}_x\text{Fe}_{12}\text{O}_{19}$ ($x = 0.0, 0.05, 0.1, 0.15, \text{ and } 0.2$) synthesized by sol-gel combustion method. *Phys. Scr.*, 2020, **95**, 095807.
- [6] Trusov L.A., Gorbachev E.A., Lebedev V.A., Sleptsova A.E., Roslyakov I.V., Kozlyakova E.S., Vasiliev A.V., Dinnebier R.E., Jansen M., Kazin P.E. Ca-Al double-substituted strontium hexaferrites with giant coercivity. *Chem. Commun.*, 2018, **54**, P. 479–482.
- [7] Gorbachev E.A., Trusov L.A., Sleptsova A.E., Kozlyakova E.S., Alyabyeva L.N., Yegiyani S.R., Prokhorov A.S., Lebedev V.A., Roslyakov I.V., Vasiliev A.V., Kazin P.E. Hexaferrite materials displaying ultra-high coercivity and sub-terahertz ferromagnetic resonance frequencies. *Mater. Today*, 2020, **32**, P. 13–18.
- [8] Obradors X., Collomb A., Pernet M., Jourbert J.C. Structural and magnetic properties of $\text{BaFe}_{12-x}\text{Mn}_x\text{O}_{19}$ hexagonal ferrites. *J. Magn. Magn. Mater.*, 1984, **44**, P. 118–128.
- [9] Collomb A., Obradors X., Isalgué A., Fruchart D. Neutron diffraction study of the crystallographic and magnetic structures of the $\text{BaFe}_{12-x}\text{Mn}_x\text{O}_{19}$ M-type hexagonal ferrites. *J. Magn. Magn. Mater.*, 1987, **69**, P. 317–324.
- [10] Thang P.D., Ho T.A., Dang N.T., Lee B.W., Phan T.L., Manh T.V., Kim D.H., Yang D.S. Mn-doped $(\text{Ba},\text{Y})\text{Fe}_{12}\text{O}_{19}$ hexaferrites: Crystal structure and oxidation states of Mn and Fe. *Current Applied Physics*, 2020, **20**, P. 1263–1267.
- [11] Okube M., Yoshizaki J., Toyoda T., Sasaki S. Cation distribution and magnetic structure of M-type $\text{BaTiMnFe}_{10}\text{O}_{19}$ examined by synchrotron X-ray and neutron studies. *J. Appl. Cryst.*, 2016, **49**, P. 1433–1442.
- [12] Adeela N., Khan U., Iqbal M., Riaz S., Ali H., Maaz K., Naseem S. Magnetic and dielectric investigations of Mn-doped Ba hexaferrite nanoparticles by hydrothermal approach. *J. Electronic Materials*, 2016, **45**, P. 5853–5859.
- [13] Kim M., Lee H., Kim J. Magnetic properties of Mn substituted strontium ferrite powders synthesized by the molten salt method. *AIP Advances*, 2020, **10**, 015325.
- [14] Trusov L.A., Gorbachev E.A., Lebedev V.A., Sleptsova A.E., Roslyakov I.V., Kozlyakova E.S., Vasiliev A.V., Dinnebier R.E., Jansen M., Kazin P.E. Ca–Al double-substituted strontium hexaferrites with giant coercivity. *Chem. Commun.*, 2018, **54**, P. 479–482.
- [15] Petříček V., Dušek M., Palatinus L. Crystallographic Computing System JANA2006: General features. *Z. Kristallogr.-Cryst. Mater.*, 2014, **229**, P. 345–352.
- [16] Shannon R.D. Revised effective ionic radii and systematic studies of interatomic distances in halides and chalcogenides. *Acta Crystallogr. A*, 1976, **32**, P. 751–767.
- [17] Xu Y., Yang G.-L., Chu D.-P., Zhai H.-R. Theory of the single ion magnetocrystalline anisotropy of 3d ions. *Phys. Stat. Sol. B*, 1990, **157**, P. 685–693.
- [18] Schilder H., Lueken H. Computerized magnetic studies on d, f, d–d, f–f, and d–S; f–S systems under varying ligand and magnetic fields. *J. Magn. Magn. Mater.*, 2004, **281**, P. 17–26.
- [19] Tenorio-González F.N., Bolarín-Miró A.M., Sánchez-De Jesús F., Vera-Serna P., Menéndez-González N., Sánchez-Marcos J. Crystal structure and magnetic properties of high Mn-doped strontium hexaferrite. *J. Alloys Compd.*, 2017, **695**, P. 2083–2090.

Submitted 29 December 2023; revised 2 January 2024; accepted 3 January 2024

Information about the authors:

Pavel E. Kazin – Department of Chemistry, Lomonosov Moscow State University, 119991 Moscow, Russia;
ORCID 0000-0002-1415-2190; kazin@inorg.chem.msu.ru

Anastasia E. Sleptsova – Max Planck Institute for Solid State Research, Heisenbergstrasse 1, 70569 Stuttgart, Germany;
ORCID 0000-0002-4788-2624; sleptsovaanastasia@gmail.com

Alexander V. Vasiliev – Department of Chemistry, Lomonosov Moscow State University, 119991 Moscow, Russia;
ORCID /0000-0003-4108-9040; a.vasiliev@inorg.chem.msu.ru

Artem A. Eliseev – Department of Chemistry, Lomonosov Moscow State University, 119991 Moscow, Russia;
ORCID 0000-0002-3644-9673; artem.a.eliseev@gmail.com

Robert E. Dinnebier – Max Planck Institute for Solid State Research, Heisenbergstrasse 1, 70569 Stuttgart, Germany;
ORCID 0000-0003-2778-2113; R.Dinnebier@fkf.mpg.de

Sebastian Bette – Max Planck Institute for Solid State Research, Heisenbergstrasse 1, 70569 Stuttgart, Germany;
ORCID 0000-0003-3575-0517; s.bette@fkf.mpg.de

Conflict of interest: the authors declare no conflict of interest.

The effect of Ag(0) colloidal crystals and nanoribbons formation as a result of the redox reaction between Ce(III) and Ag(I) cations occurring on the surface of an aqueous solution of their salts mixture

Valeri P. Tolstoy^{1,a}, Evelina E. Shilovskikh^{1,b}, Larisa B. Gulina^{1,c}

¹Institute of Chemistry, Saint Petersburg State University, St. Petersburg, 198504, Russia

^av.tolstoy@spbu.ru, ^bst084853@student.spbu.ru, ^cl.gulina@spbu.ru

Corresponding author: V. P. Tolstoy, v.tolstoy@spbu.ru

PACS 68.37Hk-68.37.Lp

ABSTRACT The proposed study shows for the first time that gaseous ammonia treatment of AgNO₃ and Ce(NO₃)₃ salts mixture aqueous solution surface gives rise to formation of a composite layer consisting of Ag(0) faceted colloidal crystals and nanoribbons, as well as CeO₂ nanocrystals. A study of such a composite carried out by FESEM, XRD, EDX, TEM, STEM and HRTEM methods has shown that the nanoribbons are about 50–150 nm wide and up to 2–3 μm long, and that there are 2–3 nm CeO₂ nanocrystals on the surface thereof. Colloidal crystals of about several micrometers consist of separate, almost identical silver nanocrystals about 20 nm in size. The obtained results provided a basis for construction of schemes of chemical reactions taking place during the synthesis, and gave grounds for recommendations on practical application of the obtained compounds.

KEYWORDS silver, colloidal crystals, nanoribbons, CeO₂, composite, interface synthesis.

ACKNOWLEDGEMENTS This work was partially supported by Russian Science Foundation grant # 23-19-00566. We are grateful to the “Center for X-ray diffraction studies” and “Nanotechnology” Research Park of Saint Petersburg State University, for their technical assistance with the synthesized samples investigation.

FOR CITATION Tolstoy V.P., Shilovskikh E.E., Gulina L.B. The effect of Ag(0) colloidal crystals and nanoribbons formation as a result of the redox reaction between Ce(III) and Ag(I) cations occurring on the surface of an aqueous solution of their salts mixture. *Nanosystems: Phys. Chem. Math.*, 2024, **15** (1), 98–103.

1. Introduction

It is known that the crystal lattice sites of the so-called colloidal crystals contain nanoparticles of almost the same size ranging from units to tens of nanometers [1]. These sizes are close to the sizes of colloidal particles contained in appropriate solutions, and this fact in many ways defined the term “colloidal crystals”. A different terminology for such nanosized structures propose the term “colloidal superstructures” [2]. These objects also include the so-called “photonic crystals”, which are formed by amorphous particles of metal oxides or polymers with sizes of tens and hundreds nanometers [3]. One example of such colloidal crystals formed by noble metals would be Au crystals with sizes of several microns consisting of Au nanoparticles about 8 nm in size [4].

These crystals are synthesized using vertical deposition [5], spin-coating [6], microfluidic [7], external-force-driven assembly [8] and other techniques. The main problem of such synthesis reduces to obtaining a large number of nanoscale particles of the same size, from which a colloidal crystal is then formed in the process of “crystallization”. As a rule, metal nanoparticles of the same size are obtained in several stages, which include both the nanoparticles synthesis stage, and the stage of nanoparticles separation by size, while at the stage of synthesis when stirring reagents, even under thorough stirring, it is difficult to obtain monodisperse nanoparticles. In this regard, the synthesis of nanoparticles at the solution-gas interface offers unique opportunities. Treating such an interface with a gaseous reagent allows one to avoid concentration gradient of reactants in the planar direction due to isotropic distribution of concentration of reagents interacting with gas molecules over the surface of the solution.

Another important topic in the preparative chemistry of nanosized noble metals is the synthesis of 1D Ag(0) nanocrystals with the morphology of the so-called nanowires [9] and nanoribbons [10]. As follows from the analysis of the literature sources, the focus on the morphology is mainly caused by the solution of the urgent problem of creating conductive and transparent coatings for optoelectronics [11].

The purpose of the present study was to investigate the conditions needed for formation of nanosized Ag(0) particles during the one-stage crystallization process occurring at the interface of aqueous solution of AgNO₃ and Ce(NO₃)₃ salts mixture with air containing gaseous ammonia or, in other words, under the Gas Solution Interface Technique conditions (GSIT) [12–14]. These reagent compositions were chosen given the known fact that the redox reaction occurs in a

weakly alkaline medium with the participation of Ag(I) and Ce(III) cations, in which Ag(0) and CeO₂ nanoparticles are formed [15]. As is known, such nanosized crystals and the composites based thereon find application, for example, in biomedicine [16–18], catalysis [19] and photocatalysis [20, 21].

2. Experiment

AgNO₃ and Ce(NO₃)₃ · 6H₂O salts (chemically pure) provided by Vekton were used as reagents. Aqueous solutions of the above salts were prepared using high purity Milli-Q water with a resistivity greater than 18 MΩ/cm and under stirring on a magnetic stirrer for at least 30 minutes. The experiments on the synthesis of composites were performed with the use of a series of solutions of the said salt mixtures taken in ratios of 1/4, 1/2, 1/1, 2/1, 4/1. In doing so, 3 series of solutions were prepared with total concentrations equal to 0.1, 0.2 and 0.4 M.

To carry out interfacial synthesis, a flat open container with the working solution (2 mL) was placed into a closed reactor with a volume of 100 cm³. Close to the container with the solution there was an open vessel with 3 % ammonium hydroxide, which served as a source of gaseous ammonia. The exposed surface area of each reagent solution was 2 cm². The reaction proceeded under steady-state conditions for 0.5–15 min. During this time, a semi-transparent films with different thicknesses were formed on the surface of the aqueous solution of salt mixture AgNO₃ and Ce(NO₃)₃ · 6H₂O. After that, the film was next transferred carefully to the surface of pure distilled water in order to remove excess solution. After 10–15 min of exposure, the film was transferred by the Langmuir-Schafer technique to the surface of a single-crystal silicon wafer and then dried at 60°C and analyzed by XRD, FESEM, TEM, STEM, HRTEM and electron microprobe analysis. Before this treatment, the silicon wafers were washed in acetone to remove organic impurities and etched for 10 min in a “piranha” solution (a mixture of H₂O₂ and concentrated H₂SO₄ in a volume ratio of 3:7) with simultaneous ultrasonic cleaning (60 W) to prepare a hydrophilic surface and then rinsed thoroughly in water.

X-ray powder diffraction was performed on a Rigaku Miniflex II diffractometer. The measurement conditions were Cu Kα radiation, 30 kV voltage, and 10 mA current. The sample morphology was determined by Field Emission Scanning Electron Microscopy (FESEM) using Zeiss Merlin and Auriga Laser microscopes. Ion etching of the crystals was performed using an ion column of an Auriga Laser microscope using a gallium ion beam with the accelerating voltage of 30 keV, and the current of 20 pA.

3. Results and discussions

The first results of the synthesis of the aforesaid series of samples showed that the layers obtained on the surface of a salts mixture solution can be transferred to the surface of distilled water, and thus be washed from excess reagents. A preliminary study of their morphology by the FESEM method showed that the layer thickness and density significantly depend on the concentration of reagents and the time of contact of ammonia with the solution surface. In particular, at a contact time of less than 0.5 minutes, a discontinuous layer of nanoparticles is formed on the solution surface, while at a contact time of more than 5 minutes the formed layer is relatively dense, and is about 0.3 μm thick. The layer thickness increases up to 1 μm in case the sample was obtained under the 15 minutes treatment time. Morphological analysis of nanoparticles of this dense layer meets significant problems caused by relatively dense packing of individual nanocrystals in the layer, and therefore, for further study the samples with the least packing density of nanocrystals were selected, namely, those obtained using the salts mixture solution with individual salts concentrations equal to 0.1 M, and the ammonia gas treatment time equal to 5 minutes.

The study of the samples by the XRD method (Fig. 1a) showed that the obtained layer contains silver crystals with the *fcc* cubic structure, and the cerium (IV) oxide with fluorite structure [22]. Fig. 1b presents the EDX microanalysis data, which confirm that the composition includes Ce, O and Ag atoms.

A more detailed study of such samples using the FESEM method (Fig. 2) makes it possible to see whether they contain nano- and microparticles with different morphologies (Fig. 2). In particular, the general micrograph presented in Fig. 2a shows both individual nanoribbons 50–150 nm in width, up to 2–3 μm in length, and densely packed agglomerate thereof of irregular shape measuring up to 2 μm in width and up to 10–12 μm in length. It is also notable that there are faceted crystals 1–2 microns in size. EDX analysis of these objects allowed us to conclude that the nanoribbons contain both Ag and Ce atoms (Fig. 1b), and that the crystals actually contain only silver atoms, since the Ce content in them does not exceed several percent (the figure does not show the results of the crystals analysis). We did not evaluate the oxygen atoms concentration in these experiments, as oxygen can be present in the sample also as part of adsorbed water molecules.

As follows from the micrographs shown in Fig. 2b-d, the surface of such crystals is formed by silver nanoparticles of almost equal size of about 20 nm. Ion etching of these crystals with a gallium ions beam showed that their interior is also formed by nanoparticles of similar sizes (Fig. 3). Moreover, the crystals contain cavities, and thus the Ag(0) nanoparticles on the outer surface form the walls of a sort of boxes. In other words, the results of the study of such crystals indicate that they can be classified as colloidal crystals, but that these crystals have a certain feature associated precisely with the presence of a denser and stronger outer wall.

An important piece of information was derived from studying the obtained nanoribbons using EDX (Fig. 1b), STEM, TEM and HRTEM techniques (Fig. 4). Thus, according to the microphotograph shown in Fig. 4a, the nanoribbons surface

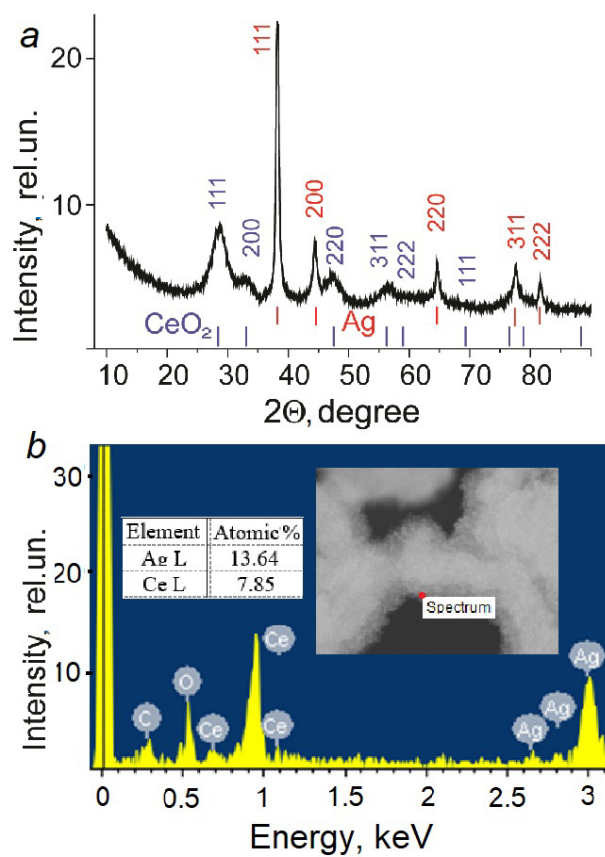


FIG. 1. XRD diffractogram (a) and EDX spectrum (b) of the layer obtained on the surface of the solution of AgNO_3 and $\text{Ce(NO}_3)_3$ salts mixture after contact with gaseous NH_3

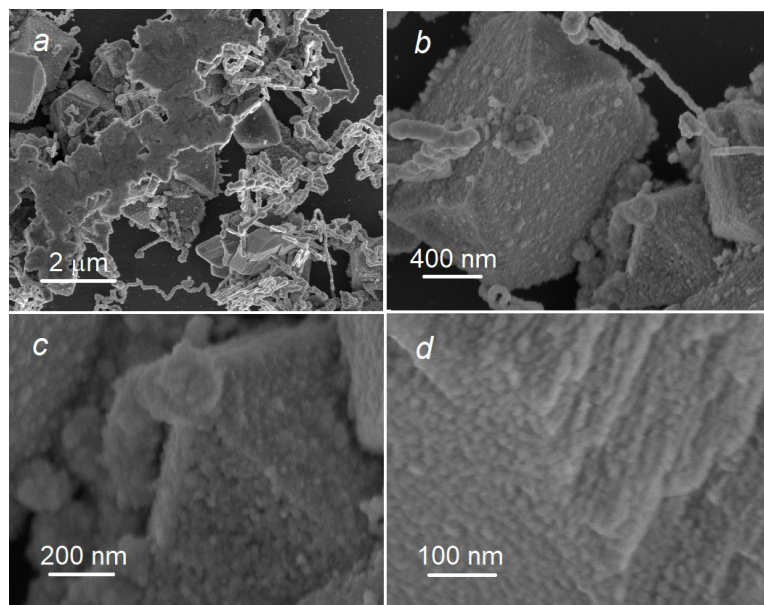


FIG. 2. FESEM images of $\text{Ag(0)}_x\text{CeO}_2$ composite, obtained with different magnifications

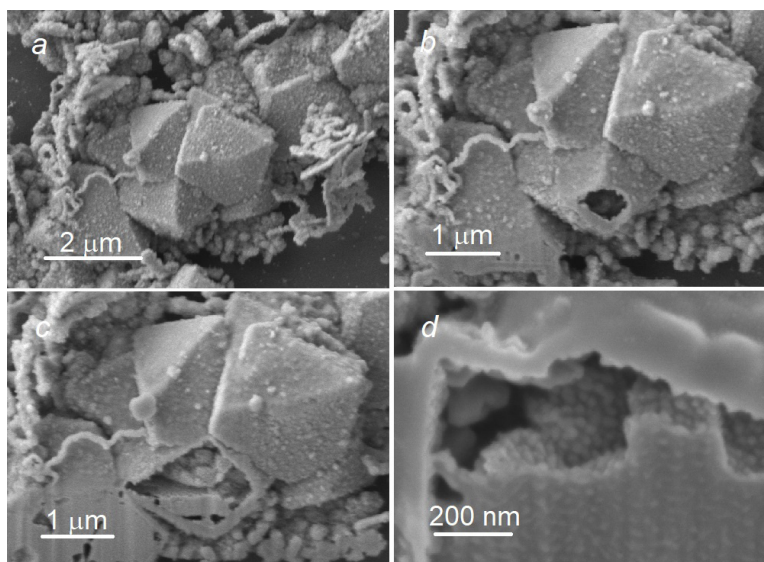


FIG. 3. FESEM images of Ag(0) colloidal crystals during etching thereof with a beam of gallium ions

is not atomically smooth, and individual 2–3 nm nanoparticles can be identified on it. These nanoparticles, however, practically do not exist in the terminal section of this nanoribbon. Moreover, the ribbon terminal fragment has an implicit faceting with a peculiar circular point in the center (Fig. 4b). As follows, for example, from the study [23], such a contour is characteristic of the growth of the $\langle 111 \rangle$ face of a cubic Ag(0) crystal. A local study of the nanoribbons surface performed by the EDX method showed that the ratio of Ag and Ce atoms concentrations over their surface is not uniform: the maximum amount of Ag (up to 90%) is observed in the central part of the nanoribbon, while in the areas along its edges the Ag content decreases to approximately 50% (the figures do not show EDX spectra of these areas). Analysis of HRTEM images, including the one shown in Fig. 4c indicates that, e.g., one of the interplanar distances in nanoparticles on the nanoribbon outer surface equals to 0.31 nm, and this value is close to the interplanar distance characteristic of the $\langle 111 \rangle$ direction in the CeO₂ fluorite structure [22].

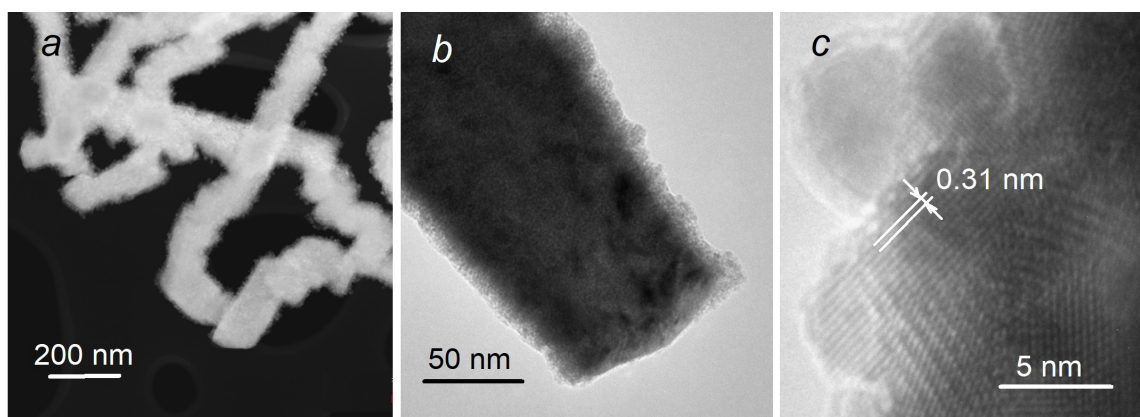


FIG. 4. STEM image of the nanoribbon array (a), TEM image of the terminal fragment of one of the nanoribbons (b) and HRTEM image of the nanoribbon edge fragment (c)

When discussing the full set of the presented results, the first thing to note is that the redox reaction involves the transfer of one electron between Ag(I) and Ce(III) cations in a weak alkaline medium; that is on the one hand, Ag(0) atoms are generated, and on the other hand, Ce(IV) cations are formed; the cations hydrolyze and then form the CeO₂ nanoparticles. At the same time, the EDX study results indicate that the number of Ag atoms in the composite is approximately one and a half times greater than that of Ce atoms. In our opinion, this effect can be observed due to the fact that a certain amount of the formed CeO₂ nanoparticles goes into solution in the form of colloidal particles.

A part of Ag(0) atoms form planar nanoribbons on the surface of a salt mixture solution, and CeO₂ nanoparticles are adsorbed on them. At a certain stage, these nanoparticles form a relatively dense layer that prevents the growth of Ag(0) crystals in a given direction. As follows from Fig. 4b, it is precisely this layer that is not presented in the terminal section of the nanoribbon, and in fact that's why the growth of a planar crystal in this direction can be observed. In other

words, the selective adsorption determines the nanoribbon longitudinal growth. Also noteworthy is the fact that some of the ribbons form closed geometric shapes in the course of such growth; as it may be observed for example, in Figures 3a and 3b that show rings with a diameter of several hundred nm.

As for the other part of the Ag(0) atoms, they form nanoparticles about 20 nm in size during the synthesis process, and these nanoparticles are practically equal in size. This effect is caused by the fact that the nanoparticles formation process occurs in the near-surface film of the solution at the phase interface, which at the first time point is characterized by isotropic concentration of reagents in the direction along the solution surface. It can be assumed that these nanoparticles are selectively adsorbed on the surface of the ribbons that form geometric patterns of regular shape, and this is the way in which a specific faceting of the growing colloidal crystal is set. Next, layer-by-layer growth of the faces of such crystals is observed, and the crystal acquires a characteristic crystal faceting as a whole. It is obvious that the density of Ag(0) nanoparticles in the surface layers of faceted crystals exceeds their density inside the crystals due to a longer time of interaction between the surface Ag(0) nanoparticles and the mother solution; therefore, after drying the samples in air and evacuating them in the electron microscope chamber the inner part of the crystals is compacted, and the cavities free from nanoparticles are formed therein.

Thus, the unique conditions that are created during the synthesis according the GSIT method make it possible to obtain, in fact at room temperature and with simple equipment, a nanocomposite consisting of Ag(0) colloidal crystals, as well as Ag(0) nanoribbons with CeO₂ nanocrystals located on the surface thereof. There is no doubt that the obtained nanocomposites can find application, in particular, as part of bactericidal materials, substrates for signal amplification in SERS, etc.

4. Conclusion

Gaseous ammonia interaction with aqueous solution of AgNO₃ and Ce(NO₃)₃ salt mixture, results in the increase of the pH value in the solution surface layer, and Ag(I) and Ce(III) cations enter into a redox reaction. As a result of the interaction, a hydrophobic layer of the Ag(0)_x-CeO₂ composite is formed on the solution surface. The composite components are characterized by crystalline structure and unique morphology. In particular, a part of Ag(0) atoms forms nanoribbons about 50–150 nm in width, and up to 2–3 μm in length on the surface of which there are CeO₂ nanoparticles 2–3 nm in size, while the other part of the Ag(0) atoms forms colloidal faceted crystals several μm in size, consisting of a collection of Ag(0) nanoparticles of equal size measuring about 20 nm. Based on the results of experimental studies a model-based approach was substantiated regarding the processes occurring on the surface of the mentioned salts mixture solution, and a forecast is made about possible areas of the synthesized compounds practical application.

References

- [1] Wan Y.-Z., Qian W. From Self-Assembly of Colloidal Crystals toward Ordered Porous Layer Interferometry. *Biosensors*, 2023, **13**(7), P. 730.
- [2] Rival J.V., Mymoona P., Lakshmi K.M., Nonappa, Pradeep T., Shibu E.S., Self-Assembly of Precision Noble Metal Nanoclusters: Hierarchical Structural Complexity, Colloidal Superstructures and Applications. *Small*, 2021, **17**(27), P. 2005718.
- [3] Dyshin A.A., Bondarenko G.V., Kiselev M.G. 3D Photonic Crystals: Synthesis and Drying in Supercritical Ethanol. *Russ. J. Inorg. Chem.*, 2022, **67**, P. 408.
- [4] Klajn R., Bishop K.J. M., and Grzybowski B.A. Light-controlled self-assembly of reversible and irreversible nanoparticle suprastructures. *PNAS*, 2007, **104**(25) P. 10305.
- [5] Jiang P., Bertone J.F., Hwang K.S., Colvin V.L. Single-Crystal Colloidal Multilayers of Controlled Thickness. *Chem. Mater.*, 1999, **11**, P. 2132.
- [6] Jiang P., McFarland M.J. Large-Scale Fabrication of Wafer-Size Colloidal Crystals, Macroporous Polymers and Nanocomposites by Spin-Coating. *J. Am. Chem. Soc.* 2004, **126**, P. 13778.
- [7] Zhao Y., Zhao X., Hu J., Xu M., Zhao W., Sun L., Zhu C., Xu H., Gu Z. Encoded Porous Beads for Label-Free Multiplex Detection of Tumor Markers. *Adv. Mater.*, 2009, **21**, P. 569.
- [8] Ge J., He L., Hu Y., Yin Y. Magnetically induced colloidal assembly into field-responsive photonic structures. *Nanoscale*, 2011, **3**, P. 177.
- [9] Sun Y., Silver nanowires - unique templates for functional nanostructures. *Nanoscale*, 2010, **2**, P. 1626.
- [10] Gulina L.B., Tolstobrov E.V., Tolstoy V.P. Silver nanoribbons synthesized on a silicon surface by the "layer-by-layer" technique. *Russ. J. Gen. Chem.*, 2010, **80**, P. 1149.
- [11] Shengyun Huang, Yannan Liu, Fan Yang, Yong Wang, Ting Yu, Dongling Ma. Metal nanowires for transparent conductive electrodes in flexible chromatic devices: a review. *Environ. Chem. Lett.*, 2022, **20**, P. 3005.
- [12] Gulina L.B., Tolstoy V.P., Solovov A.A., Gurenko V.E., Huang G., Mei Y. Gas-Solution Interface Technique as a simple method to produce inorganic microtubes with scroll morphology. *Progr. in Natur. Sci.: Mater. Intern.*, 2020, **30**(3), P. 279.
- [13] Gulina L.B., Tolstoy V.P., Kasatkin I.A., Kolesnikov I.E., Danilov D.V. Formation of oriented LaF₃ and LaF₃:Eu³⁺ nanocrystals at the gas – Solution interface. *J. of Fluor. Chem.*, 2017, **200**, P. 18.
- [14] Gulina L.B., Tolstoy V.P., Tolstobrov E.V. Facile synthesis of 2D silver nanocrystals by a gas-solution interface technique. *Mend. Commun.*, 2017, **27**(6), P. 634.
- [15] Richuan Rao, Fuliang Shao, Xiongzi Dong, Huaze Dong, Song Fang, Hai Sun, Qiang Ling, Effect of Ag-CeO₂ interface formation during one-spot synthesis of Ag-CeO₂ composites to improve their catalytic performance for CO oxidation. *Appl. Surf. Sci.*, 2020, **513**, P. 145771.
- [16] Popov A.L., Savintseva I.V., Ermakov A.M., Popova N.R., Kolmanovich D.D., Chukavin N.N., Stolyarov A.F., Shcherbakov A.B., Ivanova O.S., Ivanov V.K. Synthesis and analysis of cerium-containing carbon quantum dots for bioimaging in vitro. *Nanosystems: Phys. Chem. Math.*, 2022, **13**(2) P. 204.
- [17] Kozlova T.O., Popov A.L., Romanov M.V., Savintseva I.V., Vasilyeva D.N., Baranchikov A.E., Ivanov V.K. Ceric phosphates and nanocrystalline ceria: selective toxicity to melanoma cells. *Nanosystems: Phys. Chem. Math.*, 2023, **14**(2) P. 223.

- [18] Popov A.L., Kolmanovich D.D., Popova N.R., Sorokina S.S., Ivanova O.S., Chukavin N.N., Shcherbakov A.B., Kozlova T.O., Kalashnikova S.A., Ivanov V.K. Synthesis and biocompatibility study of ceriamildronate nanocomposite in vitro. *Nanosyst.: Phys. Chem. Math.*, 2022, **13**(1), P. 96.
- [19] Muchen Wu, Chong Ouyang, Ziran Ye, Shunbo Li, Zhanglian Hong, and Mingjia Zhi, Ag-CeO₂ composite Aerogels as Photocatalysts for CO₂ Reduction. *ACS Appl. Energy Mater.*, 2022, **5**(6) P. 7335.
- [20] Liu J., Zhang L., Sun Y., Luo Y. Bifunctional Ag-Decorated CeO₂ Nanorods Catalysts for Promoted Photodegradation of Methyl Orange and Photocatalytic Hydrogen Evolution. *Nanomater.*, 2021, **11**, P. 1104.
- [21] Xiaogang Zheng, Qian Chen, Sihao Lv, Xiaojin Fu, Jing Wen, and Xinhui Liu, Enhanced Visible-Light Photocatalytic Activity of Ag QDs Anchored on CeO₂ Nanosheets with a Carbon Coating. *Nanomater.*, 2019, **9**, P. 1643.
- [22] Mai H.-X., Sun L.-D., Zhang Y.-W., Si R., Feng W., Zhang H.-P., Liu H.-C., Yan C.-H. Shape-Selective Synthesis and Oxygen Storage Behavior of Ceria Nanopolyhedra, Nanorods, and Nanocubes. *J. of Phys. Chem. B*, 2005, **109**(51) P. 24380.
- [23] Longxia Yang, Xianjun Huang, Huating Wu, Yuanlong Liang, Mao Ye, Wencong Liu, Faling Li, Tao Xu and Haicheng Wang, Silver Nanowires: From Synthesis, Growth Mechanism, Device Fabrications to Prospective Engineered Applications. *Eng. Sci.*, 2023, **23**, P. 808.

Submitted 23 November 2023; accepted 26 December 2023

Information about the authors:

Valeri P. Tolstoy – Institute of Chemistry, Saint Petersburg State University, St. Petersburg, 198504, Russia;
ORCID 0000-0003-3857-7238; v.tolstoy@spbu.ru

Evelina E. Shilovskikh – Institute of Chemistry, Saint Petersburg State University, St. Petersburg, 198504, Russia;
ORCID 0009-0008-6893-9563; st084853@student.spbu.ru

Larisa B. Gulina – Institute of Chemistry, Saint Petersburg State University, St. Petersburg, 198504, Russia;
ORCID 0000-0002-1622-4311; l.gulina@spbu.ru

Conflict of interest: the authors declare no conflict of interest.

Fluorination of Eu-doped layered yttrium hydroxides: the role of anionic composition

Zhanbo Liu^{1,a}, Svetlana V. Golodukhina^{1,2,b}, Svetlana V. Kameneva^{1,c}, Alexey D. Yapryntsev^{1,2,d}¹Shenzhen MSU-BIT University, Shenzhen, PRC²Kurnakov Institute of General and Inorganic Chemistry of the Russian Academy of Sciences, Moscow, Russia^asdbzlb@126.com, ^bbrightorangedandelion@gmail.com, ^ckamenevasvetlanav@gmail.com,^dyapryntsev@igic.ras.ru

Corresponding author: Alexey D. Yapryntsev, yapryntsev@igic.ras.ru

PACS 61.66.Fn; 82.39.Wj; 33.50.Dq; 78.30.-j

ABSTRACT The fluorination processes of layered rare-earth hydroxides (LRHs) intercalated with various anions, including organic ones, have been compared for the first time. The fluorination process was investigated for chloride-, nitrate- and 4-sulfobenzoate-intercalated Eu-doped layered yttrium hydroxides by interaction with aqueous solutions of sodium fluoride at 100–150 °C for 2–48 hours. The final product of fluorination in all cases is the hexagonal yttrium hydroxide fluoride (YHF) phase of $\text{Na}_y\text{Y}_{0.95}\text{Eu}_{0.05}(\text{OH})_{3+y-x}\text{F}_x \cdot m\text{H}_2\text{O}$ ($x \sim 3$, $y \sim 0.2$) composition. The formation rate of the YHF increases with the interlayer spacing of the Eu-doped layered yttrium hydroxide.

KEYWORDS layered rare-earth hydroxides (LRHs), fluorination, luminescence, ion exchange, topotactic reactions, metal hydroxyfluorides.

ACKNOWLEDGEMENTS This study was supported by the scholarship for young scientists of President of the Russian Federation (SP-3504.2022.4).

FOR CITATION Liu Zh., Golodukhina S.V., Kameneva S.V., Yapryntsev A.D. Fluorination of Eu-doped layered yttrium hydroxides: the role of anionic composition. *Nanosystems: Phys. Chem. Math.*, 2024, **15** (1), 104–114.

1. Introduction

Metal hydroxyfluorides (or metal hydroxide fluoride) are a broad class of compounds, most of which possess low-dimensional structure, semiconducting properties, anisotropic particle morphology, and the presence of a large number of surface acidic/basic centers [1]. These features of metal hydroxyfluorides cause a wide range of their applied properties. For example, transition metal hydroxyfluorides (Co, Zn, Cd, Mn, Ni, Cu, Ti, Cr, etc.) can be applied in photoluminescence, photocatalysis, optoelectronics, gas sensors, supercapacitors, electrocatalysts for water splitting, oxidation catalysis, and ion batteries [1]. Rare-earth hydroxyfluorides are promising for the preparation of luminescent materials with high refractive index and low phonon energy [2–4]. The structure of metal hydroxyfluorides can be regarded as the structure of fluorine-substituted hydroxides or hydroxyl-substituted metal fluorides. Consequently, modification of metals hydroxides [5] or fluorides [6] is common to obtain hydroxyfluorides.

The hydroxyl ion is an effective luminescence quencher [7]. Therefore, eliminating traces of hydroxyl ions is crucial in synthesizing inorganic phosphors. Consequently, a systematic study focusing on the substitution of hydroxyl ions with fluoride ions represents a significant endeavor for understanding the luminescence quenching process and for developing new, efficient phosphors based on rare earth fluorides. A promising precursor for rare-earth hydroxyfluoride synthesis are layered rare-earth hydroxides (LRHs or LREHs), a unique class of anion-exchange inorganic materials discovered in 2006 [8]. The structure of these compounds consists of alternating positively charged metal-hydroxyl layers and negatively charged anion layers [9]. The high mobility of anions in the layers allows for anion exchange at room temperature. The anion exchange ability of LRHs is used to synthesize a variety of other rare-earth compounds: vanadates [10], tungstates [11], phosphates [12, 13], and fluorides [14]. The mechanism of such reactions is considered as dissolution-reprecipitation [11] and topotactic [15–17]. In the latter case, the pseudo-hexagonal arrangement of rare-earth cations is preserved, which allows the directed preparation of given modifications of rare-earth compounds, such as $\beta\text{-NaYF}_4$ [15] and hexagonal $\text{Y}(\text{OH})_{3-x}\text{F}_x$ [17].

Fluorination of LRHs allows one to obtain a variety of phases of rare-earth fluoride compounds, including $\text{Ln}_2(\text{OH})_5\text{F} \cdot n\text{H}_2\text{O}$ [14, 18–20], $\text{Ln}_2(\text{OH})_4\text{F}_2 \cdot 2\text{H}_2\text{O}$ [21], $\text{Ln}(\text{OH})_{3-m}\text{F}_m$ [14, 16, 17, 22, 23], LnF_3 [16, 21], MLn_mF_n ($M=\text{K, Na, NH}_4$; $\text{Ln} = \text{Y, Na, Pr-Lu}$) [14–16, 23]. The conditions and compositions of fluorinated layered hydroxides are summarized in Table 1. In fluorination reactions, the type of impurity cation (Li^+ , K^+ , Na^+ , NH_4^+) [16], F/Ln ratio (0.1 – 167) [14, 15], temperature (25 – 180 °C) [21], duration (0.1 – 24 h) [21] and pH [16] are varied. The alkali cations participate in the fluorination of LRHs at high concentration of fluorine [16]. Xu et al [16] showed that the ability to incorporate alkali cation into layered yttrium hydroxide with the formation of MY_mF_n decreases in the NH_4^+ , K^+ , Na^+ ,

Li^+ series, as the hydrate radii of these cations increases. The effect of F/Ln ratio on LRH fluorination was investigated by Li et al [14]. The authors consistently obtained $\text{Y}_2(\text{OH})_5\text{F}\cdot n\text{H}_2\text{O}$, hexagonal $\text{Y}(\text{OH})_{1.57}\text{F}_{1.43}$, cubic $\text{NH}_4\text{RE}_3\text{F}_{10}$, and finally cubic $\text{NH}_4\text{RE}_2\text{F}_7$ with increasing F/RE molar ratio. The balance between OH- and F- in the coordination sphere of rare-earth during fluorination can be adjusted by changing pH [16]. In the presence of HNO_3 , $\text{Y}_2(\text{OH})_5\text{NO}_3\cdot n\text{H}_2\text{O}$ interacts with NH_4F to form YF_3 and $\text{NH}_4\text{Y}_2\text{F}_7$, in the presence of $\text{NH}_4\text{OH}-\text{Y}(\text{OH})_{3-x}\text{F}_x$ and $\text{Y}_4\text{O}(\text{OH})_9\text{NO}_3$ [16]. The factors of temperature and duration of fluorination are practically not investigated in the literature. Layered rare-earth hydroxynitrates are usually used to obtain rare-earth fluorides, but there are a few works on fluorination of lanthanum hydroxysulfate [21] and yttrium hydroxychloride [18,22]. The above-mentioned references do not allow us to unambiguously identify the role of anionic composition on the LRH fluorination process. The anionic composition determines the interlayer distance and the stoichiometry of layered rare-earth hydroxides, so it can play an important role in the process of their fluorination. Moreover, the organic anion can significantly influence the morphology of the formed fluoride phases, acting as a surfactant [24].

In this work, fluorination of Eu-doped layered yttrium hydroxides (LYEuH) intercalated with different anions has been carried out. The influence of the intercalated anion nature on the composition, structure and morphology of fluorination products has been revealed. Both previously used anions (chloride and nitrate anions) in the fluorination reaction and a new organic anion, 4-sulfobenzoate, were chosen as LYEuH's intercalated anions. Special attention is paid to the influence of fluorination duration (2 – 48 h) and temperature (100 – 150 °C) on the products composition and structure.

2. Experimental section

The following reagents were used without additional purification: $\text{Y}(\text{NO}_3)_3\cdot 6\text{H}_2\text{O}$ (Aladdin, 99.5 %), $\text{Eu}(\text{NO}_3)_3\cdot 6\text{H}_2\text{O}$ (Aladdin, 99.9 %), NaCl (Shanghai lingfeng, 99.5 %), ammonia aqueous solution (Xilong scientific, 25%), potassium 4-sulfobenzoate (Aladdin, 95%), NaNO_3 (Shanghai lingfeng, 99.0%), and NaF (Shanghai lingfeng, 99.0%). Distilled water was used in all experiments.

To obtain Eu-doped layered yttrium hydroxychloride (Cl-LYEuH), 1 L aqueous solution containing 47.5 g $\text{Y}(\text{NO}_3)_3\cdot 6\text{H}_2\text{O}$, 2.794 g $\text{Eu}(\text{NO}_3)_3\cdot 6\text{H}_2\text{O}$ and 76.3 g NaCl was prepared. Aqueous ammonia solution was added to the prepared solution under constant stirring until pH=7.3. The obtained suspension was refluxed in a round bottom flask for 4 hours. The obtained precipitate was centrifuged, washed three times with water, then dried at 75% humidity over saturated NaCl solution at 60 °C for 10 days.

To obtain Eu-doped layered yttrium hydroxynitrate (NO_3 -LYEuH), 0.2 g of Cl-LYEuH was dispersed in 20 mL aqueous solution containing 2.55 g of sodium nitrate and left under constant stirring for 24 hours. The obtained precipitate was centrifuged, washed three times with water, then dried at 60 °C for 24 hours.

To obtain Eu-doped layered yttrium hydroxysulfobenzoate (4sb-LYEuH), 2.4 g of potassium 4-sulfobenzoate was dissolved in 200 mL of water and the resulting solution was adjusted to pH=6.8 with aqueous ammonia solution. 100 mg of Cl-LYEuH was suspended in 30 mL of the 4-sulfobenzoate solution, and the resulting suspension was hydrothermally treated in a 100 mL autoclave at 120 °C for 24 hours. The obtained precipitate was centrifuged, washed three times with water, then dried at 60 °C for 24 hours.

Fluorination of Eu-doped yttrium layered hydroxides was conducted according to the following scheme. Three different mixtures of 50 mL of 0.05 M NaF solution with 100 mg of Cl-LYEuH, or 110 mg of NO_3 -LYEuH, or 140 mg of 4sb-LYEuH (F:Ln ratio = 20:1) were prepared in a 100 mL Teflon autoclaves. The resulting suspensions were stirred for 5 minutes at room temperature, followed by hydrothermal treatment at 100 °C or 150 °C for 2 – 48 hours. The obtained precipitate was centrifuged, washed three times with water, then dried at 60 °C for 24 hours.

Powder X-ray diffraction (PXRD) of layered hydroxide samples was carried out by powder X-ray diffraction on a Tonga TDM-10 diffractometer using $\text{CoK}\alpha$ radiation, in the range of angles 2θ 5° – 65° with a step of 0.05°. The identification of the obtained phases was performed by comparison with previously obtained experimental diffractograms and with the PDF2 database. The unit cell parameters were refined by the Le-Bail method in MAUD software.

IR spectra were obtained in the mode of attenuated total reflection on an iCAN 9 FTIR spectrometer, using a ZnSe crystal with a resolution of 1 cm^{-1} .

Thermogravimetric analysis of 10 – 14 mg samples was performed on a Mettler Toledo TGA 2 analyzer when heated at a rate of 10K/min in an argon flow.

Microphotographs were obtained by scanning electron microscopy (SEM) on a Carl Zeiss NVision40 workstation with local X-ray spectral microanalysis (EDX). Elemental ratios were determined using INCA software.

Luminescence spectra of the powders were examined on a PerkinElmer FL8500 fluorescence spectrometer with a resolution of 0.1 nm. Excitation spectra were recorded at wavelength $\lambda_{em} = 616$ nm, luminescence spectra were recorded at wavelength $\lambda_{ex} = 394$ nm.

3. Results and discussion

According to PXRD data (Fig. 1), Cl-LYEuH was obtained without impurities as a single-phase (Fig. 1). The Cl-LYEuH diffractogram was indexed in orthorhombic system in P2_12_12 space group according to [25]. The Cl-LYEuH

TABLE 1. Fluorination conditions of layered rare-earth hydroxides according to literature data

Composition of LRHs	Reaction conditions	Composition of products	References
$\text{Ln}_2(\text{OH})_5\text{NO}_3 \cdot n\text{H}_2\text{O}$ Ln=Y/Eu or Y/Yb/Er	NH_4F F:Ln= 3 – 167 3 h 25 °C	$\text{Ln}_2(\text{OH})_5\text{F}$ $\text{Ln}(\text{OH})_{1.57}\text{F}_{1.43}$ $\text{NH}_4\text{Ln}_3\text{F}_{10}$ $\text{NH}_4\text{Ln}_2\text{F}_7$	[14]
$\text{Y}_2(\text{OH})_5\text{NO}_3 \cdot n\text{H}_2\text{O}$: Ln^{3+} Ln=Yb/Er, Yb/Tm	NaF 0.1 – 24 h 180 °C	$\beta\text{-NaYF}_4 \cdot \text{Ln}^{3+}$ (Ln=Yb/Er, Yb/Tm)	[15]
$\text{Y}_2(\text{OH})_5\text{NO}_3 \cdot n\text{H}_2\text{O}$: Eu^{3+} , Tb^{3+}	$\text{NH}_4\text{F} + \text{HNO}_3 + \text{MOH}$ (M = Li, Na, K) F:Ln=0.5-10 10 h 180 °C	YF_3 MY_mF_n $\text{Y}(\text{OH})_{3-m}\text{F}_m$	[16]
$\text{Ln}_2(\text{OH})_5\text{NO}_3 \cdot n\text{H}_2\text{O}$ Ln = Y, Pr–Lu	NH_4F 1 h 80 °C	$\text{Ln}(\text{OH})_{3-m}\text{F}_m$	[17]
$\text{Eu}_2(\text{OH})_5\text{Cl} \cdot n\text{H}_2\text{O}$	NaF 1 h 25 °C	$\text{Ln}_2(\text{OH})_5\text{F} \cdot n\text{H}_2\text{O}$	[18]
$(\text{Y}/\text{Eu})_2(\text{OH})_5\text{NO}_3 \cdot n\text{H}_2\text{O}$	NH_4F F:Ln=0.1 – 0.4 2 h 25 °C	$(\text{Y}/\text{Eu})_2(\text{OH})_5\text{F} \cdot n\text{H}_2\text{O}$	[19]
$\text{Ln}_2(\text{OH})_5\text{NO}_3 \cdot n\text{H}_2\text{O}$ Ln = Y, Pr–Er	KF 12 h 25 °C	$\text{Ln}_2(\text{OH})_5\text{F} \cdot n\text{H}_2\text{O}$	[20]
$(\text{La}_{0.97}\text{RE}_{0.01}\text{Yb}_{0.02})_2(\text{OH})_4\text{SO}_4 \cdot 2\text{H}_2\text{O}$ (RE = Ho, Er)	NH_4F F:Ln=5 0.5 – 24 h 25, 180 °C	$\text{Ln}_2(\text{OH})_4\text{F}_2 \cdot 2\text{H}_2\text{O}$ LnF_3	[21]
$\text{Y}_2(\text{OH})_5\text{Cl} \cdot 1.4\text{H}_2\text{O}$: Ln^{3+} Ln=Eu, Tb, Dy, Sm	NaF 3 h 180 °C	$\text{Y}(\text{OH})_{2.02}\text{F}_{0.98}$	[22]
$(\text{Y}_{0.95}\text{Eu}_{0.05})_2(\text{OH})_5\text{NO}_3 \cdot n\text{H}_2\text{O}$	NH_4F F:Ln= 1 – 66 3 h 90 °C	$\text{Y}(\text{OH})_{3-m}\text{F}_m$ $\text{K}_5\text{Ln}_9\text{F}_{32}$	[23]

cell parameters were refined as $a = 12.6855(15)$ Å, $b = 7.1671(7)$ Å and $c = 8.4373(9)$ Å. The parameters obtained are smaller than those for pure layered europium hydroxychloride ($a = 12.9155(3)$ Å, $b = 7.3763(1)$ Å, $c = 8.7023(3)$ Å) [26] and larger than those for pure layered yttrium hydroxychloride ($a = 12.6600(1)$ Å, $b = 7.1431(1)$ Å, $c = 8.4209(3)$ Å) [26]. This confirms the formation of layered yttrium-europium hydroxychloride solid solution. According to EDX data, the ratio Y:Eu:Cl=1:0.053(2):0.444(15), which is close to the nominal $(Y_{0.95}Eu_{0.05})_2(OH)_5Cl \cdot nH_2O$ composition.

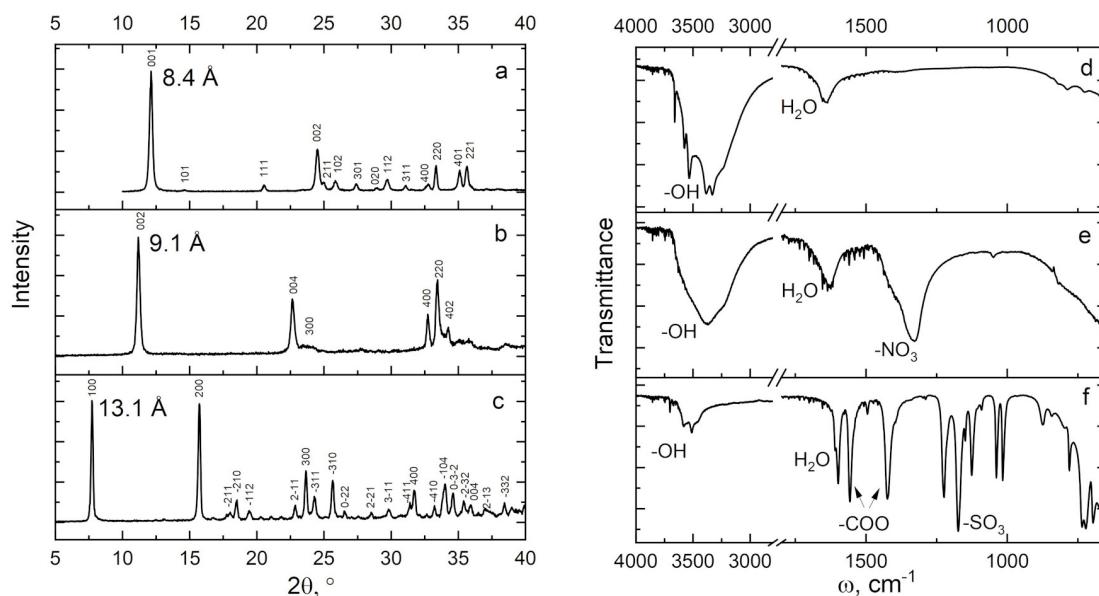


FIG. 1. Diffraction patterns (a–c) and FTIR spectra (d–f) of Eu-doped layered yttrium hydroxychloride (a, d – Cl–LYEuH) and products of its anion-exchange with sodium nitrate (b, e – NO₃–LYEuH) and potassium 4-sulfobenzoate (c, f – 4sb–LYEuH). Diffraction patterns were obtained using CoK α radiation

Figure 1 shows the diffraction patterns of NO₃–LYEuH (Fig. 1b) and 4sb–LYEuH (Fig. 1c) obtained by anion exchange from Cl–LYEuH. X-ray diffraction patterns were indexed according to literature data: NO₃–LYEuH in the Pc space group [27] and 4sb–LYEuH in the $P2_1/c$ space group [28]. As a result of anion-exchange reactions, the basal interlayer distance of Eu-doped layered yttrium hydroxide increases from 8.4 Å to 9.1 Å upon intercalation of nitrate anion (Fig. 1b) and to 13.1 Å upon intercalation of 4-sulfobenzoate anion (Fig. 1c). This agrees well with the increasing hydrated radius of anions in the series: chloride- (3.2 Å), nitrate- (3.5 Å) and 4-sulfobenzoate- anion (~8 Å) [29]. According to EDX data, the europium content is maintained in the range of 0.049 – 0.053 after anion exchange. The ratio $S/(Y+Eu)=0.28\pm 0.01$, which agrees well with the stoichiometric composition $(Y_{0.95}Eu_{0.05})_2(OH)_5(C_5H_4O_5S)_{0.5} \cdot nH_2O$ for 4sb–LYEuH.

The chloride substitution by nitrate and 4-sulfobenzoate anions is confirmed from the FTIR spectroscopy data in Fig. 1(d–f). On the FTIR spectrum of NO₃–LYEuH (Fig. 1e) a nitrate group stretching vibration band appeared with a maximum at 1624 cm^{-1} . A broad band in the NO₃–LYEuH FTIR spectra with a maximum at 3373 cm^{-1} is attributed to the O–H valence vibrations of intra-layer hydroxyl groups and inter-layer water molecules. In comparison with the FTIR spectrum of Cl–LYEuH (Fig. 1d), this band shows no fine structure, indicating the formation of more hydrogen bonds. A sulfate group stretching vibration band with a maximum at 1172 cm^{-1} and a carboxyl group stretching vibration band with a maximum at 1432 cm^{-1} appeared in the IR spectrum of 4sb–LYEuH (Fig. 1f) [28].

The PXRD results of Eu-doped layered yttrium hydroxychloride fluorination at 150°C for different durations are presented in Fig. 2. The interaction of Cl–LYEuH with sodium fluoride for 2 h results in a basal interlayer distance decrease from 8.4 Å to 7.4 Å, which is due to the replacement of chloride anions (of 3.2 Å hydrated radius) by smaller fluoride anions (of 2.6 Å hydrated radius) [29] and the formation of stronger and shorter hydrogen bonds involving the fluoride anion in the interlayer space of LRHs [20]. This substitution produces a phase of the $(Y_{0.95}Eu_{0.05})_2(OH)_5F \cdot nH_2O$ composition [14]. The diffraction pattern (Fig. 2Aa, marked with an asterisk) of the 2 hours fluorination product shows reflexes of the second phase – hexagonal Eu-doped yttrium hydroxyfluoride (YEuHF) of $Y_{0.95}Eu_{0.05}(OH)_{3-x}F_x$ composition (UCI₃ type system) [30]. This indicates that fluoride anions transform the layered structure by replacing some of the hydroxyl groups in it. Increasing the duration of hydrothermal treatment up to 12 h results in the formation of single-phase YEuHF. Further increase of duration does not affect the phase composition of the products. The matching of some reflections of Cl–LYEuH and YEuHF indicates the maintenance of some atomic planes during fluorination, which allows us to consider this transition as topotactic [15].

For single-phase $Y_{0.95}Eu_{0.05}(OH)_{3-x}F_x$ obtained from Cl-LYEuH, the a and c cell parameters have been calculated in the space group $P6_3/m$ ($Z = 2$) [30]. Both parameters slightly decrease with increasing fluorination duration: $a = 6.0486(14)$ Å, $c = 3.5610(8)$ Å for 12 h; $a = 6.0370(10)$ Å, $c = 3.5576(6)$ Å for 24 h; $a = 6.0348(23)$ Å, $c = 3.5542(15)$ Å for 48 h. Nishizawa et al [30] showed a near linear decrease in the parameter a (6.1976 – 6.0620 Å) with increasing x (0.65 – 1.43) in $Y(OH)_{3-x}F_x$. Decreasing of lattice parameters in our experiment likely indicates that x (in $Y_{0.95}Eu_{0.05}(OH)_{3-x}F_x$) increases with longer fluorination time. Although europium doping usually increases the parameters of yttrium compounds, in our case the parameter a is smaller in absolute value than for the variable composition phase $Y(OH)_{3-x}F_x$ ($x = 0.65 - 1.43$). This may indicate that $x > 1.43$, which is difficult to achieve by synthesis under mild hydrothermal conditions. According to the literature [31], sodium cations also contribute to the stabilization of phase with higher fluorine content, which could increase up to the formation of hexagonal $NaYF_4$ ($a = 5.966 - 5.976$ Å, $c = 3.518 - 3.531$ Å) [32, 33].

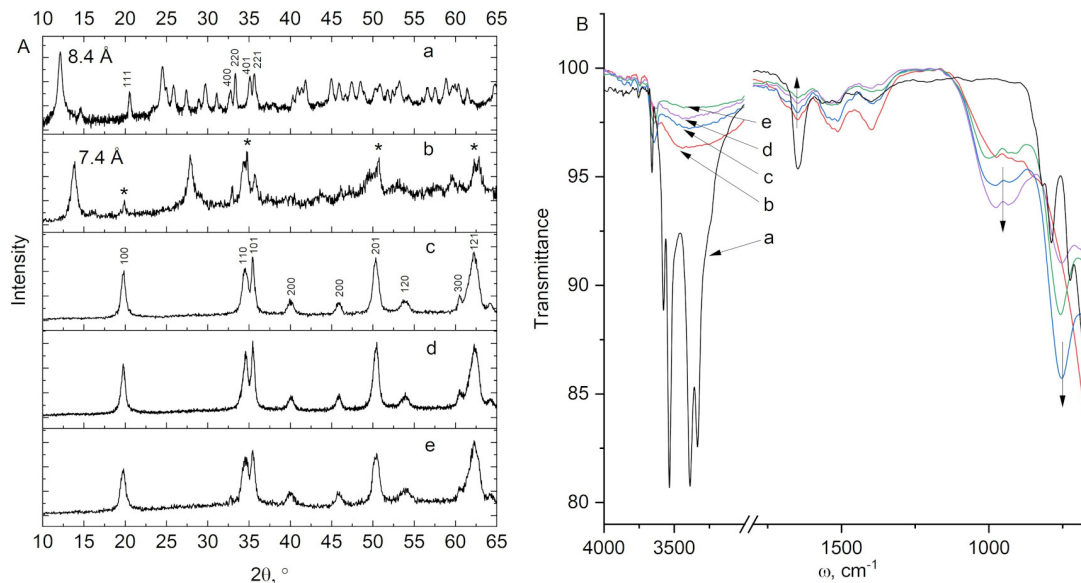


FIG. 2. (A) Diffraction patterns and (B) FTIR spectra of (a) Cl-LYEuH and the products of fluorination at 150 °C for (b) 2, (c) 12, (d) 24 and (e) 48 h. Diffraction patterns were obtained using $CoK\alpha$ radiation

Additional information on layered structure transformation during Cl-LYEuH fluorination is provided by FTIR spectroscopy data. After fluorination, the intensity of the OH stretching vibration bands (~ 3500 cm^{-1}) and HOH deformation vibrations band (~ 1650 cm^{-1}) decreases, indicating the substitution of hydroxyl groups by fluoride anions and the destruction of the layered structure, which leads to lower content of interlayer and intralayer water. At the same time, the band of water deformation vibrations (~ 1650 cm^{-1}) does not disappear completely, indicating that the composition of YEuHF can be rewritten as $Y_{0.95}Eu_{0.05}(OH)_{3-x}F_x \cdot mH_2O$. At the same time, the bands in the low-frequency region of the spectrum increase in intensity (~ 950 cm^{-1} and ~ 760 cm^{-1}). Despite the fact that these bands are characteristic for metal hydroxyfluorides [30, 34, 35], their interpretation is not obvious. Wan et al. [35] indicate that peaks at low wavenumbers ($1050 - 620$ cm^{-1}) are from M–OH and M–F bending mode vibration bands. Klevtsov et al [36] and He et al [34] attribute the absorption bands in the $550 - 800$ cm^{-1} region belong to the OH deformation frequencies. In the same region (< 1000 cm^{-1}), rocking modes of the coordinate water molecule can be observed [37].

One of the features of Eu^{3+} luminescence is the sensitivity to the local environment of europium cation [38]. This feature allows us to use luminescence spectroscopy as an additional tool for monitoring the local structure of rare-earth cations during fluorination. Fig. 3 shows the excitation ($\lambda_{em} = 616$ nm) and luminescence spectra ($\lambda_{ex} = 394$ nm) of Cl-LYEuH (Fig. 3a,c) and corresponding YEuHF (150 °C, 48 h) (Fig. 3b,d). The excitation spectra of the samples (Fig. 3a,b) are similar and in good agreement with literature data for layered europium hydroxychloride [25]. The luminescence spectra of the samples (Fig. 3c,d) excited through the maximum emission band ${}^7F_0 - {}^5L_6$ (394 nm) contain typical Eu^{3+} bands of ${}^5D_0 - {}^7F_J$ ($J = 0 - 4$) $f - f$ transitions. The ratio of the intensity ratio of the ${}^5D_0 - {}^7F_2$ electro-dipole transition (hypersensitive to the Eu^{3+} environment) to the intensity of the ${}^5D_0 - {}^7F_1$ magnetodipole transition (insensitive to the Eu^{3+} environment) increases with decreasing symmetry of the Eu^{3+} environment [39]. In layered rare-earth hydroxychloride structure, rare-earth cations occupy the eight-coordination and nine-coordination positions, in local symmetry groups of C_1 and C_{4v} , respectively [25]. After fluorination, the relative intensity of the ${}^5D_0 - {}^7F_2$ transition increases, indicating a decrease in the symmetry of the Eu^{3+} environment during fluorination. Apparently, there is a partial substitution of OH- by F- that generates some local distortions and symmetry descent.

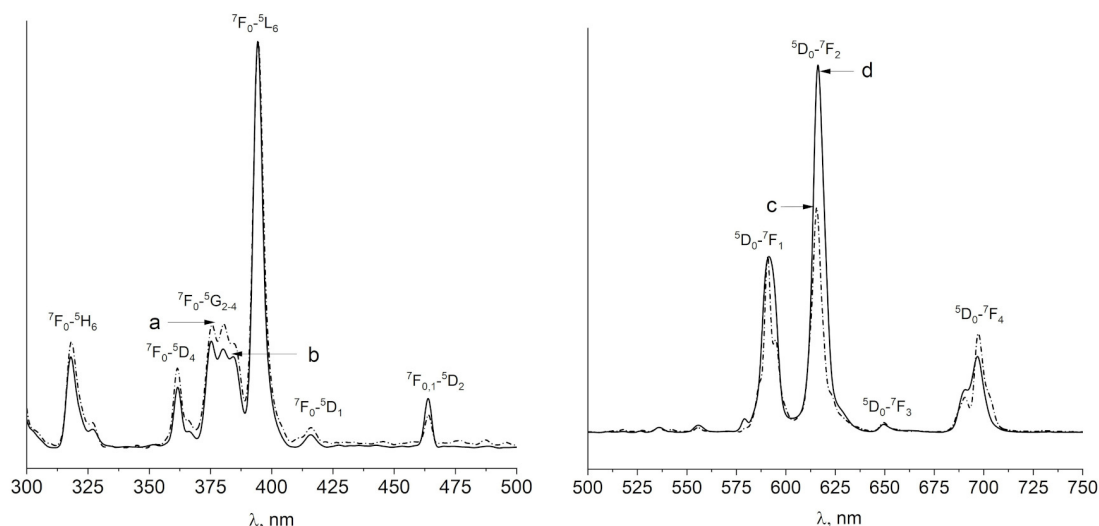


FIG. 3. Excitation (a, b) and emission (c, d) spectra of Cl-LYEuH (a, c) and the product of fluorination at 150 °C for 48 h (b, d)

Fig. 3a shows the thermal analysis data of Cl-LYEuH and its fluorination products at 150 °C for 2 h (Fig. 3b) and 48 h (Fig. 3c). Based on the mass loss in the first stage (25 – 220 °C), the hydrate water content of the Cl-LYEuH was refined as $(Y_{0.95}Eu_{0.05})_2(OH)_5Cl \cdot 1.6H_2O$. With increasing fluorination duration, a decrease in the total mass loss was observed, which is in good agreement with the decrease in the water content and hydroxyl groups in $Y_{0.95}Eu_{0.05}(OH)_{3-x}F_x \cdot mH_2O$ compared to $(Y_{0.95}Eu_{0.05})_2(OH)_5Cl \cdot 1.6H_2O$. Fig. 3d–f also shows differential thermal analysis data, which indicate a shift in the dehydroxylation temperature (220 – 350 °C) during the fluorination of $(Y_{0.95}Eu_{0.05})_2(OH)_5Cl \cdot 1.6H_2O$. For Cl-LYEuH, the temperature of the maximum dehydroxylation rate is 329 °C. After fluorination of Cl-LYEuH for 2 hours, the temperature decreases to 270 °C. This sample corresponds mainly to the $(Y_{0.95}Eu_{0.05})_2(OH)_5F \cdot nH_2O$ phase (Fig. 2b), which seems to be characterized by a smaller number of free hydroxyl groups displaced by the fluoride anion in interlayer space. The appearance of freer hydroxyl groups contributes to a lower removal temperature. Fluorination of Cl-LYEuH for 48 h results in the formation of the YEuHF phase, in which the hydroxyl groups are firmly bonded in the crystal structure. The larger number of halide ions and stronger OH-Hal hydrogen bonds in the case of $Y_{0.95}Eu_{0.05}(OH)_{3-x}F_x \cdot mH_2O$ compared to $(Y_{0.95}Eu_{0.05})_2(OH)_5Cl \cdot 1.6H_2O$ contribute to the increase of the dehydroxylation temperature up to 346 °C (Fig. 4f).

The results of PXRD and FTIR spectroscopy for the NO_3 -LYEuH fluorination at 150 °C are presented in Fig. 9 (see Appendix). As in the case of Cl-LYEuH (Fig. 2), fluorination occurs through the formation of the $(Y_{0.95}Eu_{0.05})_2(OH)_5F \cdot nH_2O$ phase (Fig. 9Ab) and is completed by the $Y_{0.95}Eu_{0.05}(OH)_{3-x}F_x \cdot mH_2O$ formation within

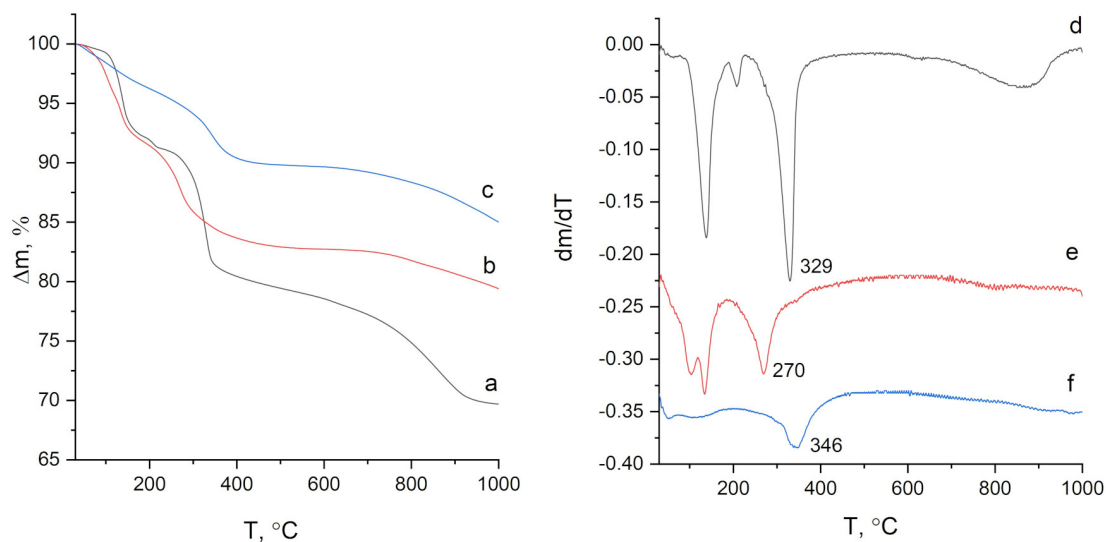


FIG. 4. Mass loss curves (a–c) and their derivatives (d–f) for Cl-LYEuH (a, d) and the products of fluorination at 150 °C for 2 h (b, e) and 48 h (c, f)

12 h (Fig. 9Ac). This is confirmed by FTIR spectroscopy data (Fig. 9B). After $\text{NO}_3\text{-LYEuH}$ fluorination, the nitrate stretching vibration band with a maximum at 1335 cm^{-1} completely disappears, and the intensity of the OH stretching vibration bands (3400 cm^{-1}) and the water deformation vibrations (1650 cm^{-1}) decreases. However, in comparison with the FTIR data for Cl-LYEuH fluorination (Fig. 2), there is a shift in the bands of deformation OH vibrations, which may indicate the formation of oriented attachment structures (mesocrystals) [34]. The disappearance of the narrow OH stretching vibration band of hydroxyl group ($> 3600\text{ cm}^{-1}$) indicates a high fluorination efficiency – the full replacement of free hydroxyl groups by fluoride ions. The higher efficiency of $\text{NO}_3\text{-LYEuH}$ fluorination compared to Cl-LYEuH is indicated by the smaller cell parameter a for YEuHF : $a = 6.0343(18)\text{ \AA}$, $c = 3.5546(10)\text{ \AA}$ for 12 h fluorination and $a = 6.0249(11)\text{ \AA}$, $c = 3.5553(5)\text{ \AA}$ for 48 h fluorination.

At $150\text{ }^\circ\text{C}$ there are no significant differences in the fluorination rates of Cl-LYEuH and $\text{NO}_3\text{-LYEuH}$. However, the situation changes when the temperature is reduced to $100\text{ }^\circ\text{C}$ (Fig. 5). As the temperature decreases, the rate of fluorination slows down in both cases. After 2 h of Cl-LYEuH fluorination, it was possible to obtain a single-phase of $(\text{Y}_{0.95}\text{Eu}_{0.05})_2(\text{OH})_5\text{F}\cdot n\text{H}_2\text{O}$ without impurity of $\text{Y}_{0.95}\text{Eu}_{0.05}(\text{OH})_{3-x}\text{F}_x\cdot m\text{H}_2\text{O}$ (Fig. 5a). The $\text{NO}_3\text{-LYEuH}$ fluorination rate at $100\text{ }^\circ\text{C}$ is markedly higher than that for Cl-LYEuH . The single phase $\text{Y}_{0.95}\text{Eu}_{0.05}(\text{OH})_{3-x}\text{F}_x\cdot m\text{H}_2\text{O}$ is formed within 24 h of $\text{NO}_3\text{-LYEuH}$ fluorination (Fig. 5d), while for Cl-LYEuH fluorination products, a mixture of $\text{Y}_{0.95}\text{Eu}_{0.05}(\text{OH})_{3-x}\text{F}_x\cdot m\text{H}_2\text{O}$ and $(\text{Y}_{0.95}\text{Eu}_{0.05})_2(\text{OH})_5\text{F}\cdot n\text{H}_2\text{O}$ phases is retained for the same time (Fig. 5b). Thus, it can be concluded that the $\text{NO}_3\text{-LYEuH}$ fluorination rate is higher than that for Cl-LYEuH .

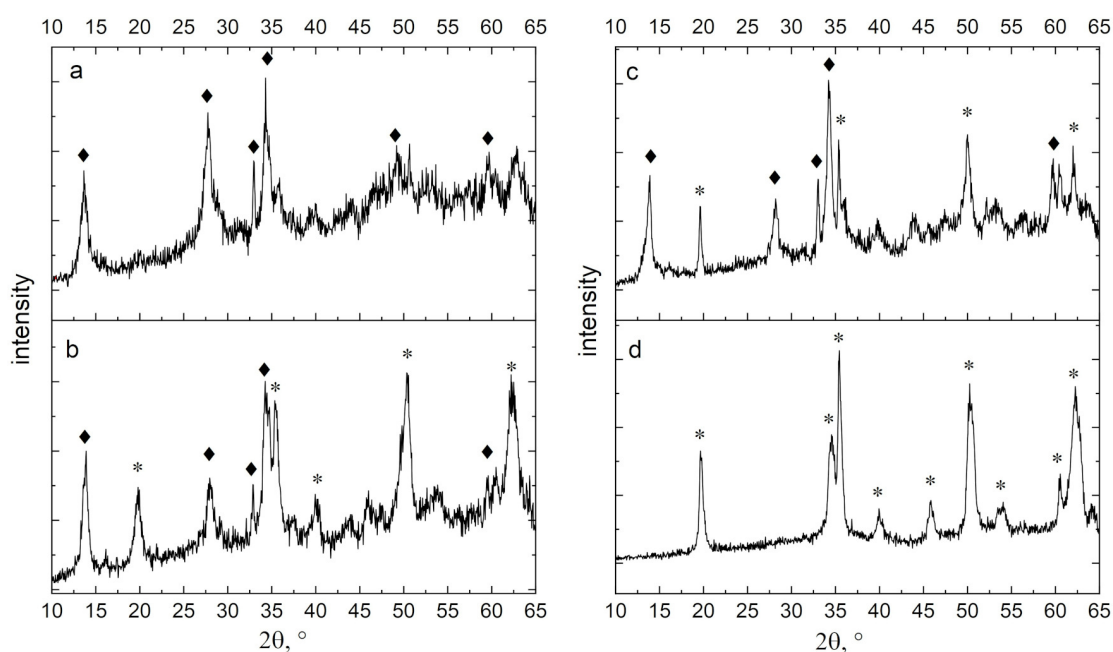


FIG. 5. X-ray diffraction patterns of (a,b) Cl-LYEuH and (c,d) $\text{NO}_3\text{-LYEuH}$ after fluorination at $100\text{ }^\circ\text{C}$ for (a,c) 2 h and (b,d) 24 h. \blacklozenge – $(\text{Y}_{0.95}\text{Eu}_{0.05})_2(\text{OH})_5\text{F}\cdot n\text{H}_2\text{O}$ phase, $*$ – $\text{Y}_{0.95}\text{Eu}_{0.05}(\text{OH})_{3-x}\text{F}_x\cdot m\text{H}_2\text{O}$ phase. Diffraction patterns were obtained using $\text{CoK}\alpha$ radiation

The 4sb-LYEuH fluorination process differs significantly from the Cl-LYEuH and $\text{NO}_3\text{-LYEuH}$ fluorination. According to PXRD (Fig. 6), the formation of single-phase $\text{Y}_{0.95}\text{Eu}_{0.05}(\text{OH})_{3-x}\text{F}_x\cdot m\text{H}_2\text{O}$ is observed within 2 h. The $(\text{Y}_{0.95}\text{Eu}_{0.05})_2(\text{OH})_5\text{F}\cdot n\text{H}_2\text{O}$ phase didn't appear during the 4sb-LYEuH fluorination process, which indicates different fluorination mechanism compared to the Cl-LYEuH and $\text{NO}_3\text{-LYEuH}$ fluorination. As well as the rates, the fluorination efficiency also increases for 4sb-LYEuH , as indicated by the decrease of the cell parameters of $\text{Y}_{0.95}\text{Eu}_{0.05}(\text{OH})_{3-x}\text{F}_x\cdot m\text{H}_2\text{O}$ to the minimum values of $a = 6.0041(10)\text{ \AA}$, $c = 3.5463(6)$ (4sb-LYEuH fluorination at $150\text{ }^\circ\text{C}$ for 48 h).

According to the FTIR spectroscopy data (Fig. 6B), 4sb-LYEuH fluorination for 2 – 12 h leads to a significant decrease in the OH stretching vibration band and 4-sulfobenzoate anion characteristic vibrations band intensities. This indicates the retention of trace amounts of organic anion in the fluorination products for 2 – 12 h. These bands disappear completely when the fluorination duration reaches 24 h, indicating the formation of a pure product. Note that water is practically absent in the fluorination products of 4sb-LYEuH , as indicated by the very low intensity of HOH vibration band in the region of 1650 cm^{-1} . This is in good agreement with the difference in the structure of 4sb-LYEuH [28] and Cl-LYEuH [26] or $\text{NO}_3\text{-LYEuH}$ [27]. Firstly, 4sb-LYEuH has lower water per rare-earth atom ratio, and secondly, water molecules in 4sb-LYEuH interlayer space do not coordinate to the rare-earth atoms [28]. That makes inclusion of water molecules in fluorinated structure very unlikely. In the case of Cl-LYEuH or $\text{NO}_3\text{-LYEuH}$, water molecules are involved

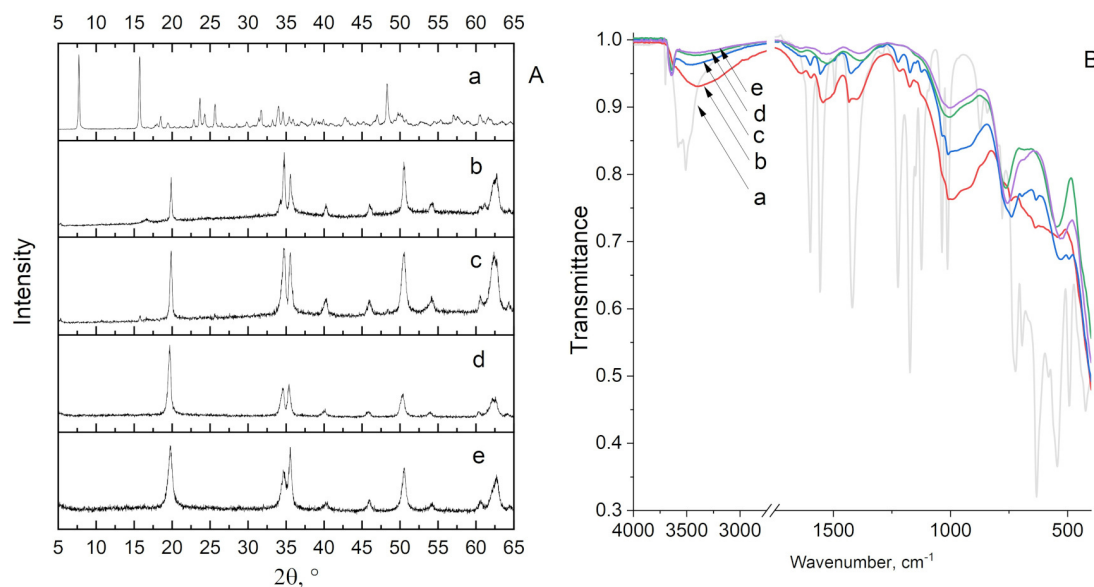


FIG. 6. (A) Diffraction patterns and (B) FTIR spectra of (a) 4sb-LYEuH and the products of fluorination at 150 °C for (b) 2, (c) 12, (d) 24 and (e) 48 h. Diffraction patterns were obtained using CoK α radiation

in the coordination sphere of rare-earth atoms [26,27], which significantly increases the probability of their capture during fluorination.

Figure 7a shows the content of elements (Y, Eu, F, Na) in the fluorination final products (duration of 48 h) of Cl-LYEuH, NO₃-LYEuH, and 4sb-LYEuH. Taking into account presence of sodium ions, the composition of fluorinated materials can be rewritten as Na_yY_{0.95}Eu_{0.05}(OH)_{3+y-x}F_x · mH₂O. According to EDX data for all compositions, $x \sim 3$, and $y \sim 0.2$. This indicates that the anionic composition does not affect the composition of the formed product. The anionic composition affects the fluorination rate, as can be seen in Fig. 7b, the rate increases in the series of anions: chloride, nitrate and 4-sulfobenzoate. The increase in the rate can be related to the increase in the interlayer distance in the corresponding series. The interlayer distance can be calculated by subtracting the thickness of the metal-hydroxide layer (5.5 Å) from the basal interlayer distance (Fig. 1) [9]. The corresponding value increases in the series of intercalated anions: chloride (2.9 Å), nitrate (3.6 Å) and 4-sulfobenzoate (7.6 Å). Apparently, increasing the interplanar distance accelerates the diffusion of fluoride anions into the yttrium-europium layered hydroxide structure, thereby increasing the contact area and interaction rate. In the case of 4-sulfobenzoate, the interplanar distance was so high that the formation of the intermediate phase of (Y_{0.95}Eu_{0.05})₂(OH)₅F · nH₂O was not observed.

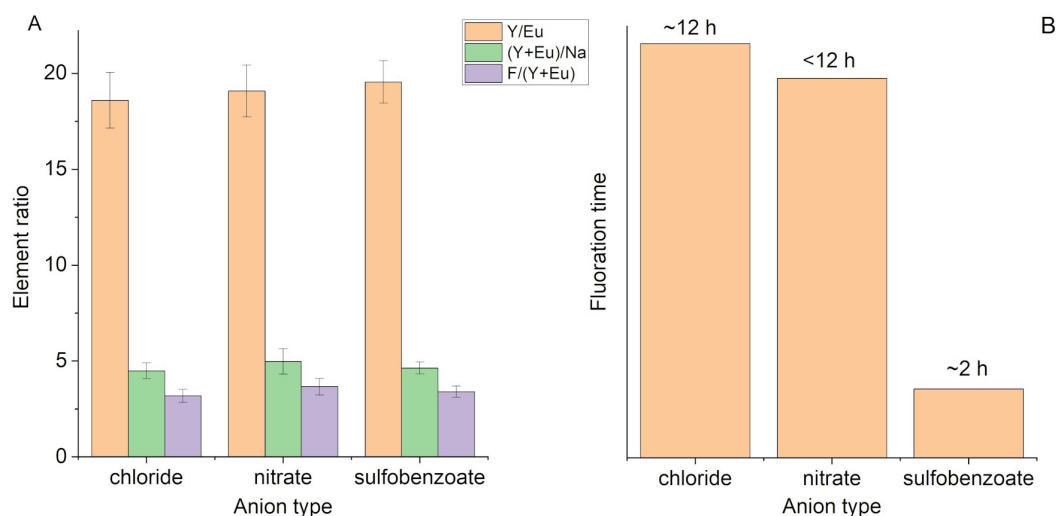


FIG. 7. (A) EDX data for Cl-LYEuH, NO₃-LYEuH, and 4sb-LYEuH after fluorination at 150 °C for 48 h. (B) Approximate duration of formation of single-phase Na_yY_{0.95}Eu_{0.05}(OH)_{3+y-x}F_x · mH₂O from Cl-LYEuH, NO₃-LYEuH, and 4sb-LYEuH at 150 °C

In order to investigate the mechanism of fluorination, the morphology of the obtained $\text{Na}_y\text{Y}_{0.95}\text{Eu}_{0.05}(\text{OH})_{3+y-x}\text{F}_x \cdot m\text{H}_2\text{O}$ particles was studied by scanning electron microscopy (Fig. 8). In all cases, fluorination results in the formation of rod-like nanoparticles of $\text{Na}_y\text{Y}_{0.95}\text{Eu}_{0.05}(\text{OH})_{3+y-x}\text{F}_x \cdot m\text{H}_2\text{O}$, whose size and shape differ depending on the anionic composition of the precursor. In the case of Cl–LYEuH and NO_3 –LYEuH fluorination, the morphology of the lamellar particles is partially preserved, indicating a topotactic reaction mechanism in these cases [15–17]. The tendency to morphology preservation is more remarkable for Cl–LYEuH, which can be explained by the lowest fluorination rate. In the case of NO_3 –LYEuH fluorination, the laminae are completely fragmented into rod-like particles, forming aggregates of interlocked particles like “bamboo mat”. Such structures are similar to the oriented attachment structures described for yttrium hydroxyfluorides [34, 40].

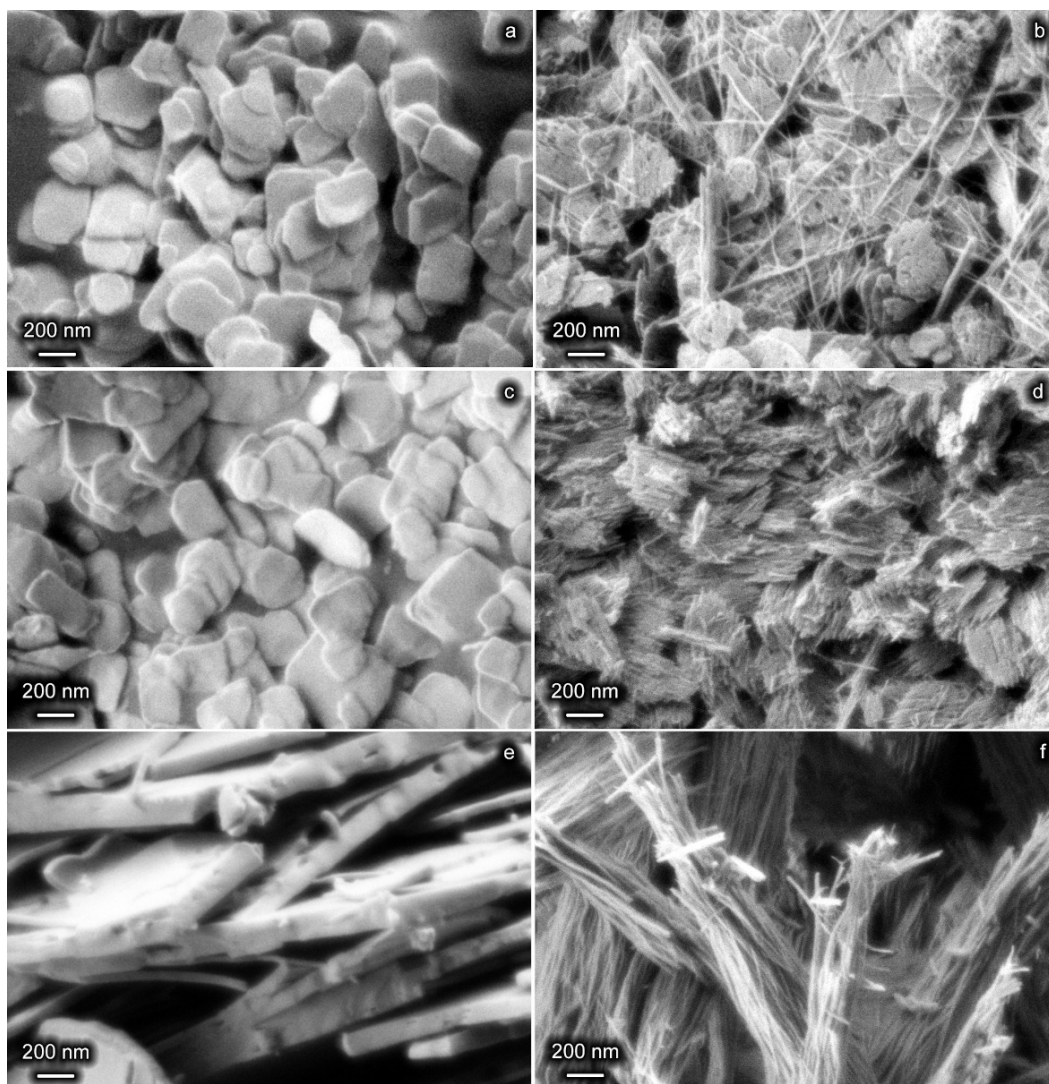


FIG. 8. SEM images of (a,b) Cl–LYEuH, (c,d) NO_3 –LYEuH, and (e,f) 4sb–LYEuH before (a,c,e) and after (b,d,f) their fluorination at 150 °C for 48 h

It should be noted that chloride anion is exchanged for nitrate anion at room temperature without change in the morphology of the lamellar particles (Fig. 8a,c). When the chloride anion is exchanged for 4-sulfobenzoate anion under hydrothermal conditions, the size of lamellar particles increases significantly (Fig. 8e), indicating the active participation of dissolution- recrystallization processes during ion exchange involving 4-sulfobenzoate anion. Despite the larger particle size, and thus slower diffusion of fluoride anions, the 4sb–LYEuH fluorination occurs most rapidly, indicating different fluorination mechanisms for 4sb–LYEuH and Cl–LYEuH or NO_3 –LYEuH. In the case of 4sb–LYEuH fluorination, sheaves of rod-like particles are formed without retaining a lamellar morphology, which agrees well with the mechanism proposed earlier in the literature for the fluorination of layered yttrium hydroxide [17]. This mechanism involves stages of ion exchange, exfoliation, oriented attachment, and Ostwald ripening. Exfoliation prevents the lamellar morphology from remaining as in the case of Cl–LYEuH or NO_3 –LYEuH. Thus, the anionic composition of the LRHs determines both the rate and mechanism of their fluorination process.

4. Conclusions

The interaction of Eu-doped layered yttrium hydroxide with aqueous solutions of sodium fluoride yielded the Eu-doped yttrium hydroxyfluoride phase of $\text{Na}_y\text{Y}_{0.95}\text{Eu}_{0.05}(\text{OH})_{3+y-x}\text{F}_x \cdot m\text{H}_2\text{O}$ ($x \sim 3$, $y \sim 0.2$) composition. For the first time, rare-earth hydroxyfluoride was prepared from layered rare-earth hydroxide intercalated with an organic (4-sulfobenzate) anion. It is shown that the increase in the reaction temperature (from 100 to 150 °C) and the increase in the interlayer distance of layered hydroxide lead to higher rate of fluorination. The formation rate of Eu-doped yttrium hydroxyfluoride increases in the following series of intercalated anions: chloride-, nitrate-, and 4-sulfobenzoate-anions. In the same series, the tendency to retain the morphology of lamellar particles after fluorination decreases. The high vs low fluorination rate, the absence vs presence of the intermediate $(\text{Y}_{0.95}\text{Eu}_{0.05})_2(\text{OH})_5\text{F} \cdot n\text{H}_2\text{O}$ phase and the sheaf-like vs lamellar morphology of the particles indicate difference in fluorination mechanism of Eu-doped layered hydroxysulfobenzoate and Eu-doped layered yttrium hydroxynitrate or hydroxychloride.

Appendix

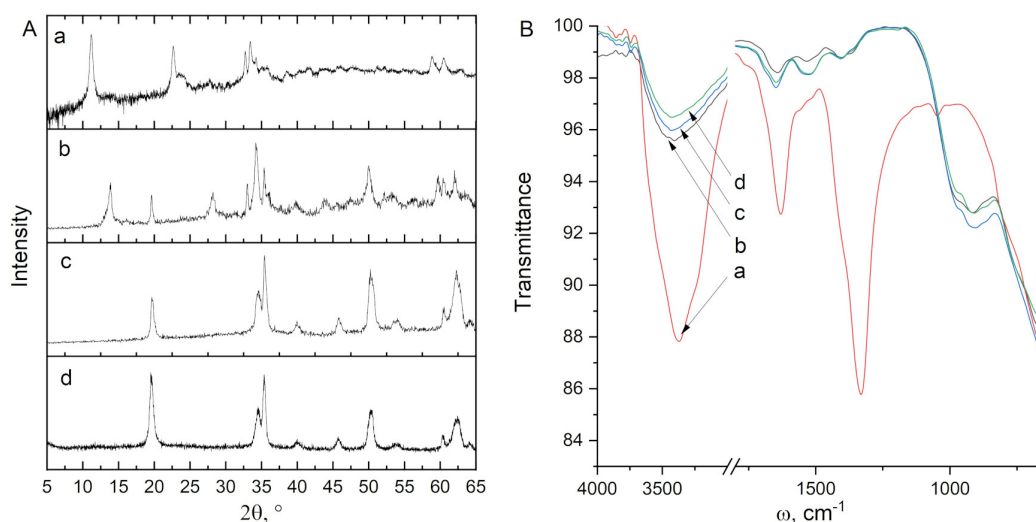


FIG. 9. (A) Diffraction patterns and (B) FTIR spectra of (a) $\text{NO}_3\text{-LYEuH}$ and the products of fluorination at 150 °C for (b) 2, (c) 12, and (d) 48 h.

References

- [1] Yao X., Wang R., Zhao J., Liu F., Jin Z., Wang Z., Wang F., Liu J., Wu. L. An overview of metal hydroxyfluoride—A novel semiconductor material *ChemPhysMater*, 2023, P. S2772571523000359.
- [2] Serna-Gallén P., Beltrán-Mir H., Cordoncillo E. The pH-dependent reactions in the sonochemical synthesis of luminescent fluorides: The quest for the formation of KY_3F_{10} crystal phases. *Ultrason. Sonochem.*, 2022, **87**, P. 106059.
- [3] Zhu L.-L., Liu B.-Q., Chen X.-Y., Feng A., Zhang Z.-J., Zhao J.-T. Synthesis, characterization and luminescence properties of $\text{NaY}(\text{OH})_x\text{F}_{4-x}$: Sm with spindle shape. *Mater. Res. Bull.*, 2015, **68**, P. 289–294.
- [4] Xu J., Zhu T., Chen X., Zhao D., Li Y., Zhang L., Bi N., Gou J., Jia L. Tri-channel tubular lanthanide nanocomposites for multimodal anti-counterfeiting. *J. Lumin.*, 2023, **256**, P. 119647.
- [5] Lima E., Pfeiffer H., Flores J. Some consequences of the fluorination of brucite-like layers in layered double hydroxides: Adsorption. *Appl. Clay Sci.* 2014, **88-89**, P. 26–32.
- [6] Booster J.L., Van Sandwijk A., Reuter M.A. Conversion of magnesium fluoride to magnesium hydroxide. *Miner. Eng.*, 2003, **16**(3), P. 273–281.
- [7] Timofeeva E., Orlovskaya E., Popov A., Shaidulin A., Kuznetsov S., Alexandrov A., Uvarov O., Vainer Y., Silaev G., Rähn M., Tamm A., Fedorenko S., Orlovskii Y. The Influence of Medium on Fluorescence Quenching of Colloidal Solutions of the Nd^{3+} : LaF_3 Nanoparticles Prepared with HTMW Treatment. *Nanomaterials*, 2022, **12**(21), P. 3749.
- [8] F. Gándara, J. Perles, N. Snejko, M. Iglesias, B. Gómez-Lor, E. Gutiérrez-Puebla, M.Á. Monge. Layered Rare-Earth Hydroxides: A Class of Pillared Crystalline Compounds for Intercalation Chemistry. *Angew. Chem. Int. Ed.*, 2006, **45**(47), P. 7998–8001.
- [9] Yaprntsev A.D., Baranchikov A.E., Ivanov V.K. Layered rare-earth hydroxides: a new family of anion-exchangeable layered inorganic materials. *Russ. Chem. Rev.*, 2020, **89**(6), P. 629–666.
- [10] Zhang H., Chen T., Qin S., Huang J., Wu X. Fabrication of REVO 4 films via sacrificial conversion from layered rare-earth hydroxide (LRH) films: the investigation of the transition mechanism and their photoluminescence. *Dalton Trans.*, 2022, **51**(14), P. 5577–5586.
- [11] Wang X., Sun M., Hu Z., Du P., Liu W., Zhang F., Li J.-G. Synthesis of $\text{NaLn}(\text{WO}_4)_2$ phosphors via a new phase-conversion protocol and investigation of up/down conversion photoluminescence. *Adv. Powder Technol.*, 2020, **31**(10), P. 4231–4240.
- [12] Wang Z., Li J.-G.G., Zhu Q., Li X., Sun X. Sacrificial conversion of layered rare-earth hydroxide (LRH) nanosheets into $(\text{Y}_{1-x}\text{Eu}_x)\text{PO}_4$ nanophosphors and investigation of photoluminescence. *Dalton Trans.*, 2016, **45**(12), P. 5290–5299.
- [13] Wang Z., Li J.-G., Zhu Q., Li X., Sun X. Hydrothermal conversion of layered hydroxide nanosheets into $(\text{Y}_{0.95}\text{Eu}_{0.05})\text{PO}_4$ and $(\text{Y}_{0.96-x}\text{Tb}_{0.04}\text{Eu}_x)\text{PO}_4$ ($x = 0\text{--}0.10$) nanocrystals for red and color-tailorable emission. *RSC Adv.*, 2016, **6**(27), P. 22690–22699.

- [14] Li J., Li J.-G., Zhu Q., Sun X. Room-temperature fluorination of layered rare-earth hydroxide nanosheets leading to fluoride nanocrystals and elucidation of down-/up-conversion photoluminescence. *Mater. Des.*, 2016, **112**, P. 207–216.
- [15] Feng Y., Shao B., Song Y., Zhao S., Huo J., Lü W., You H. Fast synthesis of β -NaYF₄ : Ln³⁺ (Ln = Yb/Er, Yb/Tm) upconversion nanocrystals via a topotactic transformation route. *CrystEngComm.*, 2016, **18**(39), P. 7601–7606.
- [16] Xu Z., Tang G., Meng W., Feng H., Zhang Z., Zhao J. Controlled synthesis of hydrophilic yttrium-based fluorides by transformation from layered rare-earth hydroxides. *Opt. Mater. Elsevier B.V.*, 2020, **108**(May), P. 110220.
- [17] Shao B., Zhao Q., Lv W., Jiao M., Lü W., You H. Novel Two-step topotactic transformation synthetic route towards monodisperse LnOF: Re,₃₊ (Ln = Y, Pr-Lu) Nanocrystals with down/upconversion luminescence properties. *Adv. Opt. Mater.*, 2015, **3**(4), P. 583–592.
- [18] Omwoma S., Stephen Odongo A., Otieno Z., Lagat S., Lalah J.O. Layered Rare-Earth Hydroxide Unilamellar Nanosheets: Synthesis, Characterization, and Adsorption. *J. Chem.*, 2020, **2020**, P. 8923871.
- [19] Liu S., Li J.G., Liu W., Cui H., Liu M., Chen J., Zhu H., Li X., Sun X. A novel method for improving particle growth and photoluminescence through F- substituting for gallery NO³⁻ in layered Y/Eu hydroxides. *Chem. Eng. J. Elsevier*, 2020, **380**, P. 122618.
- [20] Wu X., Li J.-G.J.G.J.-G.J.G., Zhu Q., Liu W., Li J.-G.J.G.J.-G.J.G., Li X., Sun X., Sakka Y. One-step freezing temperature crystallization of layered rare-earth hydroxide (Ln(2)(OH)(5)NO(3 center dot)nH(2)O) nanosheets for a wide spectrum of Ln (Ln = Pr-Er, and Y), anion exchange with fluorine and sulfate, and microscopic coordination probed via. *J. Mater. Chem. C.*, 2015, **3**(14), P. 3428–3437.
- [21] Wang X., Hu Z., Sun M., Du P., Liu W., Huang S., Li J.G. Phase-conversion synthesis of LaF₃:Yb/RE (RE = Ho, Er) nanocrystals with Ln₂(OH)₄SO₄ · 2H₂O type layered compound as a new template, phase/morphology evolution, and upconversion luminescence. *J. Mater. Res. Technol. Korea Institute of Oriental Medicine*, 2020, **9**(5), P. 10659–10668.
- [22] Dong J., Wang X., Xiong H., Song H., Wu R., Gan S. A novel synthetic route towards monodisperse yttrium hydroxide fluoride by anion exchange and luminescence properties. *Opt. Laser Technol.*, 2019, **111**, P. 372–379.
- [23] Li J., Wang X., Zhu Q., Kim B.-N., Sun X., Li J.-G. Interacting layered hydroxide nanosheets with KF leading to Y/Eu hydroxyfluoride, oxyfluoride, and complex fluoride nanocrystals and investigation of photoluminescence. *RSC Adv.*, 2017, **7**(83), P. 53032–53042.
- [24] Liu B.-Q., Guo K., Wang J., Zhang Z.-J., Tao Y., Huang Y., Zhao J.-T. Mild hydrothermal synthesis and photoluminescence of needle-like Y(OH)_{1.1}F_{1.9}:Tb³⁺. *Mater. Lett.*, 2013, **100**, P. 245–247.
- [25] Geng F. et al. New layered rare-earth hydroxides with anion-exchange properties. *Chem. - Eur. J.*, 2008, **14**(30), P. 9255–9260.
- [26] Geng F., Matsushita Y., Ma R., Xin H., Tanaka M., Izumi F., Iyi N., Sasaki T. General synthesis and structural evolution of a layered family of Ln₈(OH)₂₀Cl₄ · nH₂O (Ln = Nd, Sm, Eu, Gd, Tb, Dy, Ho, Er, Tm, and Y). *J. Am. Chem. Soc.*, 2008, **130**(48), P. 16344–16350.
- [27] Geng F., Matsushita Y., Ma R., Xin H., Tanaka M., Iyi N., Sasaki T., Renzhi M., Xin H., Tanaka M., Iyi N., Sasaki T., Ma R., Xin H., Tanaka M., Iyi N., Sasaki T. Synthesis and properties of well-crystallized layered rare-earth hydroxide nitrates from homogeneous precipitation. *Inorg. Chem.*, 2009, **48**(14), P. 6724–6730.
- [28] Yapryntsev A., Abdusatorov B., Yakushev I., Svetogorov R., Gavrikov A., Rodina A., Fatyushina Y., Baranchikov A., Zubavichus Y., Ivanov V. Eu-Doped layered yttrium hydroxides sensitized by a series of benzenedicarboxylate and sulphobenzoate anions. *Dalton Trans.*, 2019, **48**(18).
- [29] Marcus Y. Ionic radii in aqueous solutions. *Chem. Rev.*, 1988, **88**(8), P. 1475–1498.
- [30] Nishizawa H., Okumoto K., Mitsushio T. Preparation and thermal decomposition of yttrium hydroxide fluorides. *J. Solid State Chem.*, 1991, **92**(2), P. 370–379.
- [31] Grzechnik A., Bouvier P., Mezouar M., Mathews M.D., Tyagi A.K., Köhler J. Hexagonal Na_{1.5}Y_{1.5}F₆ at High Pressures. *J. Solid State Chem.*, 2002, **165**(1), P. 159–164.
- [32] Fedorov P., Mayakova M., Voronov V., Baranchikov A., Ivanov V. Preparation of “NaREF₄” phases from the sodium nitrate melt. *J. Fluor. Chem.*, 2019, **218**, P. 69–75.
- [33] Krämer K.W., Biner D., Frei G., Güdel H.U., Hehlen M.P., Lüthi S.R. Hexagonal Sodium Yttrium Fluoride Based Green and Blue Emitting Upconversion Phosphors. *Chem. Mater.*, 2004, **16**(7), P. 1244–1251.
- [34] He X., Yan B. Yttrium hydroxide fluoride based monodisperse mesocrystals: additive-free synthesis, enhanced fluorescence properties, and potential applications in temperature sensing. *CrystEngComm.*, 2015, **17**(3), P. 621–627.
- [35] Wan S., Qi J., Zhang W., Wang W., Zhang S., Liu K., Zheng H., Sun J., Wang S., Cao R. Hierarchical Co(OH)F Superstructure Built by Low-Dimensional Substructures for Electrocatalytic Water Oxidation. *Adv. Mater.*, 2017, **29**(28), P. 1700286.
- [36] Klevtsov P.V., Bembel' V.M., Grankina Z.A. Crystalline hydroxychlorides, Ln(OH)₂Cl, of the rare-earth elements of the cerium group. *J. Struct. Chem.*, 1970, **10**(4), P. 543–547.
- [37] Nakamoto K. *Applications in Coordination Chemistry. Infrared and Raman Spectra of Inorganic and Coordination Compounds*. John Wiley & Sons, Inc., 2008, P. 1–273.
- [38] Utochnikova V.V. The use of luminescent spectroscopy to obtain information about the composition and the structure of lanthanide coordination compounds. *Coord. Chem. Rev.*, 2019, **398**, P. 113006.
- [39] Binnemans K. Interpretation of europium(III) spectra. *Coord. Chem. Rev.*, 2015, **295**, P. 1–45.
- [40] Zhuang J., Yang X., Fu J., Liang C., Wu M., Wang J., Su Q. Monodispersed β -NaYF₄ Mesocrystals: In Situ Ion Exchange and Multicolor Up- and Down-Conversions. *Cryst. Growth Des.*, 2013, **13**(6), P. 2292–2297.

Submitted 19 December 2023; revised 4 February 2024; accepted 12 February 2024

Information about the authors:

Zhanbo Liu – Shenzhen MSU-BIT University, Shenzhen, PRC; ORCID 0009-0007-5390-2154; sdbzlzb@126.com

Svetlana V. Golodukhina – Shenzhen MSU-BIT University, Shenzhen, PRC; Kurnakov Institute of General and Inorganic Chemistry of the Russian Academy of Sciences, Moscow, Russia; ORCID 0000-0001-9317-1340; brightorangedandelion@gmail.com

Svetlana V. Kameneva – Shenzhen MSU-BIT University, Shenzhen, PRC; ORCID 0000-0003-4860-4973; kamenevasvetlanav@gmail.com

Alexey D. Yapryntsev – Shenzhen MSU-BIT University, Shenzhen, PRC; Kurnakov Institute of General and Inorganic Chemistry of the Russian Academy of Sciences, Moscow, Russia; ORCID 0000-0001-8166-2476; yapryntsev@igic.ras.ru

Conflict of interest: the authors declare no conflict of interest.

Synthesis of strontium fluoride nanoparticles in a microreactor with intensely swirling flows

Rufat Sh. Abiev^{1,2}, Andrey V. Zdravkov¹, Yuliya S. Kudryashova¹, Alexander A. Alexandrov³, Sergey V. Kuznetsov³, Pavel P. Fedorov³

¹Institute of Silicate Chemistry I. V. Grebenshchikov RAS, St. Petersburg, Russia

²St. Petersburg State Institute of Technology, St. Petersburg, Russia

³Prokhorov General Physics Institute of the Russian Academy of Sciences, Moscow, Russia

Corresponding author: Pavel P. Fedorov, ppfedorov@yandex.ru

ABSTRACT The technique of micromixing was used for synthesis of SrF₂ nanopowders in a microreactor with intensely swirling flows. The chemical reaction between aqueous solutions of strontium nitrate ($C(\text{Sr}(\text{NO}_3)_2) = 0.15 - 0.45 \text{ M}$) and potassium fluoride ($C(\text{KF}) = 0.3 - 0.9 \text{ M}$) was realized in a microreactor with intensely swirling flows with reagent consumption 1.5 – 3.5 L/min. Colloidal solutions were obtained, during the settling of which SrF₂ powders were isolated without crystallographic faceting. An increase in the rate of reagent flow has negligible effect on the size of coherent scattering regions D , while an increase in the concentration of solutions leads to an increase in D from ~ 20 to $\sim 30 \text{ nm}$.

KEYWORDS strontium fluoride, precipitation, chemical reaction, micromixing

ACKNOWLEDGEMENTS This work was done as a part of State assignment of the Institute of Silicate Chemistry (Project No. 1021050501070-0-1.4.3 (0081-2022-0006)) and Prokhorov General Physics Institute RAS (Project No. 0097-2019-0017). The study was carried out using the equipment of the Collective Use Centers of Prokhorov General Physics Institute RAS and Kurnakov Institute of General and Inorganic Chemistry RAS.

FOR CITATION Abiev R.Sh., Zdravkov A.V., Kudryashova Yu.S., Alexandrov A.A., Kuznetsov S.V., Fedorov P.P. Synthesis of strontium fluoride nanoparticles in a microreactor with intensely swirling flows. *Nanosystems: Phys. Chem. Math.*, 2024, **15** (1), 115–121.

1. Introduction

Strontium fluoride SrF₂ is an ionic compound and dielectric with a large band gap. It crystallizes in a cubic *fcc* lattice, SSG *Fm-3m*. SrF₂ crystals, transparent in the UV, visible and IR ranges, are photonics materials [1]. Strontium fluoride occurs in nature as a rare mineral strontiofluorite [2]. Strontium fluoride easily dissolves fluorides of rare earth elements RF₃ to form solid solutions Sr_{1-x}R_xF_{2+x} ($x \leq 0.5$) [3]. Single crystals and ceramics of strontium fluoride doped with the rare earth ions are used as laser elements [4–9], effective phosphors [10] and fluoride solid electrolytes [11]. At the same time, activated strontium fluoride powders are precursors of optical ceramics [12–19], single crystals [20, 21] and films, and are also of independent interest as phosphors [22–31], including as part of composites [32].

Various methods are used for the synthesis of strontium fluoride powders [33, 34], including precipitation from aqueous solutions [13–15, 35, 36], hydro- and solvothermal synthesis [37–51], synthesis from solutions in a melt (flux technique) [52–54], sol-gel [55–59], combustion synthesis [60, 61], synthesis using ionic liquids [52], thermal decomposition of precursors [62], high-energy ball milling [63], chemical reaction at the solution/vapor interface [64], etc. In the synthesis by precipitation from aqueous solutions by chemical reactions, various fluorinating agents were used – solutions of hydrofluoric acid [35], sodium fluoride [36, 65], potassium fluoride [13–15, 36, 65], and ammonium fluoride [12, 22, 36].

When synthesizing nanopowders, including nanofluorides, at the first exploratory stages of research, not enough attention is paid to the hardware design of the process. The main efforts are aimed at clarifying the functional characteristics of the samples obtained. However, when scaling processes, taking into account the need for reproducibility of product characteristics, the hardware factor comes to the fore.

The influence of the correctness of the conditions of mixing processes, especially micromixing, on the quality of synthesized materials still remains insufficiently evaluated in the processes of solution chemistry [66]. At the same time, the organization of such conditions that allow the reagents to be distributed at the molecular or ionic level with the necessary degree of uniformity of their distribution in micro-volumes is an obvious prerequisite for obtaining nanoparticles with specified characteristics. Previously, the possibility of synthesis of nanoscale particles of oxides and fluorides in microreactors with impinging jets [67–70] and in microreactors with intensely swirling flows [67, 71–74] was experimentally proved. The influence of specific energy dissipation rate on micromixing quality was demonstrated experimentally by means of iodide-iodate method widely used for microreactors with ultimate level of micromixing [74].

The developed microreactor with impinging swirling flows of reagent solutions [67] allows one to realize a micromixing time of about 0.01 sec by creating a powerful swirling flow in a limited small volume (about 0.2 ml), where the main amount of energy is dissipated, and to carry out fine individual adjustment of the flow rate of solutions supplied to the reaction zone. The device is characterized by high performance.

This work is aimed to synthesis powders of strontium fluoride, pure and doped with erbium and ytterbium ions, by chemical precipitation reaction in a microreactor with swirling flows of reagent solutions.

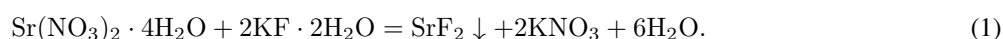
2. Experimental details

2.1. Samples preparation

The design of the microreactor with impinging swirling flows is described in [72]. The reactor from pyrex glass has two tangentially arranged nozzles for the supply of the initial components and a nozzle for the discharge of products. Characteristic dimensions of the device: the diameter of the wide part of the body is 20 mm, the diameter of the narrow part (neck) is 4 mm, the diameters of the tangential pipes are 4 mm.

The solutions of the initial media are pumped from external tanks into the pipes with the specified flow rates Q . When the solutions of the initial media are fed into the tangential pipes, the flows are swirled. Moreover the circumferential and axial velocity vectors of the two mixed flows in the mixing chamber are directed in the opposite direction. In the neck zone, extremely intensive mixing of all the supplied components occurs, due, firstly, to the high level of velocities (axial and tangential) in this zone, and secondly, to the powerful shear field induced by high velocities.

The following reagents were used for the synthesis of strontium fluoride: strontium nitrate tetrahydrate $\text{Sr}(\text{NO}_3)_2 \cdot 4\text{H}_2\text{O}$ (pure grade), potassium fluoride dihydrate $\text{KF} \cdot 2\text{H}_2\text{O}$ (pure grade), and distilled water. The synthesis was carried out at room temperature. The synthesis process can be described by the following equation:



The obtained samples were taken within 1 – 2 minutes to minimize the growth of particles in the suspension and their aggregation. The sediment was washed by decantation (on the Buchner funnel, the sediment passed through the “green ribbon” filter with pores of 3 – 5 microns). Immediately after washing, the samples were dried in a drying box. We varied the flow rates Q (1.5, 2.5 and 3.2 l/min) and the concentrations of the initial solutions (0.15, 0.30, 0.45 M $\text{Sr}(\text{NO}_3)_2$). The concentration of potassium fluoride in the solution was twice as high to ensure stoichiometry. The prepared solutions were kept for at least 12 hours before the experiments.

2.2. Samples characterization

The synthesized powders were characterized by X-ray phase analysis (XRD) and scanning electron microscopy (SEM). XRD was performed on a Bruker Advanced D8 diffractometer ($\text{CuK}\alpha$ radiation). Lattice parameters (a) and coherent scattering regions (D) were calculated using the TOPAS software ($R_{wp} < 5$).

Morphology and particle size were carried out on a Carl Zeiss NVision 40 electron scanning microscope (Germany) with an Oxford Instruments X-MAX microprobe analyzer (UK) (80 mm^2) for the energy dispersive analysis (EDX).

3. Results and discussion

Synthesis conditions, lattice parameters, coherent scattering regions are summarized in Table 1. X-ray patterns are shown in Fig. 1, micrographs – in Fig. 2. According to X-ray diffraction data, well-formed strontium fluoride nanopowders were obtained in all cases. The product lattice parameters within the error range correspond to strontium fluoride ($a = 5.800 \text{ \AA}$, JCPDS card # 06-0262). The particles are spherical without agglomerations with mean size about 20 – 30 nm. The values of the coherent scattering regions D are weakly dependent on the flow rates (Fig. 3a), but they increase markedly with increasing concentrations of solutions (Fig. 3b).

Note that strontium fluoride nanoparticles obtained as a result of syntheses are not faceted. The absence of faceting at a low synthesis temperature is a sign of processes far from equilibrium, namely, a sign of a non-classical mechanism of crystal growth by agglomeration of nanoparticles [53].

4. Conclusion

The use of a reactor with intensively swirled flows in synthesis by the method of precipitation from aqueous solutions makes it possible to regulate the driving forces of the process under conditions of intensive mixing by changing the concentration of solutions and increasing the feed rate of reagents. The use of this technique makes it possible to scale the process and obtain kilogram quantities of powder in a continuous process. The possibility of using such a reactor is shown in the synthesis of strontium fluoride nanopowders by the reaction of strontium nitrate solutions with potassium fluoride. Powders with the size of coherent scattering regions of 18 – 32 nm were obtained.

The data obtained indicate that the change in the flow rates of reagents does not significantly affect the average size of the resulting particles. This result could be explained as follows: even at the lowest flow rate of supplied solutions within studied range (from 1.5 to 3.2 L/min) the specific energy dissipation rate in the microvolume of reagents contacting was

TABLE 1. Concentration of initial solutions C , flow rates Q , lattice parameter a , and values of coherent scattering regions D

No.	$C(\text{Sr}(\text{NO}_3)_2)$, M	$C(\text{KF})$, M	Q , L/min	Lattice parameter a , Å	D , nm
1	0.15	0.3	1.5	5.8003(1)	20.1(1)
2	0.30	0.6	1.5	5.8004(1)	25.8(1)
3	0.45	0.9	1.5	5.8008(1)	30.5(1)
4	0.15	0.3	2.5	5.7999(1)	20.4(1)
5	0.30	0.6	2.5	5.8006(1)	24.3(1)
6	0.45	0.9	2.5	5.8004(1)	32.4(1)
7	0.15	0.3	3.2	5.8008(1)	18.1(1)
8	0.30	0.6	3.2	5.8010(1)	22.0(1)
9	0.45	0.9	3.2	5.8010(1)	29.0(1)

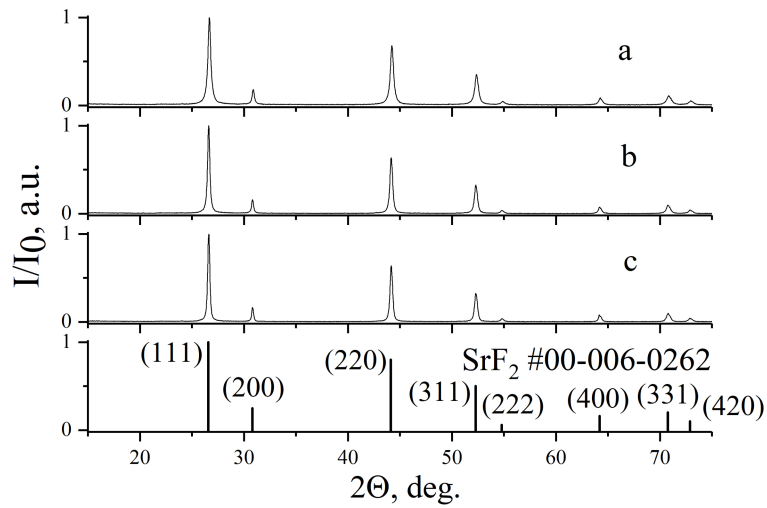


FIG. 1. XRD patterns of the samples # 1(a), 2(b), 3 (c) and SrF_2

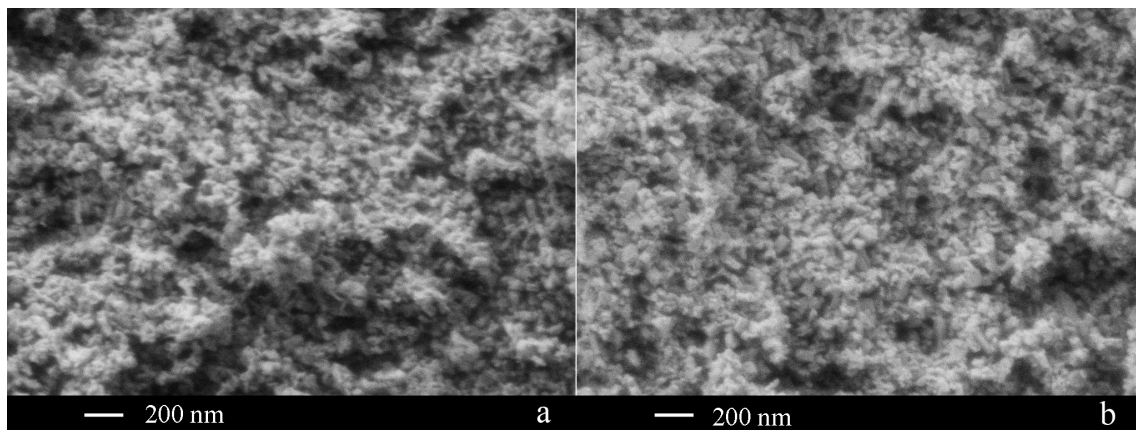


FIG. 2. SEM images of samples 1 (a) and 9 (b)

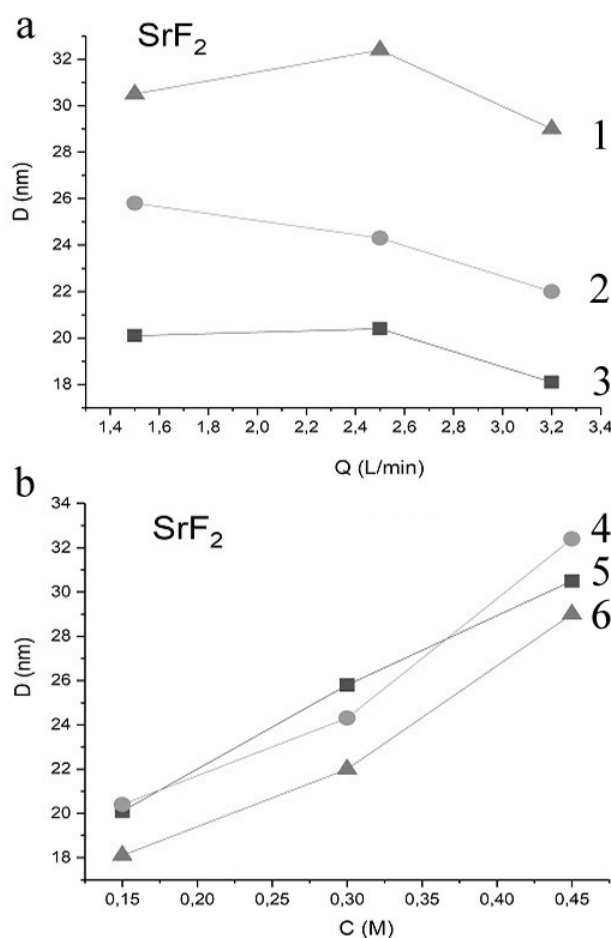


FIG. 3. The dependence of the coherent scattering values of D strontium fluoride nanoparticles synthesized in a reactor with swirling flows at different on the flow rates (a) and the concentration of strontium nitrate (b). Notations: M $\text{Sr}(\text{NO}_3)_2$ is equal to 0.45 (1); 0.30 (2); 0.15 (3); Q is equal to 2.5 L/min (4); 1.5 L/min (5); and 3.2 L/min (6).

high enough to ensure the necessary level of micromixing. This is consistent with the results obtained in the synthesis of calcium fluoride nanopowders using intensively swirled flows [67]. At the same time, as the concentration of reacting solutions increases, the particle size increases linearly in the first approximation.

Since the size of nanoparticles is an essential parameter regulating the luminescence intensity [74], the revealed patterns may be essential for optimizing technological processes, although the nature of them is not completely clear.

References

- [1] Zverev V.A., Krivopustova E.V., Tochilina T.V. *Optical materials*. Part 2. St.-Petersburg: ITMO, 2013, 248 p. (in Russian)
- [2] Yakovenchuk V.N., Ivanyuk G.Yu., Pakhomovsky Y.A., et al. Strontiofluorite, SrF_2 , a new mineral species from the Khibiny massif, Kola peninsula, Russia. *The Canadian Mineralogist*, 2010, **48**, P. 1487–1492.
- [3] Sobolev B.P., Seiranian K.B. *J. Solid State Chem.*, 1981, **39** (2), 17
- [4] Kaminskii A.A. *Laser Crystals. Their Physics and Properties*. Berlin, Springer, 1990.
- [5] Sobolev B.P. *The Rare Earth Trifluorides. Part 2. Introduction to materials science of multicomponent metal fluoride crystals*. Barcelona: Institut d'Estudis Catalans. 2001, 459 p.
- [6] Moncorge R., Braud A., Camy P., Doualan J.L. Fluoride laser crystals. In: *Handbook on solid-state lasers: materials, systems and applications*. Ed. by B. Denker, E. Shklovsky. Oxford Cambridge Philadelphia New Delhi, Woodhead Publishing Limited, UK, 2013, p. 82–109.
- [7] Druon F., Ricaud S., Papadopoulos D.N., Pellegrina A., Camy P., Doualan J.L., Moncorge R., Courjaud A., Mottay E., Georges P. On $\text{Yb}:\text{CaF}_2$ and $\text{Yb}:\text{SrF}_2$: review of spectroscopic and thermal properties and their impact on femtosecond and high power laser performance. *Opt. Mater. Express*, 2011, **1**, P. 489–502.
- [8] Alimov O.K., Basiev T.T., Doroshenko M.E., Fedorov P.P., Konyuskin V.A., Nakladov A.N., Osiko V.V. Investigation of Nd^{3+} ions spectroscopic and laser properties in SrF_2 fluoride single crystal. *Opt. Mater.*, 2012, **34** (5), P. 799–802.
- [9] Li W., Mei B., Song J. Nd^{3+} , Y^{3+} -codoped SrF_2 laser ceramics. *Opt. Mater.*, 2015, **47**, P. 108–111.

- [10] Saleta Reig D., Grauel B., Konyushkin V.A., Nakladov A.N., Fedorov P.P., Busko D., Howard I.A., Richards B.S., Resch-Genger U., Kuznetsov S.V., Turshatov A., Würth C. Upconversion properties of SrF₂:Yb³⁺, Er³⁺ single crystals. *J. Mat. Chem. C*, 2020, **8**, P. 4093–4101.
- [11] Sorokin N.I., Sobolev B.P. Correlation between the Fluorine Ion Conductivities of Sr_{1-x}R_xF_{2+x} (CaF₂ Type) and R_{1-y}Sr_yF_{3-y} (LaF₃ Type) Crystals in the SrF₂-RF₃ Systems (R = La–Nd). *Physics of the Solid State*, 2019, **61** (11), P. 2064–2069.
- [12] Rozhnova Yu.A., Kuznetsov S.V., Luginina A.A., Voronov V.V., Ryabova A.V., Pominova D.V., Ermakov R.P., Usachev V.A., Kononenko N.E., Baranchikov A.E., Ivanov V.K., Fedorov P.P. New Sr_{1-x-y}R_x(NH₄)_yF_{2+x-y} (R = Yb, Er) solid solution as precursor for high efficiency up-conversion luminophor and optical ceramics on the base of strontium fluoride. *Mater. Chem. Physics.*, 2016, **172**, P. 150–157.
- [13] Zhu T., Mei B., Li W., Yang Y., Song J. Fabrication, microstructure and spectral properties of Nd:SrF₂ transparent ceramics with different concentration of La³⁺ ions. *Opt. Mater.*, 2019, **89**, P. 598–603.
- [14] Gao Y., Mei B., Li W., Zhou Z., Liu Z. Effect of Yb³⁺ concentration on microstructure and optical properties of Yb: SrF₂ transparent ceramics. *Opt. Mater.*, 2020, **105**, 109869.
- [15] Yi G., Mei B., Li W., Song J., Liu Z., Zhou Z., Su L. Synthesis and luminescence characterization of Pr³⁺, Gd³⁺ co-doped SrF₂ transparent ceramics. *J. Am. Ceram. Soc.*, 2020, **103** (1), P. 279–286.
- [16] Zheng C., Sun Z., Li W., Yang Y., Mei B. Fabrication and spectral properties of Dy: SrF₂ transparent ceramics. *Mater. Chem. Phys.*, 2021, **273**, 125141.
- [17] Liu Z., Ji Y., Xu C., Wang Y., Liu Y., Shen Q., Yi G., Yu Y., Mei B., Liu P., Jing Qi. Microstructural, spectroscopic and mechanical properties of hot-pressed Er:SrF₂ transparent ceramics. *J. Eur. Ceram. Soc.*, 2021, **41**, P. 4907–4914.
- [18] Yang Y., Zhou Z., Mei B., Zhang Y., Liu X. Fabrication and upconversion luminescence properties of Er:SrF₂ transparent ceramics compared with Er:CaF₂. *Ceram. Int.*, 2021, **47**, P. 17139–17146.
- [19] Qin S., Song J., Wang W., Mei B., Li W., Xia Y. Study in optical and mechanical properties of Nd³⁺, Y³⁺: SrF₂ transparent ceramics prepared by hot-pressing and hot-forming techniques. *Crystals*, 2019, **619**.
- [20] Arnold M., Katzmann J., Naik A., Görne A.L., Härtling T., George J., Schuster C. Investigations on electron beam irradiated rare-earth doped SrF₂ for application as low fading dosimeter material: evidence for and DFT simulation of a radiation-induced phase. *J. Mater. Chem. C*, 2022, **10**, P. 11579–11587.
- [21] Yagoub Y.A., Swart H.C., Coetsee E. Luminescent behavior of SrF₂ and CaF₂ crystals doped with Eu ions under different annealing temperatures. *J. Alloys and Compd.*, 2021, **858**, 157741.
- [22] Wolfbeis S. An overview of nanoparticles commonly used in fluorescent bioimaging. *Chem. Soc. Rev.*, 2015, **44**, P. 4743–4768.
- [23] Richards B.S., Hudry D., Busko D., Turshatov A., Howard I.A. Photon upconversion for photovoltaics and photocatalysis. *Chem. Rev.*, 2021, **121**, P. 9165–9195.
- [24] Brites C.D.S., Marin R., Suta M., Carneiro Neto A.N., Ximenes E., Jaque D., Carlos L.D. Spotlight on luminescence thermometry: basics, challenges, and cutting-edge applications. *Advanced Materials*, 2023, **35**, 2302749.
- [25] Park C., Park S. Effective up-conversion behaviors for Er³⁺-Yb³⁺-doped SrF₂ phosphors synthesized by flux-assist method. *J. Mater. Sci. Mater. Electron.*, 2020, **31**, P. 832–837.
- [26] Joseph R.E., Hudry D., Busko D., Biner D., Turshatov A., Krämer K., Richards B.S., Howard I.A. Bright constant color upconversion based on dual 980 and 1550 nm excitation of SrF₂:Yb³⁺, Er³⁺ and β-NaYF₄:Yb³⁺, Er³⁺ micropowders – considerations for persistence of vision displays. *Opt. Mater.*, 2021, **111**, 110598.
- [27] Runowski M., Marciniak J., Grzyb T., Przybylska D., Shyichuk A., Barszcz B., Katrusiak A., Lis S. Lifetime nanomanometry – high-pressure luminescence of up-converting lanthanide nanocrystals – SrF₂:Yb³⁺,Er³⁺. *Nanoscale*, 2017, **9**, P. 16030–16037.
- [28] Ryszczynska S., Grzyb T. NIR-to-NIR and NIR-to-Vis up-conversion of SrF₂:Ho³⁺ nanoparticles under 1156 nm excitation. *Methods Appl. Fluoresc.*, 2022, **10**, 024001.
- [29] Zeng Q., He W., Luan F., Yan Y., Du H., Fu J., Guo D. Insight into the mechanism of intense NIR-to-red upconversion luminescence in Er³⁺-doped and Er³⁺-Yb³⁺ co-doped SrF₂ nanoparticles. *New J. Chem.*, 2021, **45**, P. 6469–6478.
- [30] Yagoub M.Y.A., Swart H.C., Coetsee E. Structural, surface and luminescent properties of SrF₂:Eu annealed thin films. *Vacuum*, 2021, **191**, 110362.
- [31] Yan Y., Tan Y., Li D., Luan F., Guo D. Efficient energy transfer, multi-colour emitting and temperature sensing behavior of single-phase Tb³⁺, Eu³⁺ co-doped strontium fluoride phosphors. *J. Lumin.*, 2019, **211**, P. 209–217.
- [32] Luginina A.A., Kuznetsov S.V., Ivanov V.K., Voronov V.V., Yapyrintsev A.D., Lyapin A.A., Chernova E.V., Pynenkov A.A., Nishchev K.N., Gaynutdinov R.V., Bogach A.V., Fedorov P.P. Laser damage threshold of hydrophobic up-conversion carboxylated nanocellulose/SrF₂:Ho composite films functionalized with 3-aminopropyltriethoxysilane. *Cellulose*, 2021, **28** (17), P. 10841–10862.
- [33] Fedorov P.P., Luginina A.A., Kuznetsov S.V., Osiko V.V. Nanofluorides. *J. Fluorine Chem.*, 2011, **132** (12), P. 1012–1039.
- [34] Karimov D.N., Demina P.A., Koshelev A.V., Rocheva V.V., Sokovikov A.V., Generalova A.N., Zubov V.P., Khaydukov E.V., Koval'chuk M.V., Panchenko V.Ya. Upconversion nanoparticles: synthesis, photoluminescence properties, and applications. *Nanotechnol. Russ.*, 2020, **15**, P. 655–678.
- [35] Mayakova M.N., Luginina A.A., Kuznetsov S.V., Voronov V.V., Ermakov R.P., Baranchikov A.E., et al. Synthesis of SrF₂-YF₃ nanopowders by co-precipitation from aqueous solutions. *Mendeleev Communications*, 2014, **24** (6), P. 360–362.
- [36] Ermakova Yu.A., Pominova D.V., Voronov V.V., Yapyrintsev A.D., Ivanov V.K., Tabachkova N.Yu., Fedorov P.P., Kuznetsov S.V. Synthesis of SrF₂:Yb:Er ceramics precursor powder by co-precipitation from aqueous solution with different fluorinating media: NaF, KF, and NH₄F. *Dalton Trans.*, 2022, **51**, P. 5448–5456.
- [37] Zhang C., Hou Z., Chai R., Cheng Z., Xu Z., Li C., Huang L., Lin J. Mesoporous SrF₂ and SrF₂:Ln³⁺ (Ln = Ce, Tb, Yb, Er) Hierarchical Microspheres: Hydrothermal Synthesis, Growing Mechanism, and Luminescent Properties. *J. Phys. Chem.*, 2010, **114**, P. 6928–6936.
- [38] Chen D., Yu Y., Huang F., Huang P., Yang A., Wang Y. Modifying the Size and Shape of Monodisperse Bifunctional Alkaline-Earth Fluoride Nanocrystals through Lanthanide Doping. *J. Am. Chem. Soc.*, 2010, **132**, P. 9976–9978.
- [39] Sun J., Xian J., Du H. Facile synthesis of well-dispersed SrF₂:Yb³⁺/Er³⁺ upconversion nanocrystals in oleate complex systems. *Appl. Surf. Sci.*, 2011, **257**, P. 3592–3595.
- [40] Sun J., Xian J., Zhang X., Du H. Hydrothermal synthesis of SrF₂:Yb³⁺/Er³⁺ micro-/nanocrystals with multiform morphologies and upconversion properties. *J. Rare Earth*, 2011, **29**, P. 32–38.
- [41] Peng J., Hou S., Liu X., Feng J., Yu X., Xing Y., Su Z. Hydrothermal synthesis and luminescence properties of hierarchical SrF₂ and SrF₂:Ln³⁺ (Ln = Er, Nd, Yb, Eu, Tb) micro/nanocomposite architectures. *Mater. Res. Bull.*, 2012, **47**, P. 328–332.
- [42] Yagoub M.Y.A., Swart H.C., Noto L.L., O'Connell J.H., Lee M.E., Coetsee E. The effects of Eu-concentrations on the luminescent properties of SrF₂:Eu nanoporphor. *J. Lumin.*, 2014, **156**, P. 150–156.
- [43] Yagoub M.Y.A., Swart H.C., Noto L.L., Bergman P., Coetsee E. Surface characterization and photoluminescence properties of Ce³⁺,Eu co-doped SrF₂ nanoporphor. *Materials*, 2015, **8**, P. 2361–2375.

- [44] Quintanilla M., Cantarelli I.X., Pedroni M., Speghini A., Vetrone F. Intense ultraviolet upconversion in water dispersible SrF₂:Tm³⁺, Yb³⁺ nanoparticles: the effect of the environment on light emissions. *J. Mater. Chem. C*, 2015, **3**, P. 3108–3113.
- [45] Li A.H., et al. Upconversion-luminescent/magnetic dual-functional sub-20 nm core-shell SrF₂:Yb,Tm@CaF₂:Gd heteronanoparticles. *Dalt. Trans.*, 2016, **45**, P. 5800–5807.
- [46] Xie J., Bin J., Guan M., Liu H., Yang D., Xue J., et al. Hydrothermal synthesis and upconversion luminescent properties of Sr₂LaF₇ doped with Yb³⁺ and Er³⁺ nanophosphors. *J. Lumin.*, 2018, **200**, P. 133–140.
- [47] Balabhadra S., Debasu M.L., Brites C.D.S., Ferreira R.A.S., Carlos L.D. Radiation-to-heat conversion efficiency in SrF₂:Yb³⁺/Er³⁺ upconverting nanoparticles. *Opt. Mater.*, 2018, **83**, P. 1–6.
- [48] Cortelletti P., Pedroni M., Boschi F., Pin S., Ghigna P., Canton P., et al. Luminescence of Eu³⁺ Activated CaF₂ and SrF₂ Nanoparticles: Effect of the Particle Size and Codoping with Alkaline Ions. *Cryst. Growth Des.*, 2018, **18** (2), P. 686–694.
- [49] Przybylska D., Ekner-Grzyb A., Grzeskowiak B.F., Grzyb T. Upconverting SrF₂ nanoparticles doped with Yb³⁺/Ho³⁺, Yb³⁺/Er³⁺ and Yb³⁺/Tm³⁺ ions – optimisation of synthesis method, structural, spectroscopic and cytotoxicity studies. *Scientific Reports*, 2019, **9**, 8669.
- [50] Du S., Wang Y. A broad-range temperature sensor dependent on the magnetic and optical properties of SrF₂:Yb³⁺/Ho³⁺. *CrystEngComm.*, 2019, **21**, P. 1452–1457.
- [51] Przybylska D., Grzyb T. Synthesis and up-conversion of core/shell SrF₂:Yb³⁺/Er³⁺ @SrF₂:Yb³⁺,Nd³⁺ nanoparticles under 808, 975, and 1532 nm excitation wavelengths. *J. Alloys Compd.*, 2020, **831**, 154797.
- [52] Fedorov P.P., Alexandrov A.A. Synthesis of inorganic fluorides in molten salt fluxes and ionic liquid mediums. *J. Fluorine Chem.*, 2019, **227**, 109374.
- [53] Proydakova V.Yu., Alexandrov A.A., Voronov V.V., Fedorov P.P. Synthesis of Calcium and Strontium Fluorides Using Li₂SO₄–Na₂SO₄ Eutectic Melts. *Russ. J. Inorg. Chem.*, 2020, **65** (6), P. 834–838.
- [54] Park C., Park S. Effective up-conversion behaviors for Er³⁺–Yb³⁺-doped SrF₂ phosphors synthesized by flux-assist method. *J. Mater. Sci.: Mater. Electron.*, 2020, **31** (1), P. 832–837.
- [55] Ritter B., Haida P., Krahl T., Scholz G., Kemnitz E. Core-shell metal fluoride nanoparticles via fluorolytic sol-gel synthesis – a fast and efficient construction kit. *J. Mater. Chem. C*, 2017, **5** (22), P. 5444–5450.
- [56] Ritter B., Haida P., Fink F., Krahl T., Gawlitza K., Rurack K., et al. Novel and easy access to highly luminescent Eu and Tb doped ultra-small CaF₂, SrF₂ and BaF₂ nanoparticles – structure and luminescence. *Dalton Transactions*, 2017, **46** (9), P. 2925–2936.
- [57] Krahl T., Beer F., Relling A., Gawlitza K., Rurack K., Kemnitz E. Toward Luminescent Composites by Phase Transfer of SrF₂:Eu³⁺ Nanoparticles Capped with Hydrophobic Antenna Ligands. *ChemNanoMat.*, 2020, **6** (7), P. 1086–1095.
- [58] Yusenko K.V., Kabelitz A., Schökel A., Wagner R., Prinz C., Kemnitz E., et al. Local Structure of Europium-Doped Luminescent Strontium Fluoride Nanoparticles: Comparative X-ray Absorption Spectroscopy and Diffraction Study. *ChemNanoMat.*, 2021, **7** (11), P. 1221–1229.
- [59] Monks M.-J., Würth C., Kemnitz E., Resch-Genger U. Dopant ion concentration-dependent upconversion luminescence of cubic SrF₂:Yb³⁺, Er³⁺ nanocrystals prepared by a fluorolytic sol-gel method. *Nanoscale*, 2022, **32**.
- [60] Rakov N., Guimaraes R.B., Franceschini D.F., Maciel G.S. Er:SrF₂ luminescent powders prepared by combustion synthesis. *Mater. Chem. Phys.*, 2012, **135**, P. 317–321.
- [61] Rakov N., Guimaraes R.B., Maciel G.S. Managing optical heating via Al³⁺-doping in Er³⁺:SrF₂ powder phosphors prepared by combustion synthesis. *DaltonTrans.*, 2019, **48** (14), P. 4589–4595.
- [62] Glazunova T.Yu., Boltalin A.I., Fedorov P.P. Synthesis of calcium, strontium, and barium fluorides by thermal decomposition of trifluoroacetates. *Russ. J. Inorg. Chem.*, 2006, **51** (7), P. 983–987. <https://doi.org/10.1134/S0036023606070011>
- [63] Heise M., Scholz G., Krahl T., Kemnitz E. Luminescent properties of Eu³⁺ doped CaF₂, SrF₂, BaF₂ and PbF₂ powders prepared by high-energy ball milling. *Solid State Sciences*, 2019, **91**, P. 113–118.
- [64] Gulina L.B., Schäfer M., Privalov A.F., Tolstoy V.P., Murin I.V., Vogel M. Synthesis and NMR investigation of 2D nanocrystals of the LaF₃ doped by SrF₂. *J. Fluorine Chem.*, 2016, **188**, P. 185–190.
- [65] Fedorov P.P., Mayakova M.N., Maslov V.A., Baranchikov A.E., Ivanov V.K., Pynenkov A.A., Uslamina M.A., Nishchev K.N. The solubility of sodium and potassium fluorides in the strontium fluoride. *Nanosystems: Physics, Chemistry, Mathematics*, 2017, **8** (6), P. 830–834.
- [66] Falk L., Commenge J.-M. Performance comparison of micromixers. *Chem. Eng. Sci.*, 2010, **65**, P. 405–411.
- [67] Abiev R.Sh., Zdravkov A.V., Kudryashova Yu.S., Alexandrov A.A., Kuznetsov S.V., Fedorov P.P. Syntheses of calcium fluoride nanoparticles in a microreactor with intensely swirling flows. *Russ. J. Inorg. Chem.*, 2021, **66** (7), P. 1049–1054.
- [68] Abiev R.Sh. Impinging-Jets Micromixers and Microreactors: State of the Art and Prospects for Use in the Chemical Technology of Nanomaterials (Review). *Theor. Found. Chem.*, 2020, **54**, P. 1131–1147.
- [69] Abiev R.Sh., Sirotkin A.A. Influence of Hydrodynamic Conditions on Micromixing in Microreactors with Free Impinging Jets. *Fluids*, 2020, **5** (4), 179.
- [70] Proskurina O.V., Abiev R.Sh., Nevedomskiy V.N. Influence of using different types of microreactors on the formation of nanocrystalline BiFeO₃. *Nanosystems: Phys. Chem. Math.*, 2023, **14** (1), P. 120–126.
- [71] Lomakin M.S., Proskurina O.V., Abiev R.Sh., Leonov A.A., Nevedomskiy V.N., Voznesenskiy S.S., Gusarov V.V. Pyrochlore phase in the Bi₂O₃–Fe₂O₃–WO₃–(H₂O) system: Physicochemical and hydrodynamic aspects of its production using a microreactor with intensely swirled flows. *Advanced Powder Technology*, 2023, **34**, 104053.
- [72] Abiev R.S., Kudryashova Y.S., Zdravkov A.V., Fedorenko N.Y. Micromixing and Co-Precipitation in Continuous Microreactors with Swirled Flows and Microreactors with Impinging Swirled Flows. *Inorganics*, 2023, **11**, 49.
- [73] Barashok K.I., Panchuk V.V., Semenov V.G., Almajshava O.V., Abiev R.Sh. Formation of cobalt ferrite nanopowders in an impinging-jets microreactor. *Nanosystems: Phys., Chem., Math.*, 2021, **12** (3), P. 303–310.
- [74] Pominova D., Romanishkin I., Proydakova V., Kuznetsov S., Grachev P., Ryabova A., Tabachkova N., Fedorov P., Loschenov V. Study of synthesis temperature effect on β-NaGdF₄: Yb³⁺, Er³⁺ upconversion luminescence efficiency and decay time using maximum entropy method. *Methods and Applications in Fluorescence*, 2022, **10**, 024005.

Information about the authors:

Rufat Sh. Abiev – Institute of Silicate Chemistry I. V. Grebenshchikov RAS, Makarova emb. 2, St. Petersburg, Russia 199034; St. Petersburg State Institute of Technology, Moskovsky Pr. 26, St. Petersburg, Russia 190013; ORCID 0000-0003-3571-5770; abiev.rufat@gmail.com

Andrey V. Zdravkov – Institute of Silicate Chemistry I. V. Grebenshchikov RAS, Makarova emb. 2, St. Petersburg, Russia 199034; ORCID 0000-0002-9056-0823; a.v.zdravkov@gmail.com

Yuliya S. Kudryashova – Institute of Silicate Chemistry I. V. Grebenshchikov RAS, Makarova emb. 2, St. Petersburg, Russia 199034; ORCID 0000-0003-2555-4969; kadulinajul@mail.ru

Alexander A. Alexandrov – Prokhorov General Physics Institute of the Russian Academy of Sciences, Vavilova str. 38, Moscow, Russia 119991; ORCID 0000-0001-7874-7284; alexandrov1996@yandex.ru

Sergey V. Kuznetsov – Prokhorov General Physics Institute of the Russian Academy of Sciences, Vavilova str. 38, Moscow, Russia 119991; ORCID 0000-0002-7669-1106; kouznetzovsv@gmail.com

Pavel P. Fedorov – Prokhorov General Physics Institute of the Russian Academy of Sciences, Vavilova str. 38, Moscow, Russia 119991; ORCID 0000-0002-2918-3926; ppfedorov@yandex.ru

Conflict of interest: the authors declare no conflict of interest.

Determining Young's and shear moduli of a rod-shaped object in an AFM bending test

Alexander V. Ankudinov^{1,a}, Mikhail S. Dunaevskiy^{1,b}, Andrei A. Krasilin^{1,c},
Maksim M. Khalisov^{1,2,d}, Ekaterina K. Khrapova^{1,e}

¹Ioffe Institute, St. Petersburg, Russia

²Pavlov Institute of Physiology, Russian Academy of Sciences, St. Petersburg, Russia

^aalexander.ankudinov@mail.ioffe.ru, ^bmike.dunaeffsky@mail.ioffe.ru, ^cikrasilin@mail.ioffe.ru,

^dkhalisovmm@infran.ru, ^earganella@yandex.ru

Corresponding author: A. V. Ankudinov, alexander.ankudinov@mail.ioffe.ru

PACS 07.79.Lh, 62.20.F, 81.70.Bt

ABSTRACT The technique of AFM bending test of a suspended nanoobject has been improved. An analytical method has been created for calculating Young's and shear moduli of object's material based on data of such tests. In Timoshenko approximation, we consider problems of bending a beam one or both ends of which lie on elastic Winkler foundations. The obtained solutions are used to eliminate uncertainties in the calculation of elastic moduli that arise when the conditions of fixing an object (console or bridge) on the edges of a recess in the substrate are unknown.

KEYWORDS atomic force microscopy, bending, nanoscroll, elastic moduli, elastic Winkler foundation.

ACKNOWLEDGEMENTS This work was supported by the Russian Science Foundation, project no. 19-13-00151.

FOR CITATION Ankudinov A.V., Dunaevskiy M.S., Krasilin A.A., Khalisov M.M., Khrapova E.K. Determining Young's and shear moduli of a rod-shaped object in an AFM bending test. *Nanosystems: Phys. Chem. Math.*, 2024, **15** (1), 122–129.

1. Introduction

Atomic force microscopy (AFM) [1,2] is effectively used for bending tests [3–6] of suspended rod-shaped nanoobjects (consoles, bridges). According to the theory of elasticity for slight bending of rods in the Euler–Bernoulli approximation [7], based on the stiffness or deformation profiles measured using AFM and the dimensions of the suspended part of the object, one can calculate the Young's modulus E of the object. First of all, it is important to exclude possible errors in AFM measurements of contact stiffness associated with the characteristics of the tip–sample contact (whether the tip slides along the surface or is clamped), the sample topography, and other factors, see [8]. Then, for correct calculation, it is necessary to know the conditions for fixing the object to recess edges. This information can be obtained by comparing test data with model bending profiles [9–15]. In paper [15], analytical dependence was obtained for the bending profiles of model beams (consoles and bridges), supported, in particular, on elastic Winkler foundations [16].

To apply the Euler–Bernoulli approximation, it is required that the shear displacements w_S be much less than the bending displacements w_B . In an isotropic elastic material, $G/E \geq 1/3$ (the shear modulus $G = E/(2[1 + \nu])$, Poisson's ratio $\nu \in [-1, 0.5]$). Therefore, in a thin rod (with the transverse diameter d much smaller than the length l), this requirement is satisfied, $w_S/w_B \sim d^2/l^2 \ll 1$. It is also believed [17] that for an anisotropic crystalline material in this approximation the Young's modulus E is determined along the long axis of the rod-shaped object. However, from the theoretical point of view [18], there is no limit for the value of ν for an anisotropic material, and G/E can be so small that $w_S \sim w_B$. This necessitates allowance for shear strains in AFM bending test of a rod-shaped object.

In this paper, the problems of bending of model consoles and bridges are solved taking into account shear strains in the Timoshenko approximation [19]. As before [15], three types of conditions for fixing the ends of the beam were studied, Fig. 1: clamping, ring spring, and elastic Winkler foundation. The analytical dependence obtained for the bending profiles of consoles and bridges was used to process the data from AFM bending tests of $\text{MgNi}_2\text{Si}_2\text{O}_5(\text{OH})_4$ nanoscrolls [15].

2. Calculation results

Figure 2 shows diagrams of shear only (a) and bending only (b) of a console loaded with a vertical force. In Fig. 2a, only tangential mechanical stresses τ_{xz} act in the console section with area A . They are parallel to the force $\mathbf{F} = F_z$ and balance it in any such console section. The console displacement w_S is proportional to the distance x to the pinch point and inversely proportional to G ,

$$w_S = \theta x, \quad F_z = A\tau = AG\theta, \quad w_S = [F_z/GA]x, \quad (1)$$

where θ is the angle. Strictly speaking, τ_{xz} is distributed nonuniformly over the beam section. This can be taken into account by adjusting the shear modulus $G = \kappa G$ using the Timoshenko shear coefficient κ , $\kappa = 6(1 + \nu)/(7 + 6\nu) \approx 1$ for a cylindrical rod [19, 20].

In Fig. 2b, only normal mechanical stresses σ_{xx} act in the console section at point x . They are perpendicular to F_z and balance the moment of force $F_z(l - x)$. The console displacements w_B obey the differential equation

$$d^2 w_B / dx^2 \cong 1/R(x) = [F_z(1 - \nu^2)/EI](l - x), \quad (2)$$

where I is the moment of inertia of the beam section ($I = \pi d^4/64$ for a circular section with diameter d). Usually ν is small (≈ 0.25), and the factor $(1 - \nu^2)$ is close to unity and may not be presented in the formula for solving Eq. (2) [7],

$$w_B = [F_z/6EI]x^2(3l - x). \quad (2a)$$

The resulting console displacement is $w = w_B + w_S$. In AFM, the displacement of a suspended object can only be measured at the point where the force is applied. The theoretical dependence for such a displacement is obtained by using the substitution $l = x$ in the formula for w_B ,

$$w = [F_z/3EI]x^3 + [F_z/GA]x. \quad (3)$$

To interpret AFM data, it is convenient to use the normalized displacement profile $\zeta(\chi) = w/w_{MAX}$, depending on the dimensionless variable $\chi = x/l$,

$$\zeta_{C1}(\chi) = (\chi^3 + 3\gamma\chi)/(1 + 3\gamma), \quad (4)$$

for the following fitting parameter $\gamma = [EI/GAl^2]$.

Let us write expression (3) in two equivalent ways:

$$w = [F_z l^3/3EI](\chi^3 + 3\gamma\chi), \quad (3a)$$

$$w = [F_z l/GA](\chi + \chi^3/3\gamma). \quad (3b)$$

If $\gamma = 0$, then only the cubic dependence of the bending on x remains in (3a). If $\gamma \rightarrow \infty$, only the linear dependence of the shear on x is left in (3b). Assuming that the experiment satisfies one of these limiting extremes, we can calculate only E or only G of the console, which below are referred to as the zero versions of elastic moduli or their values according to the zero model,

$$\begin{aligned} E_{C0} &= [F_z l^3/3w_{MAX}I] = [l^3/3I]k_C, \\ G_{C0} &= [l/A]k_C, \end{aligned} \quad (5)$$

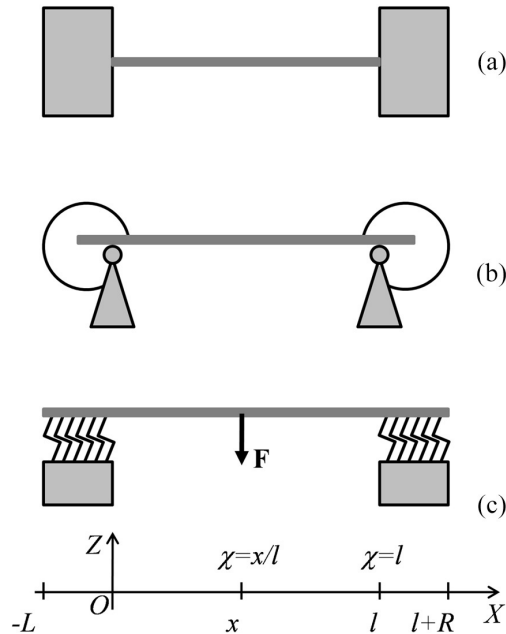


FIG. 1. Options for fixing conditions. Clamping: (a), model 1. Ring spring: (b), model 2. Elastic Winkler foundation (Winkler coefficient k_W , lengths L and R , origin on the left support, bridge length l , force F applied at point x): (c), model 3.

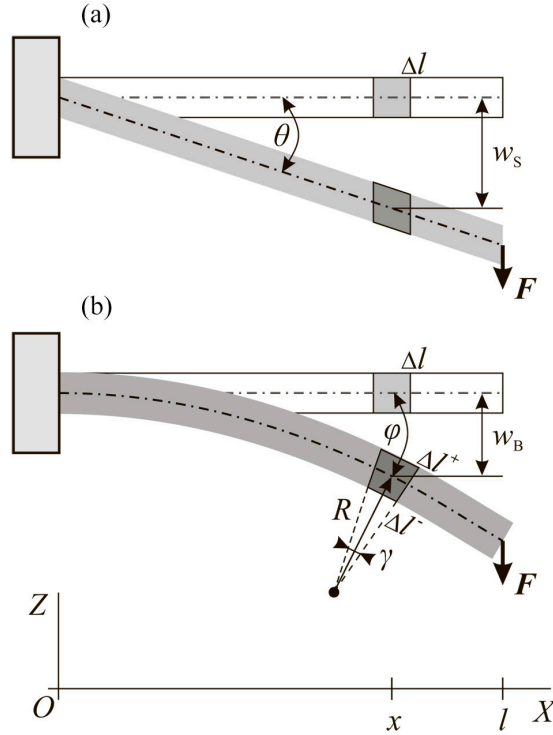


FIG. 2. Shear only (a) and bending only (b) of a console of length l and thickness t . The force $\mathbf{F} = F_z$ transforms a rectangular section of length Δl into a parallelepiped with vertex angles $\pi/(2 \pm \theta)$ (a) and into an isosceles trapezoid with bases stretched to Δl^+ and compressed to Δl^- and an angle between the sides $\gamma = (\Delta l^+ - \Delta l^-)/t$, corresponding to the local curvature radius $R = \Delta l/\gamma$ (b).

where k_C is the minimum console stiffness. For a bridge with minimum stiffness k_B , the formulas for calculating the zero versions of elastic moduli are as follows:

$$\begin{aligned} E_{B0} &= [l^3/192I]k_B, \\ G_{B0} &= [l/4A]k_B. \end{aligned} \quad (5a)$$

Based on the value of γ that matches the fitting dependences (3) and (4) with the experimental bending profile, both elastic moduli can be determined in intermediate cases,

$$\begin{cases} E_1 = \Phi_{EC1}E_{C0}, & \Phi_{EC1} = 1 + 3\gamma, \\ G_1 = \Phi_{GC1}G_{C0}, & \Phi_{GC1} = 1 + (3\gamma)^{-1} = \Phi_{EC1}(3\gamma)^{-1}, \end{cases} \quad (6)$$

where we have introduced Φ_{EC1} and Φ_{GC1} — correction factors according to model 1, Fig. 1.

Relations similar to (4) and (6) can also be derived for models 2 and 3 of boundary conditions, Fig. 1. The displacements of the suspended beam span in the Timoshenko approximation satisfy the equations

$$\begin{cases} d^3\varphi/dx^3 = 0, \\ dw/dx = \varphi - [EI/GA]d^2\varphi/dx^2. \end{cases} \quad (7)$$

In this approximation, the displacements of a beam segment on an elastic foundation obey the equations

$$\begin{cases} d^4\varphi/dx^4 - [k_W/GA]d^2\varphi/dx^2 + [k_W/EI]\varphi = 0, \\ w = -[EI/k_W]d^3\varphi/dx^3. \end{cases} \quad (8)$$

When a rigid cylinder is pressed into a softer elastic base with Young's modulus E_B , the Winkler coefficient in (8) is estimated to be $k_W \approx E_B$ [15].

General solutions to systems (7) and (8) are, respectively, $w = \sum_{k=0}^3 a_k x^k$ and $w = A_0 \exp(\beta_1 x) + A_1 \exp(-\beta_1 x) + A_2 \exp(\beta_2 x) + A_4 \exp(-\beta_2 x)$. The exponents β_1 and β_2 are related by $\beta_1^2 + \beta_2^2 = [k_W/GA]$ and $\beta_1^2 \beta_2^2 = [k_W/EI]$. If $[k_W EI/4G^2 A^2] < 1$, then β_1 and β_2 are a pair of complex conjugate numbers, otherwise positive real numbers. The unknowns a_k and A_k are found from the boundary conditions (see Table 1). As a result, for a bridge and console in each case of fixing conditions in Fig. 1, we obtained simultaneous systems of linear equations, which were solved analytically,

see, for example, the paper [15]. To speed up the calculations, we used computer algebra programs `Mathematica` (Wolfram Research, USA) and `Mathcad` (PTC, USA).

Tables 2 and 3 list the final fitting relationships and correction factors for a console and bridge in the cases of clamped ends and ends supported on ring springs (Fig. 1). More cumbersome solutions for the model with an elastic Winkler foundation are discussed separately below.

For a cantilever beam (a suspended segment of length l , a segment on an elastic foundation of length L), the following exact fitting relationship was obtained:

$$\zeta_{C3}(\chi) = \sum_0^3 c_k \beta_l^k \chi^k / \sum_0^3 c_k \beta_l^k. \quad (9)$$

$$\begin{aligned} c_0 &= 6 \sin(\theta) \left[\sin(\theta/2) \sinh(2\lambda\beta_l \cos(\theta/2)) - \cos(\theta/2) \sin(2\lambda\beta_l \sin(\theta/2)) \right], \\ c_1 &= 6 \sin^2(\theta) \left[\cosh(2\lambda\beta_l \cos(\theta/2)) - \cos(2\lambda\beta_l \sin(\theta/2)) \right], \\ c_2 &= 6 \sin(\theta) \left[\sin(\theta/2) \sinh(2\lambda\beta_l \cos(\theta/2)) + \cos(\theta/2) \sin(2\lambda\beta_l \sin(\theta/2)) \right], \\ c_3 &= 2 \left[\sin^2(\theta/2) \cosh(2\lambda\beta_l \cos(\theta/2)) + \cos^2(\theta/2) \cos(2\lambda\beta_l \sin(\theta/2)) - 1 \right]. \end{aligned}$$

The factors for correction of elastic moduli corresponding to (9) are

$$\begin{aligned} \Phi_{EC3} &= \sum_0^3 c_k \beta_l^k / 2D, \\ \Phi_{GC3} &= [\beta_l^2 / 6 \cos \theta] \Phi_{EC3}; \\ D &= \beta_l^3 \left[1 - \sin^2(\theta/2) \cosh(2\lambda\beta_l \cos(\theta/2)) - \cos^2(\theta/2) \cos(2\lambda\beta_l \sin(\theta/2)) \right]. \end{aligned} \quad (10)$$

TABLE 1. Versions of boundary conditions

Boundary	Conditions
Clamping	$w = \varphi = 0$
Foundation	$w = d\varphi/dx = 0$
Ring spring	$w = 0, d\varphi/dx = [4/\lambda l]\varphi$
Free end	$d\varphi/dx = d^2\varphi/dx^2 = 0$
Point of load F on console	$d\varphi/dx = 0,$ $d^2\varphi/dx^2 = -[F/EI]$
Point of load F on bridge	$w_+ - w_- = \varphi_+ - \varphi_- = 0,$ $d(\varphi_+ - \varphi_-)/dx = 0,$ $d^2(\varphi_+ - \varphi_-)/dx^2 = [F/EI]$

TABLE 2. Calculation of elastic moduli of console in Timoshenko approximation ($\lambda, \gamma \in [0, \infty)$, $\chi \in [0, 1]$. $E_j = \Phi_{ECj} E_{C0}$, $G_j = \Phi_{GCj} (3\gamma)^{-1} G_{C0}$. $E_{C0} = 64[l^3/3\pi d^4]k_C$, $G_{C0} = 4[l/\pi d^2]k_C$).

j , model no.	ζ_{Cj}	Φ_{ECj}
1	$\frac{\chi^3 + 3\gamma\chi}{1 + 3\gamma}$	$1 + 3\gamma$
2	$\frac{\chi^3 + 3\lambda\chi^2 + 3\gamma\chi}{1 + 3\lambda + 3\gamma}$	$1 + 3(\lambda + \gamma)$

TABLE 3. Calculation of elastic moduli of bridge in Timoshenko approximation ($\lambda, \gamma \in [0, \infty)$, $\chi \in [0, 1]$. $E_j = \Phi_{EBj} E_{B0}$, $G_j = \Phi_{EBj} (3\gamma)^{-1} G_{B0}$. $E_{B0} = [l^3/3\pi d^4] k_B$, $G_{B0} = 4[l/\pi d^2] k_B$.

j , model no.	ζ_{Bj}	Φ_{EBj}
1	$64 \left\{ \frac{(\chi - \chi^2)^3 + 3\gamma(\chi - \chi^2)^2}{(1 + 12\gamma)(1 + 48\gamma)} + \frac{3\gamma(\chi - \chi^2)}{(1 + 48\gamma)} \right\}$	$1 + 48\gamma$
2	$64 \left\{ \frac{(2\lambda + 1)(\chi - \chi^2)^3 + 3[\lambda(4\lambda + 1) + (8\lambda + 1)\gamma](\chi - \chi^2)^2}{(1 + 6\lambda + 12\gamma)(1 + 8\lambda + 48(2\lambda + 1)\gamma)} + \frac{3(2\lambda + 1)\gamma(\chi - \chi^2)}{(1 + 8\lambda + 48(2\lambda + 1)\gamma)} \right\}$	$\frac{1 + 8\lambda}{1 + 2\lambda} + 48\gamma$

The dimensionless parameters in (9) and (10) are: $\lambda = L/l$, measured from AFM topography data, and β_l and θ , determined by fitting. Here are the expressions for the fitting parameters:

$$\begin{aligned} \beta_l &= l \sqrt[4]{k_W/EI}, \\ \cos \theta &= \sqrt{k_W EI/4G^2 A^2}. \end{aligned} \quad (11)$$

In (11), β_l is $\sqrt{2}$ times greater than the parameter designated in the same way in the paper [15]. The Winkler elastic foundation coefficient is calculated as

$$k_W = 2GA\beta_l^2 \cos \theta/l^2.$$

For a bridge with span length l (see Fig. 2), only asymptotic solutions ($L\beta_l/l, R\beta_l/l \gg 1$) turn out to be relatively compact,

$$\zeta_{B3}(\chi) = \sum_0^3 b_k \beta_l^k (\chi - \chi^2)^k / \sum_0^3 b_k \beta_l^k 2^{-2k}. \quad (12)$$

$$\begin{aligned} b_0 &= 6[(48 + 24\beta_l^2 + \beta_l^4) \cos(\theta/2) + 2\beta_l^3 \{3 + 4\cos\theta\} + 24 \cos(3\theta/2) - 24\beta_l \cos(2\theta)], \\ b_1 &= 6[\beta_l(6 + \beta_l^2) - 24 \cos(\theta/2) - \beta_l(72 + \beta_l^2) \cos \theta - 8(6 + \beta_l^2) \cos(3\theta/2) + 24 \cos(5\theta/2)], \\ b_2 &= 6 \cos(\theta/2) [\beta_l^2 + 6\beta_l \cos(\theta/2) + 2 - 16 \cos \theta], \\ b_3 &= \beta_l + 4 \cos(\theta/2). \end{aligned}$$

$$\Phi_{EB3} = \frac{192[1 + 2 \cos \theta] - 192\beta_l \cos(3\theta/2) + 48\beta_l^2 [1 - 2 \cos \theta] + 16\beta_l^3 \cos(\theta/2) + \beta_l^4}{\beta_l^3 [\beta_l + 4 \cos(\theta/2)]}, \quad (13)$$

$$\Phi_{GB3} = [\beta_l^2/96 \cos \theta] \Phi_{EB3}.$$

If $\theta = \pi/2$ (this corresponds to $G \rightarrow \infty$), then applying the substitution $\beta_l = \beta_l/\sqrt{2}$ in (9), (10), (12), and (13) yields expressions for the Euler–Bernoulli approximation derived in the papers [15] and [21].

Relations (9)–(12) are valid for $k_W EI < 4G^2 A^2$ and $\theta \in (0, \pi/2]$. This requires large values of G . Considering $k_W \approx E_B$ and the beam to be cylindrical, we obtain the condition $G > \sqrt{E_B E}/16\pi$. The consistency of (9) or (13) with measurements for $\theta = 0$ violates this condition. In this case, for small values of G , relations (9)–(13) should be applied after substitution $\theta \rightarrow i \cdot \theta^*$, and the fitting parameter should be varied in the range $\theta^* \in (0, \infty)$.

3. Analysis of AFM data

The test for the suitability of the model consists of comparing the results of an analysis of bending tests for various types of objects, namely, consoles and bridges. Data were taken from AFM bending tests [15] of $\text{MgNi}_2\text{Si}_2\text{O}_5(\text{OH})_4$ phyllosilicate nanoscrolls grown by hydrothermal synthesis [22]. Nanoscrolls were deposited on a calibration grating of rectangular grooves TGZ2 (period 3 μm , groove depth 110 nm, NT-MDT SI, Russia); they formed consoles and bridges over the grooves. The bending tests were carried out in the PeakForce QNM AFM mode, FMG01 cantilevers (NT-MDT SI, Russia) were used, and the spring constant was refined using the thermal-noise-based method [23]. AFM signals of height, peak force error and deformation were recorded [14, 15, 21]. The deformation signal was corrected taking into account the contribution of methodological factors, including slipping of the AFM tip on inclined sections of the sample [8, 14, 15]. The Gwyddion 2.55 [24] program was used to process the AFM data.

Figure 3 presents test data for a console and bridge. The processing results are, respectively, as follows: $l_C = 1037$ nm, $l_B = 1463$ nm; $d_C = 80$ nm, $d_B = 66$ nm; $k_C = 0.61$ N/m, $k_B = 8.32$ N/m; $E_{C0} = 113$ GPa, $G_{C0} = 0.13$ GPa; $E_{B0} = 146$ GPa, $G_{B0} = 0.89$ GPa; $\Phi_{EC1} = 1.26$, $\Phi_{GC1} = 4.82$; $\Phi_{EB1} = 1.55$, $\Phi_{GB1} = 2.81$; $\Phi_{EC2} = 2.56$, $\Phi_{GC2} \rightarrow \infty$; $\Phi_{EB2} = 1.58$, $\Phi_{GB2} = 2.73$; $\Phi_{EC3} = 1.82$, $\Phi_{GC3} \rightarrow \infty$; $\Phi_{EB3} = 1.38$, $\Phi_{GB3} = 5.76$.

In total, AFM test data from 27 bridges and 18 consoles were processed. It is convenient to present the results on phase planes (Fig. 4).

In Fig. 4a, each studied object is characterized by a point on the phase plane: the abscissa is the value of the ratio of the squared diameter to the length of the suspended object, d^2/l , and the ordinate is the value of $k^G = k_B$ for a bridge

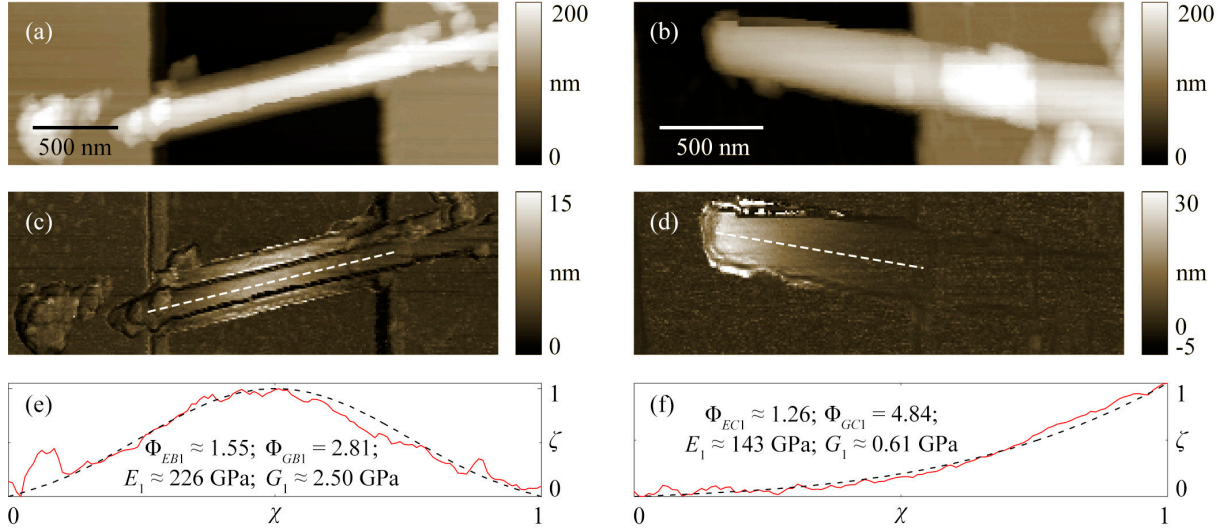


FIG. 3. AFM height images of the relief of the TGZ2 grating fragments with a recess overlapped by (a) a bridge and (b) a console of $\text{MgNi}_2\text{Si}_2\text{O}_5(\text{OH})_4$ nanoscrolls. AFM maps of the corrected deformation signal of the bridge (c) and console (d). The dashed lines indicate where the deformation profiles were extracted. Normalized deformation (displacement) profiles of the bridge (e) and console (f): red solid lines — experiment, black dashed lines — approximation according to model 1. AFM imaging was performed with Peak Force Amplitude and Frequency of 150 nm and 1 kHz, respectively. The Peak Force Setpoint and the Scan Rate were as follows: 60 nN, 0.3 Hz (bridge) and 15 nN, 0.2 Hz (console).

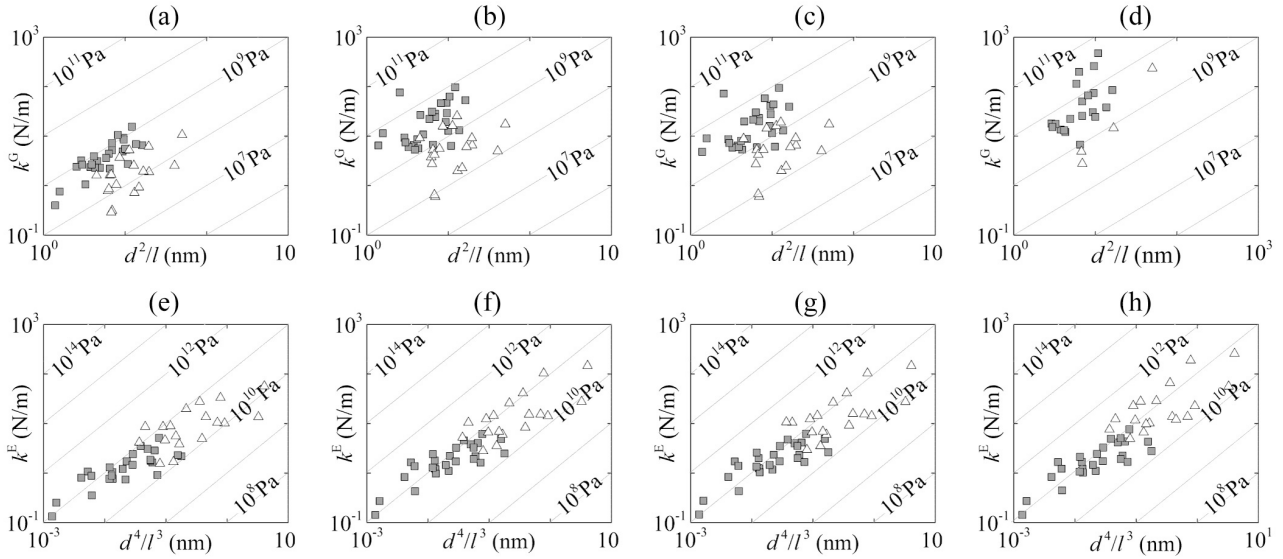


FIG. 4. Distributions of AFM bending test data for bridges (filled squares) and consoles (hollow triangles) made of $\text{MgNi}_2\text{Si}_2\text{O}_5(\text{OH})_4$ on phase planes. Calculation results: shear only (a) and bending only (e); model 1, (b) and (f); model 2, (c) and (g); model 3, (d) and (h). The inclined straight lines show the isolines of the shear modulus G in (a)–(d) and the isolines of the Young's modulus E in (e)–(h).

or $k^G = 4k_C$ for a console. On a log-log scale, according to (5a) and (5), the isolines of G are straight lines with a unit slope. The results of applying models 1–3 are depicted in Figs. 4b–4d; $k^G = \Phi_{GBj}k_B$ for a bridge and $k^G = 4\Phi_{GCj}k_C$ for a console, $j = 1-3$.

On the phase planes in the bottom row of Fig. 4, the abscissa of a point is the value of d^4/l^3 , and the ordinate is the value of $k^E = k_B$ for a bridge or $k^E = 64k_C$ for a console, Fig. 4e; in Figs. 4f–4h, the ordinate of a point is, respectively, the value of $k^E = \Phi_{EBj}k_B$ or $k^E = 64\Phi_{ECj}k_C$, $j = 1-3$. According to (5a) and (5), in this representation the isolines of E have a unit slope coefficient.

TABLE 4. Elastic moduli for $\text{MgNi}_2\text{Si}_2\text{O}_5(\text{OH})_4$. Results of using different models for processing data of AFM bending tests of a suspended object. ¹The number of test objects.

j , model no.	$G \pm \sigma(G)$ (GPa)			$E \pm \sigma(E)$ (GPa)		
	Bridge	Console	Both	Bridge	Console	Both
0	0.7 ± 0.3 (27)	0.2 ± 0.1 (18)	0.5 ± 0.3 (45)	74 ± 51 (27)	51 ± 48 (18)	66 ± 49 (45)
1	4.3 ± 5.5 (27)	0.7 ± 0.7 (18)	2.9 ± 4.6 (45)	100 ± 69 (27)	75 ± 62 (18)	90 ± 67 (45)
2	3.9 ± 5.2 (27)	0.7 ± 0.6 (17)	2.7 ± 4.4 (44)	104 ± 72 (27)	84 ± 79 (18)	96 ± 75 (45)
3	9.7 ± 11.5 (20)	1.7 ± 2.0 (4)	8.3 ± 10.9 (24)	97 ± 63 (27)	115 ± 92 (18)	103 ± 75 (45)

Since a bridge with the average span length $\langle l_B \rangle = 1.6 \pm 0.2 \mu\text{m}$ is several times longer than a console with $\langle l_C \rangle = 0.5 \pm 0.2 \mu\text{m}$, on the phase planes, data on bridges are located to the left of console data. In the zero version (Table 4), the Young's modulus of a bridge is approximately one and a half times greater than that of a console. Therefore, in Fig. 4e, the cluster of points is elongated at a flatter angle than the isolines of E . In Figs. 4f—4h, the average slope coefficients of the clusters of points become closer to unity, in accordance with the decrease in the discrepancy between the average Young's moduli of bridge and console determined from models 1–3 (Table 4). Application of model 3 produces minimal discrepancy.

In the zero version, the values of G for consoles and bridges differ several times, and the discrepancy increases after processing with the use of models 1–3. Unlike the bottom row in Fig. 4, on the phase planes of the top row, clusters of points are not aligned along isolines. This demonstrates the fact that in AFM testing, the displacement of a suspended object is controlled by bending strains rather than shear strains. In the fitting curves (Table 2 and (9) for consoles and Table 3 and (12) for bridges), the coefficients of the terms linear in χ and $\chi - \chi^2$ decrease with increasing shear modulus. For the boundary conditions of model 3, the linear terms will also be presented in shear-neglecting fitting dependences obtained in the Euler–Bernoulli approximation [15]. This is partly why the values of G determined in the Timoshenko approximation using this model are the largest in Table 4, at the level of 10 GPa. Note that the calculation of the elastic moduli of chrysotile nanoscrolls using the density functional theory (DFT) method gives shear moduli comparable to this level [14, 22]. This closeness of calculations with measurements and, at the same time, better consistency of the average values of the Young's modulus of bridges and consoles makes model 3 preferable. It remains to add that the six-fold difference in the shear moduli of bridges and consoles according to this model in Table 4 is overrated — out of eighteen consoles, fourteen consoles correspond to the case of $G \rightarrow \infty$ without participating in the statistics.

4. Conclusions

The procedure for AFM bending test of suspended rod-shaped objects has been improved. To process measurements and determine Young's and shear moduli of the material of objects, theoretical dependences of the bending of a suspended beam segment at a load point on the position of this point on the segment are obtained. Three models of boundary conditions are considered. The suitability of the models was studied by processing data from AFM bending tests of bridges and consoles made of $\text{MgNi}_2\text{Si}_2\text{O}_5(\text{OH})_4$ nanoscrolls. The minimum discrepancy between the average Young's moduli of such bridges and consoles and, at the same time, the best agreement between the experimental values of elastic moduli and the results of DFT calculations is provided by the Winkler model of a beam on an elastic foundation.

References

- [1] Binnig G., Quate C.F., Gerber Ch. Atomic Force Microscope. *Phys. Rev. Lett.*, 1986, **56**(9), P. 930–933.
- [2] Bhushan B. *Nanotribology and Nanomechanics. An Introduction*. Springer-Verlag, Berlin–Heidelberg, 2005, 928 p.
- [3] Salvétat J.-P., Kulik A. J., Bonard J.-M., Briggs G., Andrew D., Stöckli T., Méténier K., Bonnamy S., Béguin F., Burnham N. A., Forró L. Elastic Modulus of Ordered and Disordered Multiwalled Carbon Nanotubes. *Adv. Mater.*, 1986, **11**(2), P. 161–165.
- [4] Cuenot S., Demoustier-Champagne S., Nysten B. Elastic Modulus of Polypyrrole Nanotubes. *Phys. Rev. Lett.*, 1999, **85**(8), P. 1690–1693.
- [5] Kis A. Mechanical properties of mesoscopic objects. // PhD Thesis. Lausanne, 2003, 166 p.
- [6] Gangadean D., McIlroy D.N., Faulkner B.E., Aston D.E. Winkler boundary conditions for three-point bending tests on 1D nanomaterials. *Nanotechnology*, 2010, **21**(22), P. 225704.
- [7] Landau L.D., Lifshitz E.M. *Theory of Elasticity*. Pergamon Press, Oxford, 1970. 177 p.
- [8] Ankudinov A.V., Khalisov M.M. Contact Stiffness Measurements with an Atomic Force Microscope. *Tech. Phys.*, 2020, **65**(11), P. 1866–1872.
- [9] Mai W., Wang Zh.L. Quantifying the elastic deformation behavior of bridged nanobelts. *Appl. Phys. Lett.*, 2006, **89**(7), P. 073112.
- [10] Chen Yu., Dorgan B.L., McIlroy D.N., Eric Aston D. On the importance of boundary conditions on nanomechanical bending behavior and elastic modulus determination of silver nanowires. *J. Appl. Phys.*, 2006, **100**(10), P. 104301.
- [11] Kluge D., Abraham F., Schmidt S., Schmidt H.-W., Fery A. Nanomechanical Properties of Supramolecular Self-Assembled Whiskers Determined by AFM Force Mapping. *Langmuir*, 2010, **26**(5), P. 3020–3023.

- [12] Ankudinov A.V. A New Algorithm for Measuring the Young's Modulus of Suspended Nanoobjects by the Bending-Based Test Method of Atomic Force Microscopy. *Semiconductors*, 2010, **53**(14), P. 1891–1899.
- [13] Khalisov M.M., Lebedev V.A., Poluboyarinov A.S., Garshev A.V., Khrapova E.K., Krasilin A.A., Ankudinov A.V. Young's modulus of phyllosilicate nanoscrolls measured by the AFM and by the in-situ TEM indentation. *Nanosyst.: Phys. Chem. Math.*, 2021, **12**(1), P. 118–127.
- [14] Krasilin A.A., Khalisov M.M., Khrapova E.K., Kunkel T.S., Kozlov D.A., Anuchin N.M., Enyashin A.N., Ankudinov A.V. Surface Tension and Shear Strain Contributions to the Mechanical Behavior of Individual Mg-Ni-Phyllosilicate Nanoscrolls. *Part. Part. Syst. Charact.*, 2021, **38**(12), P. 2100153.
- [15] Ankudinov A., Dunaevskiy M., Khalisov M., Khrapova E., Krasilin A. Atomic force microscopy bending tests of a suspended rod-shaped object: Accounting for object fixing conditions. *Phys. Rev. E.*, 2021, **107**(2), P. 025005.
- [16] Winkler E. *Die Lehre von der Elastizität und Festigkeit*. Dominicus, Prague, 1867, 388 p.
- [17] Lekhnitskii S.G. *Theory of Elasticity of an Anisotropic Body*. Holden-Day, San Francisco, 1963, 404 p.
- [18] Ting T.C.T., Chen T. Poisson's ratio for anisotropic elastic materials can have no bounds. *Q. J. Mech. Appl. Math.*, 2005, **58**(1), P. 73–82.
- [19] Timoshenko S.P. On the correction for shear of the differential equation for transverse vibrations of prismatic bars. *London Edinburgh Dublin Philos. Mag. J. Sci.*, 1921, **41**(245), P. 744–746.
- [20] Cowper G.R. The Shear Coefficient in Timoshenko's Beam Theory. *J. Appl. Mech.*, 1966, **33**(2), P. 335–340.
- [21] Ankudinov A.V., Khalisov M.M. Bending test of nanoscale consoles in atomic force microscope. *Tech. Phys. Lett.*, 2022, **48**(2), P. 21–24.
- [22] Khrapova E.K., Ugolkov V.L., Straumal E.A., Lermontov S.A., Lebedev V.A., Kozlov D.A., Kunkel T.S., Nominé A., Bruyere S., Ghanbaja J., Belmonte T., Krasilin A.A. Thermal behavior of Mg-Ni-phyllosilicate nanoscrolls and performance of the resulting composites in hexene-1 and acetone hydrogenation. *ChemNanoMat*, 2021, **7**(3), P. 207–207.
- [23] Hutter J.L., Bechhoefer J. Calibration of atomic-force microscope tips. *Rev. Sci. Instrum.*, 1993, **64**(7), P. 1868–1873.
- [24] Nečas D., Klapetek P. Gwyddion: an open-source software for SPM data analysis. *Open Phys.*, 2012, **10**(1), P. 181–188.

Submitted 24 November 2023; accepted 12 February 2024

Information about the authors:

Alexander V. Ankudinov – Ioffe Institute, Polytekhnicheskaya, 26, St. Petersburg, 194021, Russia; ORCID 0000-0002-3450-0420; alexander.ankudinov@mail.ioffe.ru

Mikhail S. Dunaevskiy – Ioffe Institute, Polytekhnicheskaya, 26, St. Petersburg, 194021, Russia; ORCID 0000-0001-6038-223X; mike.dunaeffsky@mail.ioffe.ru

Andrei A. Krasilin – Ioffe Institute, Polytekhnicheskaya, 26, St. Petersburg, 194021, Russia; ORCID 0000-0002-3938-3024; ikrasilin@mail.ioffe.ru

Maksim M. Khalisov – Ioffe Institute, Polytekhnicheskaya, 26, St. Petersburg, 194021, Russia; Pavlov Institute of Physiology, Russian Academy of Sciences, Makarova emb., 6, St. Petersburg, 199034, Russia; ORCID 0000-0002-5171-4690; khalisovmm@infran.ru

Ekaterina K. Khrapova – Ioffe Institute, Polytekhnicheskaya, 26, St. Petersburg, 194021, Russia; ORCID 0000-0003-2674-9653; arganella@yandex.ru

Conflict of interest: the authors declare no conflict of interest.

Sorption of polar and non-polar liquids by GO powders according to DSC experiments

Alexander V. Kaplin^{1,2,a}, Elena A. Eremina^{1,b}, Mikhail V. Korobov^{1,c}¹Moscow State University, Chemistry Department, Moscow, Russia²Semenov Federal Research Center of Chemical Physics, Russian Academy of Sciences, Moscow, Russia^aalex1997kaplin@mail.ru, ^bea_er@mail.ru, ^cmkorobov49@gmail.com

Corresponding author: Alexander V. Kaplin, alex1997kaplin@mail.ru

PACS 68.43.-h

ABSTRACT The sorption properties of Hummers (HGO) and Brodie (BGO) graphite oxides with respect to various liquids were studied by the DSC method. In the case of HGO, the reduced material (RHGO) was obtained by hydrothermal synthesis. The effective reduction of the material was confirmed by XRD. The difference in the sorption of water and acetonitrile by HGO and RHGO was experimentally observed. The DSC experimental procedure was developed to estimate the selective sorption of the component from the immiscible liquid mixtures. The procedure has been tested on the sorption of the water-octane mixture by HGO. It was shown that water can be sorbed by HGO from the mixture in an amount equal to equilibrium sorption of pure water by HGO at 273 K. The results obtained will serve as the basis for further studies of the sorption properties of GO.

KEYWORDS graphite oxide, sorption, DSC**ACKNOWLEDGEMENTS** The study was supported by the Russian Science Foundation (RSF 22-29-00544).**FOR CITATION** Kaplin A.V., Eremina E.A., Korobov M.V. Sorption of polar and non-polar liquids by GO powders according to DSC experiments. *Nanosystems: Phys. Chem. Math.*, 2024, **15** (1), 130–134.

1. Introduction

Graphite oxide (GO) is a non-stoichiometric graphite derivative, on the basis of which it is possible to obtain materials with various functional properties. Unlike graphite, GO exhibits hydrophilic properties, it can be dispersed in polar solvents and easily sorbs polar solvents in the interlayer space, which leads to the increase of the interplanar distance [1]. Ultrasonication in polar solvents leads to the solubilization of graphite oxide with the formation of the dispersed oxide graphene, which can be further reduced to graphene [2]. In GO, most of the carbon atoms are sp^3 hybridized and are bound to various functional groups ($-COOH$, $-C(O)O-$, $>C=O$, $-OH$). The known methods for the GO synthesis do not provide control over the oxygen content in the resulting substance. As a result, it is impossible to accurately determine the composition of GO and its structure [3, 4].

The preparation of GO was first described by Brodie in 1855 [5]. He used a mixture of potassium chlorate and fuming nitric acid to oxidize graphite. Currently, the Hummers synthesis [6] or its more environmentally friendly version – the improved Hummers method [7] are commonly used. Graphite oxides obtained by the Brodie method (BGO) and the Hummers method (HGO) have different physicochemical properties [8]. These materials differ in the interplanar distance (XRD), the C:O ratio (XPS) and the concentration and composition of the oxygen-containing functional groups (IR-spectra). Also, HGO and BGO differ in their sorption properties with respect to polar liquids [2, 9, 10]. The interaction of GO with polar liquids leads to swelling, that is, sorption with the simultaneous increase in the interplanar space in GO. Sorption and swelling make it possible to actively use GO to remove toxic pollutants and purify water [11–13]. The sorption of water and organic liquids by various GO samples was measured in [2] using isopiestic experiment and the DSC method. The isopiestic experiments makes it possible to measure the sorption into GO at room temperature from the gas phase. The DSC method enables one to evaluate the sorption at the melting point of a liquid upon direct contact of the material with the liquid phase [2]. In this work, we obtained the data on the sorption of some polar and non-polar liquids by the HGO and BGO powders. Also, we obtained the reduced form of HGO (RHGO) using hydrothermal synthesis. Only a few works are known about the sorption of liquids by RHGO materials [17].

We demonstrated that DSC allows one to determine the partial sorptions of the components from the binary mixtures of polar and non-polar liquids into the GO materials. This method is useful to evaluate the properties of the GO materials as sorbents for the purification of water.

2. Materials and methods

2.1. GO powders

HGO powders were prepared by the improved Hummers method with a sulfuric to phosphoric acid ratio of 9:1 [9]. The sample of RHGO was obtained by the hydrothermal synthesis. 30 ml of HGO suspension in water with (3 mg/ml) was autoclaved for 12 hours at 140 °C. The resulting sample was dried from water in a desiccator with P₂O₅ to a constant weight. BGO powders were synthesized by the method described in ref. [14] with double oxidation of the original graphite. The liquids used in the study are: water (deionized, $\approx 0.5 \mu\text{S}/\text{cm}$), octane (Sigma-Aldrich, $\geq 99.8 \%$), trifluoroethanol (Sigma-Aldrich, $\geq 99 \%$), propionitrile (Sigma-Aldrich, $\geq 99 \%$).

2.2. Instruments

XRD measurement were performed using the diffractometer Rigaku D/MAX 2500 (Japan) with Bragg–Brentano geometry with the rotating anode (CuK α radiation, $\lambda = 1.5418 \text{ \AA}$). Registration was carried out in a step-by-step mode in the angle range $2\Theta = (2 - 80)^\circ$ with the step of 0.02° in 2Θ with an exposure of 2 seconds per point. The obtained data were processed using the standard packages of the WinXpow program. Before recording the diffraction patterns of the graphite oxide samples, the samples were dried in a desiccator with P₂O₅.

The DSC method was used to measure the sorption of polar liquids by GO powders at the melting temperature. The mass ratio of the polar liquid to the GO material in the samples studied varied from 1:1 to 5:1. Before the DSC experiments, the GO sample was pre-dried in a desiccator with P₂O₅, then a fixed amount of polar liquid was added to the GO. The DSC experiments were performed with the low-temperature calorimeter “Mettler DSC – 30”. The heating traces were used for the quantitative determination of sorption. The scanning rates were 2, 5 and 10 grad·min⁻¹. The procedure is described in detail in ref. [2].

3. Discussion

3.1. Synthesis and XRD

HGO and BGO were prepared by the common synthetic methods [2, 9, 13, 14]. According to the method of BJH nitrogen desorption, the specific surface area and pore size in the materials were determined (Table 1). The size of nanopores does not correspond to the interplanar distance in the layered structure of both HGO and BGO.

TABLE 1. BJH and XRD data for HGO and BGO powders

HGO	BGO	Method
1519	814	Surface area (BJH), m ² /g
11.0	10.9	Pore radius (BJH), Å
7.8	6.6	Interplane distance (XRD), Å

This confirms that nitrogen does not intercalate into the interplanar space of GO. Hydrothermal synthesis was used to obtain the reduced graphite oxide RHGO from HGO. In hydrothermal synthesis, water acts as the reducing agent. The dried RHGO is a black powder which forms the unstable suspensions in water, even after ultrasonication.

Figure 1 shows the XRD patterns of the studied materials. As compared to the initial HGO, the (001) peak of RHGO is significantly broadened and shifted to higher angles. Decrease in the interplanar distance (to 3.7 from 7.5 Å) almost by the value of the interplanar distance in graphite (3.4 Å) proves the efficient reduction of the material [16]. The broadening of the RGO peak may indicate a decrease in the size of the particles in the reduced material, or/and the formation of the inhomogeneous sample with wide distribution of interplanar distances.

3.2. Sorption properties of HGO and RHGO

A comparative experimental study of the sorption properties of HGO and its reduced analogue RHGO has not been previously presented in the literature. We assumed that the obviously more hydrophobic material RHGO would sorb water and acetonitrile in significantly less amounts than HGO. Table 2 shows the results of sorption measurements by the DSC using the method described in ref. [2]. As seen from the Table 2 RHGO sorbs less water and acetonitrile than HGO, but the difference is not dramatic. It was shown in [17] that the reduced forms of GO sorb water, but in significantly less amounts compared to the initial GO. Only the original graphite does not sorb water at all. It is worth mentioning that acetonitrile was sorbed by all graphite materials studied, regardless of the degree of oxidation, including the pristine graphite. Apparently, the presence of methyl group in a molecule of a liquid plays a significant role in intercalation into materials with a low degree of oxygenation.

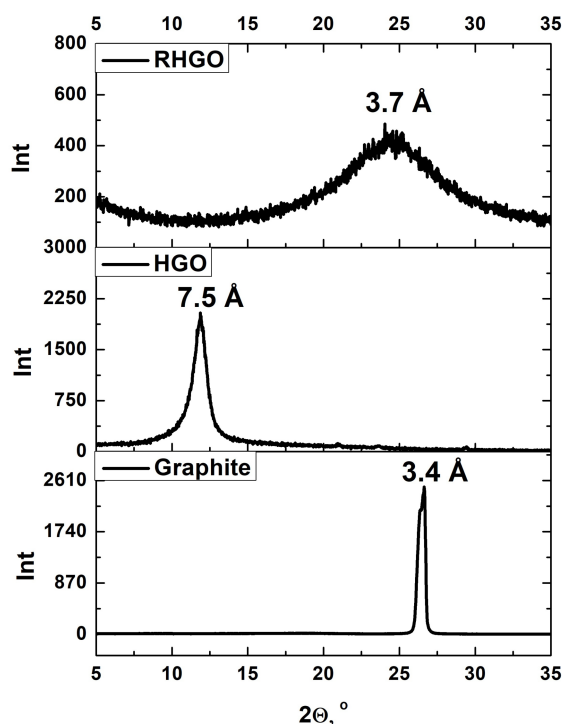


FIG. 1. Parts of the XRD spectra of RHGO, HGO and the original graphite

TABLE 2. Sorption of water and acetonitrile at melting temperatures. *Melting temperature of the sorbed liquid

Material	Sorption of H ₂ O ($T = 273$ K)*, g/g	Sorption of CH ₃ CN ($T = 229$ K)*, g/g
HGO	0.63 ± 0.06 [9]	0.47 ± 0.06 [9]
RHGO	0.50 ± 0.05	0.37 ± 0.03
Graphite	≈ 0	0.24 ± 0.03

3.3. Sorption properties of BGO

Table 2 demonstrates the influence of polarity of a sorbed liquid on the sorption values for the BGO material. The correlation is shown between the values of sorption by the BGO material and the Dimroth–Reichardt “general polarity” parameter [15]. It was previously known that various polar liquids are sorbed by GO materials, but sorption of, e.g. aromatic benzene is close to zero [9]. The authors of [18] demonstrated a slight increase in the interplanar distance in GO after intercalation of liquid benzene due to the π – π interaction of the aromatic system of benzene with the unoxidized regions of GO. We showed that octane is almost not sorbed into BGO, despite the fact that BGO is a less oxidized material than HGO. Octane is also not sorbed in HGO.

In Table 3, the data on sorption of two more polar liquids – propionitrile and trifluoroethanol – are presented. These polar liquids are sorbed into BGO to a significant extent, comparable to the sorption of water and acetonitrile.

3.4. DSC study of system “water + octane” and “HGO + water + octane”

The “water + octane” system was studied by the DSC method. It was shown that the peaks corresponding to the melting peaks of liquids do not overlap and are well spaced along the temperature axis in the DSC trace. This makes it possible to quantify how selectively the highly oxidized HGO material can sorb water from a “water + octane” mixture. The lower part of Fig. 2 shows the DSC curve after adding of HGO to a mixture of water and octane. We conclude from the figure that water was completely removed from the liquid mixture and sorbed by HGO, because the amount of HGO for the experiment was selected based on the data on sorption of pure water in HGO (≈ 0.6 g/g, see Table 1). If both liquids can be individually intercalated into the material, then we would observe a change in the equilibrium sorption values due to the competition at the sorption centers. This was not the case for the water – octane mixture.

TABLE 3. Sorption of polar and non-polar liquids at melting temperatures. *Melting temperature of the sorbed liquid

Sorption (g/g) of	H ₂ O (<i>T</i> = 273 K)*	CH ₃ CN (<i>T</i> = 229 K)*	CH ₃ CH ₂ CN (<i>T</i> = 180 K)*	CF ₃ CH ₂ OH (<i>T</i> = 230 K)*	Octanol-1 (<i>T</i> = 257 K)*	Octan (<i>T</i> = 216 K)*
BGO	0.33 ± 0.04 [2] 0.30 ± 0.02 [8]	0.53 ± 0.04 [2] 0.54 ± 0.09 [8]	0.34 ± 0.04	0.54 ± 0.05	1.13 ± 0.05 [13] 1.05 ± 0.15 [8]	≈ 0
Parameter <i>E_T</i> 30 [14]	63.1	45.6	No data	No data	48.1	31.1
Dielectric constant ϵ	78.5	38.0	No data	No data	9.9	1.9

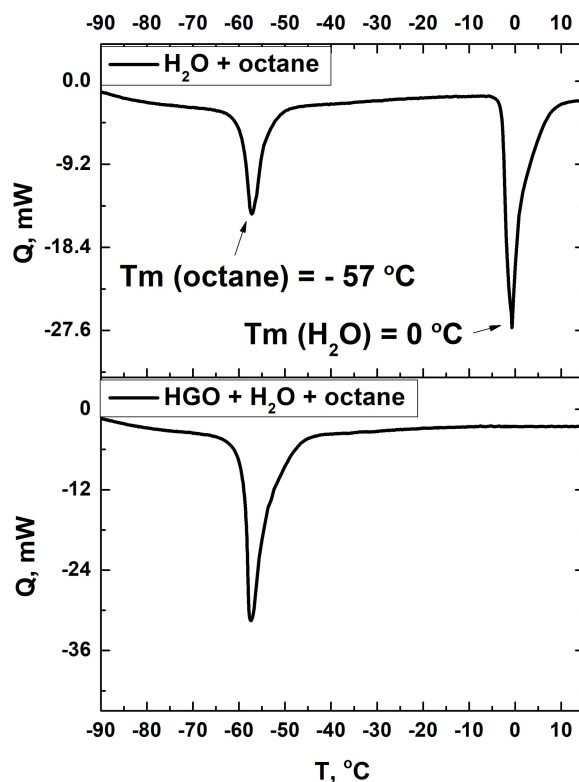


FIG. 2. DSC curves for the systems “water+octane” and “HGO+water+octane”

It is also worth noting that the necessary condition for applying the method described above is the significant difference in the melting temperatures of liquids. For example, sorption from a mixture of benzene ($T_m = 5.5$ °C) and water ($T_m = 0$ °C) cannot be measured quantitatively due to the overlap of the melting peaks of these liquids.

4. Conclusion

The reduced RHGO material was synthesized and characterized in comparison with HGO and pristine graphite. It was shown that the RHGO material sorbs water and acetonitrile slightly less than HGO. We plan to compare sorption properties of RHGO reduced by various methods and to follow the trends of sorption properties along the series of liquids with changing polarity.

The sorption of polar and non-polar liquids by BGO was studied with octane, trifluoroethanol and propionitrile. The octane sorption data confirm that non-polar liquids are not sorbed by the HGO and BGO materials. The same result was obtained in [9] for benzene.

The DSC experimental procedure was developed to quantify the selectivity of sorption from the mixtures of the immiscible liquids. We plan to extend the list of water-immiscible liquids in order to test the efficiency of the procedure.

References

- [1] Paredes J.I., Villar-Rodil S., Martínez-Alonso A., Tascón J.M.D. Graphene Oxide Dispersions in Organic Solvents. *Langmuir*, 2008, **24**, P. 10560–15604.
- [2] Korobov M.V., Talyzin A.V., Rebrikova A.T., Shilayeva E.A., Avramenko N.V., Gagarin A.N., Ferapontov N.B. Sorption of polar organic solvents and water by graphite oxide: Thermodynamic approach. *Carbon*, 2016, **102**, P. 297–303.
- [3] Dreyer D.R., Park S., Bielawski C.W., Ruoff R.S. The chemistry of graphene oxide. *Chemical Society Review*, 2010, **39**, P. 228–240.
- [4] Ferrari A.C., Bonaccorso F., Falco V. Science and technology roadmap for graphene related two-dimensional crystals, and hybrid systems. *Nanoscale*, 2015, **7**, P. 4598–4810.
- [5] Brodie B.C. On the atomic weight of graphite. *Philosophical Transactions of the Royal Society of London*, 1859, **149**, P. 249–259.
- [6] Hummers W.S., Offeman R.E. Preparation of graphitic oxide. *J. of the American Chemical Society*, 1958, **80**, P. 1339–1343.
- [7] Higginbotham A.L., Kosynkin D.V., Sinitskii A., Sun Z., Tour J.M. Lower – Defect Graphene Oxide Nanoribbons from Multiwalled Carbon Nanotubes. *ASC Nano*, 2010, **4**, P. 2059–2069.
- [8] Talyzin A.V., Mercier G., Klechikov A., Hedenstrom M., Johnels D., Wei D., Cotton D., Opitz A., Moons E. Brodie vs Hummers graphite oxides for preparation of multi-layered materials. *Carbon*, 2017, **115**, P. 430–440.
- [9] Kaplin A.V., Rebrikova A.T., Eremina E.A., Chumakova N.A., Avramenko N.V., Korobov M.V. Sorption of Polar Sorbents into GO Powders and Membranes. *Membranes*, 2023, **53** (13), P. 1–12.
- [10] Liu X.L., Ma R., Wang X.X., Ma Y., Yang Y.P., Zhuang L., Zhang S., Jehan R., Chen J.R., Wang X.K. Prepared GO functionalized with lignosulfonate (LS) and polyaniline (PANI) for the adsorption of Pb ions. *Environ. Pollut.*, 2019, **252**, P. 62–73.
- [11] Romanchuk A.Y., Slesarev A.S., Kalmykov S.N., Kosynkin D.V., Tour J.M. Graphene oxide for effective radionuclide removal. *Phys. Chem. Chem. Phys.*, 2013, **15**, P. 2321–2327.
- [12] Kuzenkova A.S., Romanchuk A.Y., Trigub A.L., Maslakov K.I., Egorov A.V., Amidani L., Kittrell C., Kvashnina K.O., Tour J.M., Talyzin A.V., Kalmykov S.N. New insights into the mechanism of graphene oxide and radionuclide interaction. *Carbon*, 2020, **158**, P. 291–302.
- [13] Szabo T., Berkesi O., Forgo P., Josepovits K., Sanakis Y. Evolution of Surface Functional Groups in a Series of Progressively Oxidized Graphite Oxides. *Chemistry of Materials*, 2006, **18**, P. 2740–2749.
- [14] Rebrikova A.T., Klechikov A., Iakunkov A., Sun J., Talyzin A.V., Avramenko N.V., Korobov M.V. Swollen Structures of Brodie Graphite Oxide as Solid Solvates. *J. Phys. Chem. C*, 2020, **124**, P. 23410–23418.
- [15] Marcus Y., Smith A.L., Korobov M.V., Mirakyan A.L., Avramenko N.V., Stukalin E.B. Solubility of C60 Fullerene. *J. Phys. Chem. B*, 2001, **105**, P. 2499–2506.
- [16] Vipul Agarwal, Per B. Zetterlund Strategies for reduction of graphene oxide – A comprehensive review. *Chemical Engineering J.*, 2019, **405**, 12708.
- [17] Iakunkov A., Skrypnichuk V., Nordenstro A., Shilayeva E.A., Korobov M., Prodana M., Enachescu M., Larsson S.H., Talyzin A.V. Activated graphene as a material for supercapacitor electrodes: effects of surface area, pore size distribution and hydrophilicity. *Physical Chemistry Chemical Physics*, 2019, **21**, P. 17901–17912.
- [18] Barroso-Bujans F., Cerveny S., Alegria A., Colmenero J. Sorption and desorption behavior of water and organic solvents from graphite oxide. *Carbon*, 2010, **48**, P. 3277–3286.

Submitted 27 November 2023; revised 9 January 2024; accepted 10 January 2024

Information about the authors:

Alexander V. Kaplin – Moscow State University, Chemistry Department, Moscow, Russia; Semenov Federal Research Center of Chemical Physics, Russian Academy of Sciences, Moscow, Russia; ORCID 0000-0003-2513-0306; alex1997kaplin@mail.ru

Elena A. Eremina – Moscow State University, Chemistry Department, Moscow, Russia; ORCID 0000-0002-4003-9028; ea_er@mail.ru

Mikhail V. Korobov – Moscow State University, Chemistry Department, Moscow, Russia; ORCID 0000-0002-0099-9008; mkorobov49@gmail.com

Conflict of interest: the authors declare no conflict of interest.

Simulation and evaluation of perovskite solar cells utilizing various electron transport layers

R.K. Shukla, Anchal Srivastava, Shikha Rani, Nidhi Singh, Vishnu Kumar Dwivedi, Sharda Pandey, Navina Wadhvani

Physics Department, Lucknow University, Lucknow-226007, India

Corresponding author: Navina Wadhvani, navinawadhvani@gmail.com

ABSTRACT Solar cells that contain perovskite have been a significant object for consideration within the field of solar energy, consistently enhancing their efficiency year by year. In our study, we devised a novel architectural configuration for a tin-based perovskite solar cell, incorporating FTO/ZnO/CH₃NH₃SnI₃/Spiro-OMeTAD/Au. Our investigation into the working of this solar cell involved the utilization of the SCAPS-1D, a versatile tool tailored for the analysis of solar cell behavior. Through this simulation software, we explored different electron-transporting layer (ETL) materials and made adjustments to multiple parameters, including ETL and absorber layer thickness. The outcomes of our research produced promising results, showcasing significant enhancements in different solar cell parameters. These favorable findings underscore the growing allure and potential of perovskite solar cells within the realm of renewable energy. The reported CH₃NH₃SnI₃-based PSCs provide a viable path to the implementation of environmentally benign, low-cost, and high-efficiency PSCs.

KEYWORDS solar cells, perovskite, electron transporting material, SCAPS, ZnO

ACKNOWLEDGEMENTS The authors extend their sincere appreciation to Professor Marc Burgelman of Gent University for graciously supplying the software in this research work.

FOR CITATION Shukla R.K., Srivastava A., Rani S., Singh N., Dwivedi V.K., Pandey S., Wadhvani N. Simulation and evaluation of perovskite solar cells utilizing various electron transport layers. *Nanosystems: Phys. Chem. Math.*, 2024, **15** (1), 135–146.

1. Introduction

The evolution of solar cell technology has passed through distinct phases. The first generation was characterized by the utilization of crystalline and amorphous inorganic materials, exemplified by silicon (Si) and gallium arsenide (GaAs) solar cells. In the second generation, thin-film nanocrystalline solar cells like copper indium gallium selenide and cadmium telluride were introduced. The transition to the third generation marked the emergence of diverse solar cell technologies, encompassing organic, hybrid, nanostructures/quantum dots, and electrochemical (semiconductor/liquid junction) solar cells, including perovskite, plastic, and dye-sensitized solar cells [1–7].

Solar Cells based on perovskite represent a promising alternative to conventional solar cell technologies. Their appeal lies in the cost-effectiveness of their materials and their ability to produce a high number of solar cells using minimal resources, owing to the thin profile of the absorber layer. Significantly, these solar cells are eco-friendly and devoid of lead, positioning them as potential successors to silicon solar cells in the future. This research is dedicated to the investigation of lead-free and environmentally conscious solar cell technologies, employing the SCAPS-1D software for simulations.

Over the years, perovskite solar cells (PSC) have made substantial advancements, with their photoelectric power conversion efficiency (PCE) experiencing significant growth, progressing from 3.80 % in 2003 [8] to an impressive 25.70 % in 2022 [9]. This remarkable progress positions them as frontrunners for the 4th generation of solar cell technologies.

PSCs offer a multitude of advantages when compared with conventional silicon-based solar cells:

- i) PSCs demonstrated remarkable PCEs that exceed 25.00 %, bringing them near the power conversion efficiency levels of commercial Si-solar cells [10].
- ii) The production of PSCs can be achieved using cost-effective solution-based methods such as spin-coating or printing techniques. This potential reduction in manufacturing costs stands in contrast to the complex and expensive processes required for silicon solar cells [11].
- iii) Perovskite materials provide the unique ability to tune their bandgap by adjusting their composition, enabling the absorption of a wider spectrum of solar radiation. This tunability makes PSCs suitable for both single-junction and tandem solar cell configurations [12].
- iv) PSCs manufactured on different types of substrates, like flexible and lightweight materials, simplifying their integration into diverse applications such as building-integrated photovoltaics, wearable electronics, and portable devices [13].

PSCs hold significant potential for achieving efficient and profitable solar energy conversion. With ongoing research and development efforts, these cells have the potential to revolutionize the field of photovoltaics and contribute to the widespread adoption of renewable energy sources [14–21].

Several simulation models, including SCAPS, AMPS, GPVDM, and others, are available for simulating solar cells. These models analyze the properties of different layers within solar cells and their respective roles in optimizing overall solar cell performance. SCAPS, is a numerical simulation program operating in one dimension, incorporating seven layers. It was established by a team of researchers specializing in solar cells at the University of Gent. Comprehensive information about the program employed can be found in the literature [22–25].

Choosing to simulate and evaluate perovskite solar cells utilizing various electron transport layers is a strategic decision with several merits. Firstly, perovskite solar cells have emerged as promising candidates for efficient and cost-effective solar energy conversion. By simulating their performance, we gain valuable insights into optimizing their efficiency and stability. The focus on different electron transport layers is particularly relevant because the choice of this layer significantly influences the overall performance of the solar cell. Through simulation, we can systematically assess the impact of various electron transport materials on key parameters like charge transport, recombination rates, and overall device efficiency. Simulating these scenarios provides a cost-effective and time-efficient way to explore a wide range of possibilities, aiding in the identification of optimal electron transport layers for enhanced device performance. This research is crucial for advancing the understanding of perovskite solar cells and contributes to the ongoing efforts to make solar energy more accessible and sustainable. Ultimately, the chosen simulation approach allows for a comprehensive evaluation that can guide experimental efforts toward more efficient and stable perovskite solar cell designs.

2. The elaborate structure of perovskite solar cells

Perovskite is a mineral comprising Calcium, Titanium, and Oxygen with the chemical formula CaTiO_3 . In a more comprehensive context, the term 'perovskite structure' refers to any compound that possesses the ABX_3 composition and shares crystallographic characteristics resembling those of the Perovskite mineral. In this context, 'A' signifies an organic cation, 'B' denotes a larger inorganic cation, and 'X₃' indicates a somewhat smaller halogen anion.

The conventional perovskite solar cell adopts an n-i-p type configuration, where 'n' represents the electron-conductive layer, 'i' signifies the absorber layer, and 'p' serves as the hole-conductive layer. For our study, we opted for $\text{CH}_3\text{NH}_3\text{SnI}_3$ as the absorber layer, and we conducted a systematic evaluation of Electron Transport Layer (ETL) by choosing materials from a range of options, including zinc oxide (ZnO), La-doped BaSnO₃ (LBSO), Tin(IV) oxide (SnO_2), Ceric oxide (CeO_2), Phenyl-C61-butiric acid methyl ester (PCBM), Tungsten trioxide (WO_3), Indium Gallium Zinc Oxide (IGZO), Cadmium sulfide (CdS), Copper monoxide (CuO), and Buckminsterfullerene (C60). The hole-conductive layer (HTL) utilized in our design is 2,2',7,7'-Tetrakis(N,N-di-p-methoxyphenylamine)9,9'-spirobifluorene (Spiro-OMeTAD). Fig. 1 provides an illustration of the perovskite solar cell architecture under investigation, and Table 1 offers essential material parameters necessary for conducting the simulation.

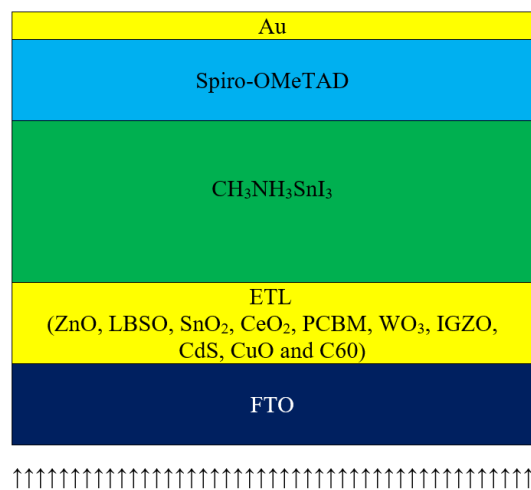


FIG. 1. The architecture of the studied PSC

TABLE 1. Parameters of the materials used in simulation

Parameters	FTO	ZnO	CH ₃ NH ₃ SnI ₃	Spiro-OMeTAD
t (nm)	250	50	500	50
E_g (eV)	3.2	3.3	1.30	3.2
η (eV)	4.4	3.9	4.2	2.10
ε_r (relative)	9.0	9.0	10	3.0
N_c (cm ⁻³)	2.2·10 ¹⁸	1·10 ¹⁹	1·10 ¹⁸	2.5·10 ¹⁸
N_v (cm ⁻³)	1.8·10 ¹⁹	10 ¹⁹	1·10 ¹⁸	1.85·10 ¹⁹
V_{nt} (cm/s)	1·10 ⁷	1·10 ⁷	1·10 ⁷	1·10 ⁷
V_{pt} (cm/s)	1·10 ⁷	1·10 ⁷	1·10 ⁷	1·10 ⁷
μ_n (cm ² /Vs)	20	50	1.6	2·10 ⁴
μ_p (cm ² /Vs)	10	0.5	1.6	2·10 ⁴
N_D (cm ⁻³)	1·10 ²¹	5·10 ¹⁷	—	0
N_A (cm ⁻³)	0	0	3.21·10 ¹⁵	1·10 ²⁰
N_t (cm ⁻³)	1·10 ¹⁵	1·10 ¹⁵	4.5·10 ¹⁶	1·10 ¹⁴
Reference	[26]	[27]	[28]	[29]

3. Results and discussion

SCAPS-1D is specifically designed for the analysis of solar cells, developed by the University of Gent, Belgium. When configuring the input data for the Electron Transport Material (ETM), Table 2 provides a comprehensive listing of all the requisite ETM parameters essential for executing the simulation.

3.1. Effect of the electron transporting layer

In this section, we carried out an evaluation of various ETMs for solar cells, including ZnO, LBSO, SnO₂, CeO₂, PCBM, WO₃, IGZO, CdS, CuO, and C60. Fig. 2 presents a performance comparison, clearly indicating that ZnO outperforms the other materials, exhibiting the highest power conversion efficiency. As a result, ZnO was identified as the optimal electron-transport material. The photovoltaic (PV) parameters for the ZnO layer are as follows: $V_{OC} = 0.81$ V, $J_{SC} = 29.80$ mA·cm⁻², Fill Factor = 67.29 %, and PCE = 16.26 % at a thickness of 50 nm for the electron transport layer. This choice underscores the effectiveness of ZnO in significantly enhancing the overall performance.

3.2. Impact of electron transport layer thickness on solar cell performance

The primary objective of this simulation is to determine the optimal thickness that results in the most favorable attributes for the PSC. Fig. 3 depicts the simulated parameters of the PSC as the thickness of the perovskite material varies. Specifically, we varied the thickness of the electron transporting layer (ETL) within a range of 10 to 300 nm. The results indicate that the open-circuit voltage (V_{OC}) remains relatively consistent, regardless of the ETL thickness. The value of J_{SC} initially increases up to 30 nm, followed by a subsequent decrease. The FF initially rises as the ETL thickness increases up to 40 nm, after which the value of FF stabilizes. Additionally, the PCE improves as the ETL thickness increases up to 40 nm but starts to decline beyond this point. Based on these findings, we selected an electron transporting layer thickness of 40 nm for further simulations, as it represents a favorable balance of performance characteristics. At this thickness, the solar cell exhibits the solar cell parameters: $V_{OC} = 0.81$ V, $J_{SC} = 29.81$ mA·cm⁻², FF = 67.29 %, and PCE = 16.27 %.

3.3. Influence of electron transport layer donor density (N_D) variation

In this simulation, we opted for various N_D values to investigate their influence on PSCs functioning. Fig. 4 visually represents the changes in solar cell parameters in relation to the logarithm of N_D . All parameter values exhibit fluctuations in response to defect density changes. The V_{OC} initially remains constant, then rises, and finally decreases as the electron transport layer donor density increases from 1 to 1·10²² cm⁻³. Similarly, the J_{SC} remains constant up to N_D equal to

TABLE 2. Physical parameters of different ETL materials

Material	LBSO	TiO ₂	ZnO	FTO	SnO ₂	CeO ₂	PCBM	WO ₃
t (nm)	50	50	50	50	50	50	50	50
E_g (eV)	3.12	3.2	3.3	3.2	3.5	3.5	2	2.6
η (eV)	4.4	4	4	4	4	4.6	3.9	3.8
ϵ_r	22	9	9	9	9	9	3.9	4.8
N_c (cm ⁻³)	$1.8 \cdot 10^{20}$	$1 \cdot 10^{19}$	$3.7 \cdot 10^{18}$	$2.2 \cdot 10^{18}$	$4.36 \cdot 10^{18}$	$1 \cdot 10^{20}$	$2.5 \cdot 10^{21}$	$2.2 \cdot 10^{21}$
N_v (cm ⁻³)	$1.8 \cdot 10^{20}$	$1 \cdot 10^{19}$	$1.8 \cdot 10^{19}$	$1.8 \cdot 10^{19}$	$2.52 \cdot 10^{19}$	$2 \cdot 10^{21}$	$2.6 \cdot 10^{21}$	$2.2 \cdot 10^{21}$
V_{nt} (cm·s ⁻¹)	$1 \cdot 10^7$	$1 \cdot 10^7$	$1 \cdot 10^7$	$1 \cdot 10^7$	$1 \cdot 10^7$	$1 \cdot 10^7$	$1 \cdot 10^7$	$1 \cdot 10^7$
V_{pt} (cm·s ⁻¹)	$1 \cdot 10^7$	$1 \cdot 10^7$	$1 \cdot 10^7$	$1 \cdot 10^7$	$1 \cdot 10^7$	$1 \cdot 10^7$	$1 \cdot 10^7$	$1 \cdot 10^7$
μ_n (cm ² V ⁻¹ s ⁻¹)	0.69	0.02	100	20	20	100	0.2	30
μ_p (cm ² V ⁻¹ s ⁻¹)	0.69	2	25	10	10	25	0.2	30
N_D (cm ⁻³)	$2 \cdot 10^{21}$	$1 \cdot 10^{12}$	$1 \cdot 10^{18}$	$1 \cdot 10^{19}$	$1 \cdot 10^{18}$	$1 \cdot 10^{21}$	$2.93 \cdot 10^{17}$	$6.35 \cdot 10^{17}$
N_A (cm ⁻³)	—	—	—	—	—	—	—	—
N_t (cm ⁻³)	$1 \cdot 10^{15}$	$1 \cdot 10^{15}$	$1 \cdot 10^{15}$	$1 \cdot 10^{15}$	$1 \cdot 10^{15}$	$1 \cdot 10^{15}$	$1 \cdot 10^{15}$	$1 \cdot 10^{15}$
Reference	[30]	[31]	[27]	[26]	[31]	[36]	[31]	[32]

Material	IGZO	CdS	CuO	C60
t (nm)	50	50	50	50
E_g (eV)	3.05	2.4	1.5	1.7
η (eV)	$4.16 \cdot 10^{18}$	4.18	4.07	3.9
ϵ_r	10	10	18.1	4.2
N_c (cm ⁻³)	$5 \cdot 10^{18}$	$5 \cdot 10^{18}$	$2.2 \cdot 10^{19}$	$8 \cdot 10^{19}$
N_v (cm ⁻³)	$5 \cdot 10^{18}$	$5 \cdot 10^{18}$	$5.5 \cdot 10^{20}$	$8 \cdot 10^{19}$
V_{nt} (cm·s ⁻¹)	$1 \cdot 10^7$	$1 \cdot 10^7$	$1 \cdot 10^7$	$1 \cdot 10^7$
V_{pt} (cm·s ⁻¹)	$1 \cdot 10^7$	$1 \cdot 10^7$	$1 \cdot 10^7$	$1 \cdot 10^7$
μ_n (cm ² V ⁻¹ s ⁻¹)	15	100	100	$8 \cdot 10^{-2}$
μ_p (cm ² V ⁻¹ s ⁻¹)	0.1	25	0.1	$3.5 \cdot 10^{-3}$
N_D (cm ⁻³)	$1 \cdot 10^{18}$	$1 \cdot 10^{15}$	$1 \cdot 10^{15}$	$1 \cdot 10^{17}$
N_A (cm ⁻³)	—	—	—	—
N_t (cm ⁻³)	$1 \cdot 10^{15}$	$1 \cdot 10^{15}$	$1 \cdot 10^{15}$	$1 \cdot 10^{15}$
Reference	[33]	[34]	[34]	[35]

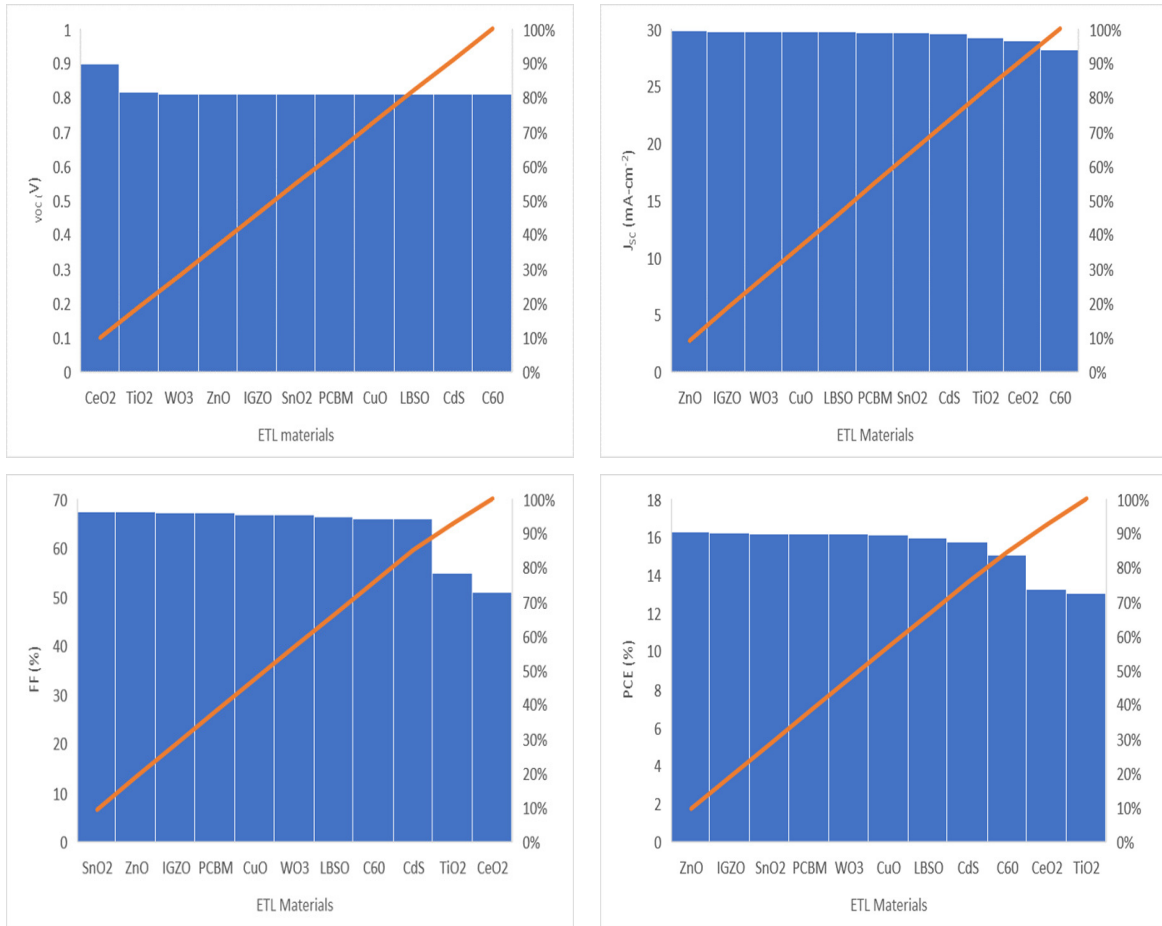


FIG. 2. Performance of PV parameters of different ETL materials

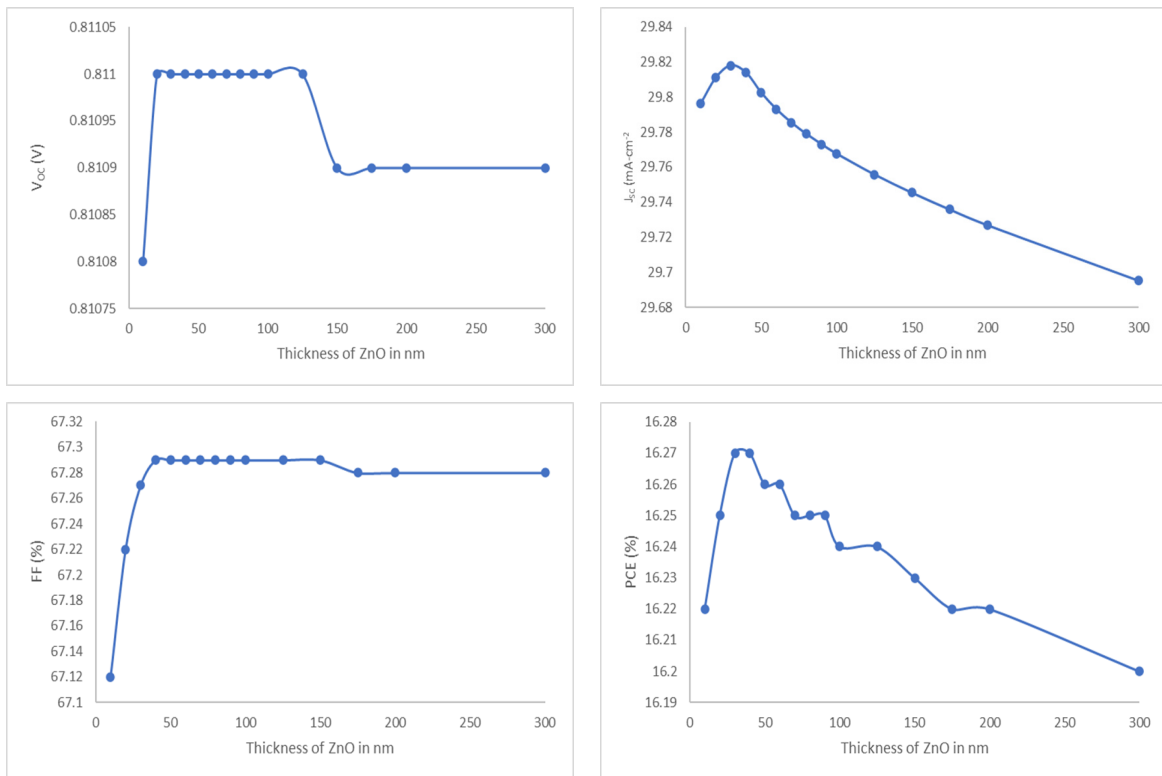


FIG. 3. Effects of ZnO thickness on PSC performance

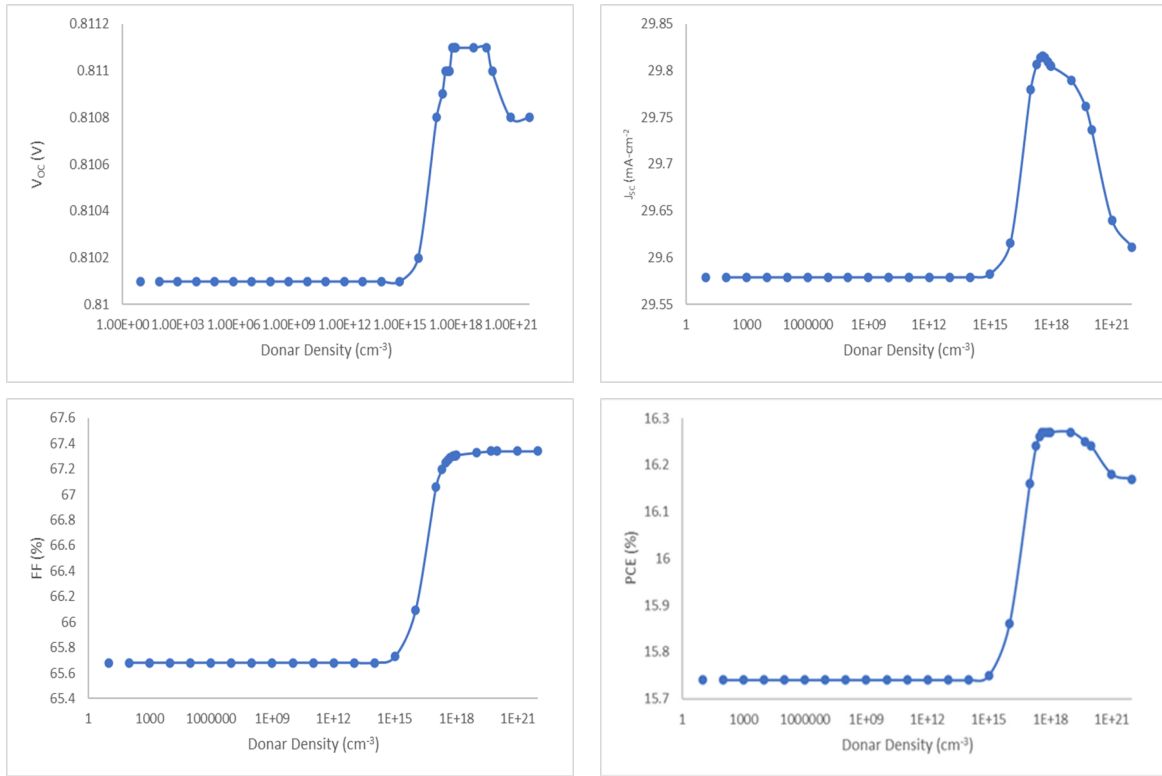


FIG. 4. Illustrates the influence of ZnO donor density (N_D) on PSC functioning

$1 \cdot 10^{13} \text{ cm}^{-3}$, then increases as N_D increases to $1 \cdot 10^{18} \text{ cm}^{-3}$, followed by a decrease. The fill factor remains constant up to N_D value of 10^{14} cm^{-3} , then increases as N_D increases to $1 \cdot 10^{19} \text{ cm}^{-3}$ and finally becomes stable. The power conversion efficiency remains constant at 15.74 % as N_D rises to $1 \cdot 10^{14} \text{ cm}^{-3}$, then power conversion efficiency rises to 16.27 % as N_D rises to $1 \cdot 10^{19} \text{ cm}^{-3}$ but decreases subsequently. Consequently, we identify the optimal value of N_D as $4 \cdot 10^{17} \text{ cm}^{-3}$ for further calculations.

3.4. Impact of absorber layer thickness on cell functioning

In this section, we explored the influence of varying the thickness of the absorber sheet $\text{CH}_3\text{NH}_3\text{SnI}_3$, ranging from 50 to 3000 nm, on the performance of the solar cell. The outcomes revealed intriguing trends in the solar cell's performance metrics. As the absorber film's thickness increased, the V_{OC} exhibited a decline until the absorber film thickness reached 500 nm, at which point V_{OC} stabilized at approximately 0.81 V. The J_{SC} initially rose from 9.86 to 30.15 $\text{mA} \cdot \text{cm}^{-2}$, reaching its peak for the absorber film thickness of 1200 nm, but as the absorber film thickness increased further the J_{SC} began to decrease. Concurrently, the FF demonstrated a continuous decrease, spanning from 79.62 to 65.87 % with increasing thickness of the absorber layer. The PCE exhibited an increase from 6.72 to 16.27 % for the 50 to 500 nm thickness of the absorber layer, followed by a slight decline to 16.11 % as the absorber layer thickness increased beyond 500 nm, as depicted in Fig. 5. At a thickness of 500 nm, the PV parameters were as follows: $V_{OC} = 0.81 \text{ V}$, $J_{SC} = 29.81 \text{ mA} \cdot \text{cm}^{-2}$, Fill Factor = 67.27 %, and PCE = 16.27 %. These findings led us to select an absorber thickness of 500 nm for further simulations, as it offered an optimal balance of performance characteristics.

3.5. Influence of varying acceptor density (N_A) in the absorber layer on cell performance

The presence of defects has a substantial impact on the optimization of device performance. Higher concentrations of defects in the absorber layer result in increased recombination due to the formation of pinholes, faster degradation of the film, and reduced stability, leading to an overall deterioration in device performance. To ascertain the ideal defect concentration in the absorber layer for optimal parameters, simulations were carried out, varying the defect density from 10 to $1 \cdot 10^{22} \text{ cm}^{-3}$.

Figure 6 illustrates that in order to achieve higher efficiency, it is essential to reduce defects in the perovskite to $8 \cdot 10^{15} \text{ cm}^{-3}$. At this optimal defect concentration, the solar cell exhibited the following parameters: $V_{OC} = 0.83 \text{ V}$, $J_{SC} = 29.63 \text{ mA} \cdot \text{cm}^{-2}$, Fill Factor = 68.48 %, and PCE = 16.91 %. These findings underscore the importance of minimizing defects in the absorber layer to enhance the total performance of the device.

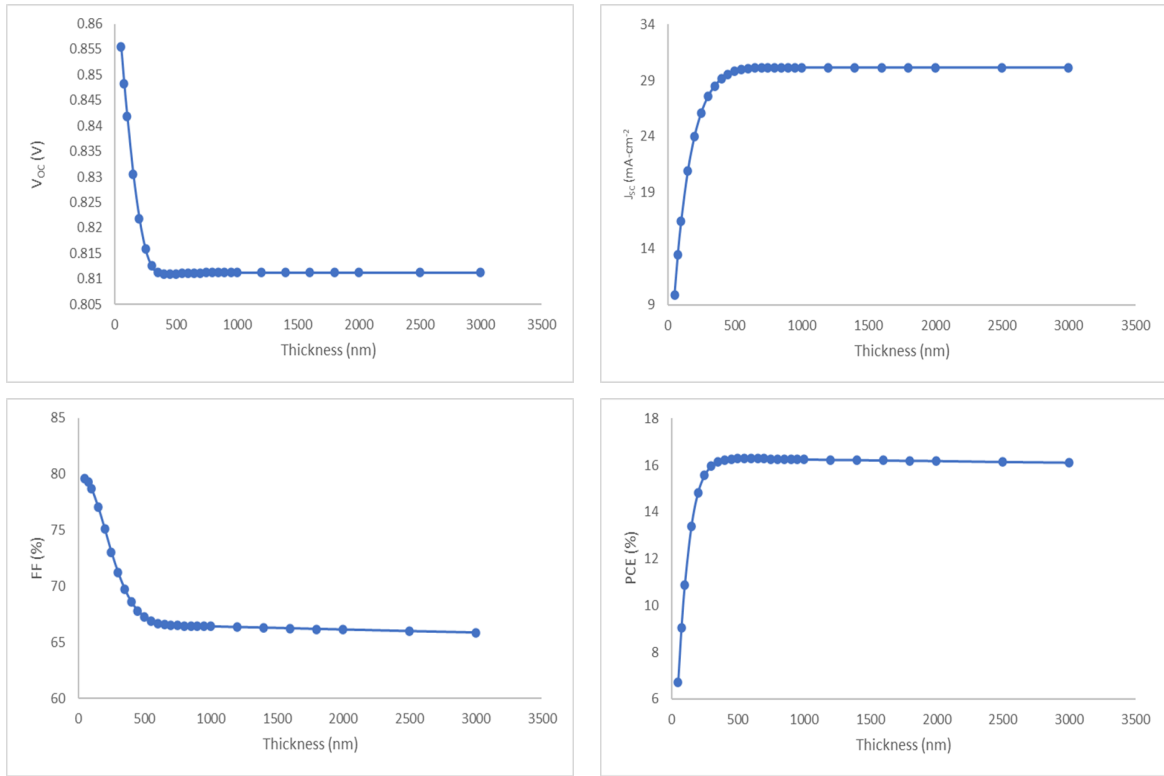


FIG. 5. Influence of $\text{CH}_3\text{NH}_3\text{SnI}_3$ thickness on PSC performance

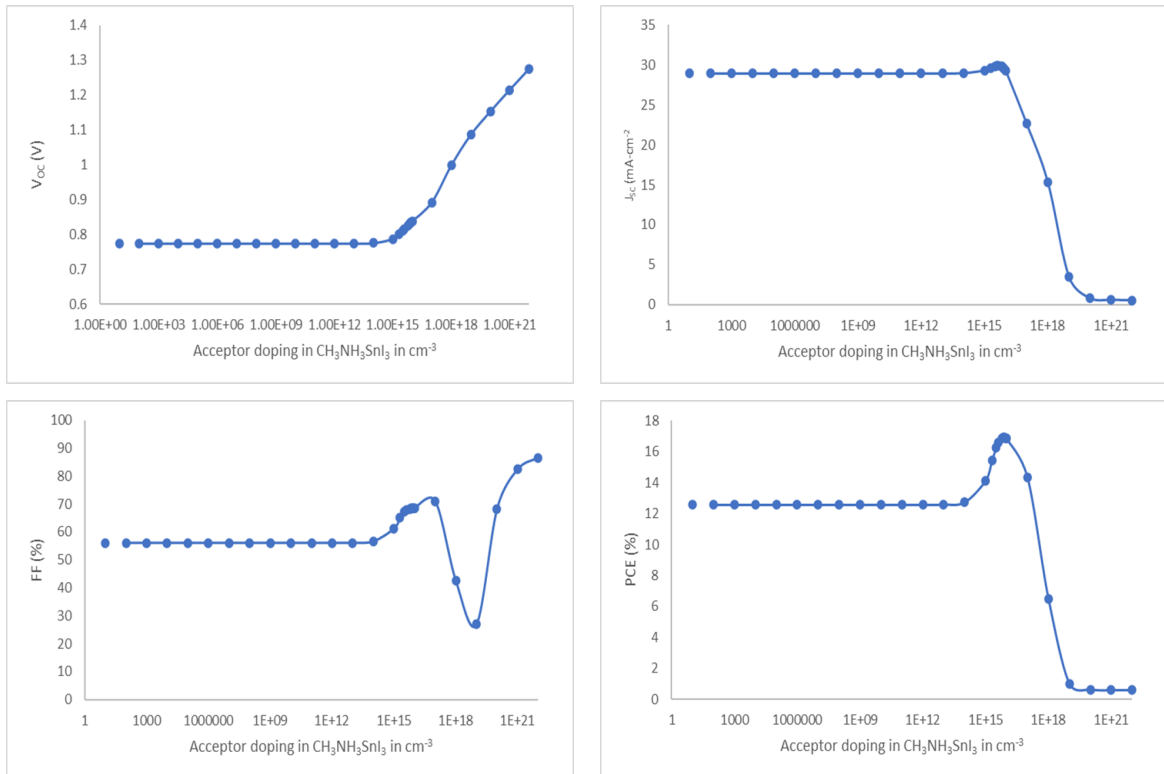


FIG. 6. Illustrates the influence of $\text{CH}_3\text{NH}_3\text{SnI}_3$ acceptor density (N_A) on PSC performance

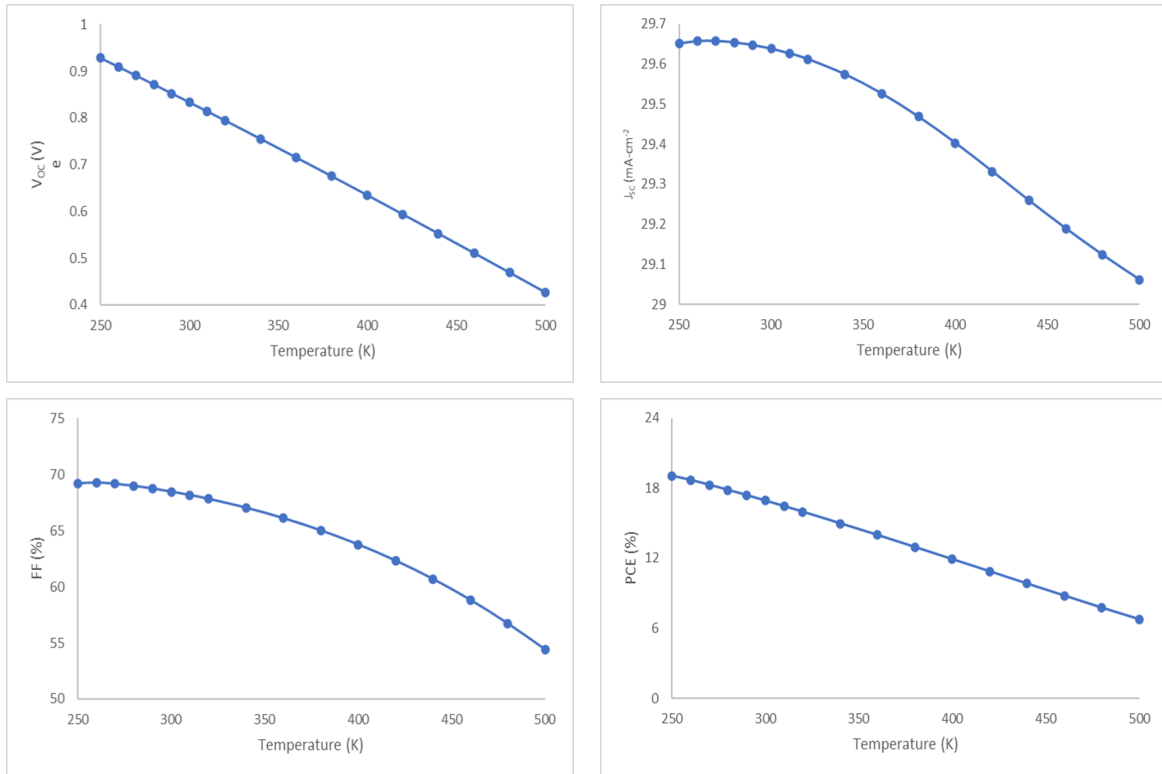


FIG. 7. Variations in solar cell characteristics with changing temperature

3.6. Influence of temperature on cell performance

Much like other semiconductor devices, solar cells are susceptible to temperature fluctuations, especially when deployed outdoors, where temperatures can surpass 300 K. It is crucial to examine how temperature affects the performance of solar cells. Fig. 7 provides insights into the variations in V_{OC} , J_{SC} , Fill Factor, and PCE at different temperatures. With an increase in temperature from 250 to 500 K, there is a notable decline in PCE, plummeting from 19.04 % to 6.76 %. At 300 K, the solar cell demonstrates the following performance parameters: $V_{OC} = 0.83$ V, $J_{SC} = 29.63$ $\text{mA}\cdot\text{cm}^{-2}$, Fill Factor = 68.48 %, and PCE = 16.91 %. These findings underscore the significance of considering and optimizing solar cell performance across varying temperature conditions.

3.7. Influence of series resistance on cell performance

The presence of series resistance plays a pivotal role in influencing the behavior of solar cells, stemming from the metal contacts on both the solar cell and layer surfaces. To evaluate the solar cell's efficiency, we systematically adjusted the series resistance within a range of 0 to 12 $\text{Ohm}\cdot\text{cm}^2$. Fig. 8 provides a visual representation of the outcomes, showing that as the series resistance increases, both J_{SC} and Fill Factor decrease, resulting in higher leakage currents and subsequently leading to reduced PCE. Interestingly, the V_{OC} exhibits relative stability across this spectrum of series resistance values.

3.8. Effect of shunt resistance on cell performance

A solar cell with a low shunt resistance experiences elevated power losses since it permits the light-generated current to deviate along an alternative route. As illustrated in Fig. 9, the fill factor (FF) is the parameter most influenced by this situation, yielding higher values for both V_{OC} and PCE, while the J_{SC} remains relatively unaffected.

3.9. Optimized short-circuit photocurrent density and open-circuit photovoltage curve

After establishing and maintaining the optimized values for both the thickness of the ETL and the absorber layer, along with the defect density, we determined the resulting photovoltaic (PV) parameters: $V_{OC} = 0.83$ V, J_{SC} of 29.63 $\text{mA}\cdot\text{cm}^{-2}$, FF = 68.48 %, and PCE = 16.91 %. Fig. 10 visually depicts the optimized current density versus voltage relationship.

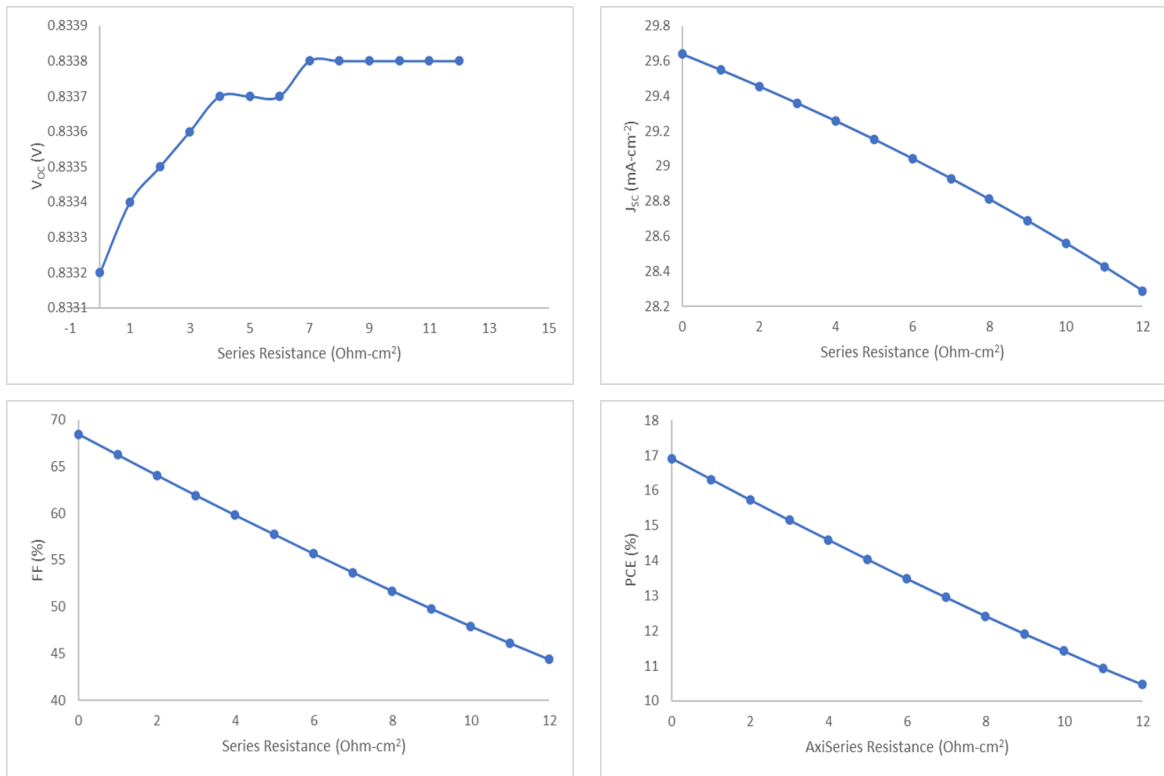


FIG. 8. Illustrates the effect of series resistance on PSC performance

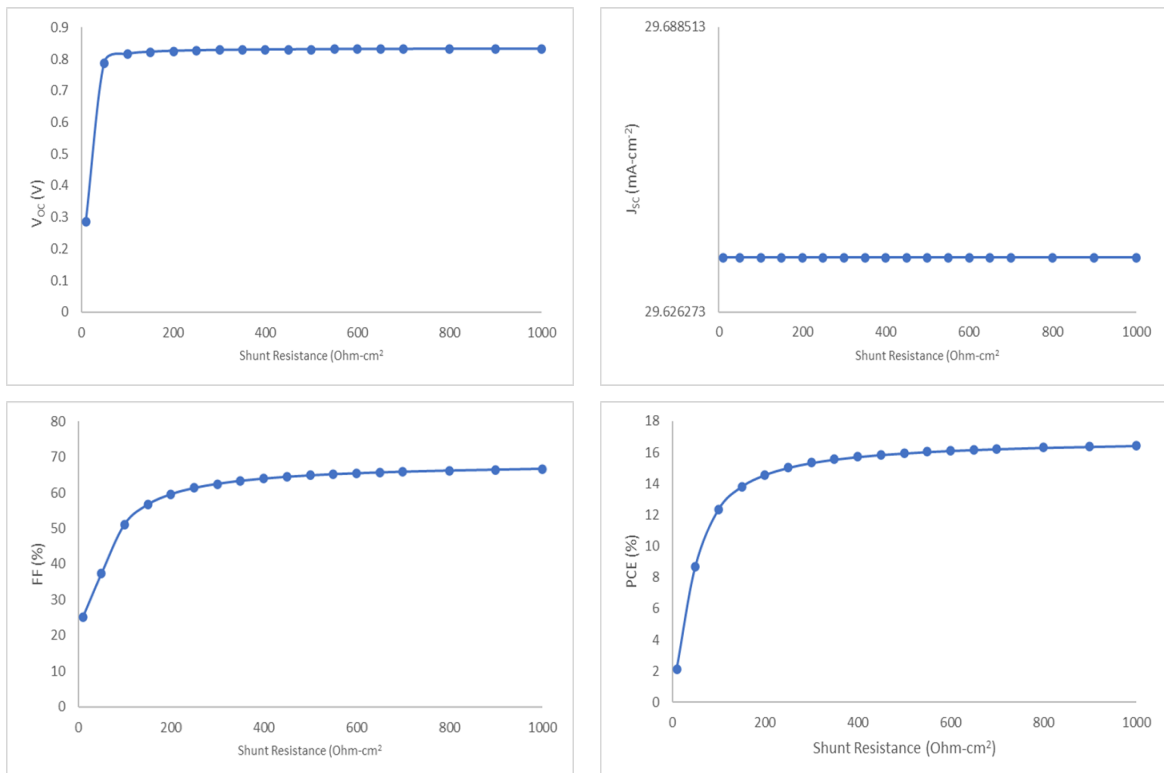


FIG. 9. Illustrates the influence of shunt resistance on PSC performance

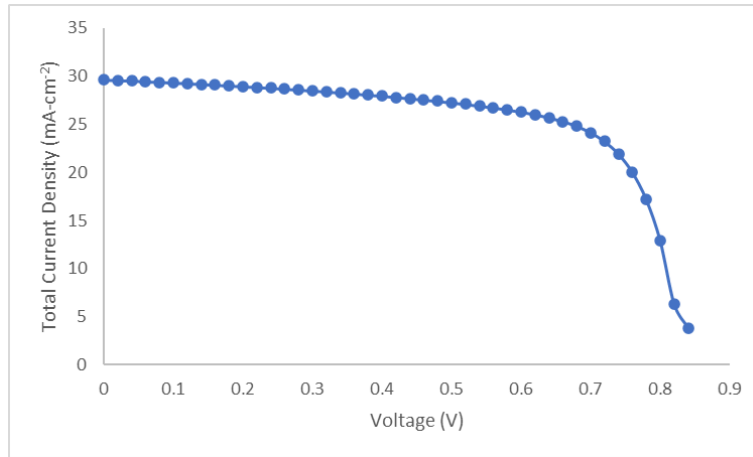


FIG. 10. Variations in short-circuit photocurrent density and open-circuit photovoltage of the investigated solar cell at $T = 300$ K

3.10. Quantum efficiency (QE)

The QE of a PSC measures the current produces when exposed to photons of specific wavelengths. Fig. 11 provides an illustration of the QE curve for a perovskite solar cell, encompassing wavelengths ranging from 300 to 900 nm. Remarkably, the QE values consistently exceed 90 % across most of this spectrum. Upon closer examination of the graph, it becomes apparent that QE increases as the wavelength extends from 300 to 390 nm. QE maintains a consistently high level exceeding 90 % up to wavelengths equal to 400 nm. However, beyond this threshold, QE gradually declines, exhibiting reduced values as the wavelength extends further to wavelengths equal to 900 nm.

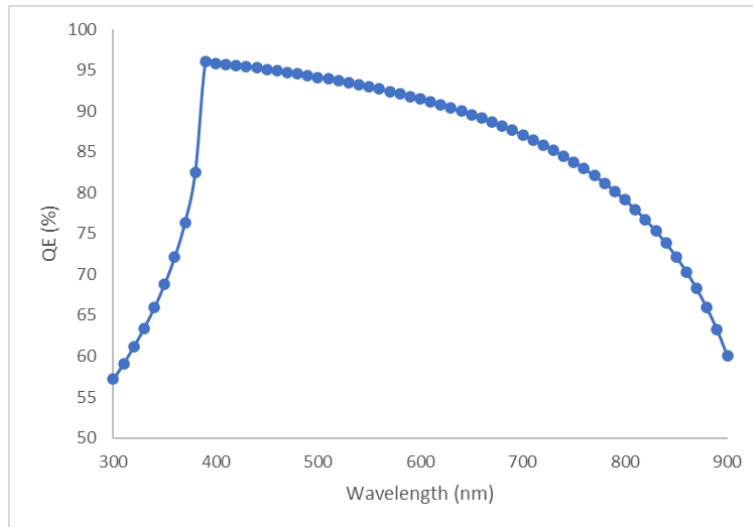


FIG. 11. Quantum efficiency curve of studied solar cell

4. Conclusion

We conducted SCAPS-1D simulations to investigate the performance of ETM in lead-free PSCs. We systematically tested various ETL materials to identify the one that offers the best solar cell performance. Subsequently, we identified the optimal ETL material. Furthermore, we independently adjusted the thickness of both the ETL and the absorber layer, along with fine-tuning the working temperature and resistances within the solar cell circuit. The outcomes of these simulations revealed significant results, showcasing the following critical performance metrics for the solar cell: V_{OC} of 0.83 V, J_{SC} of 29.63 mA-cm⁻², FF of 68.48 %, and PCE of 16.91 %. Upon thorough analysis, we concluded that the most efficient configuration for the solar cell involves a ZnO (ETL) thickness of 40 nm and a CH₃NH₃SnI₃ (absorber layer) thickness of 500 nm. These precise dimensions resulted in the highest efficiency, offering valuable insights for optimizing future designs of lead-free perovskite solar cells.

References

- [1] Richter A., Hermle M., Glunz S.W. Reassessment of the limiting efficiency for crystalline silicon solar cells. *IEEE J. Photovolt.*, 2013, **3**, P. 1184–1191.
- [2] Sharma P., Goyal P. Evolution of PV technology from conventional to nano-materials. *Mater. Today Proc.*, 2020, **28**, P. 1593–1597.
- [3] Crabtree G.W., Lewis N.S. Physics of sustainable energy, using energy efficiently and producing it renewably. *Proceedings of the AIP Conference*, Berkeley, CA, USA, 1–2 March 2008; Melville, NY, USA, American Institute of Physics, 2008.
- [4] Goetzberger A., Hebling C., Schock H.W. Photovoltaic materials, history, status and outlook. *Mater. Sci. Eng. R. Rep.*, 2003, **40**, P. 1–46.
- [5] Nayeripour M., Mansouri M., Orooji F., Waffenschmidt E., ed. *Solar Cells*. IntechOpen Limited. London, UK, 2020, P. 1–50.
- [6] Saga T., Advances in crystalline silicon solar cell technology for industrial mass production. *NPG Asia Mater.*, 2010, **2**, P. 96–102.
- [7] Law M., Greene L.E., Johnson J.C., Saykally R., Yang P., Nanowire dye-sensitized solar cells. *Nat. Mater.*, 2005, **4**, P. 455–459.
- [8] Akihiro Kojima, Kenjiro Teshima, Yasuo Shirai, Tsutomu Miyasaka, Organometal Halide Perovskites as Visible-Light Sensitizers for Photovoltaic Cells. *J. of the American Chemical Society*, 2009, **131** (17), P. 6050–6051.
- [9] Best Research-Cell Efficiency Chart. URL: <https://www.nrel.gov/pv/cell-efficiency.html>.
- [10] Lin C. Stabilizing Organic-Inorganic Lead Halide Perovskite Solar Cells with Efficiency Beyond 20. *Front Chem.*, 2020, **8**, P. 592.
- [11] Bhaskar Parida, Arjun Singh, Abdul Kareem Kalathil Soopy, Sambasivam Sangaraju, Madhulita Sundaray, Satrujit Mishra, Shengzhong (Frank) Liu, Adel Najar. Recent Developments in Upscalable Printing Techniques for Perovskite Solar Cells. *Adv. Sci.*, 2022, **9**, 2200308.
- [12] Terry Chien-Jen Yang, Peter Fiala, Quentin Jeangros, Christophe Ballif. High-Bandgap Perovskite Materials for Multijunction Solar Cells. *Joule*, 2018, **2** (8), P. 1421–1436.
- [13] Julianna Panidi, Dimitra G. Georgiadou, Theresa Schoetz, Themis Prodromakis. Advances in Organic and Perovskite Photovoltaics Enabling a Greener Internet of Things. *Adv. Funct. Mater.*, 2022, **32**, 2200694.
- [14] Li W., Jiang Q., Yang J., Luo Y., Li X., Hou Y., Zhou S. Improvement of photovoltaic performance of perovskite solar cells with a ZnO/Zn₂SnO₄ composite compact layer. *Sol Energy Mater Sol Cells*, 2017, **159**, 143.
- [15] Ye T., Xing J., Petrovic M., Chen S., Chellappan V., Subramanian G.S., Sum T.C., Liu B., Xiong Q., Ramakrishna S. Temperature effect of the compact TiO₂ layer in planar perovskite solar cells: an interfacial electrical, optical and carrier mobility study. *Sol Energy Mater Sol Cells*, 2017, **163**, 242.
- [16] Apostolopoulou A., Sygkridou D., Rapsomanikis A., Kalarakis A.N., Stathatos E. Enhanced performance of mesostructured perovskite solar cells in ambient conditions with a composite TiO₂-In₂O₃ electron transport layer. *Sol Energy Mater Sol Cells*, 2017, **166**, 100.
- [17] Huang X., Hu Z., Xu J., Wang P., Wang L., Zhang J., Zhu Y. Low-temperature processed SnO₂ compact layer by incorporating TiO₂ layer toward efficient planar heterojunction perovskite solar cells. *Sol Energy Mater Sol Cells*, 2017, **164**, 87.
- [18] Amrit Kumar Mishra, Shukla R.K. Simulation of photovoltaic material (donor blends PTB7:PC70BM) polymer for solar cell application. *Materials Today: Proceedings*, 2021, **46** (6), P. 2288–2293.
- [19] Amrit Kumar Mishra, Shukla R.K. Effect of Humidity in the Perovskite Solar Cell. *Materials Today: Proceedings*, 2020, **29**, P. 836–838.
- [20] Amrit Kumar Mishra, Shukla R.K. Fabrication and Characterization of Perovskite (CH₃NH₃PI₃) Solar Cells. *SN Applied Sciences*, 2020, **2**, 321.
- [21] Shukla R.K., Amrit Misra. Tuning of Perovskite material for Solar Cell Application. *Int. J. of Latest Trends in Engineering and Technology*, 2019, **13** (3), P. 28–33.
- [22] Decock K., Khelifi S., Burgelman M. Modelling multivalent defects in thin film solar cells. *Thin Solid Films*, 2011, **519**, P. 7481–7484.
- [23] Burgelman M., Marlein J. Analysis of graded band gap solar cells with SCAPS. *Proceedings of the 23rd European Photovoltaic Solar Energy Conference*, 2008, Valencia, P. 2151–2155.
- [24] Verschraegen J., Burgelman M. Numerical modeling of intra-band tunneling for heterojunction solar cells in SCAPS. *Thin Solid Films*, 2007, **515**, P. 6276–6279.
- [25] Yuxiang W., Juan L., Jian X., Yangyang D., Like H., Jian N., Hongkun C., Jianjun Z. Organic-inorganic hybrid CH₃NH₃PbI₃ perovskite materials as channels in thin-film field-effect transistors. *RSC Advances*, 2016, **6**, P. 16243–16249.
- [26] Sidra Khatoun, Vishwadeep Chakraborty, Satish Kumar Yadav, Sujata Diwakar, Jyotsna Singh, Rajendra Bahadur Singh. Simulation study of CsPbI_xBr_{1-x} and MAPbI₃ heterojunction solar cell using SCAPS-1D. *Solar Energy*, 2023, **254**, P. 137–157.
- [27] Rai N., Rai S., Singh P.K., et al. Analysis of various ETL materials for an efficient perovskite solar cell by numerical simulation. *J. Mater. Sci.: Mater. Electron*, 2020, **31**, P. 16269–16280.
- [28] Patel P.K. Device simulation of highly efficient eco-friendly CH₃NH₃SnI₃ perovskite solar cell. *Sci. Rep.*, 2021, **11**, 3082.
- [29] Tiwari P., Alotaibi M.F., Al-Hadeethi Y., Srivastava V., Arkook B., Sadanand, Lohia P., Dwivedi D.K., Umar A., Algadi H., et al. Design and Simulation of Efficient SnS-Based Solar Cell Using Spiro-OMeTAD as Hole Transport Layer. *Nanomaterials*, 2022, **12**, 2506.
- [30] Parvesh K. Deendyala, Shweta Dhakla, Harpreet, Sarvesh Kumar, Manish K. Kashyap. Suitability of LBSO/CuI as an Effective ETL/HTL for Perovskite Solar Cells: A Dry Lab Approach. *Indian J. of Pure & Applied Physics*, 2023, **61**, P. 931–933.
- [31] Faiza Azri, Afak Meftah, Nouredine Sengouga, Amjad Meftah. Electron and hole transport layers optimization by numerical simulation of a perovskite solar cell. *Solar Energy*, 2019, **181**, P. 372–378.
- [32] Medina J.C.Z., Andrés E.R., Ruíz C.M., Espinosa E.C., Yarce L.T., Galeazzi Isasmendi R., Trujillo R.R., Salgado G.G., Solis A.C., Caballero F.G.N. Numerical Simulation and Performance Optimization of a Solar Cell Based on WO₃/CdTe Heterostructure Using NiO as HTL Layer by SCAPS 1D. *Coatings*, 2023, **13**, 1436.
- [33] Raoui Y., Ez-Zahraouy H., Tahiri N., El Bounagui O., Ahmad S., Kazim S. Performance analysis of MAPbI₃ based perovskite solar cells employing diverse charge selective contacts: Simulation study. *Sol. Energy*, 2019, **193**, P. 948–955.
- [34] Zapukhlyak Z.R., Nykyryu L.I., Rubish V.M., Wisz G., Prokopiv V.V., Galushchak M.O., Lishchynskyy I.M., Katanova L.O., Yavorskyi R.S. SCAPS Simulation of ZnO/CdS/CdTe/CuO Heterostructure for Photovoltaic Application. *Physics and Chemistry of Solid-State*, 2020, **21** (4), P. 660–668.
- [35] Singh A.K., et al. Performance optimization of lead free-MASnI₃ based solar cell with 27 % efficiency by numerical simulation. *Opt. Mater.*, 2021, **117**, 11193.
- [36] Hossain M.K., Rubel M.H.K., Toki G.F.I., Alam I., Rahman M.F., Bencherif H. Deep Insights into the Coupled Optoelectronic and Photovoltaic Analysis of Lead-Free CsSnI₃ Perovskite-Based Solar Cell Using DFT Calculations and SCAPS-1D Simulations. *ACS Omega*, 2022, **7** (47), P. 43210–43230.

Information about the authors:

R. K. Shukla – Physics Department, Lucknow University, Lucknow-226007, India; ORCID 0000-0001-8505-963; rajeshkumarshukla00@gmail.com

Anchal Srivastava – Physics Department, Lucknow University, Lucknow-226007, India; ORCID 0000-0002-2588-5541; asrivastava.lu@gmail.com

Shikha Rani – Physics Department, Lucknow University, Lucknow-226007, India; ORCID 0009-0003-3326-0706; shikharani0395@gmail.com

Nidhi Singh – Physics Department, Lucknow University, Lucknow-226007, India; ORCID 0009-0004-6393-2056; nidhisingh1396@gmail.com

Vishnu Kumar Dwivedi – Physics Department, Lucknow University, Lucknow-226007, India; ORCID 0000-0001-6698-7598; vishnudmts@gmail.com

Sharda Pandey – Physics Department, Lucknow University, Lucknow-226007, India; ORCID 0000-0001-9950-1195; sharda2012536@gmail.com

Navina Wadhvani – Physics Department, Lucknow University, Lucknow-226007, India; ORCID 0009-0005-0465-0486; navinawadhvani@gmail.com

Declaration of Competing Interest: The authors declare that they have no known competing financial interests or personal relationships that could have appeared to influence the work reported in this paper.

Conflict of interest: The authors declare no conflict of interest.



NANOSYSTEMS:

PHYSICS, CHEMISTRY, MATHEMATICS

INFORMATION FOR AUTHORS

The journal publishes research articles and reviews, and also short scientific papers (letters) which are unpublished and have not been accepted for publication in other magazines. Articles should be submitted in English. All articles are reviewed, then if necessary come back to the author to completion.

The journal is indexed in Web of Science Core Collection (Emerging Sources Citation Index), Chemical Abstract Service of the American Chemical Society, Zentralblatt MATH and in Russian Scientific Citation Index.

Author should submit the following materials:

1. Article file in English, containing article title, the initials and the surname of the authors, Institute (University), postal address, the electronic address, the summary, keywords, MSC or PACS index, article text, the list of references.
2. Files with illustrations, files with tables.
3. The covering letter in English containing the article information (article name, MSC or PACS index, keywords, the summary, the literature) and about all authors (the surname, names, the full name of places of work, the mailing address with the postal code, contact phone number with a city code, the electronic address).
4. The expert judgement on possibility of publication of the article in open press (for authors from Russia).

Authors can submit a paper and the corresponding files to the following addresses: nanojournal.ifmo@gmail.com, popov1955@gmail.com.

Text requirements

Articles should be prepared with using of text editors MS Word or LaTeX (preferable). It is necessary to submit source file (LaTeX) and a pdf copy. In the name of files the English alphabet is used. The recommended size of short communications (letters) is 4-6 pages, research articles– 6-15 pages, reviews – 30 pages.

Recommendations for text in MS Word:

Formulas should be written using Math Type. Figures and tables with captions should be inserted in the text. Additionally, authors present separate files for all figures and Word files of tables.

Recommendations for text in LaTeX:

Please, use standard LaTeX without macros and additional style files. The list of references should be included in the main LaTeX file. Source LaTeX file of the paper with the corresponding pdf file and files of figures should be submitted.

References in the article text are given in square brackets. The list of references should be prepared in accordance with the following samples:

- [1] Surname N. *Book Title*. Nauka Publishing House, Saint Petersburg, 2000, 281 pp.
- [2] Surname N., Surname N. Paper title. *Journal Name*, 2010, **1** (5), P. 17-23.
- [3] Surname N., Surname N. Lecture title. In: Abstracts/Proceedings of the Conference, Place and Date, 2000, P. 17-23.
- [4] Surname N., Surname N. Paper title, 2000, URL: <http://books.ifmo.ru/ntv>.
- [5] Surname N., Surname N. Patent Name. Patent No. 11111, 2010, Bul. No. 33, 5 pp.
- [6] Surname N., Surname N. Thesis Title. Thesis for full doctor degree in math. and physics, Saint Petersburg, 2000, 105 pp.

Requirements to illustrations

Illustrations should be submitted as separate black-and-white files. Formats of files – jpeg, eps, tiff.



NANOSYSTEMS:

PHYSICS, CHEMISTRY, MATHEMATICS

Журнал зарегистрирован

Федеральной службой по надзору в сфере связи, информационных технологий и массовых коммуникаций

(свидетельство ПИ № ФС 77 - 49048 от 22.03.2012 г.)

ISSN 2220-8054

Учредитель: федеральное государственное автономное образовательное учреждение высшего образования

«Национальный исследовательский университет ИТМО»

Издатель: федеральное государственное автономное образовательное учреждение высшего образования

«Национальный исследовательский университет ИТМО»

Отпечатано в Учреждении «Университетские телекоммуникации»

Адрес: 197101, Санкт-Петербург, Кронверкский пр., 49

Подписка на журнал НФХМ

На второе полугодие 2024 года подписка осуществляется через

ОАО «АРЗИ», подписной индекс Э57385